



[www.icens.eu](http://www.icens.eu)


# ICENS

---

7TH INTERNATIONAL CONFERENCE ON  
ENGINEERING AND NATURAL  
SCIENCES

---

**BOOK OF PROCEEDINGS**



*June 23-27, 2021*

# Organized by



**CSUN**



# Partners



**7th INTERNATIONAL CONFERENCE ON ENGINEERING AND NATURAL  
SCIENCES (ICENS)**

**ISBN 978-605-81426-1-9**

**ISSN 2687-2447**

**PROCEEDINGS OF THE  
7th INTERNATIONAL CONFERENCE ON ENGINEERING AND NATURAL  
SCIENCES (ICENS) (ICENS 2021)  
JUNE 23 TO 27, 2021 (HYBRID CONFERENCE)**

**Edited by**

Prof. Dr. Özer Çınar

© CNR Group, 2021

**Published by:**

**info@icens.eu  
www.icens.eu  
www.cnrgroup.eu**

CNR Group Laboratuvar ve Arge Hizmetleri Sanayi Ticaret Limited Şirketi Çifte Havuzlar Mah., Eski Londra Asfaltı Cad., Kuluçka Mrk., A1 Blok, 151/1C, İç Kapı No:1 B-20, Esenler / İstanbul, 34220

This work is subject to copyright. All rights are reserved, whether the whole or part of the material is concerned. Nothing from this publication may be translated, reproduced, stored in a computerized system or published in any form or in any manner, including, but not limited to electronic, mechanical, reprographic or photographic, without prior written permission from the publisher. The individual contributions in this publication and any liabilities arising from them remain the responsibility of the authors. The publisher is not responsible for possible damages, which could be a result of content derived from this publication.

ISBN 978-605-81426-1-9

ISSN 2687-2447

## SCIENTIFIC COMMITTEE

1. Prof. Dr. Adisa Parić - University of Sarajevo - Bosnia and Herzegovina
2. Prof. Dr. Aleksandar Dimitrov - Ss. Cyril and Methodius University - North Macedonia
3. Prof. Dr. Alexander Golub - National University of Kyiv-Mohyla Academy - Ukraine
4. Prof. Dr. Alexander Litvinenko - National University of Food Technologies (Kyiv) - Ukraine
5. Prof. Dr. Alit Ibraimi - University of Tetova - North Macedonia
6. Prof. Dr. Anita Grozdanov - Ss. Cyril and Methodius University - North Macedonia
7. Prof. Dr. Asif Šabanović – International University of Sarajevo - Bosnia and Herzegovina
8. Prof. Dr. Bekir Erol Ak - Harran University - Turkey
9. Prof. Dr. Cem Şensöğüt - Dumlupınar University - Turkey
10. Prof. Dr. Christos Douligeris - University of Erlangen-Nurnberg - Germany
11. Prof. Dr. Dragutin T. Mihailović - University of Novi Sad - Serbia
12. Prof. Dr. Evgeniy Shtefan - National University of Food Technologies (Kyiv) - Ukraine
13. Prof. Dr. Falko Dressler - University of Paderborn - Germany
14. Prof. Dr. Houssam Toutanji – Western Michigan University - USA
15. Prof. Dr. Ian F. Akyıldız – Georgia Institute of Technology - USA
16. Prof. Dr. İsmail Usta - Marmara University - Turkey
17. Prof. Dr. Kateryna Derevska - National University of Kyiv-Mohyla Academy - Ukraine
18. Prof. Dr. Liljana Gavrilovska - Ss Cyril and Methodius University - Macedonia
19. Prof. Dr. Lukman Thalib - Qatar University - Qatar
20. Prof. Dr. M. Asghar Fazel – University of Environment - Iran
21. Prof. Dr. Mikhailov Volodymyr - Taras Shevchenko National University of Kyiv - Ukraine
22. Prof. Dr. Mykola Glybovets - National University of Kyiv-Mohyla Academy - Ukraine
23. Prof. Dr. Muammer Koç - Hamad bin Khalifa University - Qatar
24. Prof. Dr. Nadia Bilko - National University of Kyiv-Mohyla Academy - Ukraine
25. Prof. Dr. Özer Çınar – Yıldız Technical University - Turkey
26. Prof. Dr. Perica Paunovik - Ss. Cyril and Methodius University - Macedonia
27. Prof. Dr. Rifat Škrijelj – University of Sarajevo - Bosnia and Herzegovina
28. Prof. Dr. Samir Đug - University of Sarajevo - Bosnia and Herzegovina
29. Prof. Dr. Tanju Karanfil – Clemson University - USA
30. Prof. Dr. Ümit Alver – Karadeniz Technical University - Turkey
31. Prof. Dr. Wolfgang Gerstaecker - University of Erlangen-Nurnberg - Germany
32. Prof. Dr. Vladyslav Sukhenko - National University of Life and Environmental Sciences of Ukraine (Kyiv) - Ukraine
33. Prof. Dr. Vullnet Ameti - University of Tetova - North Macedonia
34. Prof. Dr. Yılmaz Yıldırım - Bülent Ecevit University - Turkey
35. Prof. Dr. Yousef Haik - Hamad bin Khalifa University - Qatar
36. Assist. Prof. Dr. Agon Memeti - University of Tetova - North Macedonia
37. Assoc. Prof. Dr. Alaa Al Hawari - Qatar University - Qatar
38. Assist. Prof. Dr. Arianit Reka - University of Tetova - North Macedonia
39. Assoc. Prof. Dr. Fatih Urgan - Cumhuriyet University - Turkey
40. Assoc. Prof. Dr. Izudin Dzafic - International University of Sarajevo - Bosnia and Herzegovina
41. Assoc. Prof. Dr. Kateryna Syera - National University of Life and Environmental Sciences of Ukraine (Kyiv) - Ukraine
42. Assist. Prof. Dr. Muhamed Hadziabdic - International University of Sarajevo - Bosnia and Herzegovina
43. Assoc. Prof. Dr. Nusret Drešković - University of Sarajevo - Bosnia and Herzegovina
44. Assoc. Prof. Dr. Polina Vakuliuk - National University of Kyiv-Mohyla Academy - Ukraine
45. Assoc. Prof. Dr. Senija Tahirovic - International University of Sarajevo - Bosnia and Herzegovina
46. Assoc. Prof. Dr. Victor Karamushka - National University of Kyiv-Mohyla Academy - Ukraine
47. Assoc. Prof. Dr. Victoria Konovalova - National University of Kyiv-Mohyla Academy - Ukraine
48. Assoc. Prof. Dr. Yuriy Kravchenko - National University of Life and Environmental Sciences of Ukraine (Kyiv) - Ukraine
49. Assist. Prof. Dr. Fatih Taktak - Uşak University - Turkey
50. Assist. Prof. Dr. Fouzi Tabet - German Biomass Research Center - Germany
51. Assist. Prof. Dr. Haris Gavranovic - International University of Sarajevo - Bosnia and Herzegovina
52. Assist. Prof. Dr. Hüseyin Pehlivan - Gebze Technical University - Turkey
53. Assist. Prof. Dr. Sasan Rabieh - Shahid Beheshti University - Iran
54. Assist. Prof. Dr. Ševkija Okerić - University of Sarajevo - Bosnia and Herzegovina
55. Assist. Prof. Dr. J. Amudhavel - VIT Bhopal University - India
56. Dr. Zsolt Hetesi - National University of Public Service, Budapest - Hungary
57. Dr. Zsolt T. Németh - National University of Public Service, Budapest - Hungary

## **ORGANIZATION COMMITTEE**

### **Chairman of the Conference**

Prof. Dr. Özer Çınar – Yıldız Technical University

### **Members of the Committee**

Prof. Dr. Ümit Alver (Co-Chairman) - Karadeniz Technical University - Turkey

Assist. Prof. Dr. Sasan Rabieh - Shahid Beheshti University - Iran

Alma Ligata - Zenith Group - Bosnia and Herzegovina

Ismet Uzun - Zenith Group - Bosnia and Herzegovina

Musa Kose - Zenith Group - Bosnia and Herzegovina

# ***WELCOME TO ICENS 2021***

*On behalf of the organizing committee, we are pleased to announce that the 6th International Conference on Engineering and Natural Sciences (ICENS 2021) held from June 23 To 27, 2021 (Hybrid Conference). ICENS provides an ideal academic platform for researchers to present the latest research findings and describe emerging technologies, and directions in Engineering and Natural Sciences issues. The conference seeks to contribute to presenting novel research results in all aspects of Engineering and Natural Sciences. The conference aims to bring together leading academic scientists, researchers and research scholars to exchange and share their experiences and research results about all aspects of Engineering and Natural Sciences. It also provides the premier interdisciplinary forum for scientists, engineers, and practitioners to present their latest research results, ideas, developments, and applications in all areas of Engineering and Natural Sciences. The conference will bring together leading academic scientists, researchers and scholars in the domain of interest from around the world. The scientific program will focus on current advances in the research, production and use of Engineering and Natural Sciences with particular focus on their role in maintaining academic level in Engineering and Applied Sciences and elevating the science level. The conference's goal will to provide a scientific forum for all international prestige scholars around the world and enable the interactive exchange of state-of-the-art knowledge. The conference will focus on evidence-based benefits proven in clinical trials and scientific experiments.*

***Best regards,  
Prof. Dr.Özer ÇINAR***

CONTENT	Country	Page
Targeted Dual Therapy with Curcumin Encapsulated Liposomes for Treatment of Glioblastoma	Turkey	1
Reference Sources for Calibration of Forehead Thermometers	Turkey	10
Derivation of Mechanical Properties of Polyester Geogrids Using Constant Strain Rate Loading Test	Egypt	15
Detection of Micron-Scale Particles on Optical Surfaces by Photothermal Method	Turkey	25
On the Calibration of Diffraction Grating Based Monochromators	Turkey	29
Numerical investigation of natural convection heat transfer of nanofluids in a square cavity	Algeria	38
Evaluation of a novel bio-waste obtained from sawdust as an adsorbent for removal of Pyronin B	Turkey	47
Control Algorithms for Bosonic Quantum Batteries: Parallel versus Collective Charging	Turkey	55
Non-classical Algorithm to Control Epileptiform Regime in the Small Population of Hodgkin-Huxley Neurons	Turkey	60
Simulation of Streamflow Using SWAT Model	Turkey	67
Determination of Watershed Features Using Geographic Information System (GIS)	Turkey	75
Geo-electrical characteristics of the Erecek-Canakkale region	Turkey	83
Towards High Precision Satellite Based Real Time Positioning with Trimble RTX Service	Turkey	90
A New Filtering and Analysis Approach for Poor Quality GNSS Data	Turkey	96
Experimental Results and Analysis of Structural Monitoring Using GNSS and Other Positioning Techniques	Turkey	105

Autonomous Network Management in Software Defined Networks	Turkey	112
The Developed FEA-Based Program for Planar Static Analysis with a Special 12x12 Rectangular Element	Turkey	117
The Developed FEA-Based Program for Planar Dynamic Analysis with a Special 12x12 Rectangular Element	Turkey	125
Sparse Matrix Converter Modelling And Simulation	Turkey	134
Investigation of the Potential In Vitro Usage of Asialoglycoprotein Receptor Targeted Magnetic Nanoparticles for Hepatocellular Carcinoma	Turkey	143
Asialoglycoprotein Receptor Targeted Magnetic Nanoparticles For Hepatocellular Carcinoma Treatment	Turkey	149
The Transition of Romanian Agriculture: From Traditional Agriculture to a Digital, Sustainable Agriculture	Romania	156
Taxidermy effluent characterisation: A case study in the City of Tshwane	South Africa	163
The Importance Of Successive Or Double Agricultural Crops In South-Eastern Of Romania, In The Climatic Change Perspective	Romania	172
Fever Detection from Human Thermal Images with Deep Learning Methods	Turkey	181
Prediction of long-term modulus, and correlation of local to global strain for polyester geogrids under services loading	Egypt	188
Performance Analysis of Long Baseline GPS RTK	Turkey	198
Prevalance of Wolbachia in Culex pipiens populations in Turkey	Turkey	205
Validation of QuEChERS Method for the Analyses of Chlorpyrifos-methyl, Lambda-cyhalothrin and Tebuconazole Residues in Grapes*	Turkey	211



# Targeted Dual Therapy with Curcumin Encapsulated Liposomes for Treatment of Glioblastoma

*Belguzar Karadag<sup>1\*</sup>, Guliz Ak<sup>1,2</sup>, Tugba Karakayali<sup>1,2</sup>, Baris Gumustas<sup>2</sup>, Gulce Danaci Ozmen<sup>2</sup>, Senay Sanlier<sup>1,2</sup>*

## Abstract

*Glioblastoma multiforme is one of the most aggressive brain tumors occurring in the central nervous system and should be treated immediately as it spreads very quickly. One of the most important limiting effects in treatment is the inability of the drug to cross the blood-brain barrier. In this situation, it is important to develop new treatment approaches for glioblastoma. In this study, carmustine, doxorubicin and curcumin-loaded, and polyethylene glycol coated liposomes were developed for efficient and targeted therapy of glioblastoma. As active components, carmustine is in the alkylating agent class, while curcumin is a herbal agent with a therapeutic effect. In addition, doxorubicin is used in many cancer treatments, including glioblastoma.*

*First, a pre-emulsion was prepared using different lipids, and the lipid emulsion was passed through a microfluidic device to obtain liposomes. Empty liposomes were studied under the specified conditions and the hydrodynamic size, polydispersity index (PDI) of the samples were determined. Then, triple drug-loaded liposomes were prepared using diluted amounts of each drug, carmustine, doxorubicin, and curcumin. The encapsulation efficiency (%) of drugs was determined using HPLC analysis. The hydrodynamic size of the triple drug-loaded liposomes was  $139.30 \pm 13.23$  nm, and PDI value was  $0.197 \pm 0.072$ . Finally, the surfaces of the liposomes were coated with DSPE-mPEG<sub>2000</sub> to cross the blood-brain barrier. Liposomes were also characterized. Consequently, liposomes are predicted to have the potential for further in vitro and in vivo studies.*

**Keywords:** Carmustine, curcumin, doxorubicin, glioblastoma, liposome, targeted drug delivery

## 1. INTRODUCTION

Liposomes are nano- or micro-sized vesicles consisting of one or more lipid layers surrounding an aqueous compartment ([1], [2], [3]). The hydrophilic compounds can either be attached to the aqueous core of the liposomes or placed at the interface between the lipid bilayer and the outer water phase. Lipophilic or

hydrophobic drugs are generally almost completely entrapped in the hydrophobic core of the lipid bilayers of liposomes.

Liposomes have the advantage of providing good biocompatibility, biodegradability, low toxicity, drug-targeted delivery, and controlled drug release ([4], [5]). The application of liposomes to aid drug release has an important impact in many biomedical fields. It is stated that liposomes are useful in stabilizing therapeutic compounds, overcoming barriers to cellular and tissue uptake, and improving the biodistribution of compounds

\*Corresponding author: Ege University, Department of Biochemistry, 35040, Bornova/Izmir, Turkey.  
[belguzar.karadag@hotmail.com](mailto:belguzar.karadag@hotmail.com)

<sup>1</sup>Ege University, Department of Biochemistry, 35040, Bornova/Izmir, Turkey.

<sup>2</sup>Ege University Center for Drug Research, Development, and Pharmacokinetics Applications (ARGEFAR), 35100, Bornova/Izmir, Turkey.

to target sites in vivo. It enables these compounds to be delivered to target sites effectively while minimizing systemic toxicity [6].

Glioblastoma multiforme (GB) is one of the most aggressive and common primary brain tumors arising in the central nervous system. Because glioblastomas spread so quickly, they should be treated as soon as possible. Treatment options include surgical intervention, radiation, and chemotherapy. Although some progress has been made in diagnosis and treatment over the years, there is no definitive cure for GB.

Since many drugs on the market cannot cross the blood-brain barrier and reach the brain and are ineffective in the treatment of brain diseases, recent research has aimed that the drug is effective in the targeted area, show the therapeutic effect in a shorter time, and show its effect by reducing its side effects. The use of liposomes is advantageous in reducing the side effects of drugs, providing passage through the blood-brain barrier, and effecting the drug on the desired region through active targeting [6].

To improve blood circulation and brain-specific delivery, the liposome surface can also be modified by adding macromolecules such as polymers, polysaccharides, peptides, antibodies, or aptamers. Optimizing the ideal liposome to cross the blood-brain barrier (BBB) has important implications for the treatment of neurological diseases. Different liposomal formulations and strategies have been developed to increase drug delivery to the BBB. However, the efficacy of various anticancer drugs has been measured by liposome delivery. Since many drugs on the market cannot cross the blood-brain barrier and reach the brain and are ineffective in the treatment of brain diseases, recent research aims that the drug is effective in the targeted area and show the therapeutic effect in a shorter time. The use of liposomes is advantageous to reduce the side effects of drugs, to ensure their passage through the blood-brain barrier, and to effect the drug on the desired region through active targeting. The ease of preparation of the selected drug delivery system and its contribution to the reduction of treatment costs increase its usability in clinical applications [6].

Significant research and preclinical studies have yielded positive results in liposome-assisted drug delivery over the past 50 years. For this reason, liposomes were preferred in the study. One of the most important phospholipids in the liposome structure is phosphatidylcholine (PC). Cholesterol, one of the bilayer compounds, is often incorporated into the bilayer to increase in vitro and in vivo stability. Cholesterol affects the fluidity of the phospholipid bilayers, thereby reducing their permeability for captured drugs. Cholesterol above a threshold concentration also reduces the enthalpy change associated with membrane phase transition, making liposomes less heat-sensitive [7].

In this study, PEG-coated liposomes with triple-drug load (BCNU, DOX, and CUR) were used to reduce the side effects of drugs, to ensure the passage through the blood-brain barrier, and to affect the drug on the desired region through active targeting.

## 2. MATERIAL AND METHOD

### 2.1. Material

Potassium chloride (KCl), potassium dihydrogen phosphate ( $H_2KO_4P$ ), cholesterol, doxorubicin (DOX) and curcumin (CUR), carmustine (BCNU) used in the project were purchased from Sigma-Aldrich. Disodium Phosphate ( $Na_2HPO_4$ ) and sodium chloride (NaCl) were obtained from the brand Riedel-de Haen. 2-Propanol (IPA) from Carlo Erba and HiPerSolv CHROMANORM, ethanol and acetonitrile (ACN) from Merck, phosphatidylcholine from LIPOID P75-3, lecithin from IFF Lucas MEYER Cosmetic.

### 2.2. Method

#### 2.2.1. Preparation of empty liposome

The liposome preparation, phosphatidylcholine, lecithin, and cholesterol were weighed in a 6:6:1 weight ratio, respectively [9]. It was then dissolved in ethanol by heating at 50-60°C. This ethanolic lipid solution (v/v) was diluted with pH 7.4 phosphate-buffered saline (PBS). Next, this pre-emulsion solution was applied through a certain pass at a certain pressure through the microfluidics brand Microfluidizer Processor M-110L to reduce the size of the liposomes [8]. For characterization studies, particle size and PDI of empty liposomes were determined using the Zetasizer Ultra (Malvern) instrument. In addition, a Thermo Scientific Apreo S scanning electron microscope (SEM) was used to determine the morphological structures of empty liposomes.

### 2.2.2. Preparation of liposomes containing BCNU, DOX, and CUR

Conditions for liposome formation were determined, and then the active substance loading (triple-drug loading) step was started. First, each drug was dissolved in its solvent. Because some drugs can dissolve better in different solvents. Thus, BCNU was dissolved in ethanol, CUR in acetonitrile, and DOX in PBS buffer. A certain amount of a mixture of drug solutions was used in the preparation of liposomes (Three drugs were mixed with liposomes).

Liposome samples were collected by passing the liposome suspension containing BCNU, DOX, and CUR through the microfluidic device at a certain pressure, at a certain pass. A schematic representation of the drug loading steps (BCNU, DOX, and CUR) into liposomes is given in Figure 1. After flow, the liposomes encapsulated in BCNU, DOX and CUR were centrifuged and the supernatant separated. Washing was done twice with PBS buffer under the same conditions. Unbound drugs were removed by these procedures.

The encapsulation efficiency (%) of the drugs was determined by performing the analysis on samples containing the supernatant and wash water for each, using high-performance liquid chromatography (HPLC) branded SHIMADZU LC-20AT, SHIMADZU LC-20AT (PDA), and SHIMADZU LC-20A. (equation 1). The image of the liposome suspension containing BCNU, DOX, and CUR prepared in the microfluidic device under the specified conditions is given in Figure 1. For characterization studies, the particle size of the triple drug-loaded liposomes and the PDI Zetasizer Ultra (Malvern) brand device were determined.

$$\text{Encapsulation Efficiency (\%)} = \frac{[\text{Initial drug amount (mg)} - \text{Encapsulated drug amount (mg)}]}{\text{Initial amount of drug (mg)}} \times 100 \quad (1)$$

### 2.2.3. Preparation of DSPE-mPEG<sub>2000</sub> coated liposome

For the preparation of DSPE-mPEG<sub>2000</sub> coated liposomes, a certain amount of PEG was weighed and dissolved with 1 mL of PBS. Afterward, the PEG formed was stirred at 60°C for a certain time, and the temperature was brought to 25°C immediately as a result of the process [10]. Then the prepared PEG solution 2.2.1. was added to the empty liposome obtained in. Thus, 10% PEG solution was prepared. After this stage, these prepared solutions were dialysis process for a certain period. Then, hydrodynamic size, and PDI of the PEG-coated liposome were performed for characterization study.

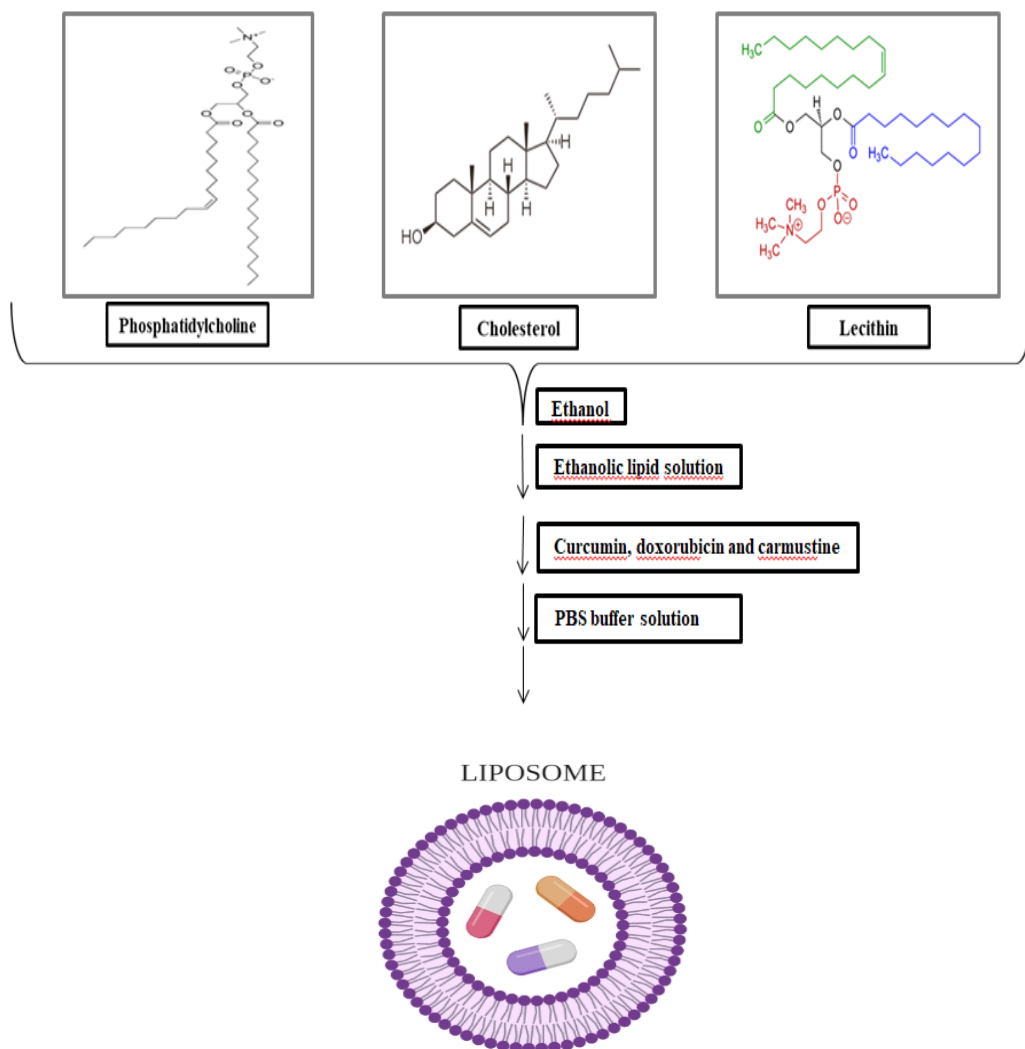


Figure 1. Schematic representation of drugs (BCNU, DOX, and CUR) loading steps into liposomes (drug-loaded liposome image was drawn with Biorender Program).

### 3. RESULTS AND DISCUSSION

#### 3.1. Preparation of empty liposome

Thanks to the use of liposome, one of the nanoparticle systems, in the treatment of glioblastoma, it is aimed to reduce the negative effects of chemotherapy in cancer treatment and to increase drug delivery to the cell level. In addition, it is of great importance to minimize the toxic properties of drugs by providing effective and safe treatment at low doses and to obtain the desired pharmacological response in the target area without harming healthy tissues.

In the study, a pre-emulsion was first prepared using phosphatidylcholine, lecithin, and cholesterol. To obtain the desired size liposome, the lipid solution forming the pre-emulsion was given to the microfluidic device, and the liposome sample was obtained. Considering the flows determined from the microfluidic device in the study of [8], it was determined that the liposome sizes decreased, and a more monodisperse structure was formed

with increasing pressure and increasing flow passage. Therefore, the prepared lipid mixture was passed through the microfluidic device at a certain pressure and in a certain amount to obtain a liposome of the desired size. The results of the hydrodynamic size and PDI value of the empty liposome at the specific passage through the microfluidic device are given in Table 1.

*Table 1. The results of the hydrodynamic size and PDI value of the empty liposome flow passing through the microfluidic device at a certain amount.*

	Hydrodynamic size (nm)	PDI
<b>The Designated Transition</b>	131.8±4.38	0.315±0.02

For characterization analysis, A: The hydrodynamic size plot of the empty liposome sample prepared at the passage specific passage and B: SEM analysis image to determine the morphology of the empty liposome sample are shown in Figure 2. The hydrodynamic dimensions of the empty liposome are 131.8±4.38 nm and the PDI is 0.315±0.02. The hydrodynamic size of liposomes is of great importance in the treatment of glioblastoma in terms of crossing the blood-brain barrier (KBB). It is stated in the literature that it is possible to overcome the blood-brain barrier (KBB) with nanoparticles with an average diameter of 100-400 nm [13]. The sizes in our study are in line with the literature, and the empty liposome sizes in the study are thought to have a suitable value in terms of both stability and crossing the BBB.

In the literature, liposomes loaded with 7-Ethyl-10-hydroxycamptothecin (SN-38) have been prepared using a microfluidic device. The particle size of the negatively charged liposomes was found to be 283.3 nm and their size was given as 100 nm according to SEM imaging [11]. In our study, it was determined that the particle sizes in the dry state were around 120 nm in the SEM examination. It was also found that the liposomes were nearly spherical. It is seen that the particle sizes in the dry state are lower than the particle sizes in the liquid state. It was determined that the results were in agreement with the literature.

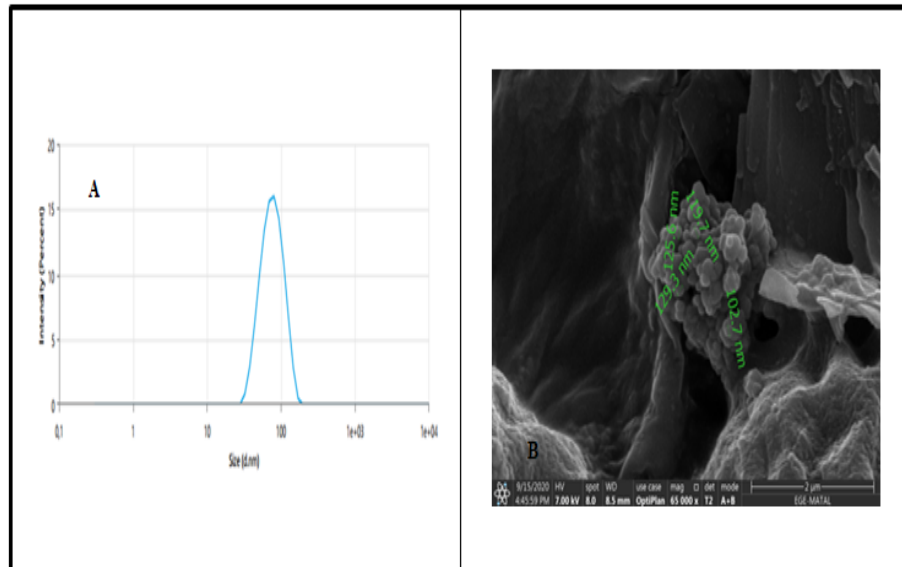


Figure 2. A: Hydrodynamic size plot of empty liposome at certain passage B: SEM image of empty liposome

### 3.2. Preparation of liposomes containing BCNU, DOX, and CUR

The hydrodynamic size and PDI values of the triple drug-containing liposomes prepared with certain initial concentrations of CUR, DOX, and BCNU for characterization studies are shown in Table 2. A: Hydrodynamic size plot of liposomes containing triple-drug prepared with certain initial concentrations of CUR, DOX, and BCNU, B: The encapsulation efficiency of liposomes containing BCNU, DOX, and CUR for each drug was determined by calculating the area values of the unencapsulated drugs in the supernatants. The results obtained are given in Figure 3. When the experimental data are examined, it is thought that the size values can exceed the BBB. It is also seen that the active substances are encapsulated in liposomes with high efficiency. It was determined that BCNU and CUR with the lipophilic structure were encapsulated at a much higher rate than DOX.

Table 2. Results of hydrodynamic size and PDI value of triple drug-containing liposome prepared with CUR, DOX, and BCNU at the determined initial concentration

BCNU, DOX and CUR concentration (µg/mL)	Hydrodynamic size (nm)	PDI
Specified Initial Concentration	139.30±13.23	0.197±0.072

For characterization studies A: Hydrodynamic size distribution plot of the liposome-containing triple-drug (CUR, DOX, and BCNU) prepared at the determined initial concentration, B: The % encapsulation efficiencies of the liposome containing the triple-drug (CUR, DOX, and BCNU) prepared at the determined initial concentration are shown in Figure 3.

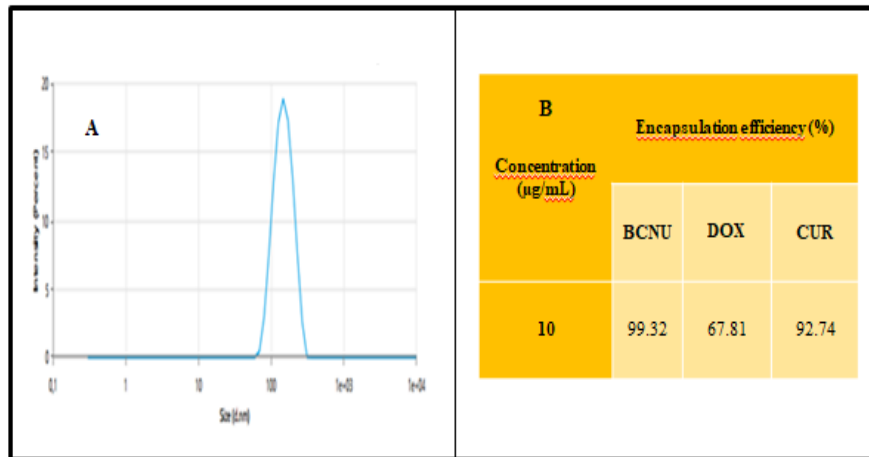


Figure 3. A: Size of liposome loaded with BCNU, CUR, and Dox, B: Encapsulation efficiency of BCNU, CUR, and Dox loaded liposome

### 3.3. Preparation of DSPE-mPEG<sub>2000</sub> coated liposome

The surfaces of the liposomes were coated with DSPE-mPEG<sub>2000</sub> to cross the BBB. Liposomes were also characterized. The hydrodynamic size and PDI value of 10% PEG-coated liposomes for characterization studies are given in Table 3. When the sizes are examined, it is thought that liposomes have an appropriate size in terms of both stability and crossing the BBB.

Table 3. Hydrodynamic size, and PDI value results of 10% PEG-coated liposome

	Hydrodynamic size (nm)	PDI
<b>10% PEG</b>	61.85±15.72	0.339±0.07

The hydrodynamic size distribution graph of 10% PEG-coated liposome for characterization studies is given in Figure 4. As a result of the experimental studies, it was determined that the size of the PEG-coated liposome was lower than the size of the empty liposome. In a study, pegylated liposomes containing SN-38 were prepared, and their properties such as particle size, encapsulation efficiency, *in vitro* drug release, and biodistribution were investigated. The encapsulation efficiency and *in the vitro* release rate of pegylated liposomes were higher than those of non-pegylated liposomes. As expected, the distribution of pegylated liposomes in body organs such as the liver, kidney, spleen, and lung was considerably lower than that of non-pegylated liposomes [12]. Dimensional analysis results in this study are consistent with our results.

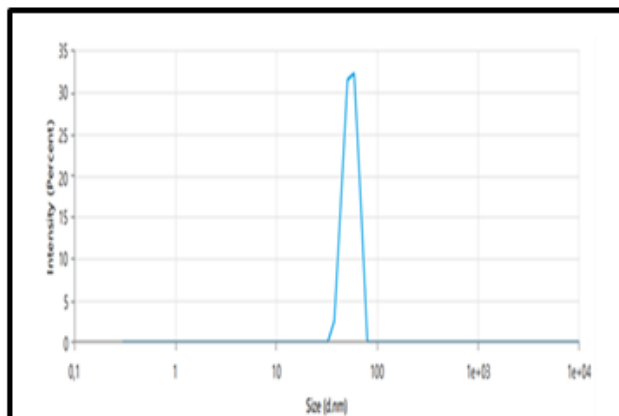


Figure 4. Hydrodynamic size distribution plot of 10% PEG-coated liposome,

#### 4. CONCLUSIONS

In the study, the hydrodynamic size and PDI values of the empty liposome were determined for characterization studies, and the SEM image was evaluated for the morphology of the empty liposomes. In addition, liposomes containing doxorubicin, carmustine, and curcumin were also evaluated in terms of hydrodynamic size, PDI values, and encapsulation efficiency was calculated. Also, the surfaces of the liposomes were coated with DSPE-mPEG<sub>2000</sub> so that they could pass through the BBB. When these studies are evaluated, it is estimated that liposomes have good potential for in vitro and in vivo studies. The fact that the experimental data yielded results compatible with the literature sheds light on the next experimental stages.

#### ACKNOWLEDGMENT

This study is financially supported by Ege University Scientific Research Projects (BAP) as a Multidisciplinary Priority Area Research Project (ONAP), project no: TOA-2020-20996. Also, The authors would like to acknowledge for Ege University Pharmaceutical Research, Development, and Pharmacokinetic Applications Center (ARGEFAR) for their support of the experimental studies.

#### REFERENCES

- [1]. Lai, F.; Fadda, A. M.; Sinico, C. Liposomes for Brain Delivery. *Expert Opin. Drug Deliv.* 2013, 10 (7), 1003–1022. <https://doi.org/10.1517/17425247.2013.766714>.
- [2]. Micheli, M. R.; Bova, R.; Magini, A.; Polidoro, M.; Emiliani, C. Lipid-Based Nanocarriers for CNS-Targeted Drug Delivery. *Recent Patents on CNS Drug Discovery.* 2012. <https://doi.org/10.2174/157488912798842241>.
- [3]. Schnyder, A.; Huwyler, J. Drug Transport to Brain with Targeted Liposomes. *NeuroRx* 2005. <https://doi.org/10.1602/neurorx.2.1.99>.
- [4]. Noble, G. T.; Stefanick, J. F.; Ashley, J. D.; Kiziltepe, T.; Bilgicer, B. Ligand-Targeted Liposome Design: Challenges and Fundamental Considerations. *Trends in Biotechnology.* 2014. <https://doi.org/10.1016/j.tibtech.2013.09.007>.
- [5]. Torchilin, V. P. Recent Advances with Liposomes as Pharmaceutical Carriers. *Nature Reviews Drug Discovery.* 2005. <https://doi.org/10.1038/nrd1632>.
- [6]. Hanson, L. R.; Fine, J. M.; Svitak, A. L.; Faltesek, K. A. Intranasal Administration of CNS Therapeutics to Awake Mice. *J. Vis. Exp.* 2013. <https://doi.org/10.3791/4440>.
- [7]. Sadeghi, N., Deckers, R., Ozbakir, B., Akthar, S., Kok, R. J., Lammers, T., and Storm, G. (2018). Influence of cholesterol inclusion on the doxorubicin release characteristics of lysolipid-based thermosensitive liposomes. *International journal of pharmaceutics*, 548(2), 778-782.



- [8]. Lajunen, T.; Hisazumi, K.; Kanazawa, T.; Okada, H.; Seta, Y.; Yliperttula, M.; Urtti, A.; Takashima, Y. Topical Drug Delivery to Retinal Pigment Epithelium with Microfluidizer Produced Small Liposomes. *Eur. J. Pharm. Sci.* 2014, 62, 23–32. <https://doi.org/10.1016/j.ejps.2014.04.018>.
- [9]. Huang, X.; Caddell, R.; Yu, B.; Xu, S.; Theobald, B.; Lee, L. J.; Lee, R. J. Ultrasound-Enhanced Microfluidic Synthesis of Liposomes. *Anticancer Res.* 2010, 30 (2), 463–466.
- [10]. Mare, R.; Paolino, D.; Celia, C.; Molinaro, R.; Fresta, M.; Cosco, D. Post-Insertion Parameters of PEG-Derivatives in Phosphocholine-Liposomes. *Int. J. Pharm.* 2018, 552 (1–2), 414–421. <https://doi.org/10.1016/j.ijpharm.2018.10.028>.
- [11]. Casadó, A., Sagristá, M. L., and Mora, M. (2018). A novel microfluidic liposomal formulation for the delivery of the SN-38 camptothecin: characterization and in vitro assessment of its cytotoxic effect on two tumor cell lines. *International journal of nanomedicine*, 13, 5301.
- [12]. Atyabi, F., FarkhondehfaL, A., Esmaceli, F., and Dinarvand, R. (2009). Preparation of pegylated nano-liposomal formulation containing SN-38: in vitro characterization and in vivo biodistribution in mice. *Acta Pharmaceutica*, 59(2), 133-144.
- [13]. Cetin M., Capan Y. (2004). “Beyne Ilac Hedeflendirilmesi”, *Ankara Eczacilik Fakultesi Dergisi*, 33 (4) 287–305.

## BIOGRAPHY

Belguzar Karadag graduated from Celal Bayar University, Department of Chemistry. She then completed her master's degree in the Department of Biochemistry, which is a sub-branch of the Department of Chemistry at Dokuz Eylul University. He is currently a PhD student at Ege University, Department of Biochemistry. She is currently working on nanoparticles, which are targeted drug delivery systems in cancer treatment.

# Reference Sources for Calibration of Forehead Thermometers

Mehtap Can<sup>1,2</sup>, Yasin Kisioglu<sup>1</sup>, Humbat Nasibov<sup>2</sup>

---

## Abstract

According to the recent studies, diseases caused by influenza and similar viruses increase the human body temperature (HBT). Therefore, measurement of HBT, continuous fever screening in social areas with human flow, detection of these diseases and then isolation of these people play an important role in reducing the spread of epidemic diseases. The concept of social distance, which has been mandated during the COVID-19 pandemic, highlighted the importance of remote and non-contact HBT measurements. For this purpose, HBT measurements, the use of forehead thermometers due to their ability to perform rapid and non-contact measurements in fever scans and thermal cameras has become widespread. On the other hand, it is critical to have traceable calibrations of these devices for accurate measurement. In this study, a comparative analysis for the performance of two different reference sources, which can be calibrated for forehead thermometers with high precision, has been completed. First of all, surface scanning of these reference has been done by using a high precision and resolution thermal camera, and a transfer standard reference radiation thermometer. Then, the obtained results have been compared. Moreover, the temperature distributions of the active radiant areas of the reference sources have been extracted from the obtained results. Subsequently, both sources have been set to the same temperature values at certain intervals and their stability has been checked. Besides, ten forehead thermometers from different manufacturers have been calibrated by using two different reference sources. According to these measurements, it has been concluded that both reference sources can be used in the calibration of forehead thermometers with high accuracy.

**Keywords:** Active Radiative Surface, Body Temperature, Calibration, Forehead Thermometer, Reference Source

---

## 1. INTRODUCTION

In various infectious diseases such as influenza or SARS-CoV-2 infections, one of the immune system's responses to infections is fever. As a result of the studies carried out in the Covid-19 pandemic, the use of non-contact infrared thermometers in human body temperature measurement has become widespread. In the measurement of body temperature from the skin, the superficial temporal artery meets the necessary needs [1]. Since it is critical to ensure that the thermometers to be used in body temperature measurements will give safe results, the thermometers to be used should be calibrated regularly in a traceable manner. Since the thermometer must be suitable for the operating temperature range and band emissivity, the total band emissivity must first be determined for the selection of the reference radiation source and calibrator to be used. The main motivation of the studies is the establishment of the mechanism to be used for the calibration of infrared forehead thermometers within the traceability chain for the first time in Turkey. In this study, it is aimed to calculate the emissivity of the reference radiation source, which is thought to be used in the calibration of forehead thermometers, and to control its homogeneity. Thanks to the system to be established, the calibrations of forehead thermometers will be carried out at the TUBITAK-UME Thermodynamic Metrology Laboratory and

---

<sup>1</sup> Corresponding author: Kocaeli University, The Institute of Science, Biomedical Engineering, 41000, Kocaeli, Turkiye, [mehtapcan2015@gmail.com](mailto:mehtapcan2015@gmail.com)

<sup>2</sup> TUBITAK-UME- National Metrology Institute, Thermodynamic Lab.41400, Gebze/Kocaeli, Turkey. [humbet.nasibli@tubitak.gov.tr](mailto:humbet.nasibli@tubitak.gov.tr)

when instructions are sent to the second level calibration laboratories, the calibrations in these laboratories will also be in accordance with the traceability chain.

## 2. RECOMMENDED METHOD

In this study, a new system was established for the measurement of emissivity of HGH brand surface type radiation source, which can be used in the traceable calibration of forehead thermometers. In this system, the Heitronics-ME30 model cavity-type standard reference black body, digital liquid baths, RTD Pt100, HGH brand reference radiation source, the controller of this source, and standard reference pyrometer are used. Figure 1 shows the measurement setup of the ME30 model blackbody radiation used as a reference with a reference pyrometer. Figure 2 shows the radiation measurement setup of the HGH DCN source with a reference pyrometer.

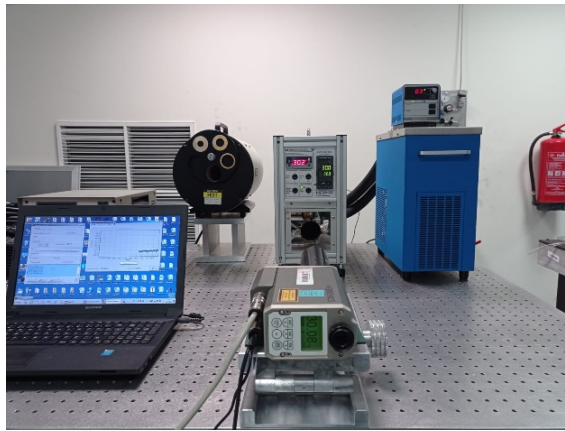


Figure 1. Measurement setup of ME30 model blackbody radiation used as a reference with a reference pyrometer

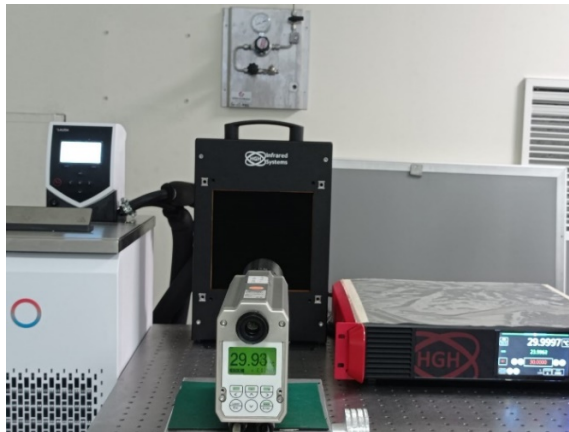


Figure 2. Radiation measurement setup of the HGH DCN model source using a reference pyrometer

The Heitronics-ME30 model blackbody was calibrated with a traceably calibrated Platinum Resistance Thermometer (RTD) in order to be used as a traceable reference radiation source. In this way, a traceability chain in accordance with ITS90 consisting of RTD, Heitronics ME30 black body, and reference pyrometer is provided.

Both radiation sources were set to temperatures of 30, 33, 36, and 40°C, respectively, and when they reached thermal equilibrium at these temperatures, thermogram images were taken with a thermal camera. In this way, the homogeneity of the active radiation surfaces was checked. After both radiation sources reached thermal

equilibrium at each temperature value separately, reading values were recorded at 1, 0.98, and 0.96 emissivity values. Then, the differences in the temperature readings due to the emissivity change at the same temperature values were compared.

In another phase of the study, 10 forehead thermometers from different manufacturers were calibrated in front of reference sources. To ensure that both sources are suitable for calibration, a surface scan was first taken with a reference pyrometer. In addition, surface temperature measurements were taken with a high-sensitivity and high-resolution thermal camera. As a result of these processes, it is seen that the active radiation surface temperature distributions of both sources are below 0.04°C. When both reference sources came to thermal equilibrium at the determined temperatures, reference values were taken with a reference pyrometer. Then, at these temperatures, it was calculated how much the reading of forehead thermometers in object mode deviated from this reference value.

### 3. EXPERIMENTAL RESULTS

In Table 1, the average temperature values read when the emissivity values of 1, 0.98, and 0.96 are adjusted from the pyrometer while both sources are in thermal equilibrium at temperature values of 30, 33, 36, and 40°C are given.

Table 1. Temperature readings of ME30 and HGH DCN model radiation sources at different temperatures and emissivity values

The Temperature at which Sources Are Set (°C)	Emissivity Value	Source Type	Temperature Reading from Pyrometer (°C)
30	1	ME30	30,056
		HGH	29,812
	0,98	ME30	30,104
		HGH	29,932
	0,96	ME30	30,161
		HGH	29,964
33	1	ME30	32,881
		HGH	32,614
	0,98	ME30	33,08
		HGH	32,834
	0,96	ME30	33,17
		HGH	32,985
36	1	ME30	35,87
		HGH	35,766
	0,98	ME30	36,011
		HGH	35,932
	0,96	ME30	36,187
		HGH	36,087
40	1	ME30	39,767
		HGH	39,664
	0,98	ME30	40,03
		HGH	39,858
	0,96	ME30	40,285
		HGH	40,055

In order to compare the change in the temperature readings of both sources depending on the emissivity change, the difference values were calculated, and using these values, the graphs as shown in Figure 3 were obtained. The difference between the mean temperature value seen when the emissivity is set as 0.98 with the serial "1" and the average temperature value when set as 1 is shown. With "2", the difference between the average

temperature value seen when the emissivity is set to 0.96 and the average temperature value is seen when set to 0.98 is shown. Figure 4 shows the deviation values of forehead thermometers from the reference value in object measurement mode, while ME30 and HGH DCN model radiation sources are at temperature values between 33°C and 42°C.

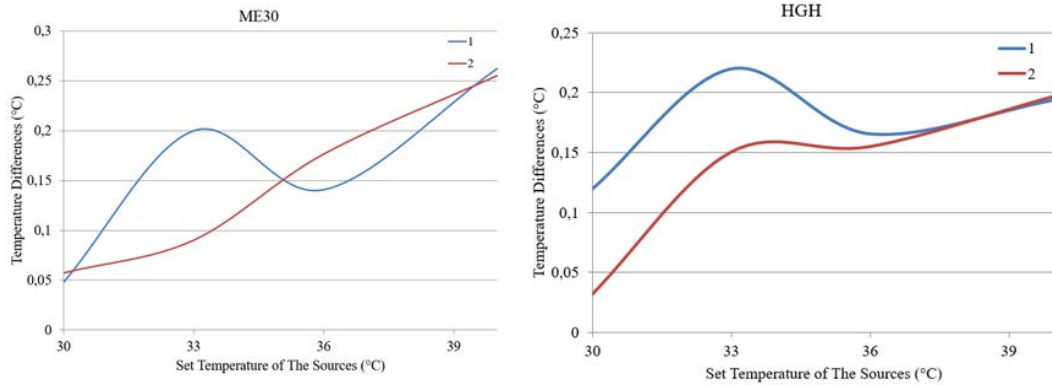


Figure 3. Average temperature changes read from sources due to emissivity change

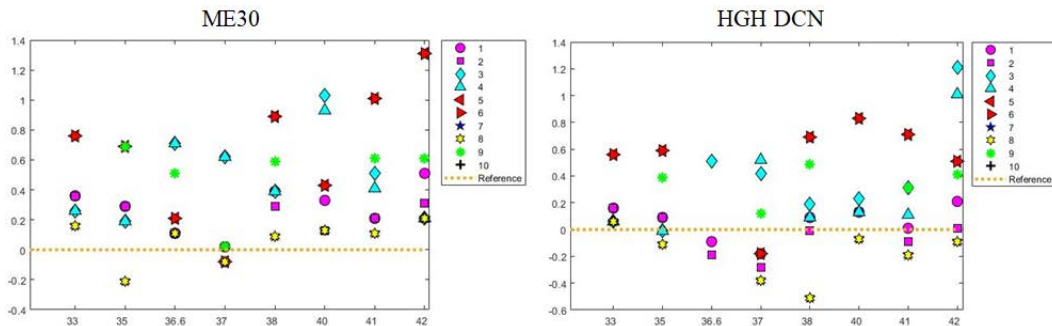


Figure 4. The deviation amounts of the values read from the forehead thermometers used compared to the reference value

## 4. CONCLUSION

The uncertainty value accepted as the international metrology standard for the calibration of forehead thermometers is 0.6°C while  $k=2$  [2]. As a result of this study, when the uncertainty component value  $\pm 0.1^\circ\text{C}$  obtained from the HGH branded source is added to the measurement uncertainty budget, the standard total calibration uncertainty does not exceed  $\pm 0.3^\circ\text{C}$ . In this way, it has been proven that the HGH DCN branded radiation source is in the 0.96-1 band of the emissivity measurement range and can be used as a calibration source in accordance with ITS90. In the calibration processes of 10 forehead thermometers from different manufacturers and with different working principles, using HGH DCN and ME30 model sources, it was observed that the resolution of all forehead thermometers used in the measurements taken at temperatures between 36.6°C and 37°C gave accurate results under the values specified by the manufacturers. It has been ensured that the forehead thermometers can be calibrated with high precision using both sources. Thanks to this setup, which was established, characterized and validated within the scope of the study, the calibration of forehead thermometers will be carried out at the TUBITAK-UME Thermodynamic Metrology Laboratory at the national and international levels. In addition, using the findings obtained, it will be ensured that the calibration of forehead thermometers can be traced in the second level calibration laboratories within the scope

of TURKAK, with the relevant instructions, guides, uncertainty budget, and training documents prepared by the UME-Thermodynamic Metrology Laboratory.

## **ACKNOWLEDGMENT**

The first author would like to express sincere thanks to TUBITAK-BIDEB COVID-19 STAR researcher scholarship.

## **REFERENCES**

- [1].M. CAN, "Emissivity Measurement of Reference Sources for Calibration of Non-Contact Human Body Temperature Meters", Kocaeli University, 2021.
- [2].I. Pušnik and J. Drnovšek, "Infrared ear thermometers-Parameters influencing their reading and accuracy," *Physiol. Meas.*, vol. 26:6, pp. 1075–1084, 2005.

# Derivation of Mechanical Properties of Polyester Geogrids Using Constant Strain Rate Loading Test

Abdelwahab Tahsin<sup>1</sup>, Rami El-Sherbiny<sup>2</sup>

---

## Abstract

The implementation of geosynthetics in civil engineering is becoming more recognized nowadays because of its superior rewards. Geosynthetics have proven to be among the most versatile and cost-effective ground strengthening techniques and soil improvement sustainable materials. The polymeric geogrids were recommended by most of International Codes as an appropriate sustainable soil reinforcement to replace the conventional metal reinforcement that used efficiently for soil improvement, roadway applications, and Mechanically Stabilized Earth MSE walls. Thus, mechanical properties and non-linear behavior of geogrids are dominant aspect in designing the soil reinforcement, MSE walls systems and significantly affect its performance and stability as well. This research work introduces analyses and results of laboratory constant strain rate (CSR) test of 20%, 10%, 6%, 3%, 1% and 0.05% strain/min conducted on five specimens of geosynthetics polyester (PET) geogrids manufactured by HUSKER. Tests were performed according to Multi-Rib tensile method ASTM D6637. Output acceptance features of tensile ultimate strength and strain at break were justified. Secant modulus at strain 1% and 2% were derived. Sensitivity of strain rate of loading on strength, stiffness and non-linear properties of geogrid was inspected. The higher CSR reveals increase of the measured secant modulus. The larger ultimate strength, the higher anticipated stiffness irrespective to loading strain rate. Based on the measured tensile load- strain relationship, the linear approximation of secant modulus is considerably acknowledged in the strain domain  $\leq 2\%$  which covers a wide scatter of geosynthetics reinforced structures conditions under service (working) loadings. The derived stiffness at 1% is larger than for 2% strain, which reflects phenomenon of non-linearity and stiffness relaxation with progressive elongation. Behavior of reinforced soil is sensitive to stiffness rather than strength of geogrid. For numerical modelling purposes, a simple correlation chart was developed to predict secant modulus of geosynthetic PET geogrid based on strength.

**Keywords:** Constant Strain Rate CSR test, Geosynthetics, Geogrid, MSE wall, non-linear, soil improvement, secant modulus

---

## 1. INTRODUCTION

The implementation of geosynthetics in civil engineering is becoming more recognized nowadays because of its superior rewards. Geosynthetics have proven to be among the most versatile and cost-effective ground strengthening techniques and soil improvement sustainable materials. The polymeric geogrids were recommended by most of International Codes as an appropriate sustainable soil reinforcement to replace the conventional metal reinforcement that used efficiently for soil improvement, roadway applications, and Mechanically Stabilized Earth MSE walls. Thus, mechanical properties and non-linear behavior of geogrids are dominant aspect in designing the soil reinforcement, MSE walls systems and significantly affect its performance and stability as well.

Hypostatically, the behavior of geosynthetic reinforced soil is complicated due to the mechanical complexity of component materials, their interactions, geosynthetic properties, and soil characteristics as well. Numerical modelling of geosynthetic reinforced soil systems is now extensively utilized for the design, prediction of

---

<sup>1</sup> Corresponding author: ACE Consulting Engineers, Cairo, Egypt, [abdelwahab.tahsin@gmail.com](mailto:abdelwahab.tahsin@gmail.com)

<sup>2</sup> Civil Engineering department, Cairo University, Egypt, [rsherbiny@gmail.com](mailto:rsherbiny@gmail.com)

measured responses, and in research to generate synthetic data for the purpose of filling-in knowledge gaps on the behavior of these systems. (Yan Yu and Richard J. Bathurst, 2016).

In the engineering community, the available technical data sheets promoted by the geosynthetics manufacturers include only key design features of the ultimate strength and strain at break. On the contrary, the information about stiffness and secant modulus are not disclosed. These stiffness data are essential key input parameters for numerical modelling (Finite Element Method). Also, the non-linear stress-strain relationship of the geosynthetics is necessary to be investigated by conducting series of laboratory tensile test, perform date interpretation of the measured test results and identify the secant modulus at various strain domains.

In this research paper work, we are focused on conducting proper geosynthetics characterization necessary for numerical simulations that can be used to predict operational (working stress) conditions rather than incipient wall collapse. A contribution of such undertaken proper material characterization of geosynthetics is essential for numerical finite element modelling for multi- asset application of geosynthetics reinforced soils such as: (a) soil reinforcement in the exhibition of high loads while strengthening of tailing impoundments and landfills, (a) soil improvement in general applications, (c) slope stability deemed to achieve the stability of sharp slopes in the presence of low shear strength deposits, and (d) mechanically stabilized earth wall to act as an efficient retaining system in an economical design basis.

## 2. MATERIALS AND METHODS

### 2.1. OVERVIEW

The current study comprises 5 sets of nominated specimens Fortrac 35T, 55T, 80T, 110T, and 150T with varying strength and stiffness. *Table 1* listed the physical properties of geogrid types as per the technical data sheet introduced by the manufacturer HUSKER. The standard raw material of these geogrids is the high-modulus polyester (PET), which of high stiffness, low creep and uniform product strength. The geogrid specimens were tested on a tensile test machine under Constant Strain Rate (CSR) test in accordance with ASTM D6637, to investigate: (a) Tensile ultimate strength KN/m, and (b) strain at break. The secant modulus (J) KN/m at strain of 1% and 2% were derived based on the tensile force- strain relationship which is necessary for numerical modelling simulation. The CSR was varied to study the effect of strain rate of loading on the tensile strength and stiffness of the examined specimens of the PET geogrid.

*Table 1. Physical properties for the tested geogrid types as per HUSKER data sheets*

PROPERTY	TEST	35T	55T	80T	110T	150T
Mass/Unit Area (g/m <sup>2</sup> )	ASTM D-5261	185	240	320	350	440
Aperture Size (mm)	measured	25 x 25	25 x 25	25 x 25	25 x 25	25 x 25
Percent open area	CWO 22125	70%	70%	65%	65%	62%
Ultimate wide width (MD) Tensile Strength (kN/m)	ASTM D-6637	<b>35</b>	<b>55</b>	<b>80</b>	<b>110</b>	<b>150</b>
Elongation at ultimate tensile strength –MD	ASTM D-6637	≤10%	≤10%	≤10%	≤10%	≤10%
Long term design strength- MD (kN/m)*	GRI GG4	18.8	29.5	42.9	59	81
Standard Roll Size (m)		5x100	5x100	5x100	5x100	5x100
Weight (kg)		114	141	182	192	205

\* To be reduced by factors: Durability = 1.2 and Installation= 1.2.



## 2.2. TEST APPARATUS AND SPECIMEN PREPARATION

TESTOMETRIC M500- 50CT Universal Testing machine was used to perform the geogrid load-extension under Constant Strain Rate CSR. The apparatus comprises main tensile machine, pressure jack and computer control unit. The tensile machine consists mainly of clamps, sensors for recording the tensile force, and other sensors to monitor the extent of grips separation. The clamps must be attached with suitable pressure to avoid slippage. Clamping pressure must be equal for all specimens under the same test to manage consistent judgment between the anticipated results. *Figure 1* presents photo of the tensile test apparatus and specimen installation prior to start of strain loadings. According to the Multi-Rib tensile method of ASTM D6637 "Standard Test Method for Determining Tensile Properties of Geogrids by the Single or Multi-Rib Tensile Method"; the specimen is schematically illustrated at *Figure 2* should be a minimum of 200 mm wide and contains five ribs in the cross-test direction by at least three junctions or 300 mm long in the direction of the testing. The outermost ribs are cut prior to testing to prevent slippage from occurring within the clamps as instructed by ASTM D6637, clause 8.2.4. Thus, the width of intact ribs is 120 mm. The room ambient temperature was 20°C during test procedures to avoid adverse impact of the temperature in the test results.

Minimum of three to five single tests were performed on the Machine Direction (MD) for each specimen of Fortrac 35T, 55T, 80T, 110T, and 150T, in accordance with ASTM D6637 using the multi- rib tensile method. Wide scatter of Constant Strain Rate CSR of 20%, 10%, 6%, 3%, 1% to slow rate loading 0.05% strain/min. were performed. The CSR was varied to study the effect of strain rate of loading on the tensile strength and stiffness of the PET geogrid. The tensile test results are necessary to address the main output acceptance features: (a) tensile ultimate strength kN/m, and (b) strain at break. The secant modulus (J) kN/m at strain of 1% and 2% were derived based on the tensile force- strain relationship which is necessary for numerical modelling simulation. Since the geogrid CSR tests were carried out at the same in-door ambient temperature of 20°C, temperature effect was not a factor in the test results accuracy.



Figure 1. Constant Strain Rate CSR tensile test apparatus

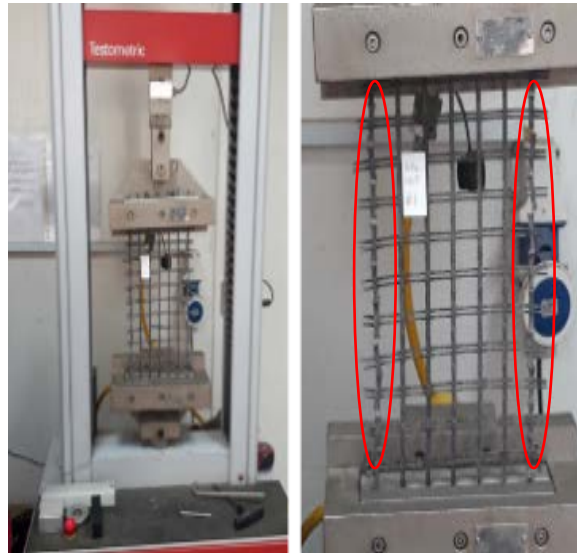
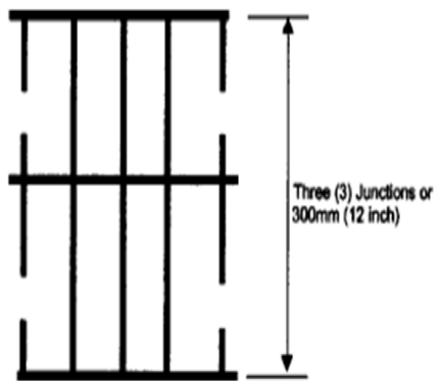


Figure 2. Specimen configuration; Multi-Rib tensile method -ASTM D6637

### 3. RESULTS AND DISCUSSION

#### 3.1. TENSILE LOAD VERSUS STRAIN TEST RESULTS

In accordance with ASTM D 4595 and after Hatami and Bathurst 2005; the determination of the ultimate strength is established on the peak strength measured during CSR of 10% strain/min. Based on the test measurement results, the Tensile Strength (kN) was derived by dividing the measured Peak Force by the width of intact ribs (120 mm). The Secant modulus kN/m at strain 2% was calculated by dividing the measured tensile force (at strain 2%) by 120 mm to get the tensile stresses then divided by 0.02 strain to result in the stiffness (secant modulus  $J_{2\%}$ ).

A range of 1.92-1.75 was derived for Factor Of Safety FOS which is safely covered the deemed long term strength as well as durability and installation factors (reductions) with wide acceptable margin as shown at Table 2. This FOS is calculated by dividing the mean measured tensile strength of the CSR tests listed in Table 2 by the long term design strength listed in Table 1 “physical properties of the examined geogrid as per the technical data sheet”. For example for 110T;  $FOS = 112.73/59.0 = 1.92$ . Hence, results are in good agreement with manufactures technical data sheet. The linear approximation of tensile load- strain response is considerable accepted in the strain domain up to 2% which covers a wide scatter of geosynthetics reinforced structures conditions under service (working) loadings. Sample of the test results for five single specimens at 20% /min of 35T, 55T, 80T, and 110T is presented at Figure 3.

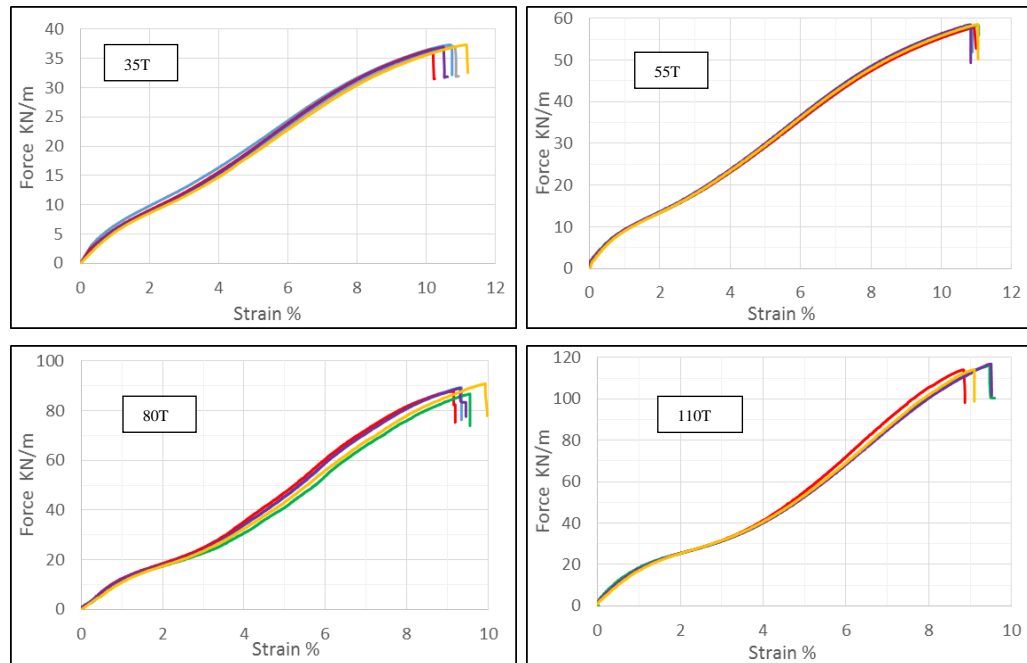


Figure 3. Force- strain response at CSR 20 %/min for the tested specimens of Fortrac 35T, 55T, 80T, and 110T

Table 2. CSR test results for 10% strain/min- ASTM D 4595

Type	Test	Peak Force (kN)	Tensile strength (kN/m)	Secant modulus kN/m (strain 2%)	Strain at peak %	Type	Test	Peak Force (kN)	Tensile strength (kN/m)	Secant modulus kN/m (strain 2%)	Strain at peak %
35T	1	4.30	35.85	384	10.3	80T	1	11.06	92.19	859	11.1
	2	4.41	36.74	377	10.6		2	9.69	80.75	822	10.0
	3	3.87	32.27	395	9.5		3	10.95	91.24	854	11.0
	4	4.21	35.07	389	10.3		4	8.81	73.42	923	9.9
	5	3.77	31.44	403	9.0		5	8.09	67.42	883	8.3
	mean	4.11	34.27	390	9.9		mean	9.72	81.00	868	10.1
55T	1	7.23	60.28	546	11.5	110T	1	15.7	130.83	1099	11.9
	2	7.08	58.98	528	11.4		2	15.08	125.67	1126	11.2
	3	6.12	51.03	512	10.7		3	14.06	117.13	1095	10.8
	4	6.05	50.43	537	9.6		4	11.48	95.67	1165	9.1
	5	6.10	50.83	558	10.8		5	11.32	94.33	1153	8.9
	mean	6.52	54.31	536	10.8		mean	13.53	112.73	1128	10.4

### 3.2. INFLUENCE OF STRAIN LOADING RATE ON STRENGTH

The CSR was varied at rates 20%/min, 10%/min, 6%/min, 3%/min, 1%/min, and 0.05%/min to study the effect of strain rate of loading on the tensile strength and stiffness of the examined PET geogrid specimens. The influence of CSR on the tensile force- strain relationship and ultimate strength is illustrated in *Figure 4* for the different geogrid examined specimens at rates 10%/min, 6%/min, 3%/min, and 1%/min where, the recorded tensile load increased as the CSR increased. The slow-rate rate 0.05%/min. was not conducted to the failure, as it consumed long time to reach the peak strain associated with failure. Testing was completed to approximate of 3% strain which cover wide range of the anticipated strain for service loading for various types of geosynthetic reinforced soil applications. Hence, the secant modulus at strain 2% was calculated accordingly.

Results show that, higher CSR reveals increase of the measured secant modulus. The larger ultimate strength, the higher anticipated stiffness irrespective to loading strain rate. Based on the measured tensile load- strain relationship, the linear approximation of secant modulus is considerably acknowledged in the strain domain  $\leq 2\%$  which covers a wide scatter of geosynthetics reinforced structures conditions under service (working) loadings. Behavior of geosynthetics reinforced soil is sensitive to stiffness rather than strength of the geogrid.

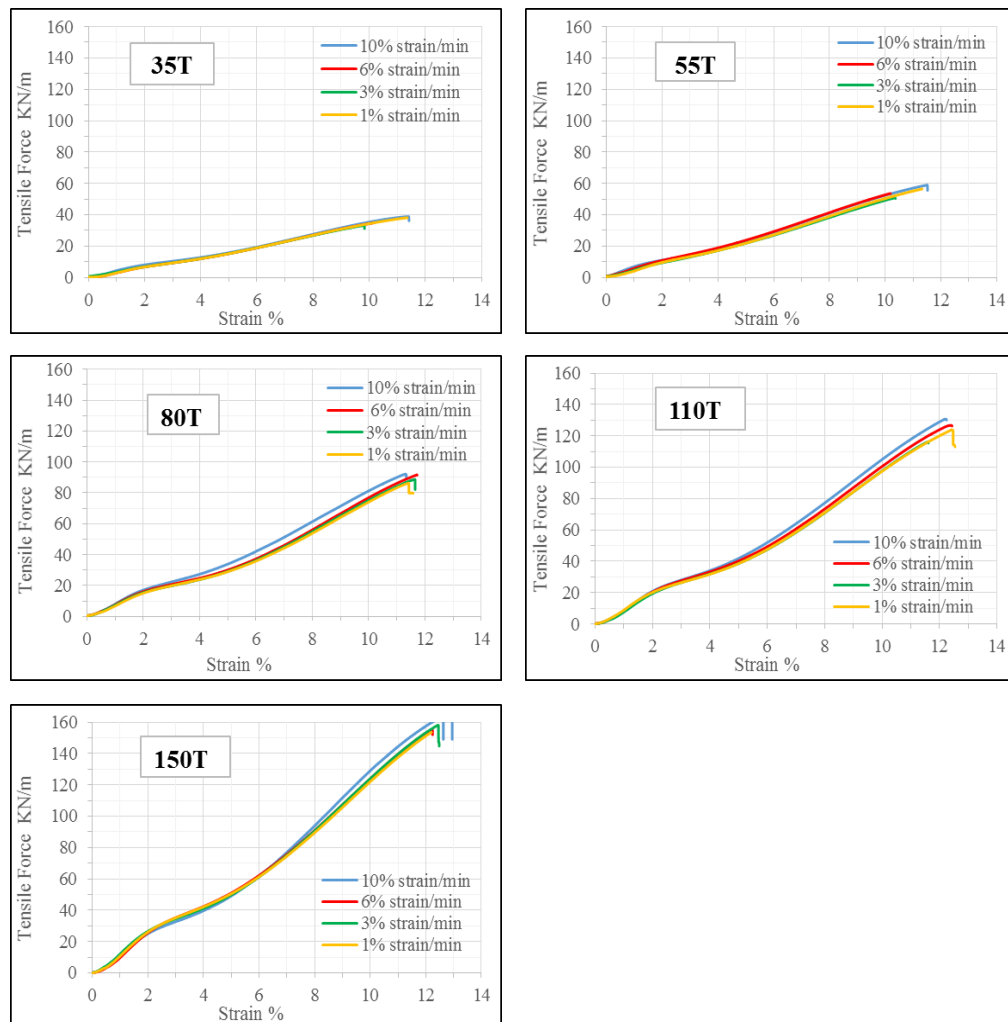


Figure 4. Influence of strain rate of 10, 6, 3 and 1%/min. on tensile force-strain relationship for Fortrac 35T, 55T, 80T, 110T, and 150T

### 3.3. SECANT MODULUS (STIFFNESS)

The sample total width is 200 mm, while the intact width is limited to 120 mm. According to ASTM D6637, clause 8.2.4 which stated that “within test methods A, B and C the outermost ribs are cut prior to testing to prevent slippage from occurring within the clamps. For those cases where the outermost ribs are severed, the test results shall be based on the unit of width associated with the number of intact ribs”. Hence, calculation of the secant modulus ( $J = EA_1$ ) at certain strain domain shall be the maximum tensile force divided by the total intact width per meter. The strength and stiffness of the geogrid is load, time, and temperature dependent. The room temperature is to be 20°C during testing procedure to avoid adverse influence of temperature on the test results. The literature (Boyle et al., 1996; Sawicki et al., 2002; Walters et al., 2002), stated that the geogrid is affected by strain rate of loading.

After Hatami and Bathurst 2005, the determination of the ultimate strength, characteristics, and secant modulus are based on the results of CSR for 10% strain/min- ASTM D4595. Accordingly, at CSR 10%/min., the derived secant moduli for stain domain of 2% are 390, 536, 868, 1128 and 1396 kN/m for types 35T, 55T, 80T, 110T and 150T, respectively. The resulting secant moduli for strain domain up to 1% are 521, 729, 1104, 1583, and 1583 kN/m for specimens 35T, 55T, 80T, 110T and 150T, respectively. *Figure 5* demonstrates the trend between ultimate tensile strength for the examined specimens of Fortrac 35T, 55T, 80T, 110T, and 150T under CSR 10%/min. and the resultant secant modulus  $J_{2\%}$  for strain domain 2% as well as secant modulus  $J_{1\%}$  for strain domain 1%. For all examined geogrid specimens, the revealed modulus at domain 1% is relatively larger than corresponding for strain domain 2%, which reflects the phenomenon of the non-linearity and relaxation of geogrid stiffness with progressive elongation (strains). The higher induced strain, the relatively lower anticipated stiffness is. As reported by Hatami and Bathurst 2005, the linear approximation of tensile load-strain response is considerable accepted in the strain domain up to 2% which covers a wide scatter of geosynthetics reinforced soil/ structures conditions under service loadings rather than the incipient collapse.

It should be pointed that, the performance of geosynthetic reinforced structure is sensitive to the geogrid stiffness rather than the geogrid strength. Values for secant modulus  $J$  at strain level 1% and 2% which were derived from the CSR tensile force- strain relationship results are utilized for derivation of the brought geogrid tensile forces based on the measured strains of the instrumented geogrid layers. Secant modulus of strain 2% is a necessary key input parameter for numerical finite element modelling of geogrid properties.

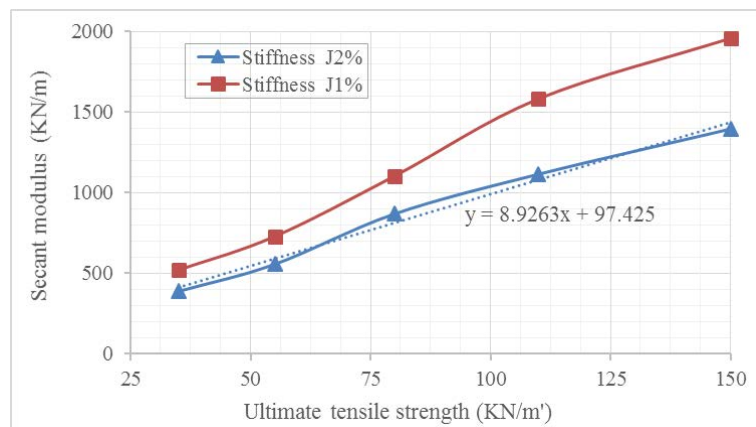


Figure 5. Trend of ultimate tensile strength versus secant modulus  $J_{2\%}$  and  $J_{1\%}$  for CSR 10%/min.

The performed CRS tests program did not involve testing of specimen 200T. Thus, correlated to the examined specimens CSR test results of 35T, 55T, 80T, 110T and 150T, a statistical prediction for the trend among strength, secant modulus  $J_{2\%}$  at 2% strain and  $J_{1\%}$  at 1% strain was used to estimate the secant modulus  $J_{1\%}$  and  $J_{2\%}$  of Fortrac 200 of value 2538 kN/m and 1893 kN/m, respectively. Ratios between stiffness ( $J_{2\%}$ ) to ( $J_{1\%}$ ) for various examined specimens and predicted stiffness values of Fortrac 200T were evaluated as presented in *Table 3*, where the predicted (fitted) secant modulus  $J_{2\%} = 8.9263 \times \text{Ultimate Tensile Strength} + 97.425$ . From a practical stand point, such expression and chart (correlation) are simple and helpful to predict secant modulus (not published by manufactures to public engineering community) of geosynthetic PET geogrid based on nominal ultimate strength, which is essential key input parameter for numerical FE modelling purposes.

The CSR was varied to assess the effect of strain rate of loading of 20%/min, 10%/min, 6%/min, 3%/min, %/min and 0.05%/min. on the secant modulus at strain 2% ( $J_{2\%}$ ) and at strain 1% ( $J_{1\%}$ ) as illustrated in *Figures 6(a) and 6(b)*, respectively. General trend of the test results shows that, the larger ultimate strength, the higher anticipated secant moduli, regardless of the strain rate of loading. For the different examined geogrid specimens, the higher CSR reveals an increase of the induced secant modulus  $J_{2\%}$  and  $J_{1\%}$  for the same examined specimen with variable ratios.

Table 3. CSR test for 10% strain/min. – secant modulus  $J_{2\%}$  and  $J_{1\%}$

	Tested specimens					Predicted
	35T	55T	80T	110T	150T	200T
Measured $J_{2\%}$ (kN/m)	390	536	868	1128	1396	
Fitted $J_{2\%}$ (kN/m)	410	588	812	1079	1436	1893
diff. (kN/m)	5.09	9.77	-6.51	-4.32	2.89	
Measured $J_{1\%}$ (kN/m)	521	729	1104	1583	1958	2538.9 (fitted)
$J_{1\%}/J_{2\%}$ ratio	1.336	1.360	1.272	1.403	1.403	average = 1.355

For practical assessment of the influence for strain rate of loading, the anticipated secant modulus for the examined specimens shall be normalized to the corresponding of the nominal representative test of rate 10%/min. of ASTM D4595 (after Hatami and Bathurst 2005). *Table 4* listed the normalized ratios of the variable strain loading rates to rate 10%/min. of  $J_{2\%}$ . For example; increasing rate to the upper bound (fast loading rate) 20 %/min provided an increased ratio of  $J_{2\%}$  from 1.03 to 1.26. On the contrary, reducing rate to the lower bound (slow loading rate) 0.05 %/min. exposed a decreased ratio of  $J_{2\%}$  from 0.80 to 0.87.

*Table 5* shows the normalized ratios of the variable strain loading rates to rate 10%/min. of secant modulus  $J_{1\%}$ . For example; increasing rate to the upper bound (fast loading rate) 20 %/min provided an increased ratio of  $J_{1\%}$  from 1.08 to 1.27. In contrast, decreasing rate to the lower bound (slow loading rate) 0.05 %/min. exposed a reduced ratio of  $J_{1\%}$  ranged from 0.71 to 0.83.

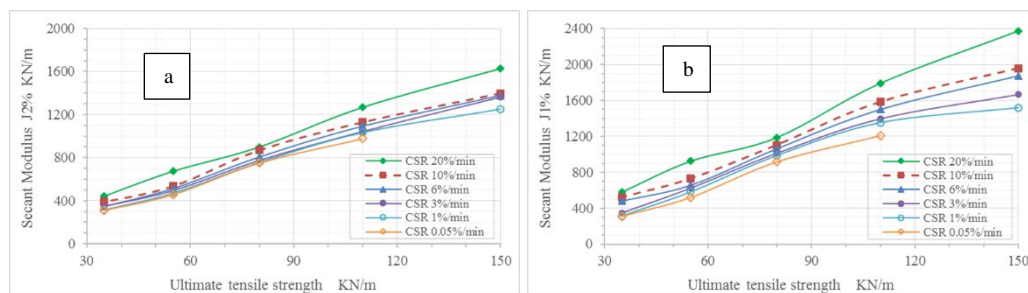


Figure 6. Influence of strain rate of 20, 10, 6, 3, 1, and 0.05 %/min. on geogrid secant modulus: (a)  $J_{2\%}$  and (b)  $J_{1\%}$

Table 4. Influence of CSR at modulus  $J_{2\%}$ -normalized to 10% strain/min.

	CSR 20%/min.	CSR 6%/min	CSR 3%/min	CSR 1%/min	CSR 0.05%/min
150T	1.17	0.99	0.98	0.90	
110T	1.12	0.97	0.92	0.92	0.87
80T	1.03	0.93	0.89	0.87	0.86
55T	1.26	0.96	0.92	0.88	0.85
35T	1.13	0.89	0.89	0.81	0.80

Table 5. Influence of CSR at modulus  $J_{1\%}$ - normalized to 10% strain/min.

	CSR 20%/min.	CSR 6%/min	CSR 3%/min	CSR 1%/min	CSR 0.05%/min
150T	1.21	0.96	0.85	0.78	
110T	1.13	0.95	0.88	0.86	0.76
80T	1.08	0.96	0.92	0.89	0.83
55T	1.27	0.90	0.86	0.80	0.71
35T	1.11	0.92	0.88	0.76	0.76

#### 4. CONCLUSIONS AND RECOMMENDATIONS

This paper introduces analyses, interpretation, and results for series of laboratory constant strain rate (CSR) tests of 20%, 10%, 6%, 3%, 1%, and 0.05% strain/ min. conducted on five sets of geosynthetics polyester (PET) geogrid specimens. Tests were performed according to the Multi-Rib tensile method of ASTM D6637. Main output acceptance features of tensile ultimate strength and strain at break were justified. Results are in good agreement with manufactures technical data sheet. Values for Secant modulus J at strain level 1%, and 2% were derived from the tensile force- strain relationship results, which are necessary for numerical Finite Element modelling. Sensitivity for the influence of strain rate of loading on strength, stiffness, and non-linear properties of geogrid was inspected for the different examined specimens. We are focused on simulations that can be used to predict operational (working stress) under static conditions rather than incipient collapse. The main findings might be summarized as follows:

- The measured tensile force- strain relationship showed a non-linear behavior of the examined geosynthetics PET geogrid specimens.
- The higher CSR reveals increase of the measured secant modulus. The larger ultimate strength, the higher anticipated stiffness irrespective to loading strain rate.
- Based on the measured tensile load- strain relationship, the linear approximation of secant modulus is considerably acknowledged in the strain domain  $\leq 2\%$  which covers a wide scatter of geosynthetics reinforced structures conditions and mechanically stabilized earth walls under service (working) loadings.
- The derived stiffness at 1% is larger than corresponding for 2% strain, which reflects phenomenon of non-linearity and stiffness relaxation with progressive elongation associate with loading increments.
- Performance of geosynthetics- reinforced soil is sensitive to stiffness rather than strength of geogrid.
- For numerical modelling purposes, a simple correlation chart was developed to predict secant modulus (not published to public) of geosynthetic PET geogrid based on the nominated ultimate strength.
- For practical assessment of the influence for strain rate of loading on stiffness; tables were developed for the normalized ratios to rate of 10% strain/min. (ASTM D4595) for  $J_{2\%}$  and  $J_{1\%}$ .

## ACKNOWLEDGMENT

The authors would like to express their gratitude to the technical support of Dr. Mohy El-Mashad, and members of Geotechnical Institute Laboratory, National Irrigation Research Center in Qanater, Egypt

## REFERENCES

- [1]. AASHTO (2002). Standard Specifications for Highway Bridges. American Association of State Highway and Transportation Officials, 17th Ed., Washington, DC, USA.
- [2]. Allen, T. M., and Bathurst, R. J. (2002a). "Observed long-term performance of geosynthetic walls, and implications for design." *Geosynthetic Int.*, 9(5-6), 567-606.
- [3]. ASTM D 6637. "Standard test method for determining tensile properties of geogrids by the single or multi-rib tensile method." American Society for Testing and Materials, Pennsylvania, USA.
- [4]. ASTM D4595 "Standard test method for tensile properties of geotextiles by the wide-width strip method." American Society for Testing and Materials, West Conshohocken, Pennsylvania, USA
- [5]. Bathurst, R.J., Allen, T.M., and Walters, D.L., (2002), "Short-term strain and deformation behavior of geosynthetic walls at working stress conditions", *geosynthetics international*, vol. 9, nos. 5-6, pp. 451-482.
- [6]. Boyle, S.R, Gallagherand, M. Holtz, R.D. (1996). "Influence of strain rate, specimen length and confinement on measured geotextile properties." *Geosynthetics International Journal*, 3 (2), pp. 205-225.
- [7]. Hatami, K. and Bathurst, R. J. (2005). "Development and verification of a numerical model for the analysis of geosynthetic-reinforced soil segmental walls under working stress conditions." *Journal of Geotechnical and Geoenvironmental Engineering, ASCE*, 132(6), 673-684.
- [8]. Yan Yu, Bathurst, R. J., and Allen, T. M. (2016). "Numerical modelling of the SR-18 geogrid reinforced modular block retaining walls." *Journal of Geotechnical and Geoenvironmental Engineering, ASCE*, 142 (5): 04016003.
- [9]. Sawicki, A., and Kazimierowicz-Frankowska, K. (2002). "Influence of strain rate on the load-strain characteristics of geosynthetics." *Journal of Geosynthetics International*, 9 (1), pp. 1-19
- [10]. Walters, D. L., Allen, T. M., & Bathurst, R. J. (2002). "Conversion of geosynthetic strain to load using reinforcement stiffness." *Geosynthetics International*, 9 (5-6), pp. 483-523.

## BIOGRAPHY

*Abdelwahab Tahsin* has completed his MSc. and PhD in Civil engineering from Faculty of Engineering, Cairo University, Egypt. Research work is focused on civil, geotechnical, and foundation engineering. Special care was considered in the topics of soil-structure interaction, deep excavation supporting system, slope stability, mechanically stabilized earth walls, Geosynthetics, field monitoring, and numerical modeling (3D finite element). He is a professional Consultant engineer, certified PMP and design director at ACE consulting office, Cairo, Egypt. Participating and managing large complicated civil engineering projects across multiple asset classes in Egypt, Gulf, Middle East, and Africa. Strong experience of international standards through interactive collaboration with International Managed Joint Ventures. He is an Assistant professor (Instructor part-time basis) supervising graduation projects at the Egyptian Russian and 6<sup>th</sup> of October Universities, Egypt. He has been serving as a reviewer of the research journal "Innovative Infrastructure Solutions" (IISS). He is sharing at numerous conferences, workshops, and invited talks. He is an associate organizing member of GEOAFRICA 2023 international conference, hosted by the International Geosynthetics Society IGS, Egypt chapter.



# Detection of Micron-Scale Particles on Optical Surfaces by Photothermal Method

*Pervin Tuzun<sup>1,2\*</sup>, Fikret Yildiz<sup>3</sup>, Semih Yurtseven<sup>1</sup>, Humbat Nasibov<sup>1</sup>*

---

## Abstract

Since the physical sizes of viruses and bacteria are in nano-scale range, optical methods are more efficient among the others, due to the fast detection ability. Optical force and interferometric methods stand out among these methods. On the other hand, photothermal spectroscopy methods are widely used to investigate the optical surfaces. Due to high spatial resolution the Common-Path Interferometry (PCI) method, has been widely used in the measurement of the absorption value of optical components and coatings in recent years. Since the PCI method comprises a combination of pump/probe lasers, the accuracy of the measurements directly depends on the stability of the lasers used. In this study, the short-term stability of the aforementioned lasers was increased and thus, the sensitivity of the measurements of phase-difference was increased accordingly. The optical absorption of various optical glass substrates and optical coatings was examined with the PCI method. In addition, within the scope of this study, the surfaces of various optical glasses and optical coatings were examined using the PCI method at one-dimension and 2D. During the experiments, using a single-mode continuous wavelength laser with wavelength of 640 nm and a long coherence length ( $>100$  m), various dust and particles on the optical surfaces up to 100 microns in size were investigated. The effect of these particles on the optical absorption values of various optical surfaces (BK7, Fused-silica glasses, different dielectric coatings, etc.) was analyzed and discussed.

**Keywords:** CW Laser, Interferometer, Optical Absorption, Phase Difference, Photothermal Method

---

## 1. INTRODUCTION

Photothermal spectroscopy is a high-precision group of measurement methods used to measure the optical absorption and thermal properties of materials [1]. Photothermal spectroscopy is based on the generation of photo-induced changes in the thermal state of materials [2]. Photo-induced absorption increases with increasing laser intensity. Optical absorption phenomena, especially the absorption of high-power laser radiation on the surface of optical components, cause a number of physical phenomena in the optical component [3]. Once light energy is absorbed by the material, it causes heating in the material. This heating causes a temperature gradient in the material. Laser-induced photothermal effects cause changes in some thermodynamic parameters such as temperature, pressure, density in optical components. By observing, measuring, and analyzing these changes, information about the characteristic properties of the optical component can be obtained. The Photothermal Common-Path Interferometry (PCI) method is one of the photothermal spectroscopy methods, and it is widely used to measure the ultra-weak absorption values of optical components. The method allows to retrieve a 2D map of ultra-weak optical absorption measurements on the optical surface with a very high spatial resolution. This ability of the PCI method can be used to detect various particles and contamination on optical surfaces [4-6].

---

<sup>1\*</sup> Corresponding author: TUBITAK National Metrology Institute, 41470, Gebze Turkey

[p.tuzun2019@gtu.edu.tr](mailto:p.tuzun2019@gtu.edu.tr), [humbet.nasibli@tubitak.gov.tr](mailto:humbet.nasibli@tubitak.gov.tr), [semih.yurtseven@tubitak.gov.tr](mailto:semih.yurtseven@tubitak.gov.tr)

<sup>2</sup> Gebze Technical University, Institute of Natural and Applied Sciences, Department of Physics, Kocaeli, Turkey

<sup>3</sup> Gebze Technical University, Faculty of Science, Department of Physics, Kocaeli Turkey

[fildiz@gtu.edu.tr](mailto:fildiz@gtu.edu.tr)

## 2. MATERIAL AND METHOD

The PCI, used for low absorption measurements, is based on the pump/probe technique [7]. The method is used for measurements of weak optical absorption values of optical coatings, glasses, crystals, etc. [8]. Briefly, the in this method a high-power single mode laser, named as a pump laser (denoted as a Pump Laser in Figure 2.1), is focused on optical surface under the test (Sample) by means of a lens (L1). The other laser, namely a probe laser (Probe Laser in Figure 2.1) with more weak output power and different wavelength is focused on the same point on the sample surface with a second lens (L2). The waist diameter of the probe beam should be at least 3 times greater than the waist diameter of the pump beam [7]. The pump and probe beams have intersected an angle between them at about  $20^\circ$  or less. The reason for directing the beams at this angle is to obtain as much intersection area as possible within the optical component.

In the PCI method, a high 3D resolution is achieved by obtaining the intersecting pump/probe geometry and it is ensured that no signal is produced other than the signal coming from the optical component. By the overlapping pump and probe geometry of the PCI method, photothermal signals can be obtained from both the bulk and the coating of a coated optical components. The optical power absorbed by the optical component in the PCI setup, heats the sample inhomogeneously. This absorption state generates a radially varying temperature gradient in the optical component. This temperature change causes optical distortion in the wavefront of the probe laser due to photothermal effects. Thermal lens formation is one of these photothermal effects. This thermal lens formed in the optical component produces weak distortion of the phase of the probe laser. This phase distortion is detected by a photodetector (PD) and processed by a lock – in amplifier device.

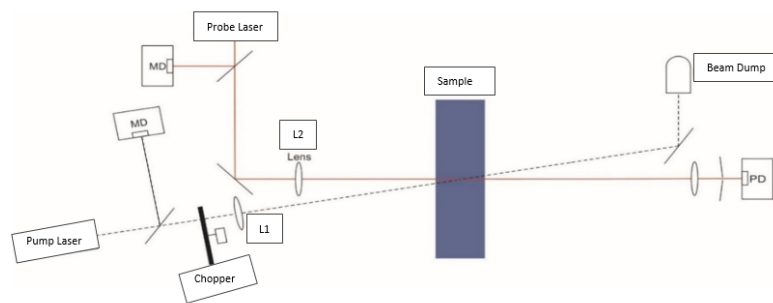


Figure 2.1. The optical schema of PCI setup, within the scope of this study.

In this study a solid-state single mode laser with a wavelength of 640 nm and an output power of about 1 W is used as a pump laser. The low power probe laser is a single mode He-Ne laser with wavelength of 543 nm and an output power of 2 mW. The beam waists (at  $1/e^2$ ) of the pump laser and probe laser are about  $30 \mu\text{m}$  and  $110 \mu\text{m}$ , respectively. The pump laser heats on the sample an area with a diameter of about laser beam waist and causes a deformation of the sample surface. The probe beam with a diameter of about three times greater than the diameter of the distorted area is very accurately collinearly positioned on the distorted area. When the probe beam passed through this area the distortion in the center of the probe beam is formed. This distortion causes the interference between the distorted central part and the undistorted outer part of the probe beam. This effect is called “the self interference” phenomena and constitutes the physical base of the PCI method. In the setup established in this study, the sample is located on the X-Y-Z axis stepper motors, thus allowing to move the sample in the X-Y-Z direction with respect to pump/probe beams converging point. Bu this way it became possible to retrieve a 3D map of the absorption coefficient by scanning the sample in three directions.

## 3. RESULTS AND DISCUSSION

In setups was used to assess the weak absorption coefficient of high-purity optical components and dielectric coatings. A special homemade software was developed to retrieve a one-dimensional and two-dimensional map of the ultra-weak absorption measurements. Furthermore, since the stability of the probe laser in the setup directly affects the measurement results, the short time stabilities of the laser were enhanced by means of several noise-eaters. The ultra-weak optical absorption values of various optical glass substrates and optical coatings

were examined with the PCI method, and it was found that the optical absorption values with an absolute value of around 1 ppm were measured with 0.1 ppm sensitivity. In the established system, photothermal signals of various optical components were obtained in one and two dimensions. The graph is given in Figure 3.1 represents the measurements taken by gradually increasing the power of the pump laser inside an uncoated glass. The graph indicates that the photothermal signal obtained from an uncoated glass increases with the linearly increased power. The linearity of the system in this way allows the calibration of the whole system to be performed relatively.

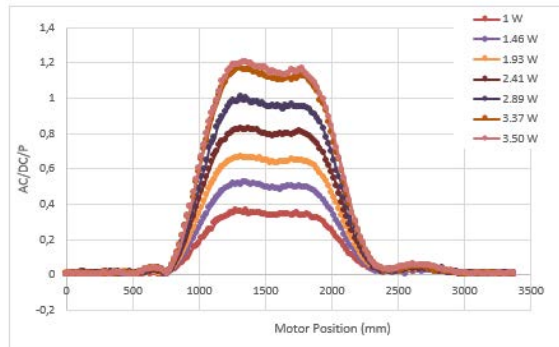


Figure 3.1. Variation of AC/DC/P signal with pump laser power in uncoated glass

Since such sensitivity was achieved, the system was used for the detection of micron-sized particles on a surface of a highly polished glass plate. During the experiments, various dust and particles on the optical surfaces 100 – 500 microns in size were investigated by using the one-dimension and two-dimensions scanning technique. The effect of these particles on the optical absorption values of various optical surfaces (uncoated windows, fused silica glasses, different dielectric coatings, etc.) was analyzed. The photothermal signals are received from a tempered glass along the two axes (2D) and one axis shown in Figure 3.2. There are particles up to 500 micrometers in size on the surface of the tempered glass. While these particles can be easily seen in the 2D photothermal signal, they cannot be seen in the one-dimensional signal. Micron-sized particles on the optical surface cause an increase or decrease in the 2D photothermal signal. The increase or decrease in the photothermal signal is determined by the current phase of the probe beam. The magnitude of this increase in the photothermal signal gives information about the size of the particle on the optical surface. Depending on the particle size, the phase of the probe beam changes, which means the larger the particle, the greater the phase change.

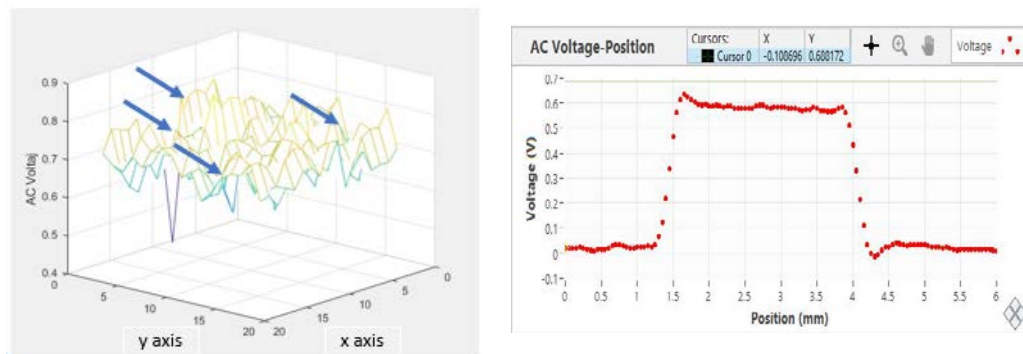


Figure 3.2. 2D and 1D photothermal signal received along the surface of the tempered glass.

Beside the particle detection on the optical surfaces the PCI method was used to detect damages on the optical surfaces. Fig.3.3 shows a 2D and one-dimensional photothermal signal from an uncoated silica glass with a surface defect of approximately 500 micrometers. 2D photothermal signal received from the uncoated damaged silica glass indicates that photothermal signal increases around the damaged point.

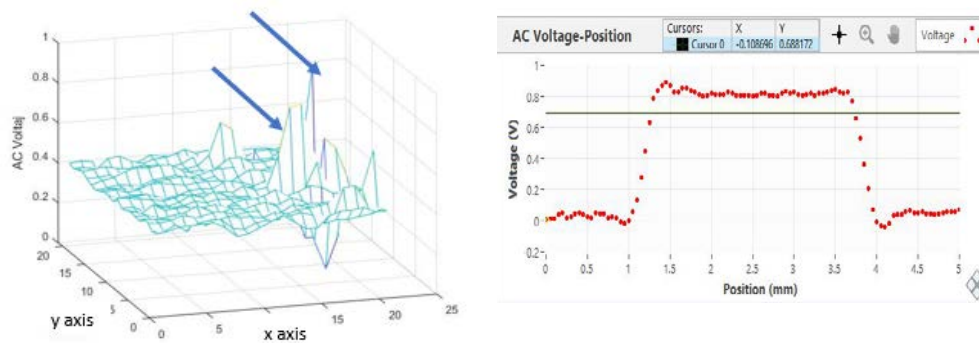


Figure 3.3. 2D and 1D photothermal signal received along the surface of the uncoated silica glass.

## 4. CONCLUSIONS

A PCI setup has been developed to measure the ultra-weak absorption values of optical bodies and optical surfaces. In this setup, a sensitivity of 0.1 ppm was achieved in the absorption measurements. In this study, since such a sensitivity was achieved, the PCI setup was used to detect micron-sized particles on the optical surfaces. During the experiments, various dust and particles on the optical surfaces 100-500 microns in size were investigated. The effect of these particles on the optical absorption values of various optical surfaces (BK7, fused-silica glasses, different dielectric coatings, etc.) was analyzed and discussed. It has been observed that in addition to particle detection at the micron scale, various damages in the optical component can also be detected.

## ACKNOWLEDGEMENT

The first author would like to express her sincere thanks to TUBITAK – BIDEB COVID-19 STAR researcher scholarship.

## REFERENCES

- [1]. S. E. Bialkowski, N. G. C. Astrath, M. A. Proskurnin, *Photothermal Spectroscopy Methods*, 2nd ed., Wiley & Sons Inc, 2019.
- [2]. L. A. Skvortsov, "Laser photothermal spectroscopy of light-induced absorption", *Quantum Electronics*, vol. 43 (1), pp. 1-13, 2013.
- [3]. U. Willamowski, D. Ristau, E. Welsch, "Measuring the absolute absorptance of optical laser components," *Applied Optics*, vol. 37, pp. 8362-8370, 1998.
- [4]. J. Zhuang, J. Yin, S. Lv, B. Wang, Y. Mu, "Advanced "lab-on-a-chip" to detect viruses – Current challenges and future perspectives", *Biosensors and Bioelectronics*, vol 163, 112291, 2020.
- [5]. J. Lukose, S. Chidangil, S. D. George, "Optical technologies for the detection of viruses like COVID-19: Progress and prospects", *Biosensors and Bioelectronics*, vol 178, 113004, 2021.
- [6]. A. Brown, A. Oglozab, K. Olson, J. Talghader, "Continuous-wave laser particle conditioning: Thresholds and time scales", *Optics & Laser Technology*, vol 89, pp. 27-30, 2017.
- [7]. A. Alexandrovski, M. Fejer, A. Markosyan, R. Route, "Photothermal Common-Path Interferometry (PCI): New Developments," in *Proc. SPIE 7193, Solid State Lasers XVIII: Technology and Devices*, 2009, 71930D.
- [8]. J. Camp, G. Billingsley, W.P. Kells, et al. "LIGO optics: initial and advanced," in *Proc. SPIE 4679, Laser-Induced Damage in Optical Material*, 2001.

# On the Calibration of Diffraction Grating Based Monochromators

Elif Asena Ozer<sup>1</sup>, Mevlut Karabulut<sup>2</sup>, Semih Yurtseven<sup>3</sup>, Humbat Nasibov<sup>4</sup>

---

## Abstract

Although mini-spectrometers based on integrated optical elements (fiber-coupled), an image sensor and a circuit are penetrating in a variety of applications, including color measurement, agriculture and food safety, process control, etc., diffraction grating based monochromators are still preserve their role as a reference device for spectral measurements. Precise characterization and calibration of spectral sensing devices, illumination sources and various optical filters and windows require a precisely calibrated monochromator. Pen-type spectral lamps filled with noble gases and their mixture are widely used for this purpose. However, these lamps are very fragile and have short life time when employed with an unproper power supply. In this work we present experimental results of application of multi-color tunable laser source for fast and precise calibration of Czerny-Turner monochromator. The obtained results are compared with those obtained by means of several different pen-type lamps. The experimental results of this comparison are discussed in this work.

**Keywords:** Czerny-Turner monochromator, Multi-color tunable lasers, Pen-type lamps

---

## 1. INTRODUCTION

Monochromators are used to obtain a nearly single wavelength light, namely monochromatic light, from the polychromatic light coming from the light sources, like lamps, the Sun, etc. Nowadays, the wavelength range of monochromators are span from UV up to far infrared region.

There are two commonly used types of monochromators: prisms and grating based systems. Although the input and the output of these devices are similar, the wavelength separation principle behind these systems are completely different. In prism based monochromators, the sole of the device is a prism that refracts the light at the interface of two surfaces (prism material and the surrounding air) with different refractive indexes, and thus creating angular dispersion (Fig.1. (a)). Historically, the prism based monochromators were the first devices to be developed in the field. However, they have some limitations. Their resolution is significantly lower than grating based monochromator system and their separation technique is non-linear; thus, it creates mechanical problems with focusing a specific wavelength on the exit slit. However, these prism based monochromators are widely used in the UV and far UV regions of the electromagnetic spectrum, due to their high resolution in this region.

---

<sup>1</sup> Gebze Technical University, Faculty of Science, Department of Physics, 2210-A Scholarship Master's Student, BIDEB-TUBITAK-UME COVID-19 Star Scholarship 41400, Gebze/Kocaeli, Turkey. [eozer2020@gtu.edu.tr](mailto:eozer2020@gtu.edu.tr)

<sup>2</sup> Gebze Technical University, Faculty of Science, Department of Physics, Gebze/Kocaeli, Turkey. [mevlutk@gtu.edu.tr](mailto:mevlutk@gtu.edu.tr)

<sup>3</sup> TUBITAK-UME-National Metrology Institute, Thermodynamic Lab.41400, Gebze/Kocaeli, Turkey. [semih.yurtseven@tubitak.gov.tr](mailto:semih.yurtseven@tubitak.gov.tr)

<sup>4</sup> TUBITAK-UME-National Metrology Institute, Thermodynamic Lab.41400, Gebze/Kocaeli, Turkey. [humbet.nasibli@tubitak.gov.tr](mailto:humbet.nasibli@tubitak.gov.tr)

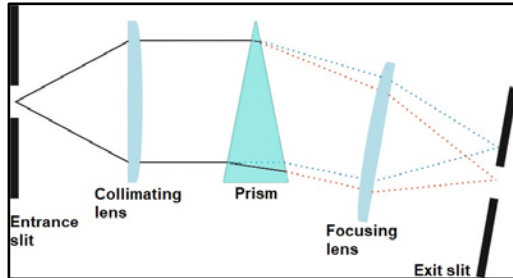
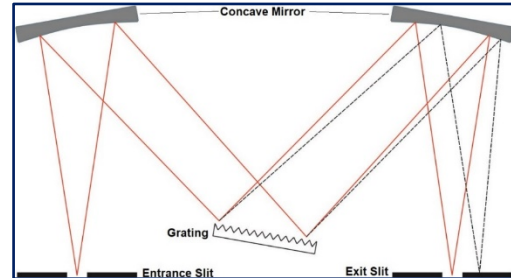


Figure 1. (a) Prism monochromator system



(b) Grating based monochromator system

Another type of monochromators is a grating-based monochromator. When monochromatic light enters the monochromator, it exits only in a direction specific to the diffraction grating; moreover, this property can be used to determine the wavelength of the monochromatic light (Fig.1. (b)).

Different types of gratings are used inside the monochromator to provide the desired wavelength output, and these gratings allow only wavelengths passed through the monochromator output, thanks to the grating equation, and the remaining beam is scattered or absorbed in the monochromator.

A monochromatic light beam of wavelength  $\lambda$  falls on a grating and is diffracted along a number of separate paths. The light refracted by each trough at a distance  $d$  between them combines to form set of diffracted wave fronts. Diffraction by a grating is shown in Figure 2. The angles,  $\alpha$  and  $\beta$  are measured from the grating normal. According to the principle of constructive interference, light from adjacent grooves will be in phase only when it is equal to the wavelength of the light  $\lambda$ , or an integer multiple thereof, which will cause constructive interference. At all other angles, waves from the groove surfaces will cause destructive interference [1]. These relationships can be expressed with the grating equation:

$$n\lambda = d(\sin\alpha + \sin\beta) \quad (1)$$

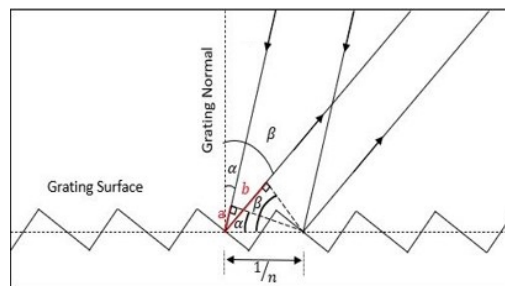


Figure 2. Diffraction by a grating

Monochromators are commonly used for the spectral calibration and characterization of spectrometers, pyrometer, illumination sources and various optical filters and windows. Monochromators used as secondary standards must be properly calibrated to ensure traceability of characterization measurements to SI standards [2]. Precise knowledge of monochromator specifications is required for accurate calibration results. Common calibration procedures rely on the measurement of spectral lines emitted by pen-type spectral lamps or lasers [2].

The spectrum of output wavelength accuracy of the grating monochromator is one of the main parameters of the monochromator. Calibration data changes after prolonged use or realignment of the grating monochromator, and it does not accurately determine wavelength, spectral resolution degrades with other problems. This should be resolved by wavelength calibration; thus, grating monochromator output wavelength calibration is an important and integral part for scientific measurement [3].

In grating based monochromators, the grating is rotated with a rotational motor system. By changing the angular position of this motor, the angle of the grating is changed depending on the incident beam and the exit slit of the monochromator. However, the angular position of the motor with respect to the incident beam should be calibrated. In other words, the calibration of the monochromator means the establishment of a relation between

the angular position of the rotational motor and the wavelength of the monochromatic light at the exit port of the monochromator.

## 2. MATERIALS AND METHOD

The standard procedure for wavelength calibration of monochromators in the visible and near infrared wavelength range is to use pen-type spectral lamps, filled with a noble gas (such as neon lamps), or their mixtures, with spectrally well-known emission lines as the primary wavelength standard [4]. A major disadvantage of this procedure is in the removal of the calibrated monochromator and replacement of the original source with standard light source in the same position which may cause variations in the incident light path before and after replacement and there may be inconsistencies after installing the standard light source [3]. In addition, lamps with spectrally well-known emission lines in the visible and near-infrared regions are available for calibration, but not for the infrared and far infrared wavelengths [3]. Therefore, the laser diffuse reflection method was proposed to perform monochromator field calibration using a monochromatic light of a laser at different wavelengths.

In this study, multi-color tunable laser source was used to eliminate the aforementioned disadvantages of pen-type lamps and the two methods were compared. In the first method, we used a pen-type spectral lamps for the monochromator calibration. In the second method, we used multicolor laser with 5 different irradiation wavelengths; 543,5 nm, 594,1 nm, 604,6 nm, 611,9 nm and 632,8 nm. In the monochromator calibration process, the effect on the output wavelength bandwidth is a function of monochromator slit width at the input and output options. The measurements were performed at various slit widths.

In the first method, we performed the calibrations with pen-type spectral lamps (Fig. 3 (a)). Pen-type spectral lamps produce light in narrow, intense ultraviolet (UV) to infrared (IR) wavelengths due to the excitation of various rare gases and metal vapors. These lamps are useful for wavelength calibration of spectroscopic instruments such as monochromators, spectrographs and spectral radiometers; however, they are very fragile and have short life time when employed with a improper power supply. We used different pen-type spectral lamps such as neon and argon as the monochromator light source for the calibration.

In our measurements, the calibration lamps were positioned as close to the entrance slit as possible (Fig. 3 (b)). Before starting the measurement, it has been waited for 1 hour for the stability of the lamps and a series of spectral measurements have been performed with the entrance slit varying between 0.5 mm - 2 mm by changing the exit slit separately at each entrance slit. Each measurement has been repeated 3 times and the average has been calculated.

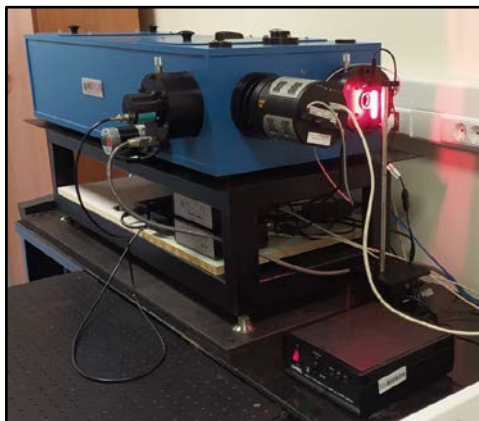
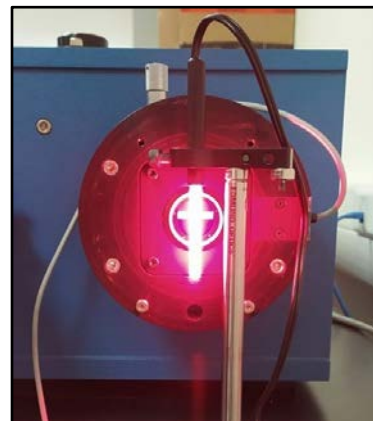


Figure 3. (a) Calibration with pen-type spectral lamp



(b) Positioning the lamp

Afterwards, the laser calibration method was introduced (Fig. 4 (a)) to measure the broad spectrum of grating monochromator output wavelength accurately, based on the grating diffraction principle and targeting the calibration need. A multi-color tunable laser source at 543,5 nm, 594,1 nm, 604,6 nm, 611,9 nm and 632,8 nm wavelengths with an output power above 2 mW has been used as the monochromator light source. Before starting the measurements, it has been waited for 1 hour for the stabilization of the laser. Si detector operating

in the 400-1200 nm wavelength range that can easily detect the wavelength change has been placed in the exit slit. In order to prevent the laser from saturating, an OD2 filter has been used in front of the laser.

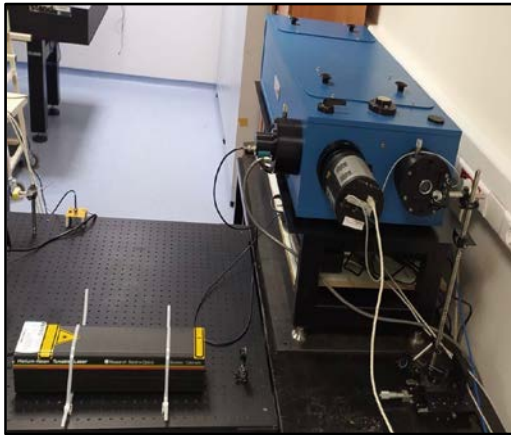
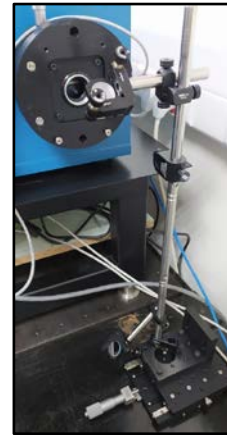


Figure 4. (a) Calibration with laser



(b) Positioning the laser beam relative to the entrance slit

### 3. RESULTS AND DISCUSSION

#### 3.1. Calibration with Neon Pen-Type Spectral Lamp

A series of spectral measurements were performed by keeping the entrance slit constant at 1 mm and changing the exit slit. The data obtained was then used for monochromator calibration. In Figure 5, intensity graph has been obtained from the spectral measurements using a neon pen type lamp emitting between 570-750 nm when the entrance and exit slits were 1 mm and 2 mm, respectively.

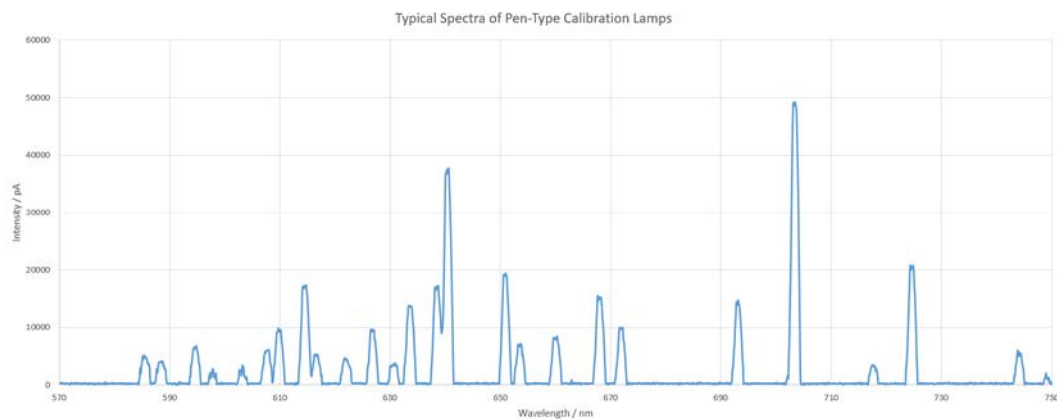


Figure 5. The intensity graph obtained with neon lamp by the entrance slit 1 mm and the exit slit 2 mm.

4 different slit widths have been selected for the spectral measurements of the neon lamp. The reference values of the neon lamp are given in the first column of Table 1. Neon lamp reference values have been compared with average values.



Table 1. Comparison of reference values and the values obtained as a result of in measurements made with a neon lamp

References / nm	Entrance slit 1 mm - Exit slit 0,25 mm	Entrance slit 1 mm - Exit slit 0,5 mm	Entrance slit 1 mm - Exit slit 0,75 mm	Entrance slit 1 mm - Exit slit 1 mm	Average	Standard Deviation
603	0,2	0,3	0,3	0,1	0,22	0,10
607,4	0,5	0,4	0,3	0,2	0,35	0,13
609,6	0,5	0,4	0,3	0,2	0,35	0,13
614,3	0,4	0,3	0,2	0,2	0,28	0,10
616,4	0,4	0,3	0,2	0,1	0,25	0,13
621,7	0,2	0,2	0,1	0,1	0,15	0,06
626,7	0,1	0,2	0,2	0,1	0,15	0,06
630,5	0,3	0,1	0	0,1	0,13	0,13
632,8	0,3	0,3	0,2	0,1	0,23	0,10
633,4	0,5	0,4	0,3	0,3	0,38	0,10
638,3	0,3	0,3	0,2	0,1	0,23	0,10
640,2	0,4	0,3	0,2	0,1	0,25	0,13
650,7	0,2	0,2	0,2	0,1	0,17	0,05
659,9	0,4	0,3	0,2	0,2	0,28	0,10
667,8	0,4	0,2	0,3	0,2	0,28	0,10
671,7	0,2	0,3	0,2	0,2	0,22	0,05
693	0,3	0,3	0,2	0,1	0,22	0,10

X

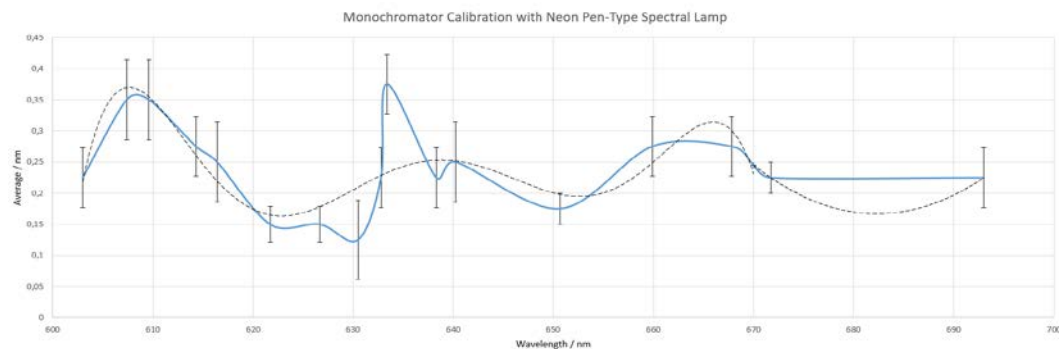


Figure 6. Correction graph between 603 - 693 nm in measurements with neon lamp

$$FIT1 = -(1 \times 10^{-9})x^6 + (5 \times 10^{-6})x^5 - 0,0078x^4 + 6,6053x^3 - 3156x^2 + 804018x - (9 \times 10^7) \quad (2)$$

$$FIT2 = 0,0005x^2 - 0,6981x + 238,33 \quad (3)$$

For the repeatability of the measurements, subsequent measurements were performed without touching the system or realigning, and the time delays were kept as short as possible. One important thing is that, increasing the slit-width increases the uncertainty of the measurements.

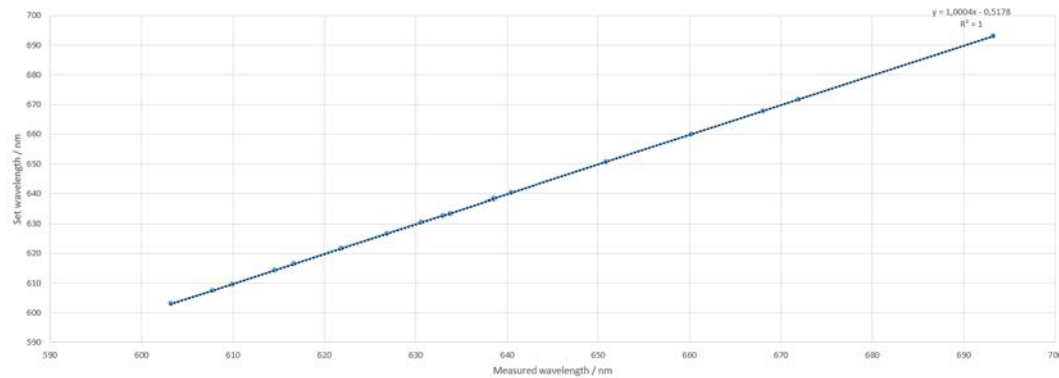


Figure 7. The comparison of the measurement data of grating monochromator and neon lamp spectrum

$$FIT3 = 1,0004x - 0,5178 \quad (4)$$

The comparison of the experimental data of grating monochromator and neon lamp spectrum is given in Figure 7 and calibration equation is given in the Equation 4.

### 3.2. Calibration with Argon Pen-Type Spectral Lamp

In the second method of the calibration, a series of spectral measurements were performed between 400 -1100 nm using an argon pen-type lamp. The intensity graph was obtained for constant entrance slit of 1 mm and the exit slit varying between 0,25 mm and 2 mm. The result is given in Figure 8.

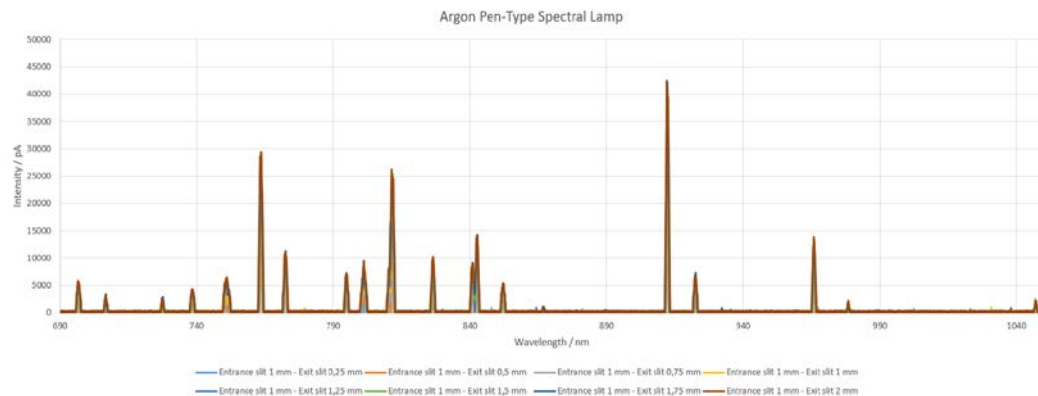


Figure 8. The intensity graph obtained with argon lamp

A comparison has been made between the reference values and the values obtained as a result of the measurements. The reference values of the argon lamp are given in the first column of Table 2.

Table 2. Comparison of reference values and the values obtained as a result of in measurements made with a argon lamp

Referen ces / nm	Entra nce slit 1 mm - Exit slit 0,25 mm	Entra nce slit 1 mm - Exit slit 0,5 mm	Entra nce slit 1 mm - Exit slit 0,75 mm	Entra nce slit 1 mm - Exit slit 1 mm	Entra nce slit 1 mm - Exit slit 1,25 mm	Entra nce slit 1 mm - Exit slit 1,5 mm	Entra nce slit 1 mm - Exit slit 1,75 mm	Entra nce slit 1 mm - Exit slit 2 mm	Avera ge	Stand ard Deviati on
696,5	0,3	0,4	0	0,1	0,1	0,2	0,3	0	0,18	0,15
738,4	0,3	0,3	0,1	0,2	0,1	0,2	0,1	0,1	0,18	0,09
750,4	0	0,3	0	0,2	0	0,1	0,3	0,3	0,15	0,14
751,5	0,3	0,1	0,2	0,2	0,2	0	0,6	0,5	0,26	0,20
763,5	0,3	0,3	0,2	0	0,1	0,1	0,2	0,2	0,18	0,10
772,4	0,2	0,2	0,1	0,1	0,1	0,1	0,1	0,2	0,14	0,05
794,8	0,2	0,2	0,1	0,1	0,1	0,1	0,2	0,1	0,14	0,05
801,5	0,2	0,1	0,2	0,1	0	0,1	0,5	0,3	0,19	0,16
811,5	0,2	0,3	0,1	0,1	0,1	0,2	0,1	0,2	0,16	0,07
826,5	0,3	0	0	0,1	0	0,1	0	0,1	0,08	0,10
840,8	0,3	0,3	0,2	0	0	0,2	0,1	0	0,14	0,13
842,5	0,2	0,2	0,1	0	0	0	0	0,2	0,09	0,10
912,3	0,2	0,2	0,1	0	0	0,1	0	0,2	0,10	0,09
922,4	0,1	0,1	0,2	0,1	0,1	0,1	0,2	0,1	0,13	0,05
965,8	0,1	0	0,1	0,1	0,1	0,1	0	0,1	0,08	0,05
1047,1	0,1	0,2	0	0,1	0	0,3	0,2	0	0,11	0,11

Using these results, for monochromator grating, the correction for 696,5 - 1047,1 nm wavelength is given in Figure 9 with the correction equation obtained using polynomial fitting (Equation 5).

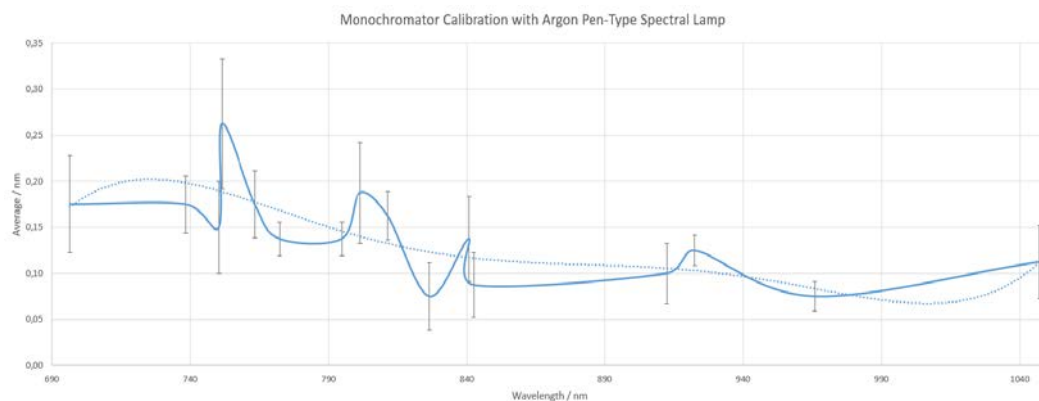


Figure 9. Correction graph between 696,5 - 1047,1 nm in measurements with argon lamp

$$FIT4 = (1 \times 10^{-12})x^5 - (7 \times 10^{-9})x^4 + (1 \times 10^{-5})x^3 - 0,0098x^2 + 4,2336x - 726,75 \quad (5)$$

### 3.3. Calibration with Laser

In the last method of the calibration, a series of spectral measurements were taken with a multi-color tunable laser by keeping the entrance slit of the monochromator constant at 1 mm and changing the exit slit between 0.25 mm and 1 mm. In the Figure 10, the laser wavelength was set as 543,5 nm and then the intensity graphs were obtained by changing the exit slits.

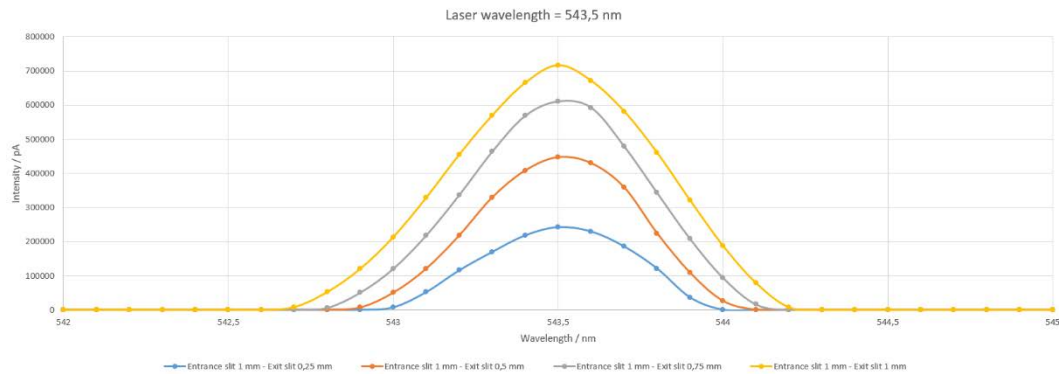


Figure 10. Intensity graph obtained with multicolor tunable laser at a wavelength of 543,5 nm

Laser reference values have been compared for these 4 different slit widths and the results are given in Table 3. The reference values of the laser are given in the first column of Table 3. Laser reference values have been compared for average values, and the obtained data is shown in Figure 11.

Table 3. Comparison of reference values and the values obtained as a result of in measurements made with a laser

References / nm	Entrance slit 1 mm - Exit slit 0,25 mm	Entrance slit 1 mm - Exit slit 0,5 mm	Entrance slit 1 mm - Exit slit 0,75 mm	Entrance slit 1 mm - Exit slit 1 mm	Average	Standard Deviation
543,5	0	0	0	0	0,00	0,00
594,1	0,1	0,1	0,1	0,1	0,10	0,00
604,1	0,9	0,8	0,8	0,7	0,80	0,08
611,9	0,3	0,2	0,1	0,1	0,18	0,10
632,8	0,4	0,3	0,2	0,1	0,25	0,13

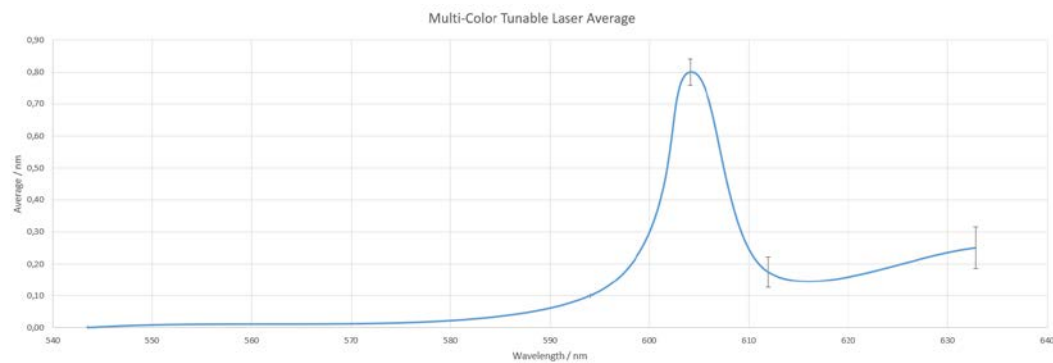


Figure 11. Correction graph between 543,5 – 632,8 nm in measurements with laser

In Figure 12, the results of the comparison with the multi-color tunable laser have been added to the comparison of the measurement data of grating monochromator and neon lamp spectrum. It has been observed that the data points of the laser are in the line with the neon lamp calibration graph which shows that the laser can also be used for monochromator calibration.

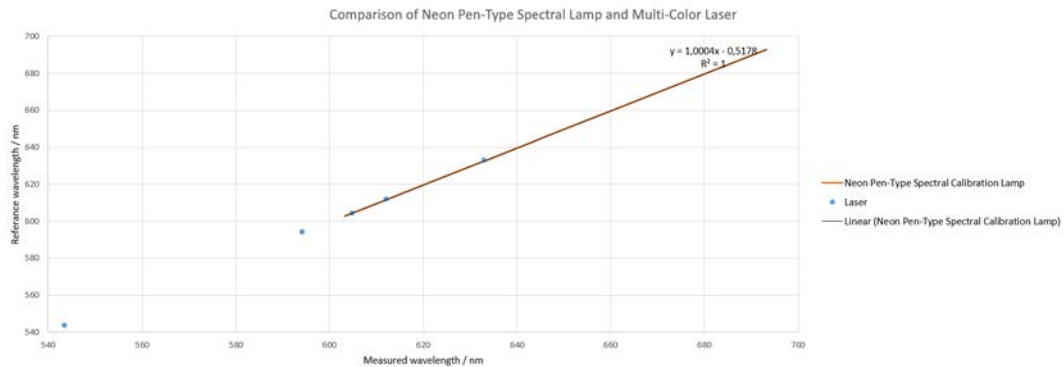


Figure 12. Adding the results of the comparison with the multicolor tunable laser to the comparison of the measurement data of the grating monochromator and the neon lamp spectrum

## 4. CONCLUSION

Calibration of the monochromator grating have been made using neon spectrum lines, argon spectrum lines and multi-color tunable laser. A wavelength correction was obtained by using the experimental data. Calibrating with different light sources have increased the accuracy of the calibration. By comparing multi-color tunable laser and neon pen-type spectral lamp, it has been shown that laser can also be used for monochromator grating calibration. A multiwavelength laser like one used in this work can be used for the fast calibration of monochromators and spectrometers.

## ACKNOWLEDGMENT

The first author would like to thank TUBITAK BIDEB Intern Researcher Scholarship Program (STAR).

## REFERENCES

- [1]. Palmer, C., & Loewen, E. G. (2005). Diffraction grating handbook.
- [2]. Baumgartner, A. (2019). Grating monochromator wavelength calibration using an echelle grating wavelength meter. *Optics express*, 27(10), 13596-13610.
- [3]. Liu, H., Ying, C., Chen, K., Wang, H., Jiang, B., Wu, B., ... & Huo, M. (2016, August). Research on calibration Technology of the wide spectrum grating monochromator wavelength accuracy. In 2016 URSI Asia-Pacific Radio Science Conference (URSI AP-RASC) (pp. 1744-1747). IEEE.
- [4]. Schwarzmaier, T., Baumgartner, A., Gege, P., & Lenhard, K. (2013, October). Calibration of a monochromator using a lambdameter. In *Sensors, Systems, and Next-Generation Satellites XVII* (Vol. 8889, p. 888910). International Society for Optics and Photonics.

# Numerical investigation of natural convection heat transfer of nanofluids in a square cavity

*Abd el malik Bouchoucha<sup>1</sup>, Rachid Bessaih<sup>2</sup>, Abdelfettah Boussaid<sup>3</sup>*

---

## Abstract

*A numerical study of natural laminar 2D convection in a square cavity with a nanofluid was made application. The application consists of a square cavity filled with a nanofluid (Cu-water). The vertical walls are kept adiabatic. While the bottom wall is hot, and the horizontal top wall of the enclosure are maintained at a relatively low temperature ( $T_c$ ). The influence of Rayleigh numbers and the concentration of nanoparticles ( $Al_2O_3$ , Cu, Ag, and  $TiO_2$ ) dispersed in a base fluid (water), on the flow and a thermal field is presented. A house code in FORTRAN, based on the finite volume method, was used to simulate 2D flow with heat transfer. The results indicate that the addition of nanoparticles in pure water makes it possible to improve the heat transfer, in particular, to low Rayleigh number. Although the addition of nanofluids ( $TiO_2$  and  $Al_2O_3$ ) also increases the heat transfer, their influence is not important as for Cu-water and Ag-water.*

**Keywords:** Natural convection, Nanofluids, Cavity.

---

## 1. INTRODUCTION

Laminar natural convection on cavities has attracted many researchers, due to its practical applications in engineering such as heat removal from solar collectors, electronic and electrical equipments and nuclear reactor design. All the authors of these papers on natural convection in cavities, some of them focused on natural convection enhancement utilizing nanofluids [1-5]. Paragraph Lam and Prakash [6] reported that the global entropy generation might be due to fluid friction is found to increase in convection dominated regime. It is also observed that with increasing of Darcy number, porosity and Rayleigh number of the surface averaged Nusselt number for both top and bottom heat sources is increased. Aminossadati and Ghasemi [7] investigated the free convection of nanofluid in a square cavity cooled from two vertical and horizontal walls and heated by a constant heat flux on its horizontal bottom wall. They reported that the type of nanoparticles and the length and location of the heat source affected significantly the heat source maximum temperature. The also reported that natural convection in an isosceles triangular enclosure with a heat source located at its bottom wall [8]. The main objective of this study is to investigate the steady laminar natural convection in a square cavity filled with nanofluid. The influence of various heat source lengths, solid volume fraction, heat source lengths location and Rayleigh number.

### 2.1 Problem Description

The configuration considered in this study is shown in Fig 1. A square cavity of dimension  $L$  is filled with pure water and nanofluid. The vertical walls are kept adiabatic. While the bottom wall is hot, and the horizontal top wall of the enclosure are maintained at a relatively low temperature ( $T_c$ ). The base fluid (water) used is incompressible, Newtonian fluid that satisfies the Boussinesq hypothesis and the nanofluids assumed to be incompressible and the flow is laminar. The thermo-physical properties of the nanofluid are constant, except for the variation of density, which is estimated by the Boussinesq hypothesis.

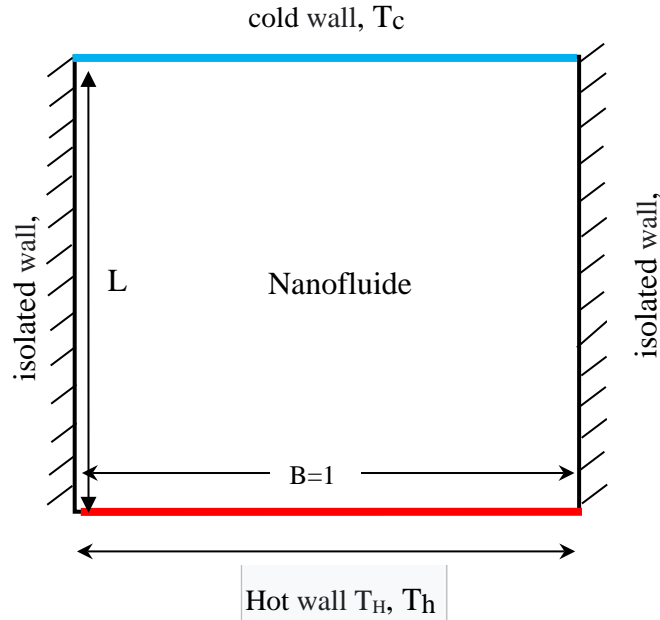
---

<sup>1</sup> Department of Science and Technology, University of Mila, Algeria

<sup>2</sup> Technology, University Frères Mentouri-Constantine 1, Route de Ain El. Bey, Constantine 25000

<sup>3</sup> Institut des Sciences et des Techniques Appliquée, University Frères Mentouri-Constantine 1, Route de Ain El. Bey, Constantine 25000

corresponding-author-bouchoucha.malik@gmail.com



## 2.2 Governing Equations

The non-dimensional continuity, momentum and energy equations are written as follows

$$\frac{\partial U}{\partial X} + \frac{\partial V}{\partial Y} = 0 \quad (1)$$

$$U \frac{\partial U}{\partial X} + V \frac{\partial U}{\partial Y} = -\frac{\partial P}{\partial X} + \frac{\mu_{nf}}{\rho_{nf} \alpha_f} \left( \frac{\partial^2 U}{\partial X^2} + \frac{\partial^2 U}{\partial Y^2} \right) \quad (2)$$

$$U \frac{\partial V}{\partial X} + V \frac{\partial V}{\partial Y} = -\frac{\partial P}{\partial Y} + \frac{\mu_{nf}}{\rho_{nf} \alpha_f} \left( \frac{\partial^2 V}{\partial X^2} + \frac{\partial^2 V}{\partial Y^2} \right) + \frac{(\rho\beta)_{nf}}{\rho_{nf} \beta_{nf}} Ra Pr \theta \quad (3)$$

$$U \frac{\partial \theta}{\partial X} + V \frac{\partial \theta}{\partial Y} = \frac{\alpha_{nf}}{\alpha_f} \left( \frac{\partial^2 \theta}{\partial X^2} + \frac{\partial^2 \theta}{\partial Y^2} \right) \quad (4)$$

The effective density of the nanofluids given as

$$\rho_{nf} = (1 - \phi) \rho_f + \phi \rho_p \quad (5)$$

Where  $\phi$  is the solid volume fraction of nanoparticles.

The thermal diffusivity of the nanofluid is

$$\alpha_{nf} = k_{nf} / (\rho C_p)_{nf} \quad (6)$$

Where, the heat capacitance of the nanofluid is given by:

$$(\rho C_p)_{nf} = (1 - \phi) (\rho C_p)_f + \phi (\rho C_p)_p \quad (7)$$

The thermal expansion coefficient of the nanofluid can be determined by

$$(\rho\beta)_{nf} = (1 - \phi) (\rho\beta)_f + \phi (\rho\beta)_p \quad (8)$$

The effective dynamic viscosity of the nanofluid given by Brinkman [9] as

$$\mu_{nf} = \frac{\mu_f}{(1-\phi)^{2.5}} \quad (9)$$

In Eq (2),  $k_{nf}$  is the thermal conductivity of the nanofluid, which for spherical nanoparticles, according to Maxwell [10] is

$$k_{nf} = k_f \left[ \frac{(k_p + 2k_f) - 2\phi(k_f - k_p)}{(k_p + 2k_f) + \phi(k_f - k_p)} \right] \quad (10)$$

In order to cast the governing equations into a dimensionless form, the following dimensionless parameters are introduced

$$X = \frac{x}{L}, Y = \frac{y}{L}, U = \frac{uL}{\alpha_f}, V = \frac{vL}{\alpha_f}, P = \frac{pL^2}{\rho_{nf}\alpha_f^2}, \theta = \frac{T - T_c}{\Delta T (= T_H - T_C)} \quad (11)$$

Where Ra and Pr are the Rayleigh and Prandtl numbers and thermal conductivity ratio defined as

$$Ra = \frac{g\beta_f L^3 (T_H - T_C)}{\nu_f \alpha_f}, Pr = \frac{\nu_f}{\alpha_f}, R_c = \frac{K_s}{K_f} \quad (12)$$

### 2.3 Boundary Conditions

The dimensionless boundary conditions are

$$X = 0, 0 \leq Y \leq 1: U = V = 0, \frac{\partial \theta}{\partial x} = 0$$

$$X = l, 0 \leq Y \leq 1: U = V = 0, \frac{\partial \theta}{\partial x} = 0$$

$$Y = 0, 0 \leq X \leq 1: U = V = 0, \theta = 1$$

$$Y = l, 0 \leq X \leq 1: U = V = 0, \theta = 0$$

### 2.4 Local and Average Nusselt numbers

The local Nusselt number on the heat source surface is defined as

$$Nu = \frac{hL}{k_f} \quad (13)$$

Where  $h$  is the heat transfer coefficient determined by

$$h = -k_{nf} \left( \frac{\partial T}{\partial x} \right)_{wall} \quad (14)$$

By using the dimensionless variables mentioned above, the local Nusselt number becomes as



$$Nu = -\frac{k_{nf}}{k_f} \left( \frac{\partial \theta}{\partial X} \right)_{wall} \quad (15)$$

Where  $\theta$  and  $X$  are the dimensionless temperature and coordinate, respectively. Finally, the average Nusselt number  $Nu_m$  along the heat source surface can be obtained as

$$Nu_m = \frac{1}{A} \int Nu \, dA \quad (16)$$

### 3. NUMERICAL METHOD

The governing equations presented in Eqs.(2) - (4) along with the boundary conditions are solved by using FORTRAN code, which using a control volume formulation [29]. The numerical procedure called SIMPLER algorithm [11] is used to handle the pressure-velocity coupling. For treatment of the convection terms in equations (2)-(4), power-law scheme was adopted. The convergence was obtained when the energy balance between the heat source and the cold wall is less than a prescribed accuracy value, i.e., 0.1%.

#### 3.1 Grid Independence Study

The study was undertaken to six grids: 60×60, 80×80, 100×100 and 120×120 nodes. Table 2 shows the variation of the maximum values  $Nu_m$  with grid size for  $Al_2O_3$ -water nanofluid,  $\phi = 0.1$  and  $Ra=10^5$ . The changes in the calculated values are very small for three 80×80, 100×100, 120×120 grids and we noticed that the variation of  $Nu_m$  between 100×100 and 120×120 nodes is less than 0.002014 (see Table 2). However and after running tests of independence between the numerical solution and the mesh, the fourth grid 100×100 nodes was chosen to complete the calculations. This grid also gives the best compromise between cost and accuracy of calculations.

**Table 1.** Grid independency results ( $Al_2O_3$ -water nanofluid,  $\phi = 0.1$  and  $Ra=10^5$ )

Grid	60×60	80×80	100×100	120×120
$Nu_m$	4.231977	4.229471	4.230342	4.232356

#### 3.2 Code Validation

To verify the accuracy of the present numerical study, the numerical code was validated with the numerical results of Aminossadati and Ghasemi [7] at  $Ra=10^5$ ,  $\phi=0$  and 0.10 for the local Nusselt number  $Nu$  Fig.2 (a) and Vertical velocity profiles along the mid-section of the enclosure Fig.3 (b). As shown in Fig.2 (a-b) the present results shows good agreement with the numerical results of Aminossadati and Ghasemi [7].

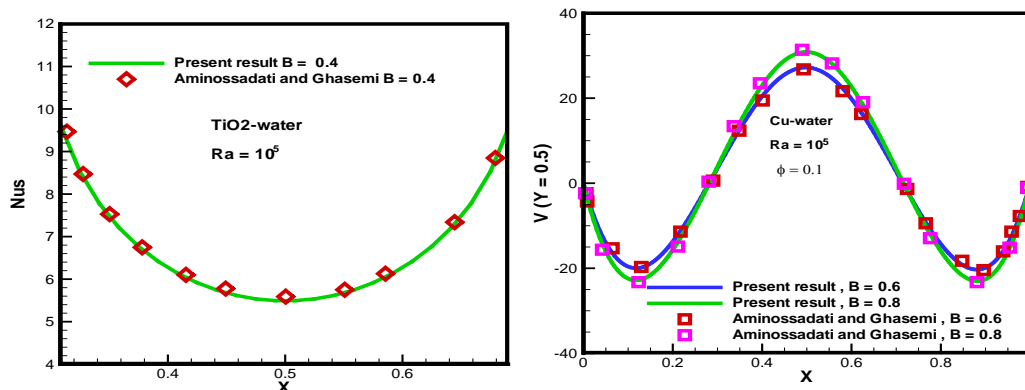


**Fig.2.** Comparison between present study and those of Aminossadati and Ghasemi [7] at  $Ra=10^5$ ,  $\phi=0$  and 0.10 (a) Local Nusselt number  $Nu_s$  along the heat source and (b) Vertical velocity profiles along the mid-section of the enclosure for various heat source lengths.

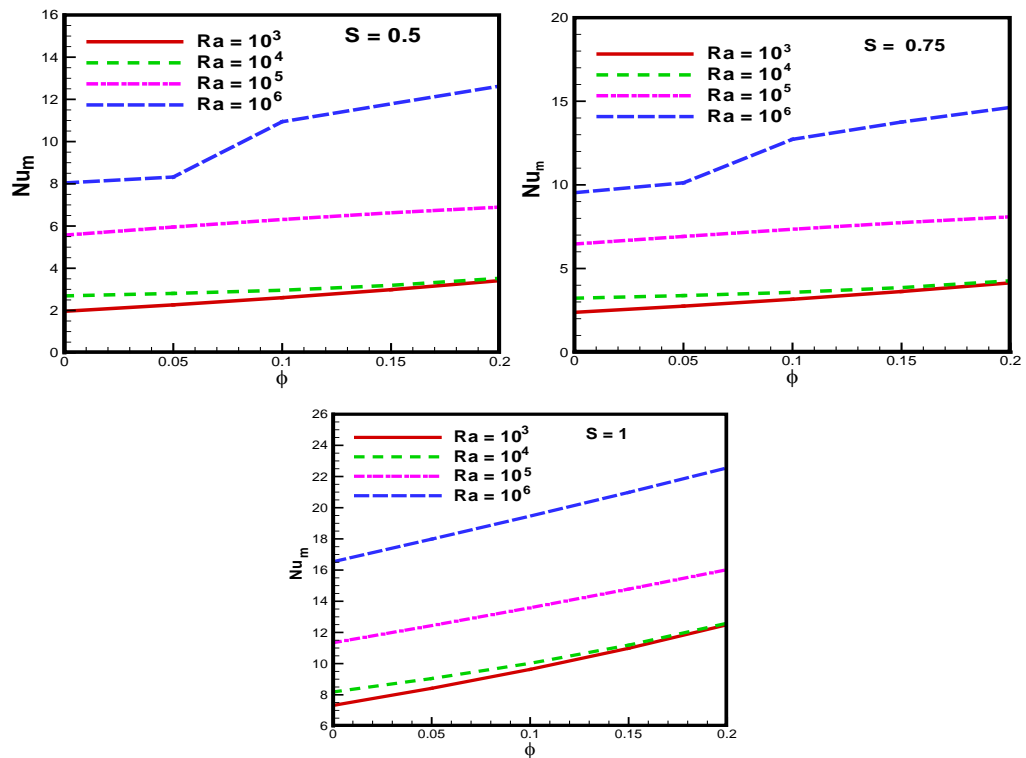


Fig.3 Variation of average Nusselt number ratio with solid volume fraction  $\phi$  at various Rayleigh numbers and various dimensionless heat source lengths.

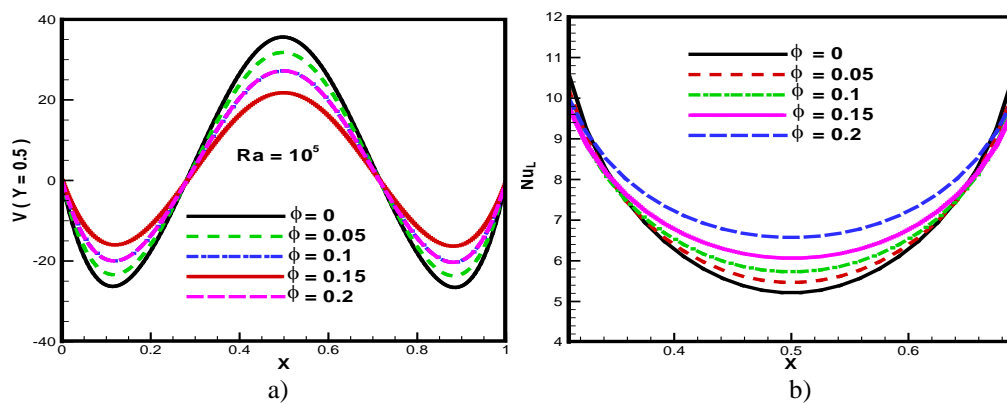


Fig. 4. a) Vertical velocity profiles along the mid-section of the enclosure for various heat source lengths (Cu-Water,  $Ra = 10^5$ ,  $D = 0.5$  and  $B = 0.4$ ), b) Profile of local Nusselt number along the heat source for various solid volume fractions (Cu-Water,  $Ra = 10^5$ ,  $D = 0.5$  and  $B = 0.4$ ).

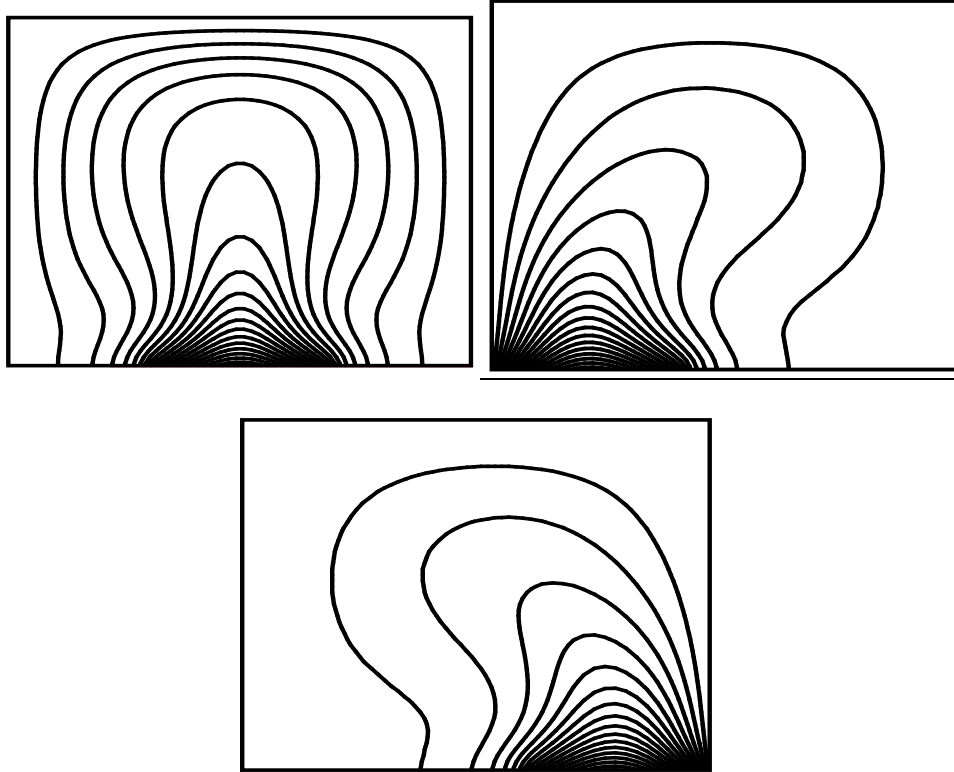


Fig. 5. Streamlines for the enclosures filled with Cu-water nanofluid for different locations of the heat source at  $\phi = 0, 1$ , et  $Ra = 10^5$ .

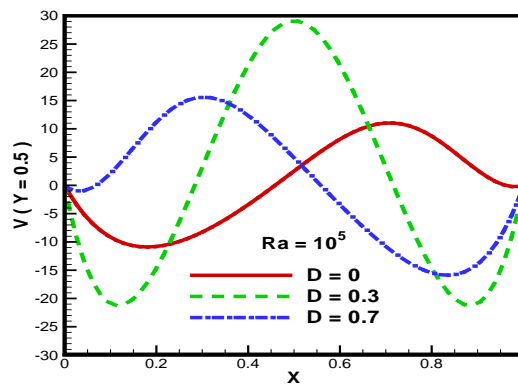


Fig. 6. Vertical velocity profiles along the mid-section of the enclosure for different locations of the heat source  $\phi = 0, 1$ , et  $Ra = 10^6$ .

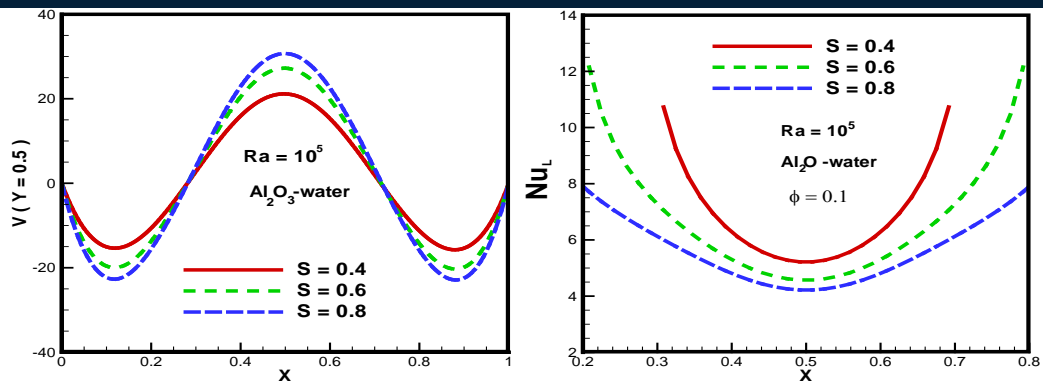
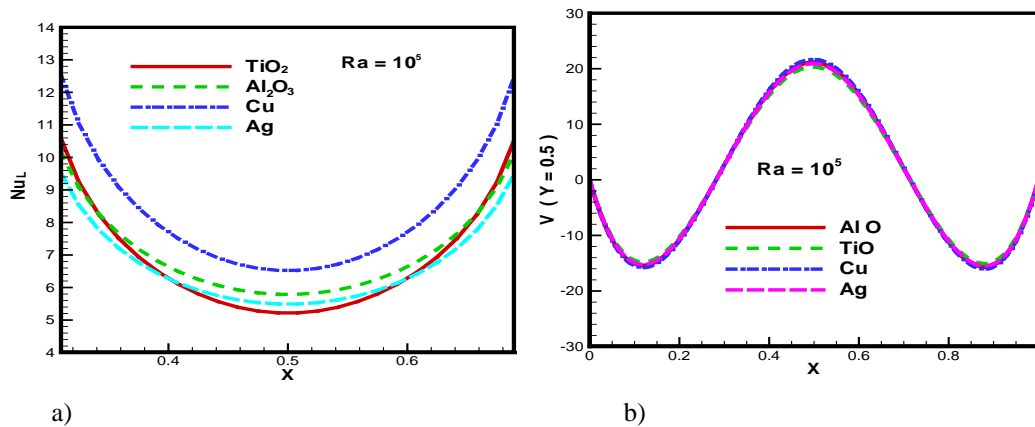


Fig. 7. Vertical velocity profiles along the mid-section of the enclosure for various heat source lengths (Profile of local Nusselt number along the heat source for various heat source lengths (Cu–Water,  $Ra = 10^5$ ,  $D = 0.5$  and  $\phi = 0.1$ ).



a)

b)

Fig. 8 a) Vertical velocity profiles along the mid-section of the enclosure for various heat source lengths. Profile of local Nusselt number along the heat source for different types of nanofluids ( $Ra = 10^5$ ,  $B = 0.4$ ,  $D = 0.5$  and  $\phi = 0.1$ ).

Fig. 3 presents the variation of the average Nusselt number with volume fraction of nanoparticles and for various Rayleigh numbers ( $10^4$ – $10^6$ ) at different various dimensionless heat source lengths. The average Nusselt number increases with increasing the volume fraction for all values of Rayleigh number. By increasing the volume fraction of nanoparticles, the viscosity of nanofluid increases slowly, which leads to a slower movement and this in turn reduces the heat transfer rate. There by, the augmentation of nanofluid thermal conductivity enhances the thermal exchange and the conductivity effect is more considerable than the viscosity. Consequently, the heat transfer increases by increasing the solid volume fraction. It is observed that when the Rayleigh number increases, the convection heat transfer becomes more dominant on one side. On the other side, an effective thermal conductivity is achieved. In addition, the viscosity of nanofluid effects becomes also important. A balance between a wanted effect of enhanced thermal conductivity and unwanted effects of increased viscosity sets the optimal volume fraction. An increase in the dimensionless heat source lengths the average Nusselt number increasing for all cases.

In order to have a better understanding of the flow behaviour in this situation, the vertical velocity profiles along the mid-section of the enclosure are presented in Fig. 4.a. Symmetrical velocity profiles are observed which indicate the direction of the flow rotation within the enclosure. In fact, the flow rises in the middle and descends near the vertical walls. It is also clear that the absolute magnitude of vertical velocity increases with increasing the volume fraction. This is because of stronger buoyant flow for higher heat generation rates. Fig.4.b shows the variation of the local Nusselt number along the heated wall for  $Ra = 10^5$  for  $\phi = 0.1$  at different for various solid volume fractions, the Rayleigh number  $Ra = 10^5$ . The circulation strength increases as a result of higher buoyancy forces. This results show an increase of the local Nusselt number. As a result of the stronger circulation produced by elevated thermal energy transport, it is observed that the local Nusselt number profiles

become symmetric for all cases. The local Nusselt number increases with increasing the volume fraction for all values of Rayleigh number.

Fig. 5 displays the isotherms for different locations of the heat source on the bottom wall at  $Ra = 10^5$ . The isotherms show that as the heat source moves away from the left cold wall, the maximum flow temperature increases. This can be explained by the distance that the fluid needs to travel in the circulating cell to exchange the heat between the heat source and the left cold wall. In fact, the closer the heat source is to the left cold wall, the higher heat removal and the lower heat source maximum temperature is achieved. It is clear that the isotherms follow the movement of the heat source and their extension in the enclosure becomes more noticeable as the heat source moves away from the left wall.

Fig. 6 presents the vertical velocity profiles along the midsection of the enclosure  $V$  at  $Y = 0.50$  (middle of the cavity) for different positions of the heat source at  $Ra = 10^5$ . We have seen that the velocity profiles varies according to the heat position, it gains maximum velocity when the heat position tans towards the middle of the cavity. So from the results it is noted that the position of the heat source plays a major role in the velocity of the nanofluid.

presents the vertical velocity profiles along the midsection of the enclosure  $V$  at  $Y = 0.50$  (middle of the cavity) for different various dimensionless heat source lengths at  $Ra = 10^5$ . In terms of  $Num$  and  $T_{max}$  values at different Rayleigh numbers and three different heat source lengths. Finally, this code has been further validated against the study for natural convection in a partially heated enclosure filled with nanofluid  $Al_2O_3$ -water nanofluid at different Rayleigh numbers. In order to have a better understanding of the behavior of the flow in this situation, the vertical velocity profiles along the mid-section of the enclosure are shown in Fig. 7 a. Symmetrical velocity profiles are observed which indicate the direction of flow in the enclosure. In fact, the flow rises in the middle and goes down near the vertical walls. It is also clear that the absolute magnitude of the vertical velocity increases with increasing length of the heat source, due to stronger floating flow for higher heat generation rates. Fig. 7.b shows the profile of local Nusselt number along the heat source for different various dimensionless heat source lengths at  $Ra = 10^5$ . This figure shows symmetrical profiles of the local Nusselt number along the heat source for different heat source lengths. As previously stated, the highest local Nusselt number is found in both ends and the lowest is obtained at the middle of the heat source, respectively. In general, increasing the length of the heat source results in a decrease in the local Nusselt profile.

Fig. 8.a shows the profile of local Nusselt number along the heat source for different types of nanofluids. Symmetrical profiles are obtained for all nanofluids with the lowest Nusselt number for the middle of the heat source. The  $TiO_2$  has the lowest value of thermal conductivity compared to other nanoparticles, hence, it has the lowest values of Nusselt number. Cu and Ag, on the other hand, have the highest values. In addition, the thermal conductivity of  $Al_2O_3$  is approximately one tenth of Cu and Ag, thus, the Nusselt number for  $Al_2O_3$  is lower than that for Cu and Ag. In order to have a better understanding of the behavior of the flow in this situation, the vertical velocity profiles along the mid-section of the enclosure are shown in Fig7.b. Symmetrical velocity profiles are observed which indicate the direction of rotation of the flow in the enclosure. In fact, the flow rises in the middle and goes down near the vertical walls. It is also clear that the absolute magnitude of the vertical velocity increases with increasing length of the heat source. This is due to a stronger floating flux for higher heat generation rates.

## 5. CONCLUSION

A numerical study of two dimensional natural convection of a nanofluid that consists of water and  $Al_2O_3$  in a square cavity filled. A comparison with previously published work was performed and the results were to be in good agreement. The results show that the effect of previous parameters has considerable effects on the flow and heat transfer. The important concluding remarks are presented below.

- Nusselt number increases with an increasing volume fraction of nanoparticles.
- Heat transfer increases with increase in the volume fraction of the nanoparticles and the heat source length.
- The number of the average Nusselt increases with increasing length of the heat source.
- the uses of the nanoparticle have a positive effect on heat transfer
- La viscosité dynamique augmente avec l'augmentation de la fraction volumique des nanoparticules ( $Al_2O_3$ -eau).

**REFERENCES**

- [1] Ho, C.J., Chen, M.W., and Li., Z.W, Numerical Simulation of Natural Convection of Nanofluid in a Square Enclosure: Effects Due to Uncertainties of Viscosity and Thermal Conductivity, *International Journal of Heat and Mass Transfer* 51(2008) 4506–4516.
- [2] M. Mahmoodi, S.M, Sebdani, Natural Convection in a Square Cavity Containing a Nanofluid and an Adiabatic Square Block at the Center, *Superlattices and Microstructures* 52 (2012) 261–275.
- [3] R.Jmai, B.Beya, and T.Lili, Heat Transfer and Fluid Flow of Nanofluid-Filled Enclosure with Two Partially Heated Side Walls and Different Nanoparticles, *Superlattices and Microstructures* 53(2013) 130–154.
- [4] R.K.Tiwari, and , M.K .Das, Heat Transfer Augmentation in a Two-Sided Lid-Driven Differentially Heated Square Cavity Utilizing Nanofluids, *International Journal of Heat and Mass Transfer* 50 (2007) 2002–2018.
- [5] E.H.Ooi and V. Popov, Numerical Study of Influence of Nanoparticle Shape on the Natural Convection in Cu-water Nanofluid, *International Journal of Thermal Sciences*65 (2013) 178-188.
- [6]P. A. K. Lam, K. A. Prakash, A numerical study on natural convection and entropy generation in a porous enclosure with heat sources, *International Journal of Heat and Mass Transfer* 69 (2014) 390–407.
- [7]S.M. Aminossadati, B. Ghasemi, Natural Convection Cooling of a Localised Heat Source at the Bottom of a Nanofluid-Filled Enclosure. *European Journal of Mechanics B/Fluids* 28(2009) 630–640.
- [8] S.M. Aminossadati, B. Ghasemi ,Enhanced Natural Convection in an Isosceles Triangular Enclosure Filled with a Nanofluid, *Computers and Mathematics with Applications* 61(2011)1739–1753.
- [9] H.C. Brinkman, the Viscosity of Concentrated Suspensions and Solution, *J. Chem. Phys.*20 (1952) 571-581.
- [10] J. Maxwell, *A Treatise on Electricity and Magnetism*, second ed. Oxford University Press, Cambridge, UK, 1904.
- [11] S.V, Patankar, *Numerical Heat Transfer and Fluid Flow*, McGraw-Hill, New York. 1980.

# Evaluation of a novel bio-waste obtained from sawdust as an adsorbent for removal of Pyronin B

Mehmet Kaya<sup>1</sup>

---

## Abstract

*In this work, the evaluation of low-cost, abundantly available, efficient and eco-friendly bio-waste adsorbent (BWA) obtained from waste tea stem (sawdust tea wood) was presented as an alternative to the current expensive methods of removing Pyronin B (PyB) dye from aqueous solution. The effects of varied factors, amount of adsorbent, initial dye concentration, contact time, etc., were studied, and optimal experimental conditions were revealed. In addition, structural and morphological characterization of BWA was confirmed by FTIR, SEM study. It was found that the Lagergren's model could be used for the estimation of the system's kinetics. The present investigation and comparison with other reported adsorbents concluded that BWA may be applied as an attractive low-cost option for removal of PyB from aqueous solution.*

**Keywords:** Adsorption, Dye Removal, Sawdust, Pyronin B, Bio-waste

---

## 1. INTRODUCTION

The agriculture industry manufactures food harvest, industrial crops and other products. It also produces billions of tones of other materials regarded as "waste". Investigations find out that a variety of agricultural waste products such as bark of trees, rice husk, saw dust of various plants, groundnut shells, coconut shells, cotton seed hulls, waste tea leaves, etc. have been experimented [1-8]. Therefore, agricultural waste recycling is one of the most important research areas for solution to the energy dilemma faced by civilizations during the last few years [9-13]. A considerable part of these research interests is related to development of novel adsorbents, which are eco-friendly due to their incomparable chemical composition, utility in abundance, renewable, low in cost and viable option for hazardous and toxic substances remediation such as dyes [14, 15]. Dyes have been largely used in food and laser industries, the textile, in many areas such as cosmetics, medicine, pharmacology, while the manufacturing and consumption of dyes worldwide has reached approximately 700,000 tonnes [16, 17]. Dyes can also hinder the growth and photosynthesis of several plants and bacteria by absorbing sunshine entering water. Troubles are getting graver owing to the fact that the complex aromatic structures of dyes render them ineffective degradation of dyes [18]. Therefore, removal of dyes from polluted wastewater is a main work for environmental preservation. There are several methods of removing dyes, however, it is rather troublesome to treat wastewater by conventional processes because of the complex molecular structure of dyes [17]. Hence, innovative treatment methods are being investigated. Among the various treatment options available for the removal of dyes from industrial effluents, adsorption is one of the most effective methods [19].

In this regard, the objective of the paper is to bring out adsorption properties of BWA sawdust obtained from tea stem for PyB dye removal and it is used in investigations for the first time corresponding with the current work. Besides, it is characterized as an adsorbent material by using Fourier transform infrared spectroscopy (FT-IR), molecular absorption spectroscopy and scanning electron microscopy (SEM) techniques. Even though many studies on the production of sawdust adsorbent from various plants referred above are present in the literature, there seems not to be a lot of comparable studies on using this adsorbent.

---

<sup>1</sup> Recep Tayyip Erdogan University, The Faculty of Arts&Sciences, Department of Chemistry, Rize, Turkey

## 2. MATERIALS AND METHODS

### 2.1. Materials

PyB as a pollutant dye model, which was purchased from Merck, was used without any further purification and its chemical formula is presented in Fig.1. Tea tree sawdust was obtained from agricultural tea tree waste in Rize/Turkey.

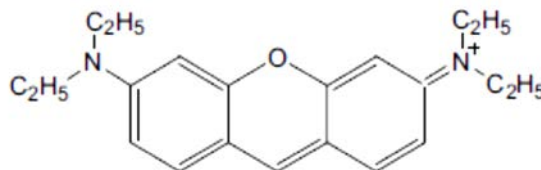


Fig. 1 Chemical Structure of PyB Dye

### 2.2. Preparation of the adsorbent and adsorbate

The biomaterial waste used as an adsorbent was intensely washed under deionized water to remove any particulate. Then, they were dried in oven at 105°C for 24 h. Sawdust adsorbents were grained and sieved by a range of sieves and only when the particles became smaller than 75 µm, they were used. A stock solution of 1.04 g/L of PyB adsorbate was prepared in deionized water. It is subsequently diluted whenever necessary considering optimum concentrations.

### 2.3. Adsorption Studies

The effect of contact time was studied by taking the samples from the shaker at predetermined time intervals and residual dye concentration was analyzed. Finally, Langmuir and Freundlich isotherms were used to analyze the equilibrium adsorption data. Perkin-Elmer (Model Lambda 35) spectrophotometer for absorption measurements was used. The amount of PyB adsorbed per unit mass of adsorbent,  $q_e$  (mg g<sup>-1</sup>), was calculated as follows:

$$q_e = \frac{(C_0 - C_e)V}{W}, \quad (1)$$

where  $C_0$  and  $C_e$  (mg L<sup>-1</sup>) correspond to the liquid-phase concentrations of PyB at initial and equilibrium, respectively,  $V$  is the volume of the solution (L), and  $W$  is the mass of adsorbent used (g). Kinetics and equilibrium studies were performed at 25, 30, 35, 40, 45 and 50 °C.

## 3. RESULTS AND DISCUSSION

### 3.1. Spectroscopic Characterization and Components of Bio-waste adsorbent

Fig. 2 shows the SEM image of bio-waste adsorbent (1000 X). It is clear that the surface of bio-adsorbent seems to be rough and protrusions, which are highly creased, can be seen throughout the micrograph. The adsorbent is a heterogeneous material consisting of particles of irregular shapes having considerable layers with pores of varying size and provides a fair possibility for the dye to be adsorbed.



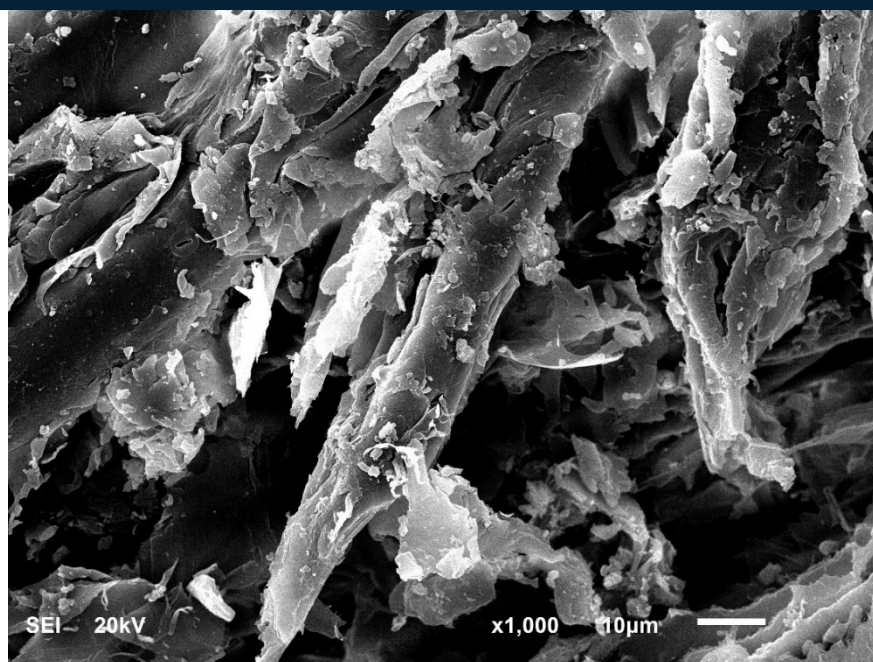


Fig. 2 SEM Image of Bio-Waste (x1000)

Fourier transform infrared (FT-IR) spectral analysis was carried out to identify the different functional groups present in the given samples. The different functional groups which are present in the given samples are OH stretching, CH stretching, C=C stretching and C-O stretching. Sawdust is essentially comprised of cellulose as well as lignin, and all these constituents represented in table 1 contribute as active sites for the adsorption of dye molecules. Fig. 3 displays the FT-IR spectra of bio-waste adsorbent in its natural form. The spectra demonstrates a number of peaks depicting that bio-waste adsorbent is composed of various functional groups which probably help in binding of dye molecules. FT-IR spectrum of the given raw bio-waste adsorbent shows that the broad and intense peak at  $3335\text{cm}^{-1}$  was attributed to the stretching of O-H group due to inter and intramolecular hydrogen bonding of cellulosic compounds such as alcohols or phenols [20]. The peak observed at  $2923\text{cm}^{-1}$  was associated with the stretching vibrations of CH bond of methyl, methylene and methoxy groups [21]. The peaks at  $1641\text{cm}^{-1}$  and  $1734\text{cm}^{-1}$  indicate the presence of C=C and C=O stretching of functional group, respectively. Besides, the peaks appearing at  $1150\text{cm}^{-1}$  and  $1027\text{cm}^{-1}$  in the spectrum contribute to C-O stretching of the phenolic group and a strong C-O bond due to ether group of cellulose, respectively [21]. Additionally, bio-waste adsorbent was performed by standard methods used for the determination of moisture and percent composition of constituents [22]. The results thus obtained have been recorded in Table 1.

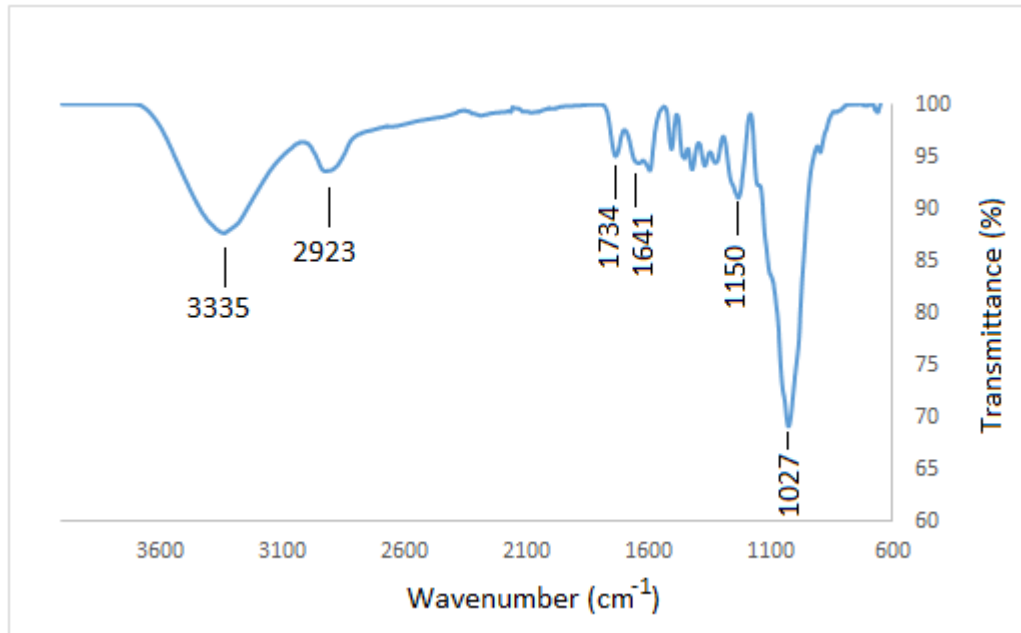


Fig. 3 FT-IR spectra of Bio-Waste Adsorbent

Table 1. Component of Bio-Waste Adsorbent

Sample	Cellulose (%)	Lignin (%)	Holocellulose (%)	Hemicellulose (%)
<b>Bio-waste adsorbent</b>	32.23 (2923 cm <sup>-1</sup> C-H stretch)	38.57 (1641 cm <sup>-1</sup> C=C stretch)	67.15	37.95

### 3.2. Effect of contact time and initial adsorbate concentration

In order to determine the optimum PyB concentration and equilibrium time ( $q_e$ ), initial concentrations of dye were changed and time ranges were evaluated until no more adsorption occurred. Fig. 4 demonstrates the removal of PyB for varied initial concentrations of the adsorbent (bio-waste sorbent) at 25°C and pH 7.0, in which  $q$  represents the ratio of the adsorbed milligram amount of PyB to the gram amount of adsorbent. With the alter in the concentration of PyB from 1.0, 5.0 and 10.0 mg/L, the amount of adsorbed PyB increased from 0.15 mg (68% removal) to 1.66 mg (91% removal). The percentage of the removal dye did not change perceptibly with regard to the initial adsorbate concentration. The equilibrium time for PyB was found to be 28 min for 1.0 mg/L, 37 min for 5.0 mg/L and 43 min for 10.0 mg/L. It was also found out that the adsorption was rapid in the initial stages and gradually decreased with the progress of adsorption.

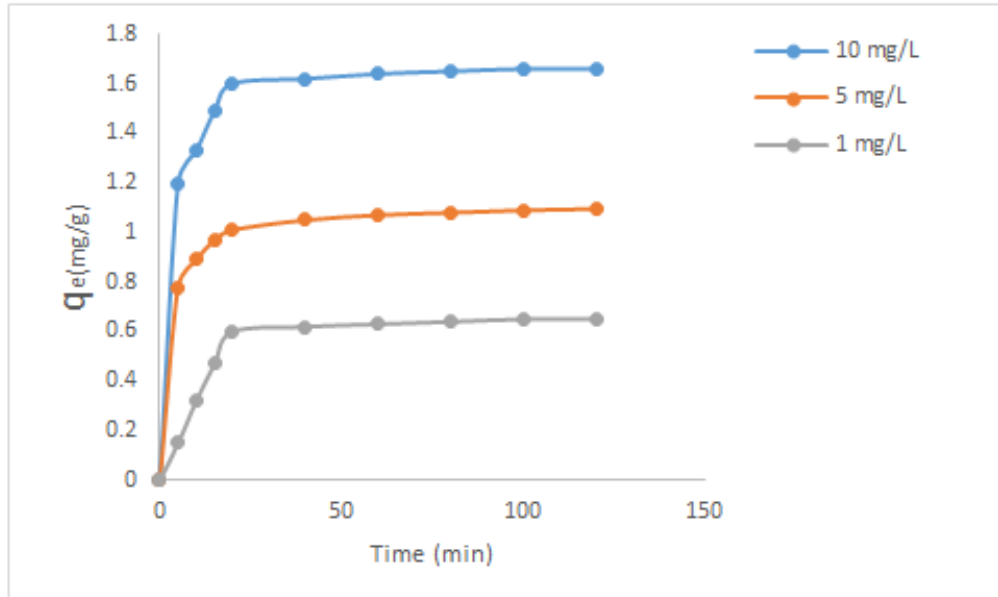


Fig. 4 Removal of Dye for Varied Initial Concentrations

### 3.3. Adsorption Isotherms

The adsorption isotherm is important for the explanation of how the adsorbate will interact with the bio-waste adsorbent and it gives an idea of the adsorption capacity of the adsorbent. The surface phase may be considered as a monolayer or multilayer. For this purpose, Langmuir (Eq.(1)) and Freundlich (Eq. (2)) isotherm equations were applied to the experimental data. The data confirm the linear form of Langmuir model given in Fig. 5.

$$\log q_e = \log K_f + \frac{1}{n} \log C_e \quad (2)$$

$$\frac{C_e}{q_e} = \frac{C_e}{q_m} + \frac{1}{K_L q_m} \quad (3)$$

where  $K_F$  and  $n$  are Freundlich constants displaying the adsorption capacity and adsorption intensity, respectively.  $C_e$  is the equilibrium concentration of the dye ( $\text{mg L}^{-1}$ ) and  $q_e$  is the amount of dye adsorbed ( $\text{mg}$ ) per unit of the adsorbent ( $\text{g}$ ). In the case of PyB adsorption onto the bio-sorbent fibers, obtained for  $n$  (0.002) and  $K_f$ (0.112).  $q_m$ (3.85), the maximum adsorption capacity( $\text{mg g}^{-1}$ ), and  $K_L$ (0.139), the equilibrium constant ( $\text{L g}^{-1}$ ), are the Langmuir constants related to monolayer coverage and the energy of adsorption, respectively. Moreover, the correlation coefficient of  $R^2 \approx 0.994$  obtained using the Langmuir isotherm, which is much higher than that of Freundlich isotherm ( $R^2 = 0.956$ ) exhibits the adsorption of PyB onto the bentonite particles perfectly. The Freundlich and Langmuir constants were summarized in Table 2.

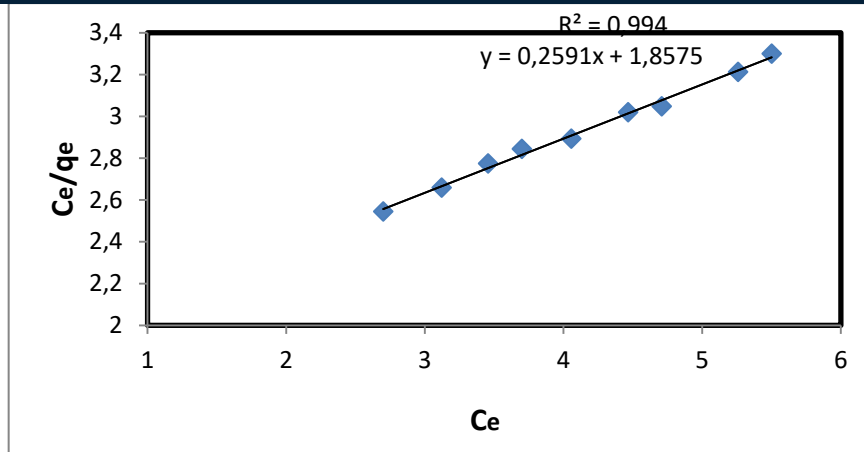


Fig. 5. Linear Graph of Langmuir Isotherm

Table 2. Experimental Results of Adsorption Isotherms

Dye	Langmuir			Freundlich		
	$q_m$ (mg/g)	$K_L$ (l/g)	$R^2$	$n$	$K_F$ (mg <sup>(1-1/n)</sup> L <sup>1/n</sup> /g)	$R^2$
PyB	3.85	0.139	0.994	0.002	0.112	0.956

### 3.4. Adsorption Kinetics

Several kinetic models are presented to define the characteristic of the adsorbent, to examine the controlling mechanism of the adsorption process and to test the experimental data. In the present study, the adsorption data were examined by using two kinetic models as the pseudo-first-order and pseudo-second-order kinetic models. The pseudo-first-order model was presented by Lagergren [23]. The Lagergren's first-order reaction model is expressed in Eq. 4 as follows:

$$\log(q_e - q_t) = \log q_e - \frac{k_1}{2.303} t \quad (4)$$

and the second order kinetic model (Eq. 5) [24] can be represented as follows:

$$\frac{t}{q_t} = \frac{1}{k_2 q_e^2} + \frac{t}{q_e} \quad (5)$$

where  $k_2$  is the equilibrium rate constant of second order adsorption ( $\text{g mg}^{-1} \text{min}^{-1}$ ). The  $k_2$  and  $q_e$  values were calculated from the plots of  $t/q$  versus  $t$  which are presented in table 3. Table 3 described the calculated results obtained from the first and second order kinetic models. In addition, the correlation coefficients for the second order kinetic were about 0.998. Therefore, the studied adsorption process obeyed the second order kinetic model.

Table 3. Experimental Results of Adsorption Kinetics

Pseudo First Order		Pseudo Second Order	
$R^2$	$k_1(\text{min}^{-1})$	$R^2$	$k_2(\text{g mg}^{-1} \text{min}^{-1})$
0.942	0.033	0.998	32.125

#### 4. CONCLUSIONS

The present study on removal of PyB from aqueous solution using naturally available material Bio-waste adsorbent (BWA) from tea stem sawdust was carried out in batch experiment. The operational parameters like contact time, initial adsorbate concentration and quantity of adsorbent have a significant effect on the removal efficiency. Kinetics data were best modeled by the second order kinetics equation. Equilibrium models like Langmuir and Freundlich isotherm models were used for the study and equilibrium data. Characterization and cellulosic components of BWA were conducted by using FT-IR spectroscopic analysis methods.

#### Acknowledgment

The author thanks the Research Fund of Recep Tayyip Erdogan University Department of Chemistry for the financial support of this work.

#### Conflict of interest

The author declares that there is no conflict of interest regarding the publication of this paper.

#### REFERENCES

- [1] Bellamy, L.J., *Alcohols and Phenols*, in *The Infra-red Spectra of Complex* [1] I. Abe, T. Fukuhara, S. Iwasaki, K. Yasuda, K. Nakagawa, Y. Iwata, H. Kominami, Y. Kera, Development of a high density carbonaceous adsorbent from compressed wood, *Carbon*, 39 (2001) 1485-1490.
- [2] M.A. Ahmad, N. Ahmad, O.S. Bello, Modified durian seed as adsorbent for the removal of methyl red dye from aqueous solutions, *Applied Water Science*, 5 (2015) 407-423.
- [3] A. Azizi, M.R.A. Moghaddam, M. Arami, Wood Waste from Mazandaran Wood and the Paper Industry as a Low Cost Adsorbent for Removal of a Reactive Dye, *J Residuals Sci Tech*, 8 (2011) 21-28.
- [4] T. Getachew, A. Hussien, V.M. Rao, Defluoridation of water by activated carbon prepared from banana (*Musa paradisiaca*) peel and coffee (*Coffea arabica*) husk, *Int J Environ Sci Te*, 12 (2015) 1857-1866.
- [5] X.J. Guo, J.K. Tak, R.L. Johnson, Ammonia removal from air stream and biogas by a H<sub>2</sub>SO<sub>4</sub> impregnated adsorbent originating from waste wood-shavings and biosolids, *Journal of Hazardous Materials*, 166 (2009) 372-376.
- [6] A. Hashem, Preparation of a new adsorbent based on wood pulp for the removal of Direct Blue 2 from aqueous solutions, *Polym-Plast Technol*, 45 (2006) 779-783.
- [7] S. Jain, R.V. Jayaram, Removal of basic dyes from aqueous solution by low-cost adsorbent: Wood apple shell (*Feronia acidissima*), *Desalination*, 250 (2010) 921-927.
- [8] G. McKay, V.J.P. Poots, Kinetics and Diffusion-Processes in Color Removal from Effluent Using Wood as an Adsorbent, *J Chem Technol Biot*, 30 (1980) 279-292.
- [9] P. Nowicki, J. Kazmierczak-Razna, R. Pietrzak, Physicochemical and adsorption properties of carbonaceous sorbents prepared by activation of tropical fruit skins with potassium carbonate, *Mater Design*, 90 (2016) 579-585.
- [10] A.S. Sartape, P.D. Raut, S.S. Kolekar, Efficient Adsorption of Chromium(VI) Ions from Aqueous Solution onto a Low-cost Adsorbent Developed from Limonia acidissima (Wood Apple) Shell, *Adsorpt Sci Technol*, 28 (2010) 547-560.
- [11] D. Sud, G. Mahajan, M.P. Kaur, Agricultural waste material as potential adsorbent for sequestering heavy metal ions from aqueous solutions - A review, *Bioresource Technol*, 99 (2008) 6017-6027.
- [12] I. Vicinivarri, S. Shanker Kumar, A.W. Nor Aimi, I. Norain, H. Nurul Izza, Preparation and characterization of phosphoric acid activated carbon from *Canarium Odontophyllum* (Dabai) nutshell for methylene blue adsorption, *Res J Chem Environ*, 18 (2014) 57-62.
- [13] M.A. Yahya, Z. Al-Qodah, C.W.Z. Ngah, Agricultural bio-waste materials as potential sustainable precursors used for activated carbon production: A review, *Renewable and Sustainable Energy Reviews*, 46 (2015) 218-235.
- [14] D. Sud, G. Mahajan, M.P. Kaur, Agricultural waste material as potential adsorbent for sequestering heavy metal ions from aqueous solutions - A review, *Bioresource Technol*, 99 (2008) 6017-6027.
- [15] C. Namasivayam, D. Sangreetha, Recycling of agricultural solid waste, coir pith: Removal of anions, heavy metals, organics and dyes from water by adsorption onto ZnCl<sub>2</sub> activated coir pith carbon, *J Hazard Mater*, 135 (2006) 449-452.
- [16] X.J. Tang, C.F. Shen, L. Chen, X. Xiao, J.Y. Wu, M.I. Khan, C.M. Dou, Y.X. Chen, Inorganic and organic pollution in agricultural soil from an emerging e-waste recycling town in Taizhou area, China, *J Soil Sediment*, 10 (2010) 895-906.
- [17] N.F.M. Yunus, M. Zaharia, M.A. Idris, D. Nath, R. Khanna, V. Sahajwalla, Recycling Agricultural Waste from Palm Shells during Electric Arc Furnace Steelmaking, *Energ Fuel*, 26 (2012) 278-286.
- [18] M.M. El-Shazly, Y.M. Chung, H.C. Wang, Y.L. Leu, M.C. Cheng, B. Barve, M. Korinek, C.L. Lee, F.R. Chang, Y.C. Wu, Recycling agricultural waste products: A tree with multiple branches, *Abstr Pap Am Chem S*, 245 (2013).
- [19] D. Briassoulis, M. Hiskakis, E. Babou, Technical specifications for mechanical recycling of agricultural plastic waste, *Waste Manage*, 33 (2013) 1516-1530.
- [20] B.H. Hameed, R.R. Krishni, S.A. Sata, A novel agricultural waste adsorbent for the removal of cationic dye from aqueous solutions, *J Hazard Mater*, 162 (2009) 305-311.

- [21] M.C.S. Reddy, Removal of direct dye from aqueous solutions with an adsorbent made from tamarind fruit shell, an agricultural solid waste, *J Sci Ind Res India*, 65 (2006) 443-446.
- [22] V. Ponnusami, S. Vikram, S.N. Srivastava, Guava (*Psidium guaiava*) leaf powder: Novel adsorbent for removal of methylene blue from aqueous solutions, *J Hazard Mater*, 152 (2008) 276-286.
- [23] A. Tabak, M. Kaya, N. Yilmaz, K. Meral, Y. Onganer, B. Caglar, O. Sungur, Pyronin Y (basic xanthene dye)-bentonite composite: A spectroscopic study, *J Mol Struct*, 1059 (2014) 271-279.
- [24] K.S. Bharathi, S.T. Ramesh, Removal of dyes using agricultural waste as low-cost adsorbents: a review, *Applied Water Science*, 3 (2013) 773-790.
- [25] A. Tabak, N. Baltas, B. Afsin, M. Emirik, B. Caglar, E. Eren, Adsorption of Reactive Red 120 from aqueous solutions by cetylpyridinium-bentonite, *J Chem Technol Biot*, 85 (2010) 1199-1207.
- [26] M. Toprak, E. Halisdemir, Removal of Pyronin B from aqueous solutions using raw and modified vermiculite, *Res Chem Intermediat*, 41 (2015) 8289-8306.
- [27] M. Toprak, A. Salci, A.R. Demirkiran, Comparison of adsorption performances of vermiculite and clinoptilolite for the removal of pyronine Y dyestuff, *React Kinet Mech Cat*, 111 (2014) 791-804.
- [28] A. Tutus, Y. Kazaskeroglu, M. Cicekler, Evaluation of Tea Wastes in Usage Pulp and Paper Production, *Bioresources*, 10 (2015) 5407-5416.
- [29] T. Standard, T 211 om-07. Ash in wood, pulp, paper and paperboard: Combustion at 525° C, *Tappi Standard*, (2007).
- [30] L.J. Bellamy, Alcohols and Phenols, in: *The Infra-red Spectra of Complex Molecules*, Springer Netherlands, Dordrecht, 1975, pp. 107-128.
- [31] J.S. Lupoi, S. Singh, B.A. Simmons, R.J. Henry, Assessment of Lignocellulosic Biomass Using Analytical Spectroscopy: an Evolution to High-Throughput Techniques, *BioEnergy Research*, 7 (2014) 1-23.
- [32] S.D. Khattri, M.K. Singh, Removal of malachite green from dye wastewater using neem sawdust by adsorption, *Journal of Hazardous Materials*, 167 (2009) 1089-1094.
- [33] M. Zanoaga, F. Tanasa, Y. Mamunya, Compatibilized Green Composites Based on Wood Chips and Thermoplastic Polymer Waste Matrices, *Cell Chem Technol*, 50 (2016) 637-648.
- [34] A. Plis, M. Kotyczka-Morańska, M. Kopczyński, G. Łabojko, Furniture wood waste as a potential renewable energy source, *J Therm Anal Calorim*, 125 (2016) 1357-1371.
- [35] Y.Z. Fu, T. Viraraghavan, Removal of a dye from an aqueous solution by the fungus *Aspergillus niger*, *Water Qual Res J Can*, 35 (2000) 95-111.
- [36] C. Namasivayam, M.D. Kumar, K. Selvi, R.A. Begum, T. Vanathi, R.T. Yamuna, 'Waste' coir pith - a potential biomass for the treatment of dyeing wastewaters, *Biomass Bioenerg*, 21 (2001) 477-483.
- [37] S.D. Khattri, M.K. Singh, Colour removal from synthetic dye wastewater using a bioadsorbent, *Water Air Soil Poll*, 120 (2000) 283-294.
- [38] S. Lagergren, About the theory of so-called adsorption of solution substances, *KUNGLIGA SVENSKA VETENSKAPSAKADEMIENS*, 24 (1898) 1-39.
- [39] S. Lagergren, About the theory of so-called adsorption of solution substances, (1898).
- [40] S.Y. Lagergren, Zur Theorie der sogenannten Adsorption geloster Stoffe, 1898.
- [41] M.R. Rostami, M. Kaya, B. Gur, Y. Onganer, K. Meral, Photophysical and adsorption properties of pyronin B in natural bentonite clay dispersion, *Appl Surf Sci*, 359 (2015) 897-904.
- [42] F. Colak, N. Atar, A. Olgun, Biosorption of acidic dyes from aqueous solution by *Paenibacillus macerans*: Kinetic, thermodynamic and equilibrium studies, *Chem Eng J*, 150 (2009) 122-130.
- [43] N. Tazrouti, M. Amrani, Chromium (Vi) Adsorption onto Activated Kraft Lignin Produced from Alfa Grass (*Stipa Tenacissima*), *Bioresources*, 4 (2009) 740-755.
- [44] C.H. Weng, Y.C. Sharma, S.H. Chu, Adsorption of Cr(VI) from aqueous solutions by spent activated clay, *Journal of Hazardous Materials*, 155 (2008) 65-75.
- [45] G. Crini, P.M. Badot, Sorption Processes and Pollution: Conventional and Non-conventional Sorbents for Pollutant Removal from Wastewaters, *Presses universitaires de Franche-Comté*, 2010.
- [46] S.J. Gregg, K.S.W. Sing, Adsorption, surface area, and porosity, 2nd ed., Academic Press, London ; New York, 1982.

# Control Algorithms for Bosonic Quantum Batteries: Parallel versus Collective Charging

Sergey Borisenok<sup>1,2</sup>

---

## Abstract

Very recently the great progress has been achieved for a new type of quantum devices: quantum batteries (QBs) which are capable to be charged, to store the energy and finally to transfer it to consumption centers and other quantum devices. We develop here our theoretical feedback control algorithm for charging Bosonic quantum batteries with two different topologies of interaction between the charger and the battery set: parallel versus collective transfer of energy. The model of QB is composed by non-mutually interacting elements (quantum harmonic oscillators) in a Markovian bath. The charger of such a battery is implemented via the field which is pumping the energy into the batteries. We study the control approach in the form of Kolesnikov's target attractor to track (i.e. to drive dynamically) the charging power of the batteries. We discuss pros and cons of the control models for different charging schemes; demonstrate their efficiency, robustness and stability. The proposed algorithms can be applied to other physical types of quantum devices: Dicke QBs and spin QBs.

**Keywords:** feedback control, quantum battery, Markovian environment

---

## 1. INTRODUCTION

**Quantum Battery (QB)** represented by systems with distinct quantum states must be able to perform its three basic tasks [1]:

- It can be **charged**, i.e. it can be transferred from its lower energy state to more energetic states. The important fact is that charging / discharging processes are not necessarily unitary, and during this process QB may interact with its environment.
- It can efficiently **store** the transferred energy at the upper energy levels.
- It can **transfer** the storage energy to consumption centers.

The schematic diagram of an open Quantum Battery  $B$  interacting with the charger  $A$  is represented in Figure 1. Each of sub-systems,  $A$  and  $B$ , are coupled individually into an environment. In addition, one can apply an external control field to charger  $A$  [2].

There are different types of quantum batteries which could be realized in particular systems:

- **Dickey QB**, where one cavity mode acting as charger is coupled to  $N$  qubits, which play the role of the battery;
- **Spin QB** composed by  $N$  qubits, acting as charger, this charger is coupled to another set of  $N$  qubits, which play the role of the battery;
- Bosonic **harmonic oscillator QB**, where the sub-system  $B$  is composed by  $N$  non-mutually interacting elements.

---

<sup>1</sup>Department of Electrical and Electronics Engineering, Faculty of Engineering, Abdullah Gul University, 38080 Kocasinan / Kayseri, Turkey. [sergey.borisenok@agu.edu.tr](mailto:sergey.borisenok@agu.edu.tr)

<sup>2</sup>Feza Gursey Center for Physics and Mathematics, Bogazici University, 34684 Uskudar / Istanbul, Turkey. [borisenok@gmail.com](mailto:borisenok@gmail.com)

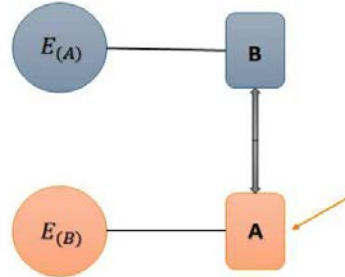


Figure 13. Diagram of an open Quantum Battery B interacting with the charger A, following [2].

Here we discuss the last type of QB: the Bosonic quantum battery with two alternative charging schemes [3], see Figure 2.

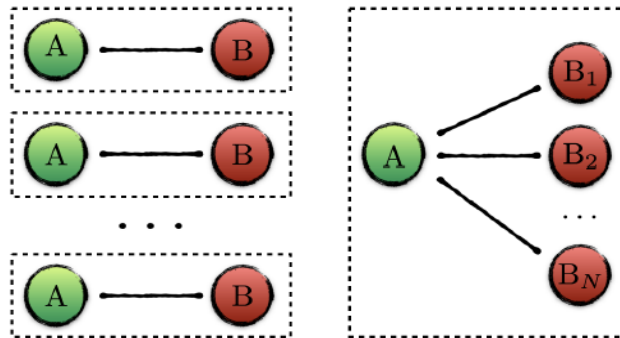


Figure 2. Two basic schemes of the parallel (left) versus collective (right) QB charging, based on [3].

Our theoretical feedback control algorithm is applied for charging Bosonic quantum batteries with two different topologies of interaction between the charger and the battery set: parallel versus collective transfer of energy. We use Kolesnikov's target attractor algorithm to track (i.e. to drive dynamically) the charging power of the batteries.

## 2. MATHEMATICAL MODEL FOR BOSONIC QUANTUM BATTERY

The model of QB is composed by non-mutually interacting elements (quantum harmonic oscillators) in a Markovian bath. The charger for such a battery is implemented via the field which controls pumping the energy into the batteries.

### ○ *Ergotropy and charging power*

The energy storage of QB depends on the time-independent reference Hamiltonian  $H$  with the finite Hilbert space of the battery system. The useful energy exacted from QB in the state  $\rho$  and its energetically lowest accessible state  $\sigma_\rho$  is defined via its *ergotropy* [4]:

$$W = \text{Tr}(\rho H) - \text{Tr}(\sigma_\rho H). \quad (1)$$

The time derivative of (1) is called the *charging power* of the battery:

$$p = \frac{dW}{dt}. \quad (2)$$



We will use our control algorithm to drive the parameter (2) dynamically, i.e. we will discuss the tracking of charging power  $p$  as a given target function.

○ **Bosonic harmonic oscillator quantum battery**

The system includes the sub-system  $A$  (charger) and the sub-system  $B$  (battery) with the corresponding Hamiltonians  $H_A$  and  $H_B$  and the Hamiltonian  $H_1$  for the coupling between  $A$  and  $B$  [1]:

$$H(t) = H_A + H_B + u(t)H_1, \quad (3)$$

where

$$\begin{aligned} H_A &= \omega_0 a^\dagger a; \\ H_B &= \omega_0 \sum_k b_k^\dagger b_k; \\ H_1 &= g \sum_k (a b_k^\dagger + a^\dagger b_k), \end{aligned} \quad (4)$$

with the corresponding creation-annihilation operators; and  $u(t)$  is a time-dependent external control parameter. The bosonic harmonic oscillator QB is composed by  $N$  non-mutually interacting elements marked with the index  $k$ .

Let's consider a single-qubit based bosonic QB in the form of quantum oscillator with the density operator  $\rho$  in a Markovian bath. Such a system is described with the Lindblad-type operator equation [5]:

$$\frac{d\rho}{dt} = -i[H_0 + u(t)\hat{Q}, \rho] + \hat{L}[\rho], \quad (5)$$

with the terms based on the creation-annihilation operators:

$$H_0 = \left(\omega_0 + \frac{1}{2}\right) b^\dagger b; \quad \hat{Q} = \frac{b^\dagger + b}{\sqrt{2\omega_0}}; \quad \hat{P} = i\sqrt{\frac{\omega_0}{2}}(b^\dagger - b). \quad (6)$$

The Lindblad operator in (5) has a form:

$$\hat{L}[\rho] = \gamma \cdot (n(t) + 1) (2b\rho b^\dagger - \rho b^\dagger b - b^\dagger b\rho) + \gamma \cdot n(t) (2b^\dagger \rho b - b b^\dagger \rho - \rho b b^\dagger). \quad (7)$$

The positive parameter  $\gamma$  plays here a role of coupling constant between the qubit and the environment. The external fields  $u(t)$  and  $n(t)$  are our control parameters.

○ **Reduced system of differential equations**

The quantum model (5)-(7) can be re-written in the form of the dynamical system with real ordinary differential equations[6]:

$$\begin{aligned} \frac{dE}{dt} &= 2\gamma \cdot (\omega_0 n(t) - E) - u(t)P; \\ \frac{dQ}{dt} &= P - \gamma \cdot Q; \\ \frac{dP}{dt} &= -\omega_0^2 Q - \gamma \cdot P - u(t), \end{aligned} \quad (8)$$

expressed via the 'quasi-classical' variables:

$$E(t) = \text{Tr}(H_0 \rho); \quad Q(t) = \text{Tr}(\hat{Q} \rho); \quad P(t) = \text{Tr}(\hat{P} \rho). \quad (9)$$

The ergotropy (1) of the system (8) is defined as:

$$W(t) = E(t) - E_0, \quad (10)$$

where  $E_0$  stands for the lowest accessible passive battery state.

### 3. CONTROL OVER THE CHARGING POWER

To perform control over the charging power we use here Kolesnikov's Target Attractor (TA) feedback approach based on the creation in the driven dynamical system a target attractor locking the trajectories in its neighborhood [7].

#### ○ *Kolesnikov's target attractor feedback*

For the purpose of tracking the charging power (2) we define the goal function:

$$G(t) = p(t) - p_*(t), \quad (11)$$

with the arbitrary differentiable target function  $p_*(t)$ . To form the Kolesnikov's attractor, we demand the exponentially fast convergence towards the tracking goal:

$$\frac{dG(t)}{dt} = -\frac{1}{T_1}G(t), \quad (12)$$

with a positive time constant  $T_1$ . Particularly, for the model (8), we define the TA control equations as the following set:

$$\begin{aligned} \frac{dE}{dt} &= -\frac{1}{T_1}(E - E_0); \\ \frac{dP}{dt} &= -\frac{1}{T_2}(P - P_*). \end{aligned} \quad (13)$$

Here  $T_2$  is also a positive constant. The system (13) has the solutions:

$$\begin{aligned} E(t) &= [E(0) - E_0] \cdot e^{-t/T_1} + E_0; \\ P(t) &= P(0) \cdot e^{-t/T_2} + P_* \cdot (1 - e^{-t/T_2}). \end{aligned} \quad (14)$$

The substitution of (14) into the system (8) restores the form of both control fields for a single battery element:

$$\begin{aligned} \frac{dn(t)}{dt} &= \frac{p(t)}{\omega_0} + \frac{1}{2\gamma\omega_0} \left[ P \frac{du(t)}{dt} + u(t) \frac{dP}{dt} + \frac{dp_*(t)}{dt} - \frac{1}{T_1}(p(t) - p_*(t)) \right]; \\ u(t) &= \frac{P - P_*}{T_2} - \gamma \cdot P - \omega_0^2 Q. \end{aligned} \quad (14)$$

By Eqs (14) we can study the achievability of the control goal.

#### ○ *Achievability of the control goal as $t \gg T_1, T_2$ : parallel vs collective charging*

Let's check the achievability of the control goal at the limit:  $t \gg T_1, T_2$ .

For the *parallel scheme* (see Fig.2, left) we can define different target  $P_*$  for each  $k$ -th battery element:

$$P_{*,k} = -\frac{\omega_0^2}{\gamma} Q_k(0). \quad (15)$$

In this case we can re-write the control fields (14) as:

$$\begin{aligned} u_k(t) &= \omega_0^2 Q_k(0) \cdot \left( 1 - \frac{\omega_0^2}{\gamma} \right) \cdot (1 - e^{-\gamma t}); \\ n_k(t) &= \int_0^t \left\{ \frac{p_*(\tau)}{\omega_0} + \frac{1}{2\gamma\omega_0^2} \cdot \frac{dp_*(\tau)}{d\tau} - \frac{\omega_0^2}{2\gamma} \left( 1 + \frac{\omega_0^2}{\gamma^2} \right) Q_k^2(0) e^{-\gamma\tau} \right\} d\tau. \end{aligned} \quad (16)$$

For the *collective scheme* (see Fig.2, right) the charger  $A$  must drive each battery for the same target state:  $P_k \rightarrow P_*$ ,  $\forall k$ . By that the dynamical parameter  $Q_k$  can be evaluated as:

$$Q_k \cong \frac{P_*}{\gamma} + \left[ Q_k(0) - \frac{P_*}{\gamma} \right] \cdot e^{-\gamma t} . \quad (17)$$

By (8) that implies for the control field  $u_k$ :

$$u_k \cong -\frac{\omega_0^2 + \gamma^2}{\gamma} P_* - \omega_0^2 \left[ Q_k(0) - \frac{P_*}{\gamma} \right] \cdot e^{-\gamma t} . \quad (18)$$

In the case if we demand for the target  $P_*$ :

$$P_* = 0 , \quad (19)$$

and the pair of control fields (14) becomes:

$$\begin{aligned} u_k &\cong -\omega_0^2 Q_k(0) \cdot e^{-\gamma t} ; \\ n_k(t) &= \int_0^t \left[ \frac{p(\tau)}{\omega_0} + \frac{1}{2\gamma\omega_0} \frac{dp_*(\tau)}{d\tau} \right] d\tau . \end{aligned} \quad (20)$$

Now we can compare the shapes of the control fields (14) for the parallel and collective approaches. For the parallel case (16) the control fields  $u_k$  are closed to 0 for each  $k$ -th battery:  $u_k \cong 0$ , while the control fields  $n_k$  are more complex for the practical computations. For the collective case of charging (20) the fields  $u_k$  tend to 0 asymptotically:  $u_k \cong -\omega_0^2 Q_k(0) \cdot e^{-\gamma t}$ , while  $n_k$  are more simple for the numerical computations.

## 4. CONCLUSIONS

The algorithm of the control over the charging power proposed here has the following basic characteristics. This algorithm is *universal* and does not depend on the initial conditions of the dynamical variables. It is *robust* and stable under the perturbation of the initial conditions and a relatively small external noise.

The proposed algorithm *can be extended for different physical realizations of quantum batteries*: Dicke QB, spin QB; and for all working stages of the QB (charging, long time storage and the energy transfer to a consumption center or engine) and it can be easily extended for a multi-qubit model. From the point of practical computation of the coherent and non-coherent fields  $u$  and  $n$  the control algorithm for Bosonic quantum batteries demonstrates different features for two alternative schemes of charging:

- For the *parallel scheme* of charging the control signal  $u$  (interaction between the battery and the charger) tends to 0 as the time is increasing. From another hand the control signal  $n$  (interaction with the Markovian environment) is more complex for computation.
- For the *collective scheme* of charging the control signal  $u$  (interaction between the battery and the charger) tends exponentially to 0 as the time is increasing. In the same time the control signal  $n$  (interaction with the Markovian environment) becomes simpler for the numerical computation.

## REFERENCES

- [1]. D. Ferraro, M. Campisi, G. M. Andolina, V. Pellegrini, M. Polini, "High-power collective charging of a solid-state quantum battery", *Phys. Rev. Lett.*, vol. 120(11), p. 117702, 2018.
- [2]. F. H. Kamin, F. T. Tabesh, S. Salimi, F. Kheirandish, A. C. Santos, "Non-Markovian effects on charging and self-discharging processes of quantum batteries", *N. J. Phys.*, vol. 22, p. 083007, 2020.
- [3]. G. M. Andolina, M. Keck, A. Mari, V. Giovannetti, M. Polini, "Quantum versus classical many-body batteries", *Phys. Rev. B*, vol. 99, p. 205437, 2019.
- [4]. G. Francica, J. Goold, F. Plastina, M. Paternostro, "Daemonic ergotropy: enhanced work extraction from quantum correlations", *npj Quantum Inf.*, vol. 3, p. 12, 2017.
- A. Pechen, "Engineering arbitrary pure and mixed quantum states", *Phys. Rev. A*, vol. 84, p. 042106, 2011.
- [5]. S. Borisenok, "Ergotropy of quantum battery controlled via target attractor feedback", *IOSR Journal of Applied Physics*, vol. 12(3), pp.43-47, 2020.
- A. Kolesnikov, *Synergetic control methods of complex systems*, Moscow: URSS Publ., 2012.

# Non-classical Algorithm to Control Epileptiform Regime in the Small Population of Hodgkin-Huxley Neurons

Sergey Borisenok<sup>1,2</sup>

---

## Abstract

*The model for controlling epilepsy discussed here is based on the seizures suppression experimental methods via the electrical stimulation of brain. It has a potential of “fine tuning” according to the epileptic pathology specifics of patients. We consider here a simplified case of an artificial neural network (ANN) with the Hodgkin-Huxley elements providing the necessary variety of dynamical regimes: individual neuron spikes and bursts which could cause the hyper-synchronized behavior of epileptiform type in the whole network. We perform a fine control of the ANN dynamics with control elements which play two roles: they detect the coming seizure and send a feedback signal to other neurons to suppress the epileptiform dynamics. To increase the quality and efficiency of the control we study non-classical (based on the quantum paradigm) algorithm. Recently we demonstrated the ability of a pair of Hodgkin-Huxley neurons to emulate some quantum classification and searching algorithms in a relatively profitable way. Here we develop our approach to detect and suppress epileptiform dynamics in the small ANN. We study the efficiency and robustness of our proposed algorithm and discuss its pros and cons to compare with our recent classical algorithm-based model of the epileptiform suppression.*

**Keywords:** feedback control, Hodgkin-Huxley neuron, epileptiform dynamics

---

## 1. INTRODUCTION

Epilepsy is a neurological disorder characterized by recurrent seizures. According to some estimations the disease affects approximately 1-2% of the world's population. In approximately 40% of epilepsy patients medicament treatment does not suppress seizures. This kind of epilepsy rapidly worsens, and this is a surgical indication. Surgery in this case includes epileptogenic zone destruction [1]. However, this method is applicable not for all patients, and also in approximately 30% of cases does not give satisfactory result. This fact makes a challenge for the fundamental study of the epileptic dynamics and stimulates scientific interest towards the alternative methods for suppressing human brain epileptic activity.

One of such seizures suppression methods is the electrical stimulation of brain [2]. It has a potential of “fine tuning” according to the epileptic pathology specifics of patients. However, for so important subject presently there are no good theories and models, which could provide a strong theoretical basis for the development of experimental methods of epileptology.

The model for controlling epilepsy discussed here is based on the seizures suppression experimental methods via the electrical stimulation of brain. It has a potential of “fine tuning” according to the epileptic pathology specifics of patients. We consider here a simplified case of an artificial neural network (ANN) with the Hodgkin-Huxley elements providing the necessary variety of dynamical regimes: individual neuron spikes and bursts which could cause the hyper-synchronized behavior of epileptiform type in the whole network. We perform a fine control of the ANN dynamics with a pair of elements which play two roles: they detect the coming seizure and send a feedback signal to other neurons to suppress the epileptiform dynamics. To increase

---

<sup>1</sup>Department of Electrical and Electronics Engineering, Faculty of Engineering, Abdullah Gul University, 38080 Kocasinan / Kayseri, Turkey. [sergey.borisenok@agu.edu.tr](mailto:sergey.borisenok@agu.edu.tr)

<sup>2</sup>Feza Gursey Center for Physics and Mathematics, Bogazici University, 34684 Uskudar / Istanbul, Turkey. [borisenok@gmail.com](mailto:borisenok@gmail.com)

the quality and efficiency of the control we study non-classical (based on the quantum paradigm) algorithm. Recently we demonstrated the ability of a single Hodgkin-Huxley neuron to emulate some quantum classification and searching algorithms in a relatively profitable way. Here we develop our approach to detect and suppress epileptiform dynamics in the small ANN. The feedback loop to other neurons could be based on optimal / suboptimal gradient approaches or on an artificial attractor forming in the dynamical system. We study the efficiency and robustness of our proposed algorithm and discuss its pros and cons to compare with our recent classical algorithm-based model of the epileptiform suppression.

## 2. THE DEUTSCH –JOSZA QUANTUM ALGORITHM

To give an example of a quantum algorithm, let's choose the simple searching problem. Suppose that we get a function  $f$  mapping  $\{0,1\}^n$  into  $\{0,1\}$ . The constrain on the function gives us only two options:

1. The function  $f$  is a *constant*:  $f(x) = 0$  for all  $x$  from  $\{0,1\}^n$  or  $f(x) = 1$  for all  $x$  from  $\{0,1\}^n$ ;
2. The function  $f$  is *balanced*: the number of outputs '0' for the mapping is equal to the number of outputs '1'.

We must check if the given function  $f$  is a constant. To do it for the classical approach we need  $2^{n-1} - 1$  evaluations. Quantum algorithms, from another hand, can perform it much faster.

The basic solution to this searching problem has been proposed by Deutsch in 1985 and generalized in 1992 in the form of the Deutsch – Jozsa algorithm for an arbitrary positive integer  $n$  [3]. The circuit for the Deutsch – Jozsa algorithm is given in Fig.1. It contains three single-qubit Hadamard gates, one two-qubit gate for the function  $f$  and one measurement operation. The symbol  $\oplus$  stands here for the addition mod 2.

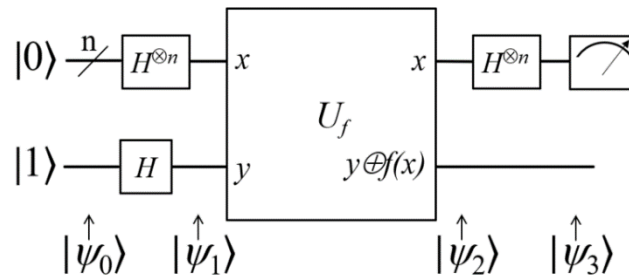


Figure 1. The quantum circuit for the Deutsch – Jozsa algorithm; based on [4].

For simplicity we will focus here on the case  $n = 1$ . Then the result of the measurement is equal to:

$$|\text{output}\rangle = \frac{1}{2} \left[ (1 + (-1)^{f(0) \oplus f(1)}) |0\rangle + (1 - (-1)^{f(0) \oplus f(1)}) |1\rangle \right]. \quad (1)$$

Eq.(1) solves the problem of searching. Indeed, if  $f(0) \oplus f(1) = 0$ , then the output is  $|0\rangle$ , and the function  $f$  is constant. If  $f(0) \oplus f(1) = 1$ , then the output is  $|1\rangle$ , and the function  $f$  is balanced. Due to the so-called quantum phasekick-backeffect in the algorithm we need only a single measurement to distinguish between those two cases.

The same is valid for the case of  $n$  bits. If all  $n$  measurement results are  $|0\rangle$ , we conclude that the function was constant. Otherwise, if at least one of the measurement outcomes is  $|1\rangle$ , we conclude that the function was balanced.

### 3. QUASI-QUANTUM ALGORITHM WITH THE HODGKIN – HUXLEY NEURONS

The quasi-quantum algorithm of the Deutsch type has been developed with the classical ANN realizations for the Hodgkin–Huxley [5] and FitzHugh – Nagumo [6] mathematical neurons. Here we reproduce briefly the scheme presented in [5].

#### ○ *Differential system for Hodgkin – Huxley Neuron*

The mathematical description of Hodgkin-Huxley (HH) neuron has been proposed by Alan Lloyd Hodgkin and Andrew Huxley in 1952 as a phenomenological model based on the experiments when the giant axon of the squid has been stimulated by the electrical current [7]. The HH differential model has the set of four dynamical variables: the output membrane action potential  $v(t)$  and three ion channels variables  $m(t)$ ,  $n(t)$ ,  $h(t)$  related to the probabilities for the membrane gates to be open or closed:

$$\begin{aligned} C_M \cdot \frac{dv}{dt} &= -g_{Na} m^3 h \cdot (v - E_{Na}) - g_K n^4 \cdot (v - E_K) - g_{Cl} \cdot (v - E_{Cl}) + I(t); \\ \frac{dm}{dt} &= \alpha_m(v) \cdot (1 - m) - \beta_m(v) \cdot m; \\ \frac{dn}{dt} &= \alpha_n(v) \cdot (1 - n) - \beta_n(v) \cdot n; \\ \frac{dh}{dt} &= \alpha_h(v) \cdot (1 - h) - \beta_h(v) \cdot h. \end{aligned} \quad (2)$$

The membrane variables  $m$ ,  $n$ ,  $h$  depend on the action potential  $v$  via the non-linear functions:

$$\begin{aligned} \alpha_m(v) &= \frac{0.1 \cdot (25 - v)}{\exp\left\{\frac{25 - v}{10}\right\} - 1}; \quad \beta_m(v) = 4 \cdot \exp\left\{-\frac{v}{18}\right\}; \\ \alpha_n(v) &= \frac{0.01 \cdot (10 - v)}{\exp\left\{\frac{10 - v}{10}\right\} - 1}; \quad \beta_n(v) = 0.125 \cdot \exp\left\{-\frac{v}{80}\right\}; \\ \alpha_h(v) &= 0.07 \cdot \exp\left\{-\frac{v}{20}\right\}; \quad \beta_h(v) = \frac{1}{\exp\left\{\frac{30 - v}{10}\right\} + 1}. \end{aligned} \quad (3)$$

The net external current  $I(t)$  stimulating the axon is a control parameter in the HH model (2). The set of constants includes the potentials  $E_{Na}$  (equilibrium potential at which the net flow of  $Na$  ions is zero),  $E_K$  (equilibrium potential at which the net flow of  $K$  ions is zero),  $E_{Cl}$  (equilibrium potential at which leakage is zero) in mV, the membrane capacitance  $C_M$  and the conductivities  $g_{Na}$  (sodium channel conductivity),  $g_K$  (potassium channel conductivity),  $g_{Cl}$  (leakage channel conductivity) in mS/cm<sup>2</sup>:

$$\begin{aligned} g_{Na} &= 120; \quad E_{Na} = 115; \\ g_K &= 36; \quad E_K = -12; \\ g_{Cl} &= 0.3; \quad E_{Cl} = 10.36. \end{aligned} \quad (4)$$

The important property of the dynamical system (2) is the variety of regimes: it can demonstrate resting (the neuron does not show a sufficient activity), spiking (the neuron produces a single spike), bursting (the neuron generates series of spikes).

A particular dynamical regime depends on the input current  $I$ . For instance, if the current is below a threshold level, the HH neuron stays in resting; if we overcome the threshold level, it generates a spike.

#### ○ *Chain model for the Hodgkin – Huxley Neurons*

If we combine few HH neurons in a linear chain, the output action potential of the previous cell defines the input of the following one. We use here our gain model for the transfer of the output signal from  $k$ -th neuron via its synapse toward the dendrite/soma input of the  $l$ -th neuron [8]:

$$I_l(t) = \alpha \cdot [v_k(t) - v_{\text{rest}}] ; \alpha = \text{const} > 0, \quad (5)$$

with the phenomenological gain constant  $\alpha$ . Here  $v_{\text{rest}}$  is the reference rest potential in the HH neuron. We use a simple linear chain of two HH neurons. The first cell plays a role of the computational element, while the second one works as a measuring element. For that we define the threshold (tr) level:

$$I_{\text{tr}} = \alpha \cdot (v_{\text{tr}} - v_{\text{rest}}) . \quad (6)$$

Now the output of the first neuron stimulates the particular regime of the second measuring element. If the first HH neuron produces the acting potential below the threshold level  $v_{\text{tr}}$ , the second neuron does not spike. If the output action potential of the first neuron  $v$  achieves the threshold level, the second one produces a single spike.

○ **Deutsch – Jozsa algorithm emulated by Hodgkin – Huxley Neurons**

To emulate the Deutsch algorithm, let's define the 'pure quantum states' for the HH neuron: the resting  $|0\rangle$  and the single spiking  $|1\rangle$ :

$$\begin{aligned} |0\rangle &= 0 \cdot I_{\text{tr}} ; \\ |1\rangle &= 1 \cdot I_{\text{tr}} , \end{aligned} \quad (7)$$

which correspond to the action potentials:

$$\begin{aligned} v_{|0\rangle} &= v_{\text{rest}} + \frac{0 \cdot I_{\text{tr}}}{\alpha} = v_{\text{rest}} ; \\ v_{|1\rangle} &= v_{\text{rest}} + \frac{1 \cdot I_{\text{tr}}}{\alpha} = v_{\text{rest}} + \frac{I_{\text{tr}}}{\alpha} . \end{aligned} \quad (8)$$

To unify both cases, let's define the goal potential via the CNOT logical operator over the function  $f$ :

$$v_* = v_{\text{rest}} + \text{CNOT}\{f(0), f(1)\} \cdot \frac{I_{\text{tr}}}{\alpha} . \quad (9)$$

The symbol \* stands here for the potential  $v$  (the out put of the first neuron) which should be the goal of our control signal  $I$  in (2).

Our network emulating the quantum algorithms consists of two sequent HH neurons (see Fig.2). The first neuron contains the information about the function  $f$ ; and it is driven by a control algorithm (5) towards the goal action potential (9). The resulting potential of the first neuron with the dendrite / soma model enters the second cell, which plays a role of the measuring element.

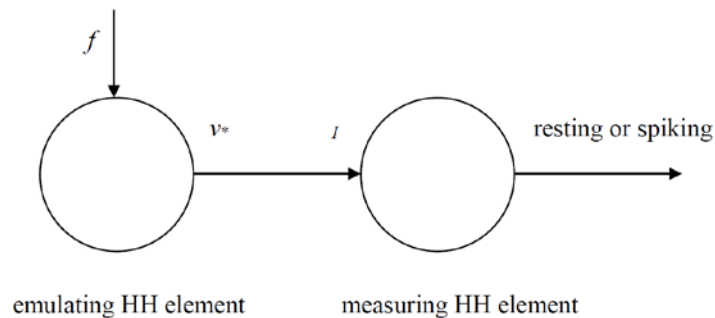


Figure 2. The pair of Hodgkin–Huxley neurons emulating the Deutsch – Jozsa algorithm.

Now suppose that we are able to drive the first neuron towards the goal potential (9). Then it will stimulate the second measuring element with two different options: the second neuron will stay in rest or will generate a single spike. Based on that we can conclude if the function  $f$  is constant or not:

If  $f(0) = f(1)$ , then  $v_* = v_{\text{rest}} = v_{|0}$ , and  $f$  is constant. (10)

If  $f(0) \neq f(1)$ , then  $v_* = v_{\text{rest}} + \frac{I_{\text{tr}}}{\alpha} = v_{|1}$ , and  $f$  is balanced.

By (10) we reproduce the complete HH analog of the Deutsch algorithm.

Finally we need to provide the necessary output (9) of the first neuron. To do it we follow Kolesnikov's approach [9]. We define the target function:

$$\psi(t) = v(t) - v_*(t). \quad (11)$$

Minimizing the magnitude of (11) we drive our system towards the target potential (9) with the control equation:

$$T \frac{d\psi(t)}{dt} = -\psi(t). \quad (12)$$

The positive constant  $T$  stands for the typical time scale of the target attractor achievement.

Eq.(12) provides the exponentially convergent dynamics of the trajectories to the neighborhood of the target attractor (11) in the phase space.

The control signal  $I$  entering the first HH neuron is restored from the substitution of (11)-(12) into the first equation of the system (2). It becomes:

$$I_{\text{TA}} = C_M \cdot \left[ \frac{dv_*}{dt} - \frac{1}{T}(v - v_*) \right] + g_{Na} m^3 h \cdot (v - E_{Na}) + g_K n^4 \cdot (v - E_K) + g_{Cl} \cdot (v - E_{Cl}). \quad (13)$$

The achievability of the goal for an arbitrary stabilization / tracking via target attractor feedback has been discussed in [10].

#### 4. QUASI-QUANTUM ALGORITHM FOR DETECTING EPILEPTIFORM DYNAMICS

The classical paradigm-based computation algorithm for the detection and suppression of the epileptiform dynamics in the small Hodgkin-Huxley ANN has been proposed in [8]. Its principle scheme is plotted on Figure 3.

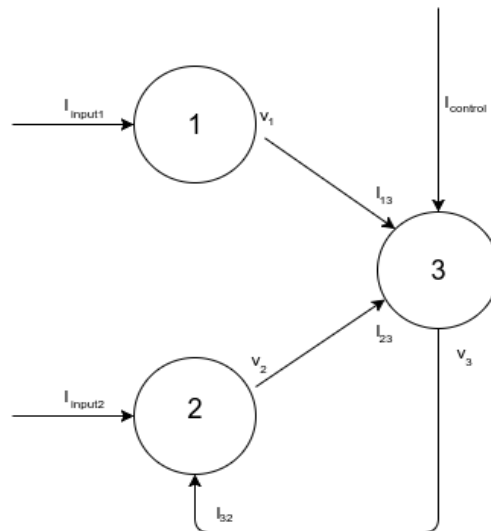


Figure 3. The classical computation algorithm scheme for the detection and suppression of the epileptiform dynamics [8].



We present on Fig.3 the simplified case of two HH neurons 1 and 2 which could form an epileptiform regime. Their action potentials  $v_1$  and  $v_2$  generate the currents  $I_{13}$  and  $I_{23}$  entering the control element 3. The element 3 with its inner control algorithm shown as  $I_{\text{control}}$  detects if there is a hyper-synchronization of the neurons 1 and 2 (for the detail of detecting see [8]), and in the case of the observation of a seize-type behavior it uses the negative feedback loop with the current  $I_{32}$  driving the neuron 2 out of the hyper-synchronization with the element 1. Out of the ictal phase the negative feedback loop is not active.

The classical computation algorithm proposed in [8] works well for the negative feedback suppression, but its detection phase is more sophisticated numerically. For that reason we propose here the faster way of the epileptiform dynamics detection based on the quantum algorithm of the Deutch type.

We need a rapid evaluation of the function  $f$  based on the inputs entering the control elements from some other neurons of the ANN. For the emulation of quantum computational process we use a pair of HH neurons in the place of the single element 3 in Fig. 3. The negative feedback loop will work in the same manner as in [8], originated in the second neuron of the control pair.

### ○ *Spiking function and the definition of the function $f$*

Let's define the spiking function for the  $n$ -th neuron in based on its action potential  $v_n$  as:

$$S_n = \begin{cases} 0, & \text{if } v_n = v_{\text{rest}} ; \\ 1, & \text{if } v_n > v_{\text{rest}} . \end{cases} \quad (14)$$

By (14) we define the function  $f$  in the form:

$$f = \frac{1}{2} \left[ 1 + (-1)^{\prod_n S_n} \right] \cdot \text{RND}\{0,1\} , \quad (15)$$

where  $\text{RND}\{0,1\}$  stands for the '0' or '1' binary random number generator.

Now let's chose the action potentials of some  $n$  neurons to form the function  $f$ . In (15) the product of spiking functions  $\prod_n S_n = 1$  only if there is an epileptiform hyper-synchronization. Indeed, for the epileptiform regime  $f = 0$  always; i.e. the function is constant. For the normal regime  $f = \text{RND}\{0,1\}$ , and we get the outputs  $f = 0$  and  $f = 1$  in the equal number of cases, i.e. the function is balanced.

Correspondingly, the inhibitor control pair of HH neurons performs the Deutch – Josza algorithm for the function  $f$  and uses the negative feedback loop to suppress the epileptiform behavior if and only if the quasi-quantum algorithm classifies the function as a constant one.

### ○ *Finalization of the algorithm*

Now we are ready to formulate the final form of our novel algorithm for the detection and suppression of the epileptiform behavior in the small population of HH neurons. Its basic phases are:

1. Forming the function  $f$  over the action potentials for an arbitrary numbers of  $n$  neurons in the population by (15).
2. Making the Deutch-type measurement of the function  $f$  with the pair of control neurons.
3. If the function  $f$  is balanced, there is a normal regime in the population dynamics. If the function  $f$  is constant, there is a epileptiform regime in the small ANN.
4. If the epileptiform regime is detected, triggering the feedback suppressing control signal from the inhibitor control HH pair to the neurons of the population.

We also should emphasize that the proposed algorithm does not demand complex numerical computations.

## 5. CONCLUSIONS

The pair of Hodgkin – Huxley neurons represented as two coupled 4d dynamical systems is capable to imitate the effects similar to the Deutsch – Jozsa quantum algorithm. Such a pair of HH elements can be used to detect the ictal phase of the epileptiform regime in the small population of other HH neurons.

The quantum paradigm-based algorithm of the detection works more efficient to compare with the classical detection algorithm proposed in [8]. In the same time it possesses all basic positive features of the classical approach: its robustness and the flexibility for the adaptation to different types of mathematical neurons (the FitzHugh – Nagumo elements and others) and for the variable topology of ANNs.

The emulation of quantum paradigm-based algorithms in the ANNs modeling the epileptiform behavior discover new opportunities for the developing *in-silico* mathematical modeling of the biological processes, and creation of a principle new type of intelligent expert systems.

## REFERENCES

- [1]. W. O. Tatum, P. W. Kaplan, P. Jallon, *Epilepsy A to Z: A Concise Encyclopedia*, Springer, 2009.
- [2]. G. K. Bergey, “Neurostimulation in the treatment of epilepsy”, *Experimental Neurology*, vol. 244, pp. 87-95, 2013.
- [3]. D. Deutsch, R. Jozsa, “Rapid solutions of problems by quantum computation”, *Proceedings of the Royal Society of London A*, vol. 439, pp. 553-558, 1992.
- [4]. P. Aradyamath, N. M. Naghabhushana, R. Ujjimatad, “Quantum computing concepts with Deutsch Jozsa algorithm”, *International Journal of Informatics Visualization*, vol. 3, pp. 59-68, 2019.
- [5]. S. Borisenok, “Can controlled Hodgkin-Huxley neuron model quantum computations?”, in *Proc. 6th International Conference on Engineering and Natural Sciences (ICENS 2020)*, 2020, pp. 9-14.
- [6]. S. Borisenok, “Deutsch – Jozsa algorithm with feedback controlled FitzHugh – Nagumo neurons”, in *Proc. II. International Conference on Innovative Engineering Applications (CIEA’2021)*, 2021, pp. 193-197.
- A. L. Hodgkin, A. F. Huxley, “Currents carried by sodium and potassium ions through the membrane of the giant axon of Loligo”, *The Journal of Physiology*, vol. 116(4), pp. 449-72, 1952.
- B.S. Borisenok, O.Catmabacak, Z. Unal, “Control of collective bursting in small Hodgkin-Huxley neuron clusters”, *Communications Faculty of Sciences University of Ankara Series A2-A3*, vol. 60, pp. 21-30, 2018. Kolesnikov, *Synergetic control methods of complex systems*, Moscow: URSS Publ., 2012.
- [7]. S. Borisenok, Z. Unal, “Tracking of arbitrary regimes for spiking and bursting in the Hodgkin-Huxley neuron”, *MATTER: International Journal of Science and Technology*, vol. 3, pp. 560-576, 2017.

# Simulation of Streamflow Using SWAT Model

Erkan Karakoyun<sup>1</sup>, Nihat Kaya<sup>2</sup>

---

## Abstract

*In parallel with the development of computer technology and developments in geographical information systems, watershed modeling studies are also developing day by day. These models are used effectively in many studies such as water quality studies, sediment, flow estimation, the effects of climate and land-use changes. The main objective of this study is to determine the hydrological properties of the Murat-1 and Murat-2 watershed which is the subbasin of the Euphrates-Tigris watershed in Turkey and predicted the streamflow of those. The Soil and Water Assessment Tool (SWAT, version 2012) integrated with ArcGIS, version 10.7 were used for this purpose. The model was calibrated and validated using the data obtained from the monitoring station between the years 2005 to 2013 by using SWAT-CUP (version 2009) software program. The calibration and validation procedures were analyzed for the monthly periods using Sequential Uncertainty Fitting 2 (SUFI-2). Results show that the model has successfully simulated and predicted the streamflow over the watershed. Performance evaluation criteria such as Nash-Sutcliffe Efficiency (NSE) and coefficient of determination (R<sup>2</sup>) were 0.73 for both during the calibration period (2006-2010) and 0.59, 0.63 respectively for the validation period (2011-2013). From these results, it is seen that simulated values are at quite acceptable ranges and the SWAT model is a suitable tool for the studied watershed. It can be also useful for the non-monitoring region by simulating the flow.*

**Keywords:** SWAT, Streamflow, ArcGIS

---

## 1. INTRODUCTION

Water has always been of great importance throughout civilizations. Reasons such as the increasing world population, global warming and climate changes threaten the future of water. For this reason, every study on water resources is meaningful. Watershed management, water quality studies, sediment and flow estimation, effects of climate and soil use changes are among these studies. These models should be calibrated with measurements taken from the field in order to be able to simulate flow, sediment and water quality accurately and reliably [1].

Flow estimation is one of the most important factors in watershed modeling studies. With an accurate flow estimation, many factors such as the flood protection plans, the assessment of environmental impacts, and the determination of agricultural policies in the basin are evaluated. In our country, the State Hydraulic Works (DSI) carries out the flow measurement with the flow observation stations it has built on the rivers. However, it is difficult to take accurate measurements due to the climatic conditions of the region, technician error or station failure. For these reasons, it may be necessary to develop a model for the basin.

---

<sup>1</sup>Corresponding author: Mus Alparslan University, Faculty of Engineering and Architecture, 49250, Mus, Turkey. [e.karakoyun@alparslan.edu.tr](mailto:e.karakoyun@alparslan.edu.tr)

<sup>2</sup>Firat University, Faculty of Engineering, Department of Civil Engineering, 23119, Elazig, Turkey. [n.kaya@firat.edu.tr](mailto:n.kaya@firat.edu.tr)

With the help of developing computer technology and GIS, basin modeling studies have been more popular. There are many programs used within the scope of these studies such as Soil and Water Assessment Tool which is physically based program. The SWAT (Soil and Water Assessment Tool) model is a widely used physical model developed by USDA-ARS (Agricultural Research Services of United States Department of Agriculture) [2]. The SWAT program is a hydrology and water quality model that efficiently reveals the effects of water, sediment and pollutant sources in watershed management. SWAT is a physically based model and it is a very comprehensive model because it requires a lot of input parameters to run the model. Since so many and different parameters to be entered into the model are obtained, it allows a preliminary interpretation of the basin properties even without simulation. The SWAT program also requires specific information such as climate data, soil types and land use. In this way, it allows modeling in places where there is no observation [3].

In this study, Murat-1 and Murat-2 basins, which are sub-basins of the Fırat-Dicle basin, were modeled using the SWAT model and flow estimation was made. Calibration and validation process was carried out with the help of the SWAT-CUP program with the flow data obtained from a flow monitoring station located on the basin. The results obtained were evaluated with the help of performance evaluation criteria and the effectiveness of the model on the basin was determined.

The SWAT program needs a GIS-based program to be able to perform the analysis. In this study, ArcGIS 10.7 program and ArcSWAT program integrated into this software were used.

## 2. MATERIALS and METHODS

### 2.1. Study Area

Murat-1 and Murat-2 basins are located in the north of the Euphrates-Tigris basin. The Murat river, which feeds the Euphrates Tigris basin, passes over the basin. Rises from the foothill of Agri Mountain then joins with the Karasu river. The location of the basin is shown in Figure 1. The minimum elevation in the basin is 871 m, the maximum elevation is 4033 m, and the average elevation is 2451 m. The basin generally receives heavy snowfall in the winter months and a significant part of the water potential is formed by snowmelt.

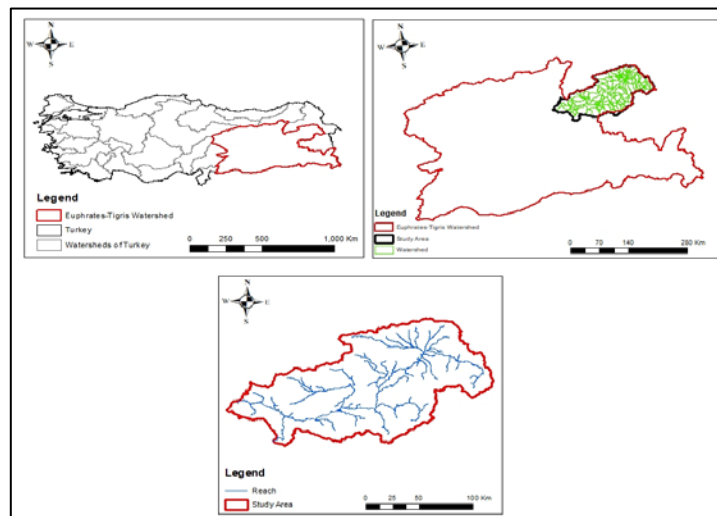


Figure 1. Location of Study Area

## 2.2. Methods

SWAT (Soil and Water Assessment Tool) is physically based model and widely used to developed model in collaboration with USDA-ARS and Texas A&M University. The model is used in surface water and groundwater modeling, water budget and water quality modelling, calculating the potential impacts of climate change, and assessing land use and best management practices. While establishing the model, characteristic features of the basin such as meteorology, topography, soil structure, vegetation and land use are used as inputs. Drainage areas, as a result of combinations of inputs, are divided into hydrological processing units called HRUs according to their hydrological characteristics, and for each HRU the processes are calculated. Surface flow, groundwater flow, evapotranspiration processes of the system are modeled [2].

The SWAT model is based on the water cycle equation on the basis of the hydrological cycle and is expressed as shown in Equation 1 below [4].

$$SW_t = SW_0 + \sum_{i=1}^t (R_{day} - Q_{sur} - E_a - w_{seep} - Q_{gw}) \quad (1)$$

In the equation;

$SW_t$  = Final soil watercontent (mm)

$SW_0$  = initial soil water content on day i (mm)

t = time (gun)

$R_{day}$  = amount of rainfall on day i (mm)

$Q_{sur}$  = amount of surface runoff on day i (mm)

$E_a$  = amount of actual total evaporation on day i (mm)

$w_{seep}$  = amount of water entering the vadose zone from the soil profile on day i (mm)

$Q_{gw}$  = amount of ground water flow on day i (mm)

Model structure is created with DEM, land use map and soil characteristics/soil type maps together with climate data. The necessary data for the model and the places to be obtained are given in Table 1. Then the hydrological response units (HRU) are determined. Different water uses, if any, in the basin are introduced to the model. After the model structure is completed, it is run and the outputs are obtained. Figure 2 shows the above-mentioned layers of the SWAT model during the establishment phase.

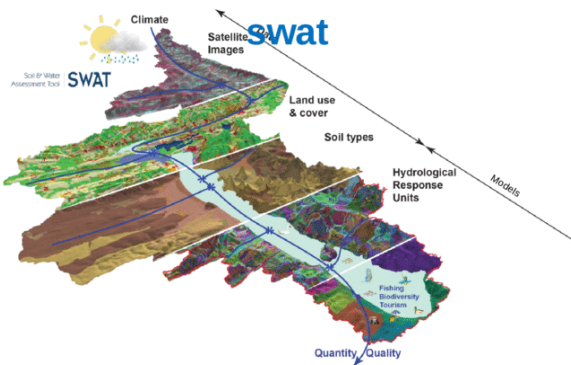


Figure 2. The layers of SWAT model [5]

Table 1. Input Data and Source of Model

Data	Source
Digital Elevation Model (DEM)	USGS
Land Use	CORINE
Soil Properties	FAO
Streamflow observation	General Directorate of State Water Works

After running the model, it needs to be calibrated. After the calibration process, the performance of the results obtained should be evaluated. The performance evaluation criteria used in the model calibration process are: coefficient of determination (R<sup>2</sup>), Nash-Sutcliffe coefficient of efficiency (NSE), Root Mean Squared Error (RMSE), Mean Absolute Error (MAE), and Percent Bias (PBIAS). The values of performance measures that can be used to evaluate the success of the models are shown in Table 2.

Table 2. Performance Limits [6]

Performans Sınırları	NSE	PBIAS
Very Good	0.75 < NSE ≤ 1	PBIAS < ±10
Good	0.65 < NSE ≤ 0.75	±10 < PBIAS < ±15
Satisfactory	0.50 < NSE ≤ 0.65	±15 < PBIAS < ±25
Unsatisfactory	NSE ≤ 0.50	PBIAS > ±25

If NSE is negative values this means the predictions are poor and if it is close to 1 means the models are satisfactory. The values of NSE is between  $-\infty$  and 1. NSE is calculated from the Equation 2.

$$NSE = 1 - \frac{\left[ \sum_{i=1}^n (Q_i^{obs} - Q_i^{sim})^2 \right]}{\left[ \sum_{i=1}^n (Q_i^{obs} - Q_{mean}^{obs})^2 \right]} \quad (2)$$

where  $Q_i^{obs}$  and  $Q_i^{sim}$  observed and simulated streamflow at time i,  $Q_{mean}^{obs}$ , average observed streamflow.

The accuracy of the results obtained with the simulation is made by comparing the measurement results obtained from the studied basin. Calibration can be defined as matching the measurement data with the model output data by changing the hydrological model coefficients [3]. The SWAT-CUP (Calibration and uncertainty program) was developed by the Swiss Federal Institute to analyze the calibration, validation and uncertainty results of the SWAT hydrological model. There are 5 algorithms in the program; Sequential Uncertainty Fit Version (SUFI-2), Particle Swarm Optimization (PSO), Generalized Probability Uncertainty Estimation (GLUE), Parameter Solution Algorithm (ParaSol) and Markov Chain Monte Carlo Algorithm (MCMC).

The SUFI-2 algorithm is used in this study. This method is based on sensitivity analysis, which determines which parameter has the greatest effect on the simulation values of a change caused by the observation values. With sensitivity analysis, the most effective parameters required in the calibration and verification process are reached [7]. SUFI-2 follows an iterative procedure where parameters are set using the new range suggested by the program. This process is continued until the desired accuracy values are reached [8-10].

### 3.RESULTS and DISCUSSION

#### 3.1. Sensitivity analysis

Climate data, DEM, soil properties, land use required for the SWAT model to work. ArcGIS 10.7 program is used to process these data. And the raster maps for required data imported into ArcSWAT 2012 interface. After all data converted the suitable format the model run and simulated for 9 years from 2005 to 2013. One year warm-up period is determined from 2005-2006. SWAT-CUP software program with SUFI-2 algorithm is used to determine sensitive parameters. From the programs output, 13 most sensitive model parameters are selected to streamflow simulation of Murat-1 and Murat-2 watershed among 25 input parameters. The most sensitive parameters are used from the years 2006 to 2011 and shown in Figure 3.

Figure 3. Most sensitive parameter for streamflow simulation

Rank	Parameter Name	t-stat	P-Value
1	R_CN2.mgt	21.451	0.000000
2	V_RCHRG_DP.gw	4.940	0.000001
3	V_ESCO.hru	4.219	0.000029
4	V_GW_DELAY.gw	2.564	0.010643
5	V_SLSOIL.hru	2.284	0.022759
6	R_SOL_AWC.sol	2.033	0.042517
7	V_ALPHA_BF.gw	1.972	0.049176
8	V_SURLAG.bsn	1.649	0.099606
9	V_CH_K2.rte	1.642	0.101072
10	R_SOL_BD.sol	1.638	0.101944
11	V_GW_REWAP.gw	1.396	0.163140
12	R_HRU_SLP.hru	1.393	0.164255
13	R_GWQMN.gw	1.355	0.175891

#### 3.2. Model Calibration

After selected the most sensitive parameters for streamflow on the watershed, the model needs to be calibrated with selected most sensitive parameters. The model calibrated the monthly time period between the years 2006 to 2011 with SWAT-CUP program. After the calibration, the streamflow estimation for monthly time series is obtained and shown in Figure 4. The model run for 500 simulation and 3 iteration. The NSE value is found 0.73,  $R^2$  is 0.73 and PBIAS values is -3.1. These results have shown that the streamflow estimation results indicate a good performance within the performance criteria [6]. Scatter plot of monthly observed streamflow versus simulated streamflow also shown in Figure 5.

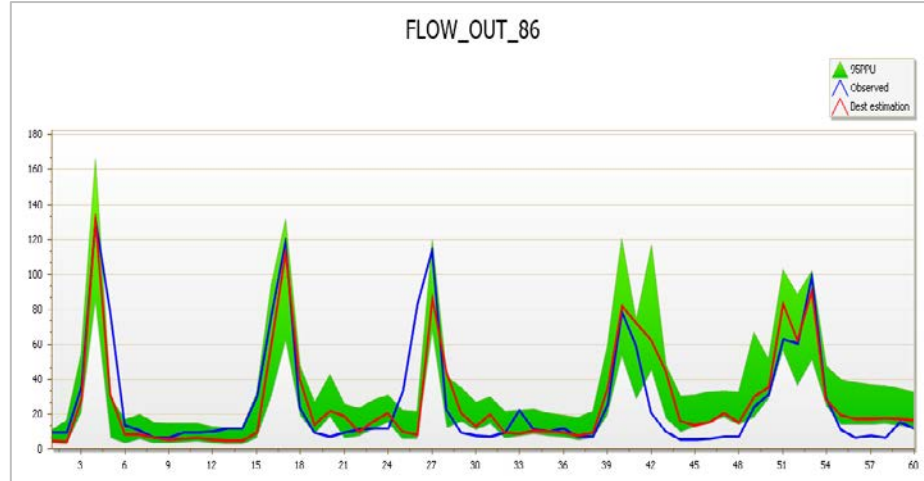


Figure 4. Observed vs Simulated Streamflow

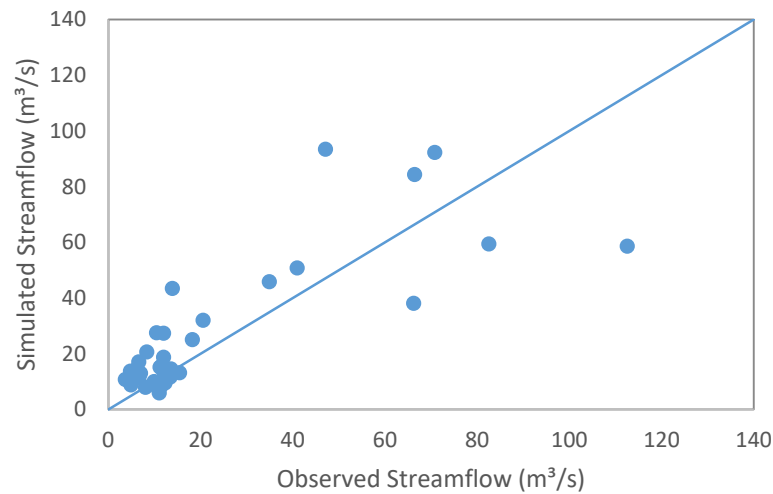


Figure 5. Scatter plot of monthly observed vs simulated streamflow for calibration period

### 3.3. Model Validation

The model is validated with the same parameters used in the calibration. 3 years validation period used from 2011 to 2013. The validation results of monthly streamflow shown satisfactory values with 0.59 NSE, 0.63  $R^2$  and -16.8 PBIAS. The hydrograph of observed vs simulated flow with the 95PPU shown in Figure 6. and also scatter plot of observed vs simulated flow shown in Figure 7.



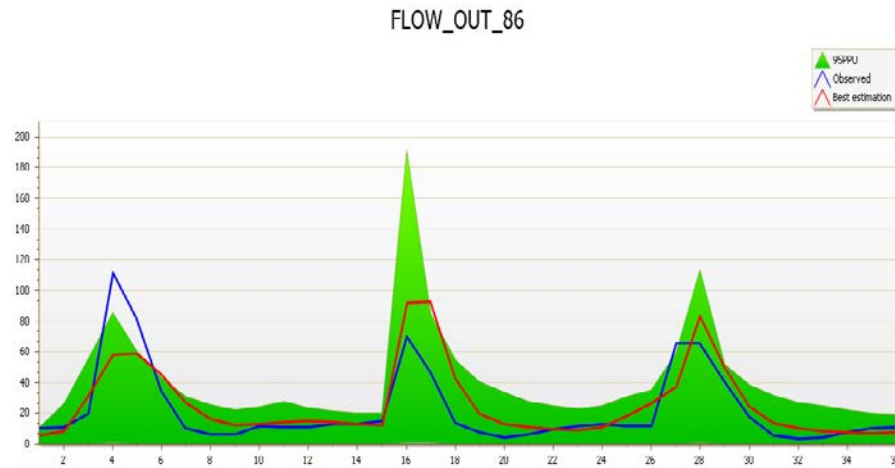


Figure 6. Observed vs Simulated Streamflow

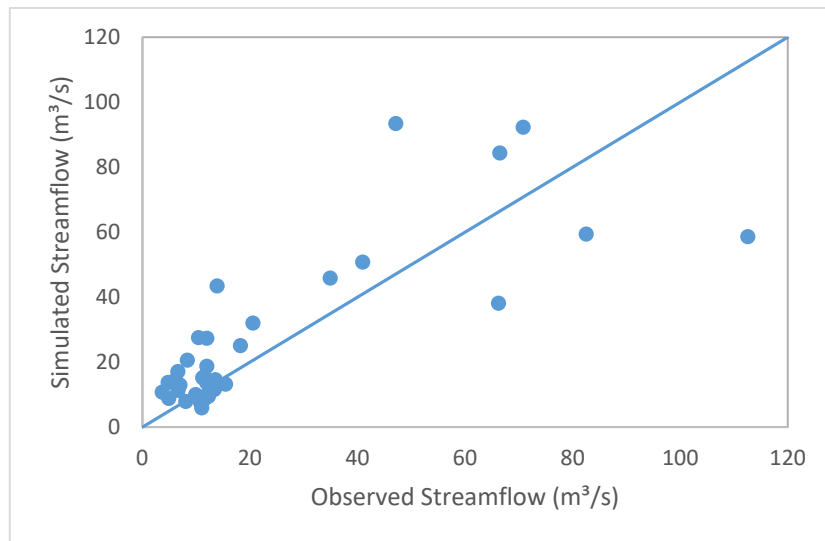


Figure 7. Figure 5. Scatter plot of monthly observed vs simulated streamflow for validation period

#### 4. CONCLUSION

In this study, Murat-1 basin located on the Euphrates-Tigris basin was modeled with the SWAT model created by using the obtained DEM, land use, soil type and meteorological data. Flow estimates were made using monthly time series. After the model was created, sensitive parameters were determined with the SWAT CUP program and

calibration and validation were performed with these parameters. 0.73 NSE value and 0.73  $R^2$  value was found during the calibration period which is good representation for the performance criteria. 0.59 NSE value and 0.64  $R^2$  value was found for the validation period which is produce satisfactory results. Based on all these results, SWAT model should be used to simulate monthly streamflow at the Murat 1 and Murat-2 watershed.

## REFERENCES

- [1]. M.W.V. Liew and A.R. Mittelstet, "Comparison of three regionalization techniques for predicting streamflow in ungaged watersheds in Nebraska, USA using SWAT model," *International Journal of Agricultural and Biological Engineering*, vol.11, no. 3, 2018.
- [2]. J. G. Arnold, R. Srinivasan, R.S. Muttiah, and J. R. Williams, "Large-area hydrologic modeling and assessment: Part I. Model development", *Journal of American Water Resources Assoc.* 34(1): 73-89, 1998.
- [3]. O. Sari, "Asagi Seyhan Havzasi Hidrolojik Dinamiklerinin Swat Ile Modellenmesi", Master Thesis, Cukurova University, Adana, Turkey, 2018.
- [4]. S.L. Neitsch, J.G. Arnold, J.R. Kiniry and J.R. Williams, "Soil and Water Assessment Tool Theoretical Documentation Version 2009", Texas A&M University, Texas, Texas Water Resources Institute Technical Report No. 406.
- [5]. Kokoszkiwicz, L., 2015, Envirogrids project overview, [Online]. Available : <https://vdocuments.site/lukasz-kokoszkiwicz-envirogrids-project-overview-swat-explanation-swat-gridification.html>.
- [6]. Moriasi, D.N., Arnold, J.G., Van Liew, M.W., Bingner, R.L., Harmel, R. D. and Veith, T.L., "Model Evaluation Guidelines for Systematic Quantification of Accuracy in Watershed Simulations". *American Society of Agricultural and Biological Engineers*, 50(3), 885-900, 2017.
- [7]. M.S. Golpinar, "Yuzey Akislarin Swat Modeli Ile Belirlenmesi: Akarsu Sulama Birligi Sahasi Ornegi", Master Thesis, Cukurova University, Adana, Turkey, 2017.
- [8]. K.C. Abbaspour, C.A. Johnson, M.T. van Genuchten, "Estimating uncertain flow and transport parameters using a sequential uncertainty fitting procedure". *Vadose Zone Journal*, 3: 1340-1352, 2004.
- [9]. K.C. Abbaspour, J. Ying, I. Maximov, R. Siber, K. Bogner, J. Mieleitner, J. Zobrist and R. Srinivasan, "Modelling hydrology and water quality in the pre-alpine/alpine Thur watershed using SWAT", *Journal of Hydrology*, 333, 413-430, 2007.
- [10]. K.C. Abbaspour, E. Rouholahnejad, S. Vaghefi, R. Srinivasan, H. Yang and B. Klove, "A continental-scale hydrology and water quality model for Europe: Calibration and uncertainty of a high-resolution large-scale SWAT model", *Journal of Hydrology*. 524, 733-752, 2015.

# Determination of Watershed Features Using Geographic Information System (GIS)

Erkan Karakoyun<sup>1</sup>, Nihat Kaya<sup>2</sup>

---

## Abstract

A water basin covers the entire area giving water to the river between the source of the river and where it ends. In simple terms, it's the area that carries the water from higher altitude to lower altitude. Factors affecting the basin, such as topography, basin size, land use, and soil type affect the process of water from upstream to downstream. For this reason, it is important to know the properties of a basin for hydrological analysis. In this study, the boundaries of the Murat-1 watershed which is the subbasin of the Euphrates-Tigris basin were determined using Geographic Information System (GIS) and some hydrological features of the basin (flow direction, accumulated flow network, drainage boundaries, slope map, aspect map) is aimed to determine. Firstly, in the study, a digital elevation map (DEM) was obtained from Shuttle Radar Topography Mission (SRTM) satellite offered by USGS. The data obtained from USGS were merged using the ArcGIS 10.7 program and then the physical properties of the watershed were determined. As a result, GIS software, which gives faster and less costly results compared to traditional methods, has been accepted as a very effective tool in determining basin characteristics and boundaries.

**Keywords:** ArcGIS, CBS, Watershed

---

## 1. INTRODUCTION

Water is the most important element for the continuation of life and the sustainability of the ecological balance. Nowadays, the increase in water pollution, decrease in the amount of usable water and natural disasters caused by water threaten the future of water. Because of this, water resources management is one of the problems that need to be solved. This has led to the conclusion that water should be used sparingly and that we should know the movements of water in nature [1]. For this reason, all necessary data collection, processing and analysis must be carried out reliably and quickly in order to protect water resources, which is one of the main objectives of integrated watershed management [2]. There are some basic components that become prominent for the basin characteristics. These are: basin area, slope, minimum, maximum and average elevation of basin, basin aspect etc. By revealing the characteristics of the basin, all definitions of the area can be made and these features can be used effectively in planning studies [3]. The process of determining the boundaries of the basin and sub-basin with classical methods is done manually from printed or digital contour maps that express the surface shapes of the land. However, these classical approaches require a very long process and cost. Especially when the size of the working area is large, the operation process becomes even more difficult [4].

---

<sup>1</sup>Corresponding author: Mus Alparslan University, Faculty of Engineering and Architecture, 49250, Mus, Turkey. [e.karakoyun@alparslan.edu.tr](mailto:e.karakoyun@alparslan.edu.tr)

<sup>2</sup>Firat University, Faculty of Engineering, Department of Civil Engineering, 23119, Elazig, Turkey. [n.kaya@firat.edu.tr](mailto:n.kaya@firat.edu.tr)

With the developments in Geographic Information Systems (GIS) in recent years, getting spatial data analysis become easier. In this context, digital elevation model (DEM) is created from various remote sensing data, and river drainage network and basin and sub-basin boundaries can be automatically extracted from DEM with various spatial analyzes in GIS environment, quickly, economically and with high accuracy [4,5].

In this study, the basin characteristics of the Murat-1 basin area, which was chosen as the study area, were determined with the help of GIS technologies and the effective role of this technology in hydrology studies was tried to be revealed.

## 2. MATERIAL and METHOD

### 2.1. Study Area

Murat River, the most important branch of the Euphrates, rises from the foothills of Agri Mountain and joins with the Karasu River, which comes from the North, after flowing for about 500 km towards the southwest. In the region where the continental climate is effective, winters are wet and cold, summers are warm and dry. In the region where the most precipitation falls in the spring, the amount of precipitation falls below 20 mm between June and October.

The Euphrates Tigris basin is the basin with the largest area in our country, Turkey. Thirty percent of the annual flow in our country flows from this basin. The important hydroelectric power plants of our country are located in this basin. The Murat-1 basin is located in the upper Euphrates basin and was selected for this study. The location of the Murat-1 basin was shown in the Figure-1.

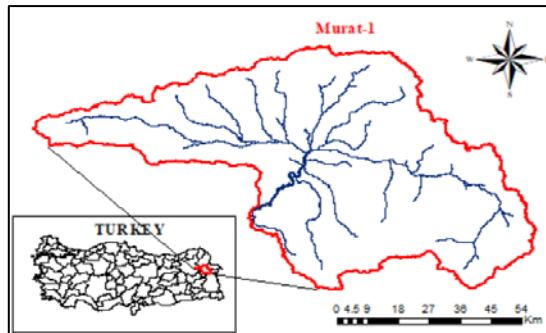


Figure 1. Study Area, Murat-1 basin

### 2.2. Method

Within the scope of determining the basin characteristics and boundaries, first of all, it is necessary to obtain a digital elevation map of the study area. In this context, 30m x 30m resolution data obtained from the Shuttle Radar Topography Mission (SRTM) satellite, whose DEM data are provided by the USGS, has been downloaded. When the downloaded data has more than one layer, tessellation, which is the process of merging according to the common areas of the satellite images, should be done to create a continuous data. This process is done with the help of the ArcGIS program. After mosaic, the DEM data is corrected. The accuracy of the DEM data is very important, because this step and the next steps are performed using DEM data. In Figure 2, mosaiced DEM data and Murat 1 basin boundaries are seen

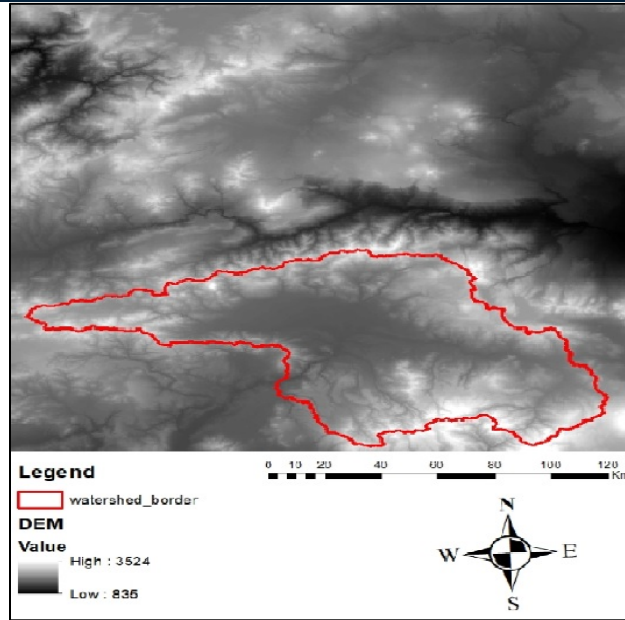


Figure 2. Mosaiced DEM and Watershed Border of Murat-1 basin

After the DEM data is transferred to the ArcGIS program, the first thing to do is to remove the errors found in the DEM. When a cell is surrounded by cells with a higher elevation, the water will flow towards the area where is the lower elevation and therefore no surface flow will occur. To eliminate this error, the spaces will be filled and the height values will be rearranged by using the Fill command in the program (Figure 3).

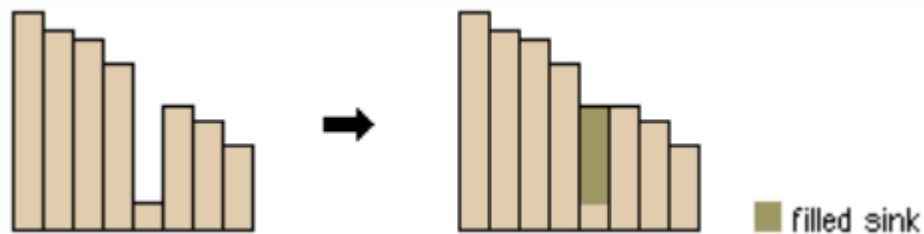


Figure 3. Correction of DEM error [6]

After the errors in the DEM are eliminated, the flow directions should be determined. Algorithms such as D8, Rho8, MFD are available for these operations. The D8 algorithm was used in the determination of the flow directions due to its ease of use and speed. D8 is a one-way algorithm that assumes that the flow in any cell is in the direction of its neighbor with the highest slope and low elevation [7]. Flow on a surface, always occurs from the highest to the lowest elevation. If the flow direction of each cell is known, the total number of cells flowing into any cell can be determined (Figure 4). Flow direction is calculated for a given grid system with the Flow Direction command in the ArcGIS program.

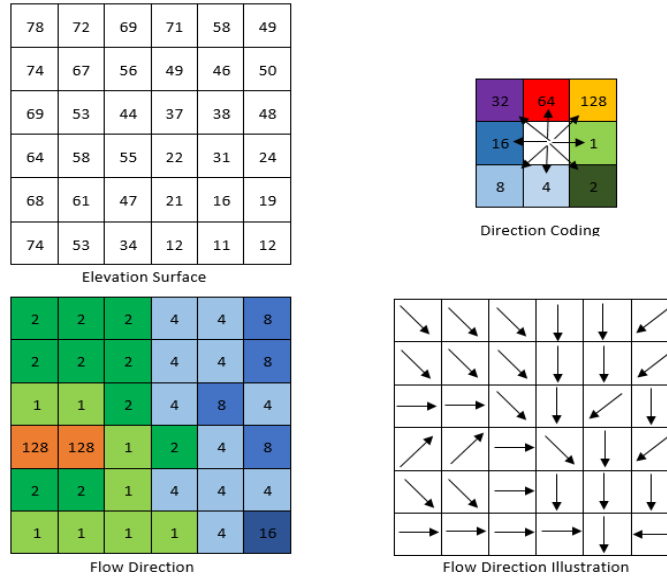


Figure 4. D8 Algorithm [6]

After determining the flow directions, the Flow Accumulation command determines where the total flow in the cell comes from. After this process, the river branches begin to appear. The flow accumulation is illustrated in the Figure 5 [6]. In Figure 6, calculated flow accumulation for the Murat 1 watershed has shown.

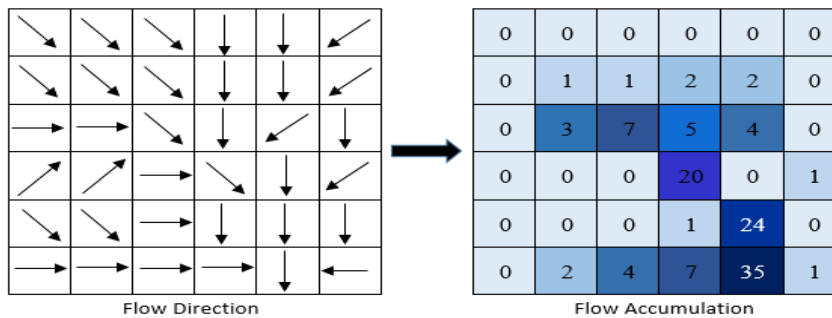
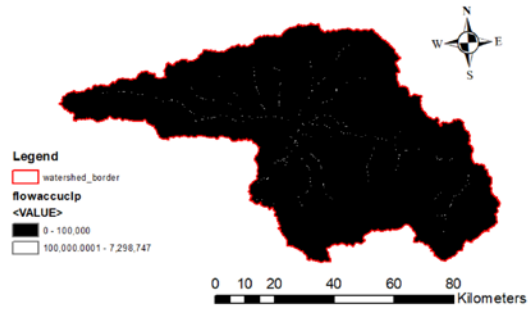


Figure 5. Flow Accumulation



*Figure 6. Murat-1 Basin Flow Accumultion*

### 3. RESULTS and DISCUSSION

After the DEM data is transferred to the ArcGIS program, first of all, the gaps in the grid are filled with the Fill command and cut with the clip command and displayed in a way that represents only the work area. The screenshot obtained from the program is shown in Figure 7.

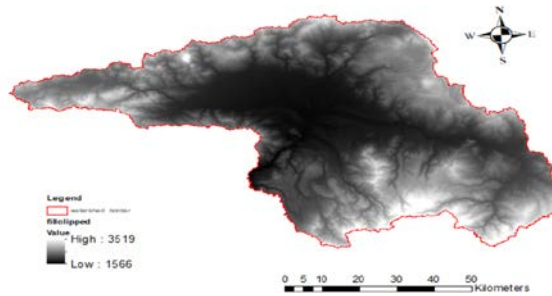


*Figure 7. Correction of DEM, Murat-1 Basin*

After filling the gaps in each grid, the flow direction is determined by the Flow Direction command. Flow directions map of Murat-1 basin obtained from the program and is given in Figure 8.

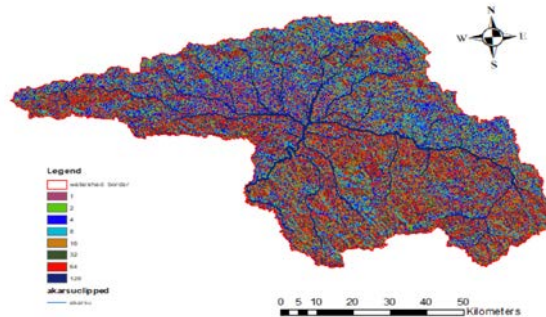


*Figure 8. Flow Direction of Murat-1 Basin*

After the determination of the basin boundaries and the river network, the hillshade map of the region was also created and loaded on the DEM map as a basemap. The final map is shown in Figure 9.



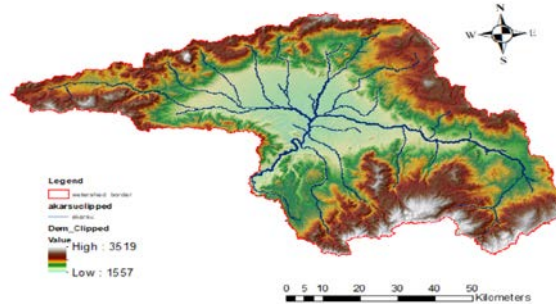


Figure 9. Murat-1 basin with defined DEM, watershed borders and river network

After all operations, it is aimed to create a slope and aspect map of the basin. The slope features of the basin are important in understanding the morphological features of the basin in the formation of floods and landslides. In addition, aspect can be explained as the direction in which the mountains in a region receive the Sun's rays or the part of their view towards the Sun. In Figure 10 and Figure 11, the slope and aspect distributions of the Murat-1 basin are shown respectively. The average slope of the basin is found at 10.6 % and the maximum slope is 70.2 %.

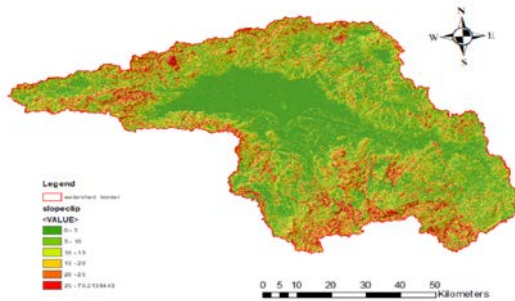


Figure 10. Slope map of Murat-1 Basin

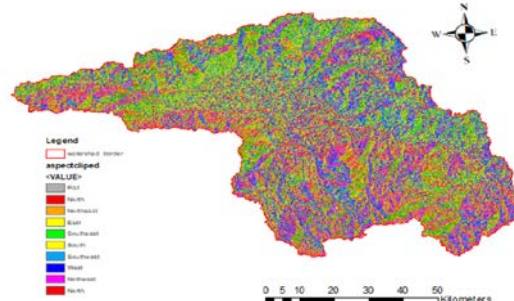


Figure 11. Aspect map of Murat-1 Basin

#### 4. CONCLUSIONS

Determination of basin boundaries, features and river drainage networks is a time-consuming and costly process with classical methods. These maps, which were obtained from topographic maps in the past, are obtained more quickly in the GIS environment with the rapid development of computer technology today. These analyzes, created by using the obtained DEM data, give fast and easily accessible results with the help of the programs used.

In this study, stream drainage networks of Murat-1 sub-basin, which is a part of the Euphrates-Tigris basin, were created using DEM data, the boundaries of the basin were determined, and maps such as slope and aspect distributions of the basin were created. As a result of the study, it has been shown that GIS programs are an important tool that can be used for data processing, determining basin boundaries, creating drainage networks and visualizing the physical and morphological features of the basin.

**REFERENCES**

- [1]. A.A.Karadag, "Kovada Golu Alt Havza Sinirlarinin Belirlenmesi", *Duzce Universitesi Ormancilik Dergisi*, 8(1), 58-76, 2012.
- [2]. B.T.Meric, "Su Kaynaklari Yonetimi ve Turkiye", *Jeoloji Muhendisligi Dergisi*, 28(1), 27-38, 2004.
- [3]. M.C.Bagdatli and B.Ozturk, "Havza morfolojik ozelliklerinin belirlenmesinde cografi bilgi sistemlerinin (CBS) etkin rolu", *SAU Fen Bilimleri Enstitusu Dergisi*, 18(1), 11, 2014.
- [4]. A.Uyar, D.Ozturk, " Kizilirmak Havzasi Drenaj Aginin ve Alt Havza Sinirlarinin Uzaktan Algilama ve CBS Ile Otomatik Cikarimi", 3, 362-365, 2018.
- [5]. T.Dindaroglu, M.Ozgul and M.Y.Canbolat, "Sayisal Yukseklik Modeli Kullanilarak Bazi Havza Karakteristiklerinin Saptanmasi ve Arazi Kullanimi", *KSU Journal of Engineering Science, Special Edition*, 197-205, 2012.
- [6]. Esri website [Online]. Available : <https://pro.arcgis.com/en/pro-app/latest/tool-reference/spatial-analyst/an-overview-of-the-hydrology-tools.htm>.
- [7]. J.F.O'Callaghan and D.M.Mark, "The extraction of ordered vector drainage networks from elevation data", *Computer Vision, Graphics and Image Processing*, 47(1), 45-58, 1989.

# Geo-electrical characteristics of the Erecek- Canakkale region

Petek Sindirgi<sup>1</sup>

---

## Abstract

*Biga Peninsula is one of the tectonically active regions in Northwestern Anatolia which the middle strand of the North Anatolian Fault Zone is crossed over by it. This work is aimed to model the subsurface geological structures via vertical electrical sounding (VES) and self-potential (SP) datasets collected from the relatively less known Southern part of the Biga Peninsula. The vertical electrical sounding (VES) and self-potential (SP) datasets collected near the Erecek village of Canakkale city were inverted by the Levenberg-Marquardt algorithm. Four profiles were generated covering some VES points to reveal the geological model. In addition, resistivity distributions at 10, 100, 200, 500, and 1000 meter depth levels were calculated. Thus, the iso-3D resistivity distribution was easily observed. Based on the VES findings, three main geological units were defined; two groups of volcanic units and a metamorphic basement. Besides, WSW-ENE and NNE-SSW trending two normal faults that have possibly water content were observed. One of them was also detected from the self-potential profile data inversion results. As a result, possible main fault locations and tectonic structures that may be associated with groundwater containment have been described using the findings of both two geo-electrical methods.*

**Keywords:** Canakkale, self-potential, vertical electrical sounding

---

## 1. INTRODUCTION

Biga Peninsula is a tectonically active region on the Alpine-Himalayan Mountain Belt that corresponds to the northward movement of the Arabian plate and the northern part of the southern segment of the NAF zone lies on it [1]. The main fault systems of this region can be listed as Balabanli, Kestanbol, Tuzla, Evciler and Edremit Faults. Accordingly (bununla iliskili olarak), this region hosts (is also hosted) also several active geothermal areas such as Tuzla, Palamutova, Kestanbol, Kucukcetmi. Many geological and geophysical studies have been done to reveal the tectonic complexity of the peninsula[1]-[11]. Most of the previous geophysical investigations were seismological studies [12], [13] related with the Northern Anatolian Fault (NAF) kinematics and structural observations. The other geophysical methods such as gravity, magnetic and electrical methods were applied in the geothermal [14], landslide [15], and archaeological [16] investigations in the region.

Geoelectrical methods supply robust information about layer rock type, thickness, and water content [17], [18]. In this study, SP and VES field datasets (Figure 1 and Figure 2) collected from near the Canakkale-Erecek village were evaluated by inverse solution techniques. This area represents the transition zone between the Beydagi Horst and Tuzla Basin. Geological units of the study area are the Balabanli volcanics, Dededag formations, and Karadag metamorphics. The Balabanli volcanics consist of pyroclastic rocks such as rhyodacitic ignimbrites and lavas. The Dededag formation contains andesitic and trachyandesitic lavas and flow-breccias. The Balabanli volcanics and Dededag formation lie over the metamorphic basement [3], [4], [8](Figure 2).

In this study, it is aimed to determine the electrical properties of an area located in northern part of Behram and western part of Erecek villages and combine with the possible tectonic features and accordingly possible

---

<sup>1</sup> Corresponding author: Dokuz Eylul University, Faculty of Engineering, Department of Geophysical Engineering, 35390, Buca /Izmir, Turkey.[petek.sindirgi@deu.edu.tr](mailto:petek.sindirgi@deu.edu.tr)

geothermal potential. For this purpose, the VES and SP data were evaluated to distinguish main subsurface lithologies and location of the faults may associated with local groundwater movement.

## 2. METHODS AND APPLICATIONS

VES method employs an artificial source of current which is introduced into the ground through two electrodes. The occurred potential difference is measured at other electrodes. Electrical resistivity and depth of the layers can be calculated using Ohm Law. Electrical resistivity varies with porosity, pore fluid salinity, and clay content. On the other hand, SP method based on the measurement of potential difference between the two points on the earth surface without artificial current source. Source parameters of potential anomalies occurred by the mineralization, thermoelectric or electrochemical coupling processes could be estimated by SP measurements. Both geo-electrical methods are widely used in the determination of the subsurface structures, and faults.

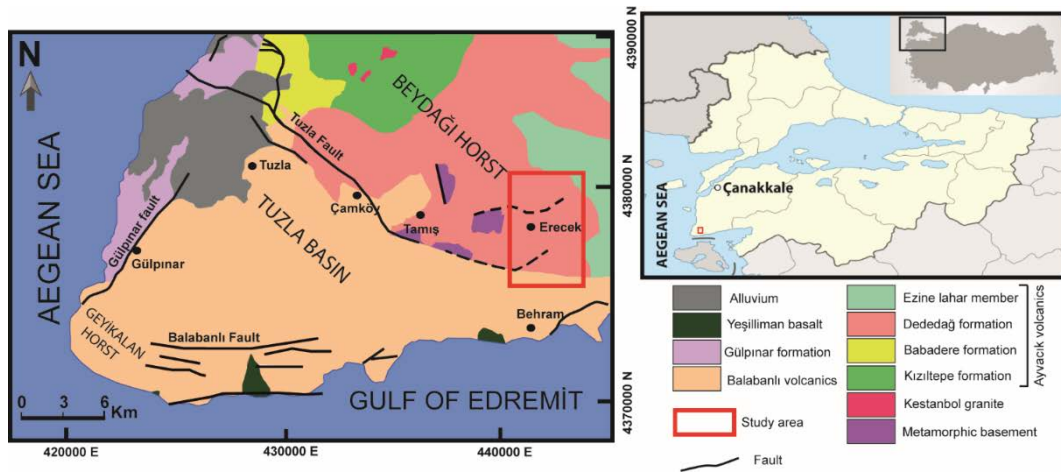


Figure 1. Geologic map of study area and surrounding (modified from [3])

In this study, investigation area is located between 26.3069N-26.3358N longitude and 39.5234E-39.5796E latitude and covers the area between the northern part of Behram and western part of Erecek villages of Çanakkale city (Figure 1). It is approximately spread over 30 km<sup>2</sup> area. The 43 vertical electrical soundings (Schlumberger array) and one SP profile data were evaluated by inversion approach. Four resistivity sections were generated based on the VES profiles including AA', BB', CC' and DD'. Based on these cross-sections and SP profile a geological model was constructed for the area. AA' and BB' profiles are aligned in NNW-SSE, and CC' and DD' profiles are aligned in WSW-ENE direction. A self-potential profile (EE') data is also aligned in WNW-ESE direction (Figure 2).

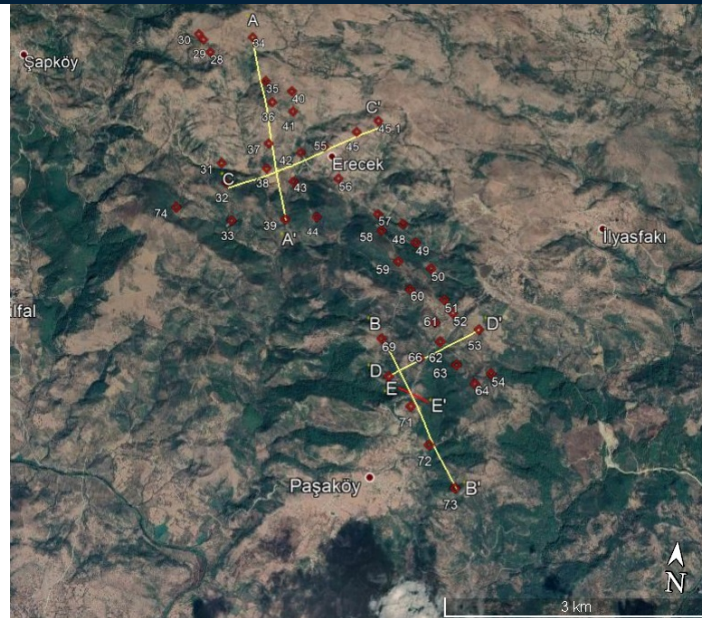


Figure 2. Location of VES points, VES and SP profiles

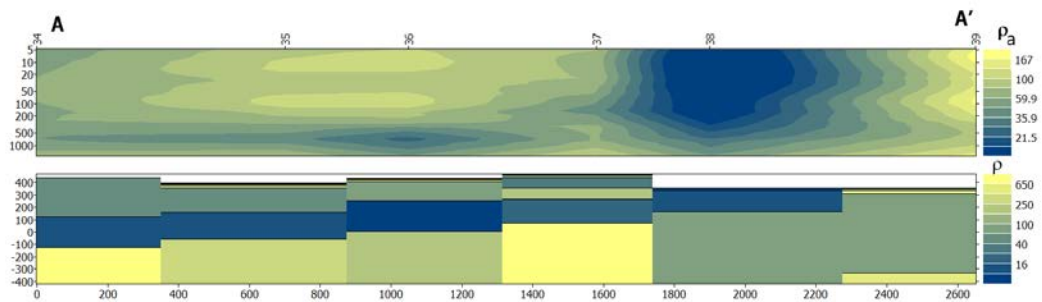


Figure 3. Pseudo and resistivity sections of AA' profile

The actual resistivity and thickness of the subsurface layers were obtained by inverse solution technique using the IPI2win software developed by the Geophysics Group Moscow State University [19]. (IPI2Win-1D Program, version 3.0.1a, 2003). The software realizes iterative minimization of the misfit between real and modelled data based on a least number of layers initial model using Tikhonov's approach. For all sounding curves inverted to obtain the actual resistivity and thickness of the subsurface layers. The fit between model response and the field data for the VES points were generally lower than 5%. In addition, pseudo and resistivity sections of four profiles were created by combining some selected points from them. To be an example, the AA' profile pseudo and resistivity sections are plotted in figure 3. According to the parameters of these sections geological models were established (Figure 4). Then, apparent resistivity distributions for many depth levels (10, 100, 200, 500, and 1000 meter) are plotted to reveal the areal resistivity distribution versus to depth (Figure 5).

The SP profile data (EE') were evaluated by Levenberg-Marquardt (LM) inversion algorithm [20]. Profile data were assumed produced by a simple sphere-shaped polarized causative body. Parameters of sphere model are electric dipole moment (K), horizontal distance (x), distance from the origin ( $x_0$ ), depth to the centre of the body ( $z_0$ ), and polarization angle ( $\theta$ ). The polarization angle is determined as the angle between vertical plane and polarization surface. Calculated SP parameters are shown in figure 6 and Table 1. The root mean standard error is 0.1155.

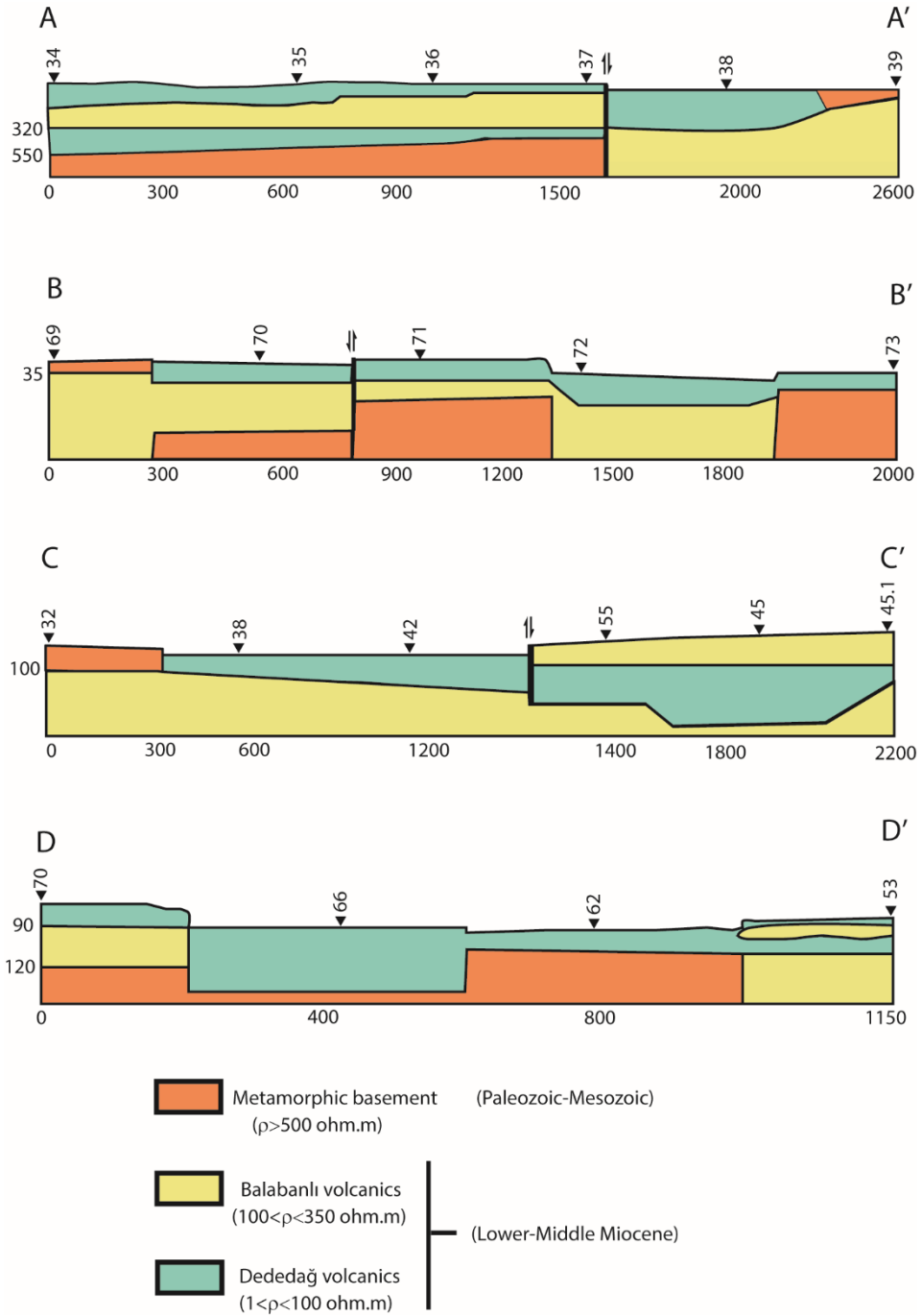


Figure 4. Geological models of VES profiles

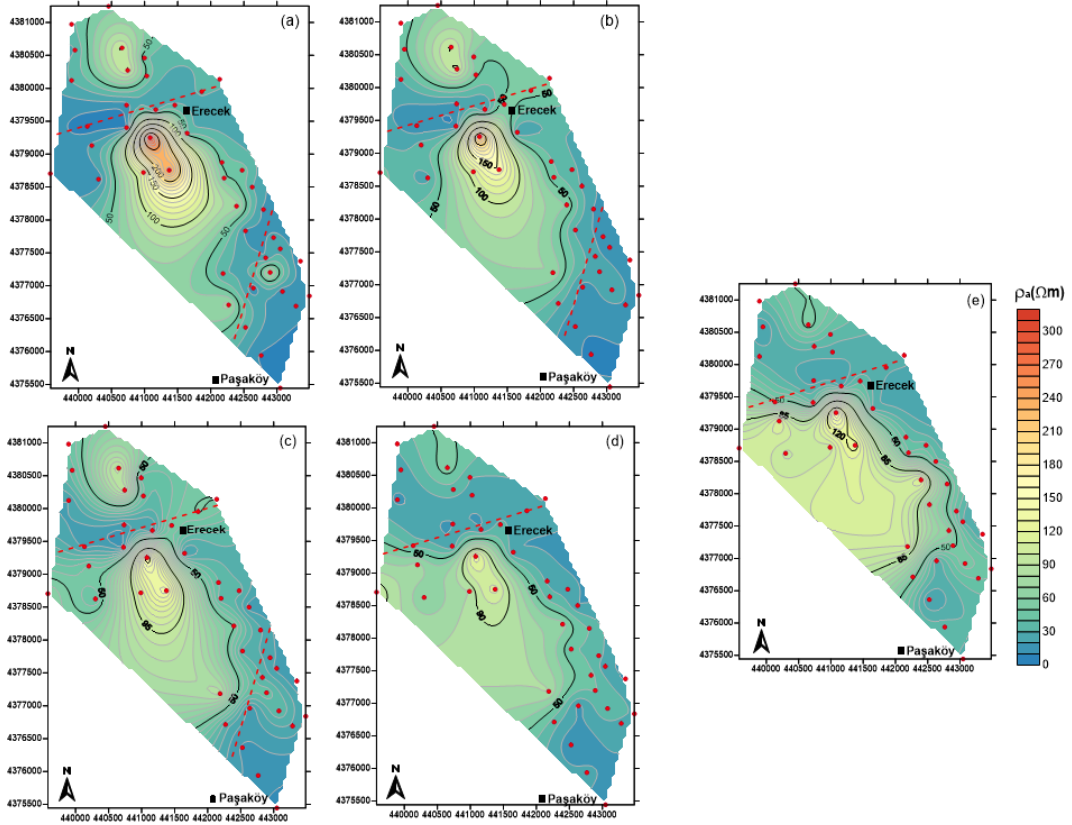


Figure 5. Contour maps of the iso-apparent resistivity values (a)  $AB/2=10m$ , (b)  $AB/2=100m$  (c)  $AB/2=200m$ , (d)  $AB/2=500m$ , (e)  $AB/2=1000m$

Table 4. Calculated SP model parameters

E. dipol moment (K)	Polarization angle ( $\theta$ )( $^{\circ}$ )	Distance from the origin ( $x_0$ )(m)	Depth ( $z_0$ ) (m)
447432.17	1.37	216.88	145.38

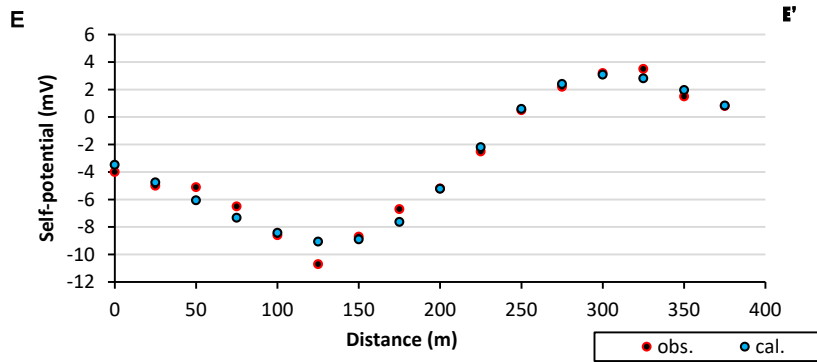


Figure 6. Observed and calculated SP values

### 3. RESULTS AND CONCLUSIONS

In this study, VES and SP methods were applied to distinguish main subsurface lithologies and locate faults that may be associated with local groundwater movement. As a result of the 1D inversion of VES, three main distinct units have been identified. The first one is the Dededag surface volcanics characterized by low and medium resistivities (1-100 ohm.m), the second one is the Balabanli volcanics having medium resistivities (100-300 ohm.m) and the third one is the metamorphic units (having resistivities higher than 1000 ohm.m) forming the basement. These geological formations were also described in the four VES profiles (AA', BB', CC' and DD'). It has been revealed that the surface volcanics become thinner and the metamorphic basement units reach to the surface near the VES 32, 38 and 69.

Not only from the cross-sections but also the depth level maps it is seen that the high resistive basement spread out over the area between the southwestern part of Erecek and the northern part of Pasakoy villages. WSW-ENE and NNE-SSW trending two normal faults that have possibly water content were observed. One of them was also detected from the self-potential profile data inversion results. The calculated polarization angle shows that the fault has a slope close to the vertical. The  $x_0$  parameter corresponds to the distance between location E and the intersection of BB' and EE' profiles in the figure 2. Since the location of fault determined as between VES 70 and 71 points at BB' profile, it well matches the  $x_0$  determined by SP inversion. Although these parameters were obtained from only one SP profile dataset, determined fault location is very similar to the results of resistivity inversion.

It is observed the areas that have resistivity values below 10 ohm.m matched the alignment of the detected two faults. These areas may have contains hot or cold groundwater. Therefore, it is recommended to search geothermal potential of these areas by other hydrogeophysical and hydrogeological methods.

### ACKNOWLEDGMENT

The author thanks to Geophysical Engineer Yasin EYUP for providing the geoelectrical data used in this study.

### REFERENCES

- [1]. D. McKenzie, "Active tectonics of the Mediterranean region", *Geophysical Journal of the Royal Astronomical Society*, vol. 30, pp. 109–185, 1972.
- [2]. D. McKenzie, "Active tectonics of the Alpine-Himalayan belt: the Aegean Sea and surrounding regions", *Geophysical Journal International*, vol. 55, pp. 217–254, 1978.
- [3]. Z. Karacik and Y. Yilmaz, "Geology of the ignimbrites and the associated volcano-plutonic complex of the Ezine area, northwestern Anatolia", *J. Volcan. Geother. Res.*, vol. 85, pp. 251–264, 1998.
- [4]. Y. Yilmaz and Z. Karacik, "Geology of the northern side of the Gulf of Edremit and its tectonic significance for the development of the Aegean grabens", *Geodinamica Acta*, vol. 14, pp. 31–43, 2001.
- [5]. F. Dewey and A. M. C. Sengor, "Aegean and surrounding regions: complex multiplate and continuum tectonics in a convergent zone", *Geological Society of America Bulletin*, vol. 90 (1), pp. 84–92, 1979.
- A. I. Okay, M. Siyako, and K. A. Burkan, "Geology and tectonic evolution of the Biga Peninsula", *Bulletin of the Technical University of Istanbul*, vol. 44, pp. 191–255, 1991.
- [6]. M. Duru, S. Pehlivan, I. O. Aral, Y. Senturk, F. Yavas, and H. Kar, "Biga Yarimadasinin Tersiyer Oncesi Jeolojisi", *Maden Tetkik ve Arama Genel Mudurlugu Yayinlari*, vol. 28, pp. 7–74, 2012.
- [7]. H. Sozibilir, O. Sumer, C. Ozkaymak, B. Uzel, T. Guler, and S. Eski, "Kinematic analysis and palaeoseismology of the Edremit Fault Zone: evidence for past earthquakes in the southern branch of the North Anatolian Fault Zone, Biga Peninsula, NW Turkey", *Geodinamica Acta*, vol. 28(4), pp. 273–294, 2016.
- [8]. E. Yigitbas and I. O. Tunc, "Biga Yarimadasini'nda Sakarya Zonunun Prekambriyen Metamorfik Kayalari; Gec Ediyakaran Gondwanaland Aktif Kita Kenari", *Geological Bulletin of Turkey*, vol. 63, pp. 277–302, 2020.
- [9]. Y. L. Ekinci and E. Yigitbas, "Investigation of Plutonic Rocks in Biga Peninsula, NW Turkey, using 3D Normalized Full Gradient of Magnetic Data", in *Proc. European Geosciences Union General Assembly, Austria*, 2012, p. 8802.
- A. Yaltirak, E. B. Isler, A. E. Aksu, and R. N. Hiscott, "Evolution of the Bababurnu Basin and shelf of the Biga Peninsula: western extension of the middle strand of the North Anatolian Fault Zone, Northeast Aegean Sea, Turkey", *Journal of Asian Earth Sciences*, vol. 57, pp. 103–119, 2012.
- [10]. T. Taymaz, J. Jackson, and D. McKenzie, "Active tectonics of the north and central Aegean Sea". *Geophysical Journal International*, vol. 106(2), pp. 433–490, 1991.
- [11]. S. Ozden, S. Over, S. A. Poyraz, Y. Gunes, and A. Pinar, "Tectonic implications of the 2017 Ayvacik (Canakkale) earthquakes, Biga Peninsula, NW Turkey", *Journal of Asian Earth Sciences*, vol. 154, pp. 125–141, 2018.



- [12]. O. Tezel and F. Ozcep, "Geothermal Exploration By Using Time Domain IP Method: Balikesir (Gure) and Canakkale (Geyikli) Cases From Turkey", *AGU Fall Meeting Abstracts* 2017, p. T41A-0603.
- A. Nart, O. Cakir, M. Erduran, Y .A. Kutlu, and Z. S. Cetiner, "A potential landslide area investigated by 2.5D electrical resistivity tomography: case study from Canakkale, Turkey", *Arab J Geosci.*, vol. 9(6), 2016.
- B.Kurcer, A. Chatzipetros, S. Z. Tutkun, S. Pavlides, S. Ozden, G. Syrides, K. Vouvalidis, E. Ulugergerli, O. Ates, and YL. Ekinci, *An assessment of the earthquakes of Ancient Troy, NW Anatolia, Turkey, in Tectonics-Recent Advances*, Sharkov, E., Ed. London, UK: InTech, 2012, pp. 171–200.
- [13]. L. R. Bentley. And M. Gharibi, "Two and three dimensional electrical resistivity imaging at a heterogeneous remediation site". *Geophysics*, vol. 69(3), pp. 674–680, 2004.
- A. Auken and A.V. Christiansen, "Layered and laterally constrained 2D inversion of resistivity data", *Geophysics*, vol. 69(3), pp. 752–761, 2004.
- B. *IP12WIN software Moscow State University*, Version 3.0; 2003 Marquardt, "An Algorithm for Least-Squares Estimation of Nonlinear Parameters", *SIAM Journal on Applied Mathematics*, vol. 11(2), pp. 431–441, 1963.

# Towards High Precision Satellite Based Real Time Positioning with Trimble RTX Service

Omer Faruk Atiz<sup>1</sup>, Abbas Qader Shakor<sup>2</sup>, Salih Alcay<sup>3</sup>, Sermet Ogutcu<sup>4</sup>

---

## Abstract

The real time precise positioning methods with Global Navigation Satellite Systems (GNSS) have been drastically enhanced in recent. The Real Time Precise Point positioning (RT-PPP) method has become available in the last years along with the commonly used relative techniques; Real Time Kinematic (RTK) and Network RTK (NRTK). In addition, Trimble introduced the RT-PPP correction service called Real Time eXtended (RTX), which delivers the correction data via L-band signals of geostationary orbit (GEO) satellites. In this study, a field test was carried out to assess the latest performance of the Trimble RTX service considering the combination of GNSSs namely, GPS-only, GPS+GLONASS, GPS+Galileo, GPS+GLONASS+Galileo, GPS+GLONASS+Galileo+Beidou. The RTX coordinates of five satellite configurations were retrieved for 9-hour, in November 2020. The results of the experiments were evaluated in terms of repeatability. The standard deviation of GPS+GLONASS combination is better than 2.0 cm in both horizontal and vertical components. Moreover, the GPS+GLONASS+Galileo combination improved the precision of GPS-only by 33.2% for the vertical component.

**Keywords:** GNSS, RT-PPP, Trimble RTX

---

## 1. INTRODUCTION

In general, Global Navigation Satellite System (GNSS) based positioning techniques are classified in two groups. The absolute positioning is conducted using a single receiver while the relative approach requires a reference station. The Real Time Kinematic (RTK) method provides centimeter level positioning accuracy regarding the base distance between rover and reference station [1], [2]. In Network RTK (NRTK) method, the RTK corrections are calculated from a GNSS network and sent to rovers via Internet [3], [4]. The main limitation of NRTK method is that it can only be used in the coverage area of the network. On the other hand, the PPP method provides millimeter-centimeter level accuracy after a convergence time for a standalone GNSS receiver around the world using precise satellite orbit and clock products [5], [6]. Moreover, the Real Time Precise Point Positioning (RT-PPP) method has become available thanks to the International GNSS Service (IGS) real time precise satellite orbit and clock products [7]. Thereupon, the correction data is streamed over Internet for the users at world-wide scale. However, a software package such as BKG Ntrip Client (BNC) [8] is compulsory to retrieve/decode the correction messages and to calculate the RT-PPP coordinates [9].

Many studies are performed on the performance of RT-PPP method. Reference [10] analyzes the positioning and zenith total delay (ZTD) estimation performance of RT-PPP considering GPS-only, GPS+GLONASS, and GPS+GLONASS+Galileo+Beidou satellite combinations. According to 4-hour RT-PPP solutions, 5 cm horizontal and 10 cm vertical accuracy is achieved. Reference [11] evaluates the convergence time and accuracy of the performance of multi-GNSS RT-PPP. The results showed that GPS+GLONASS combination improved the accuracy and convergence time of GPS-only solutions. The RT-PPP method is employed for bridge

---

<sup>1</sup> Corresponding author: Necmettin Erbakan University, Department of Geomatics Engineering, 42080, Meram, Konya, Turkey. [oiatiz@erbakan.edu.tr](mailto:oiatiz@erbakan.edu.tr)

<sup>2</sup> Necmettin Erbakan University, Department of Geomatics Engineering, 42080, Meram, Konya, Turkey. [abbasqader12@gmail.com](mailto:abbasqader12@gmail.com)

<sup>3</sup> Necmettin Erbakan University, Department of Geomatics Engineering, 42080, Meram, Konya, Turkey. [salcay@erbakan.edu.tr](mailto:salcay@erbakan.edu.tr)

<sup>4</sup> Necmettin Erbakan University, Department of Geomatics Engineering, 42080, Meram, Konya, Turkey. [sermetogutcu@erbakan.edu.tr](mailto:sermetogutcu@erbakan.edu.tr)

monitoring with GPS observations [12]. While the RT-PPP method could not capture the millimeter level movements, it showed similar results with double-differencing (DD) for centimeter-decimeter level movements.

Moreover, Trimble introduced the Real Time eXtended (RTX) service which can distribute RT-PPP corrections over L-band satellites instead of GSM/Internet [13]. This development allowed the users to perform RT-PPP around the world even the Internet connection is not available. There are few studies carried out on the performance of RTX positioning. Reference [14] examined the GPS-only performance of RTX correction service for determining ground motion. The RTX correction service provided 2.2/2.8/8.4 cm long term static positioning precision, for north, east, and up components, respectively. The accuracy of RTX service significantly decreased when the GNSS sites did not have open sky conditions [15]. The static RTX measurements using GPS+GLONASS+Galileo+Beidou satellites at different test sites showed 2 cm and 4 cm root mean square errors (RMSE) for horizontal and vertical components, respectively [16]. Reference [17] investigates the kinematic positioning performance of RTX service on a moving vessel. They concluded that RTX service can be used if the centimeter-decimeter level accuracy is enough for the surveying.

Although some studies conducted related to performance of Trimble RTX correction service, the contribution of Galileo satellites is not yet investigated after reaching Full Operational Capability (FOC) in above experiments. In this study, the latest positioning performance of RTX service was evaluated considering GPS-only, GPS+GLONASS, GPS+Galileo, GPS+GLONASS+Galileo, GPS+GLONASS+Galileo+Beidou satellite combinations.

## 2. METHOD

Five GNSS receivers were installed on the roof of Engineering Faculty building of Necmettin Erbakan University to test the performance of RTX correction service. A special apparatus was used to place five receivers on the same stand. Hence, the receivers were under same environmental conditions such as multipath error. The location of field experiment and the GNSS receivers during the measurement are illustrated in Figure 1. The CHCNAV I90 PRO GNSS receivers were used for the field experiment which are capable of tracking L-band corrections of Trimble RTX correction service. The details of GNSS receiver are given in Table 1.

Table 5. The specifications of CHCNAV I90 PRO receivers [18]

Parameter	Specification
GNSS	GPS, GLONASS, Galileo, Beidou, SBAS, QZSS, IRNSS
L-Band	RTX
Channel	336 channels
RTK accuracy	Horizontal: 8 mm + 1 ppm Vertical: 15 mm + 1 ppm
Post processing accuracy	Horizontal: 2.5 mm + 0.5 ppm Vertical: 5 mm +0.5 ppm
Time to first fix	Cold start: < 45 sec Hot start: < 10 sec
Size	159x150x110 mm
Communication	4G modem, Wi-Fi, Bluetooth, UHF radio
Data storage	32 GB
Power	Up to 10 hour for static/ External power input

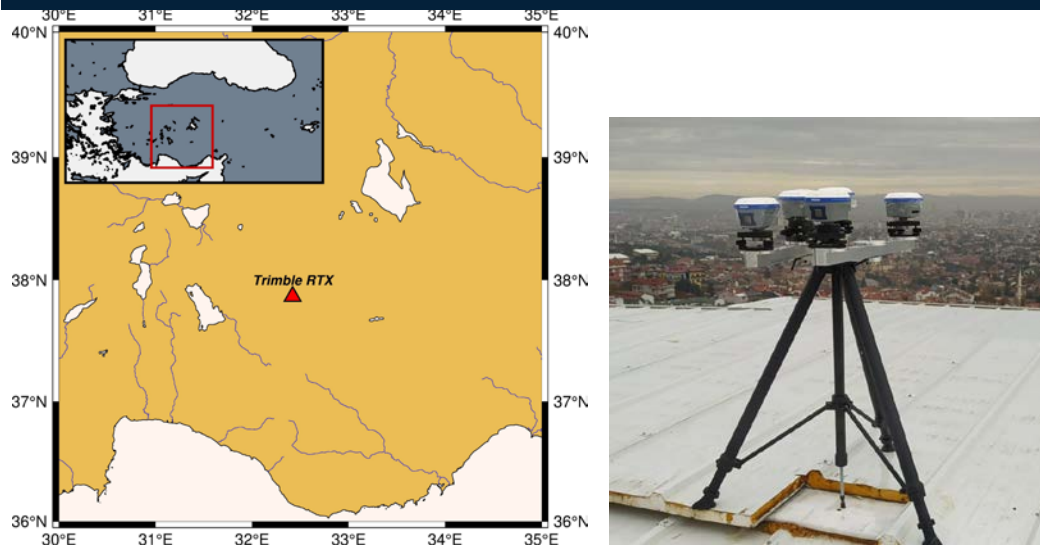


Figure 1. The location of RTX field test (left) and GNSS receivers during the measurement (right)

CHC I90 receivers were set to track GPS-only (G), GPS+GLONASS (GR), GPS+Galileo (GE), GPS+GLONASS+Galileo (GRE), GPS+GLONASS+Galileo+Beidou (GREC) satellites with  $10^\circ$  cutoff angle. After the convergence, 9-hours of RTX measurements were collected at 1 second epoch interval, in November 2020.

### 3. RESULTS

The standard deviations (STD) of G, GR, GE, and GREC modes were calculated. The statistical analysis conducted using all solutions without outlier removal. For a proper comparison, the solutions of different modes were aligned considering mutual epochs. The standard deviations of 9-hour measurements and is depicted in Table 2.

Table 2. The standard deviations

GNSS	STD (cm)		
	X	Y	Z
G	2.3	2.0	2.4
GR	1.9	1.7	1.8
GE	1.5	1.2	1.3
GRE	1.6	1.4	1.6
GREC	1.7	1.6	1.7

The GPS-only mode showed a precision of 2.3 cm, 2.0 cm and 2.4 cm for X, Y, and Z components. The multi-GNSS combinations were significantly improved the repeatability compared to GPS-only mode, particularly on the vertical component. The GR, GRE, and GREC modes showed similar results in horizontal component. GE mode is slightly better than other combinations, particularly at the vertical component. The coordinate time series are shown in the Figure 2 according to mean of 9-hour measurements for five different GNSS modes.

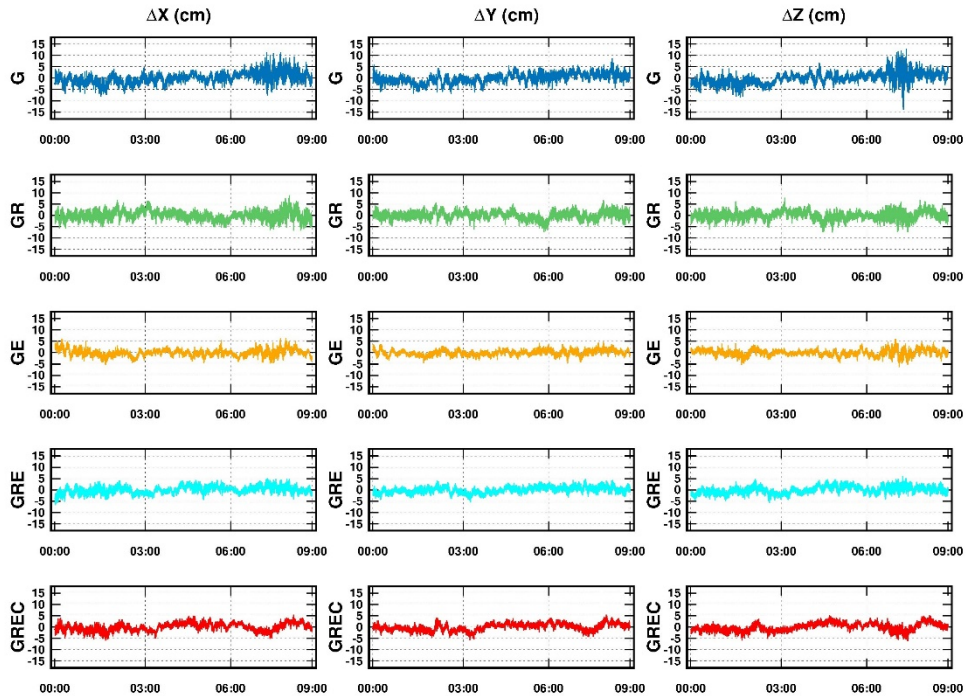


*Figure 2. Coordinate time series for G, GR, GE, GRE, and GREC modes*

As seen in Figure 1, the coordinate differences are not much than 15.0 cm for all GNSS modes. Also, a precision loss is rather seen in GPS-only mode about 07:00 UTC. The source of this precision degradation is more likely the low number of GPS satellites weakened the PPP performance. The multi-GNSS combinations are clearly reduced the precision lost in the X and Z components of GPS-only mode about 07:00 UTC.

Besides, the contribution of multi-GNSS combinations to GPS-only mode is computed through improvement percentage on STDs. The improvement percentages of GR, GE, GRE and GREC modes with respect to GPS-only mode are shown in Figure 3.

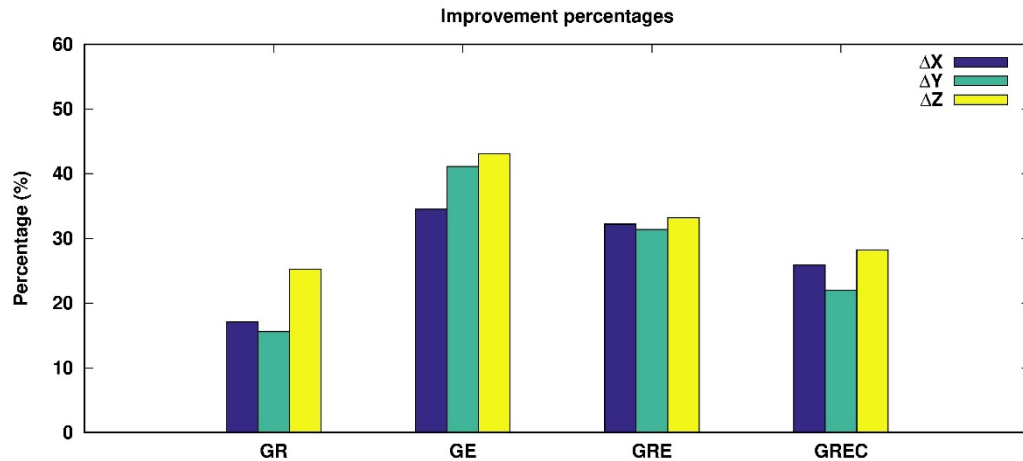


Figure 3. Improvement percentages of multi-GNSS modes with respect to GPS-only mode

The multi-GNSS combinations provided at least 15.6% in three dimensional coordinates. The GE mode produced the maximum improvement on the vertical component by 43.1%. Although GR mode is contributed to GPS-only mode, the contribution level is less than GE, GRE, and GREC modes. That can be explained with the noisier code observations of GLONASS satellites [19]. In terms of repeatability, the improvement of GRE is slightly better than GREC with respect to GPS-only solutions. Due to the BDS-2 satellites are regional, it did not significantly affect the PPP model.

#### 4. CONCLUSIONS

This paper investigates the latest performance of RTX correction service which is the one of the most recent satellite based precise positioning system. The results of this experimental study demonstrated that multi-GNSS combinations clearly improved the performance of RTX service. The GREC mode was produced a standard deviation of 1.7/1.6 and 1.7 cm on the X, Y, and Z components, respectively. The GPS+Galileo provided slightly better repeatability when compared to others. Also, the BDS-2 satellites did not significantly affect the multi-GNSS RTX. The RTX service can be used an alternative to NRTK method which requires an active internet connection to retrieve network corrections. As result, the RTX service has become a well option for satellite based positioning with the integration of multi-GNSS.

#### ACKNOWLEDGMENT

The authors thank to CHC Turkey and Ufuk R. Ozbey for their technical supports during the field experiment. This work is supported by Necmettin Erbakan University Scientific Research Projects Committee, with the project number 201219010.

#### REFERENCES

- [1]. Y. Feng, and J. Wang, "GPS RTK Performance Characteristics and Analysis," *Journal of Global Positioning Systems*, vol. 7 (1), 1–18, 2008.
- [2]. J. Wang, "Stochastic Modeling for Real-Time Kinematic GPS/GLONASS Positioning," *Navigation-Journal of the Institute of Navigation*, vol. 46 (4), pp. 297–305, 1999.
- [3]. C. Rizos, and S. Han, "Reference station network based RTK systems-concepts and progress," *Wuhan University Journal of Natural Sciences*, vol. 8, pp. 566–574, 2003.
- [4]. S. Ogutcu, and I. Kalayci, "Investigation of network-based RTK techniques: a case study in urban area," *Arabian Journal of Geosciences*, vol. 9, 199, 2016.
- [5]. J. F. Zumberge, M. B. Hefflin, D. C. Jefferson, M. M. Watkins, and F. H. Webb "Precise point positioning for the efficient and robust analysis of GPS data from large networks," *Journal of Geophysical Research*, vol. 102 (B3), pp. 5005–5017, 1997.

- [6]. J. Kouba, and P. Héroux, "Precise point positioning using IGS orbit and clock products," *GPS Solutions*, vol. 5 (2), pp. 12–28, 2001.
- [7]. M. Elsobeiey, and S. Al-Harbi, "Performance of real-time Precise Point Positioning using IGS real-time service," *GPS Solution*, vol. 20, pp. 565–571, 2016.
- [8]. (2021) The BKG Ntrip Client (BNC) website. [Online]. Available: <https://igs.bkg.bund.de/ntrip/bnc>
- [9]. Z. Wang, Z. Li, L. Wang, X. Wang, H. Yuan, "Assessment of multiple GNSS real-time SSR products from different analysis centers," *ISPRS International Journal of Geo-Information*, vol. 7 (3), 85, 2018.
- [10]. S. Alcaay, and M. Turgut, "Evaluation of the positioning performance of multi-GNSS RT-PPP method," *Arabian Journal of Geosciences*, vol. 14, 155, 2021.
- [11]. N. Abdi, A. A. Ardalan, R. Karimi, and M. H. Rezvani, "Performance assessment of multi-GNSS real-time PPP over Iran," *Advances in Space Research*, vol. 59 (12), pp. 2870–2879, 2017.
- [12]. X. Tang, G. W. Roberts, X. Li, and C. M. Hancock, "Real-time kinematic PPP GPS for structure monitoring applied on the Severn Suspension Bridge, UK," *Advances in Space Research*, vol. 60 (5), pp. 925–937, 2017.
- [13]. F. Zhang, M. Brandl, X. Chen, R. Drescher, M. Glocker, H. Landau, ... and U. Weinbach, "Trimble CenterPoint RTX—A First Study on Supporting Galileo," in *Proceedings of the European Navigation Conference 2013*, pp. 23–25.
- [14]. H. T. Berglund, F. Blume, D. Mencin, and L. H. Estey, "Comparison of Real-Time Kinematic GNSS Positioning Techniques Using Moving and Stationary Antennas," in *American Geophysical Union, Fall Meeting 2013*, paper G53B-0923.
- [15]. A. Ochałek, W. Niewiem, E. Puniach, P. Ćwiąkała, "Accuracy evaluation of real-time GNSS precision positioning with RTX Trimble technology," *Civil and Environmental Engineering Reports*, vol. 28 (4), pp. 49–61, 2018.
- [16]. V. Ilci, "Accuracy comparison of real-time GNSS positioning solutions: Case study of Mid-North Anatolia," *Measurement*, vol. 142, pp. 40–47, 2019.
- [17]. R. M. Alkan, S. Erol, V. Ilci, I. M. Ozulu, "Comparative analysis of real-time kinematic and PPP techniques in dynamic environment," *Measurement*, vol. 163, 107995, 2020.
- [18]. (2021) CHCNAV i90 PRO IMU-RTK GNSS RECEIVER. [Online]. Available: [https://www.chcnav.com/uploads/i90%20pro\\_DS\\_EN.pdf](https://www.chcnav.com/uploads/i90%20pro_DS_EN.pdf)
- [19]. Cai, C. He, R. Santerre, L. Pan, X. Cui, and J. Zhu, "A comparative analysis of measurement noise and multipath for four constellations: GPS, BeiDou, GLONASS and Galileo," *Survey review*, vol. 48 (349), pp. 287–295, 2016.

## BIOGRAPHY

Omer Faruk Atiz received his B.Sc. degree in Geomatics Engineering from Selcuk University (Turkey). He is currently an M.Sc. candidate at the Geomatics Engineering Department of Necmettin Erbakan University (Turkey). His studies focus on GNSS precise positioning.

Abbas Qader Shakor M.Sc. student at Department of Geomatics Engineering of Necmettin Erbakan University. His research interests include PPP monitoring technologies.

Sermet Ogutcu is an Associate Professor at Necmettin Erbakan University, Geomatics Engineering Department. His research interest includes PPP, Network-Based RTK techniques.

Salih Alcaay is an Associate Professor at Necmettin Erbakan University, Geomatics Engineering Department. He has received his PhD from Selcuk University. His research interest includes GNSS-based positioning, deformation analysis, and ionosphere modelling.

# A New Filtering and Analysis Approach for Poor Quality GNSS Data

Huseyin Pehlivan<sup>1</sup>, Baris Karadeniz<sup>2</sup>

---

## Abstract

*Due to its globally continuous and instantaneous geolocation capability, in many areas from scientific and engineering studies to mobile applications we use in our daily lives, satellite-based positioning systems offer a unique alternative. Structural health monitoring, determination of large and small scale deformations, vehicle tracking and time-dependent location changes in many mobile applications are obtained by GNSS. However, time-series recorded by GNSS with a high sampling rate; includes common error sources such as sudden signal loss, extraneous or outlying data points, speed drifting, and signal white noise. The fact that all or some of these error sources are effective weakens the quality of recorded data. The decrease in data quality makes it impossible to draw important conclusions. Some techniques should be used to clear this data from errors and to draw meaningful results. In this study, raw GPS data recorded with a 20 Hz sampling rate in an environment with abundant error sources were parsed into sub-signals using Fast Fourier Transform (FFT) after applying a series of filtering processes. Thus, the dominant signals representing significant periodic components were determined, regardless of the nonsense sub-signals corresponding to the erroneous measurements. Then, the signal was reconstructed using Inverse Fourier Transform with the obtained dominant frequency values, and thus, the measurement values were separated from the defective components and an interpretable real and clean signal is obtained. Graphical comparisons of raw and filtered data are presented and the effect of the proposed filtration process on raw data was explained by statistical analysis.*

**Keywords:** GNSS data, filtering, Fast Fourier transform, time series.

---

## 1. INTRODUCTION

GNSS (Global Navigation Satellite System) is a unique measurement method for time-dependent position changes needed in scientific and engineering studies. The most common and popular GNSS technique is GPS (Global Positioning System). Thanks to its high speed and accuracy in data sampling, it is the first method that comes to mind in many studies that require position determination as a function of time and examination of position changes due to velocity. Due to this feature is used in many areas such as structural health monitoring, determination of large and small-scale deformations, vehicle tracking, and mobile applications that we use in our daily lives.

The design of the measurement system and the analysis of the measured data are the main research topics in structural health monitoring (SHM). In SHM measurements, the main purpose is to model the movements of the structure and determine the displacement changes. For this reason, sensors used in measuring systems and data quality are very important. High-quality data may not always be obtained due to the measurement area and structural features ([1]). Although undesirable, there may be situations where significant position changes must be determined from low-quality GNSS data. Some previous studies have included calculations of displacements from noisy GNSS data ([2]-[6]). There are also studies in which some filtering methods are used to calculate quasi-static displacement components from low-quality, noise-containing GNSS time series ([3], [4]).

GNSS data contains a mix of different levels of low, medium and high-frequency noise. In general, it contains many sources of random error such as SA interference error, multi-path effect error, the deviation of antenna

---

<sup>1</sup> Corresponding author: Gebze Technical University, Department of Geomatics Engineering, 41400, Gebze/Kocaeli, Turkey. [hpehlivan@gtu.edu.tr](mailto:hpehlivan@gtu.edu.tr)

<sup>2</sup> Gebze Technical University, Department of Geomatics Engineering, 41400, Gebze/Kocaeli, Turkey, [b.karadeniz@gtu.edu.tr](mailto:b.karadeniz@gtu.edu.tr)



phase center for GPS receiver ([15], [16]). Poor quality GNSS data means data that is highly affected by common error sources originating from this system. To improve the quality of weak GNSS data, an ideal filtering method should be used while maintaining the integrity of the raw data source. Here, the ideal filtering method aims to minimize the effects of GPS data errors such as sudden signal loss, data spiking, signal white noise and zero speed drift. This means removing or replacing incorrect data points while minimizing the total amount of data being changed ([1], [8]-[16]).

This study aimed to find significant periodicities from weak SHM location data with significant error sources recorded with a 20 Hz sampling interval for 24 hours in poor quality. For this purpose, a new filtering and analysis approach has been tried with this sample GPS data recorded in poor quality. All operations were carried out using cyclical codes that proceed linearly in the Matlab program. Sample data recorded as a function of time were analyzed in terms of time and frequency. While statistical equations are used in time domain analysis, some complex transformation equations were used in frequency domain analysis. First of all, in the series examined in the time domain, coarse errors are filtered out, problems in the jumps in data and sampling interval are eliminated. After that, the time-dimensional filtered and prepared data was decomposed into sub-signals by transforming it into the frequency domain using Fast Fourier Transform (FFT) ([17]). Thus, the signal's frequency and amplitude periodic components were determined, regardless of the less repetitive signals, and the dominant sub-signals that repeat frequently. And as a result, when the signal was reconstructed using Inverse Fourier Transform (IFT) with the dominant sub-signals obtained, a filtered and interpretable clean signal was obtained. Thus, changes in position in sampling interval and measurement sensitivity were modelled depending on the time and variables of the measurement.

## 2. A NEW FILTRATION APPROACH FOR GNSS POSITION DATA

The measurement process involves collecting data with a certain systematic for the transition to the real world, which we accept as the analog world, and the digital world, which we accept as a model or sample of it. While there are multiple methods of collecting data, the issues are generally the same. Sensors used, sampling interval, sensitivity, resolution, measuring time, measuring environment etc. are fundamental issues such as affect measurement accuracy.

In accordance with the purpose of the measurement, the resolution and measurement time can be determined by considering the sensor used. However, errors and noise originating from the measurement environment are parameters that cannot be predicted before measurement. Therefore, they are issues that can be resolved in post-measurement analysis and evaluation. Here, measurement values collected from the real world can be recorded as distorted signals that are unpredictable and difficult to model. However, this does not prevent us from extracting meaningful information from the data. The only solution used in these cases is filtering.

Discrete-time series recorded in GPS observations generally include periodic and stochastic components as well as error components such as noise ([15]-[17]). Determining the periodic components that model the meaningful displacement changes, which is the purpose of the measurement, is only possible after separating the stochastic and noise components. Raw data, which includes many error factors such as the place where the measurement is made and the atmospheric conditions during the observation, can be evaluated and converted into meaningful signals after the processes we call filtering. The filtering process generally requires us to decide which range of data in the signal should be suppressed or decomposed. As of the general structure of GNSS data, the measurement sensitivity and positioning accuracy vary depending on the measurement method we apply and the characteristics of the receiver we use. In this sense, it helps us to determine the filter parameters to be applied. The analysis of poor quality recorded GNSS data can be performed in two ways, in time and frequency dimensions, respectively.

### *Analysis Process of GNSS Data in Time Dimension*

The GPS series contains random and coarse erroneous measurements resulting from the general nature of the measurement method. These errors need to be eliminated in the time dimension before analysis with time series. The following sequence has been followed for the filtration process of the GPS data in the time dimension.

- a) Extracting abnormal data from raw data (thresholding)
- b) Empty data points are interpolated considering the closest datasets (interpolation)
- c) Filtering to protect spikes and reduce noise (Smoothing)
- d) Re-sampling, taking into account the measurement time and sampling interval

### *Analysis Process of GNSS Data in Frequency Dimension*

After the signal is examined in the time dimension, it is converted to the complex plane by FFT. That is to the frequency dimension. In this environment, all amplitude values that make up the signal are determined by frequency and phase values. To select meaningful sub-signals with certain frequencies and to determine the dominant modes;

- 1<sup>st</sup> step: Fourier Transform
- 2<sup>nd</sup> step: Determination of Dominant Frequency Value
- 3<sup>rd</sup> step: Inverse Fourier Transform
- 4<sup>th</sup> step: Cleared Location Data

## 2.1. Analysis Process of GNSS Data in Time Dimension

### a) Extraction of abnormal data - thresholding

Real-time raw GPS data is a complex signal that includes noise at different frequencies and different amplitudes. A general threshold applied to such a signal cuts off a significant portion of the periods below the threshold. Therefore, a localized thresholding design ([12], [17]–[20]) that includes a combination of fixed, semi-soft and soft threshold rules has proven necessary for non-stationary signals.

In the first step of the filtration process, abnormal erroneous data points found in the data set are removed and replaced with interpolated data. In order to achieve this, each value in each value set in the sample data is separately compared with the determined threshold value. If the data point is found to be outside the selected limits, it replaces it with the value derived from a cubic spline interpolation drawn from neighbouring data [1] (Figure 1(a)).

### b) Interpolation

As an additional step in the interpolation process, these data points are valued by skipping from fixed-range data points to facilitate operations in the frequency domain, or by interpolation from nearest neighbour data in case of null data. Filling in blank data with interpolation provides flexibility during data processing and improves the quality of results.

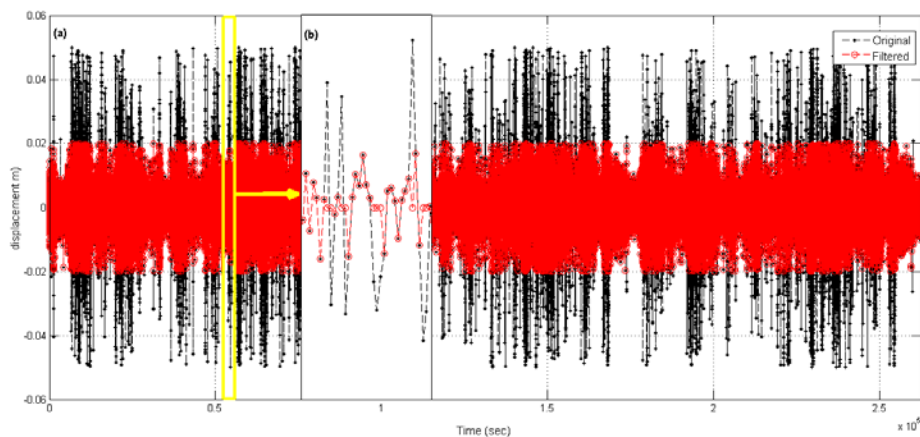


Figure 1. (a) Extraction of abnormal data (thresholding) for GPS data (b) A snapshot of the filtering process

### c) Filtering (Smoothing Filters)

The main purpose of the filtering process is to suppress the components other than the signal to be measured. If the period and frequency of the magnitude we want to measure can be predicted, we determine the type of measuring instrument, sampling interval and measuring time accordingly. However, in this range, unwanted noise and components can disrupt the recorded signal (Figure 1(b)). In this case, we try to purify the

measurement results from errors by using many filters such as low or high band pass according to the values we want to measure.

In line with this general approach, we need to apply a low-pass smoothing filter to de-noise the GNSS data and determine the quasi-static displacement of the structure. For this purpose, we can use a moving average (MA) filter with an appropriate window size to separate the series from noise and reveal its quasi-static components ([3]).

We can say that most of the applications related to smoothing are in a Low-Pass filter structure. Frequently used today; Additive, Savitzky–Golay, Ramer–Douglas–Peucker, Moving, Kalman etc. There are smoothing algorithms such as Among them, which is in the FIR filter structure and gives better results for GNSS data; We can briefly explain the features of moving, laplace, triangular algorithms as follows;

**Moving Averager:** The moving averager takes a certain number of samples and averages it according to the size of the filter with a simple FIFO (first in first out) structure. The 3D mathematical expression of this filter is as follows.

$$y(n) = \frac{x(n-1)+x(n)+x(n+1)}{3} \quad (1)$$

**Laplace Averager:** Unlike moving average, Laplace Averager does not use the filter structure in a FIFO fashion. For example, a laplace mean filter with a filter size of 10 first collects the first 10 data and divides it by 10 to obtain the first filtered element. While the next 10 samples are waiting, the previous filtered value remains constant. Although this gives us difficulty in not following the real signal, it has an advantage over the others in terms of simplicity.

**Triangular Averager:** In the triangular average, the same FIFO logic in the moving average is used. Unlike the moving average, the values measured in the triangular average are multiplied by the coefficients that will form a triangular form according to the filter size and divided by the sum of these coefficients. The mathematical expression for the 5-dimensional triangular filter is presented below.

$$y(n) = \frac{x(n-2)+2x(n-1)+3x(n)+2x(n+1)+x(n+2)}{9} \quad (2)$$

The success of the three filters summarized here depends on the short processing time proportional to the filter size and the good filtering process at short filter size.

#### d) *Re-Sampling*

First of all, GPS time series were resampled with 1-second sampling interval in order to be able to evaluate all observations holistically in the time domain and to increase the processing speed.

## 2.2. Analysis Process of GNSS Data in Frequency Dimension

In order to reach the meaningful components we want in the frequency dimension, the sampling interval of the signal should be equal, free from errors and noises. Therefore, the better we filter in the time domain, the better results we can get from the analysis in the frequency domain. The frequency spectrum of a signal shows the different frequencies embedded in those signals. Conversion of GNSS location data into the frequency domain for the analysis of dynamic properties in structural traces allows us to access all sub-signals in the frequency spectrum.

The Fourier Transform (FT) is the most widely used method in the transition to the frequency dimension, that is, to the complex plane. However, FT also has some handicaps ([12], [18], [21]). In general, signals are expressed as a function of time and as time-amplitude signals before being converted. In most cases, the most useful information will be covered by the time information of the signal. With the FT transform, the sub-signals are expressed using sine and cosine.

FT is not a suitable method for analyzing non-stationary signals with various time spectra. Also, the sine and cosine functions consisting of the FT basis function have difficulty in translating discontinuous signals and sharp spikes. In addition, it has been seen that it is not appropriate to express time and frequency at the same time. To make up for this shortcoming, Short Time Fourier Transform (STFT) is applied to analyze the signals. STFT represents a midpoint between time and frequency based evaluations of signals ([15], [16]). Using this

method, information can be obtained about when and where certain events occurred. Here the signals are divided into small units; these signals are considered "stationary" and a window function is used to obtain these values. STFT is an extended version of FT that uses a window function. However, STFT can only provide limited sensitivity determined by the size of the window. In other words, the transformation can give information about time and frequency simultaneously, but its resolution is fixed.

### 3. AN EXAMPLE OF THE LOW-QUALITY DATA ANALYSIS

As an example, the GPS signal recorded for 24 hours with a sampling interval of 20 Hz was used (Figure 2). This signal is known to be a poor quality recording containing random noise, but it is known to contain predicted displacements.

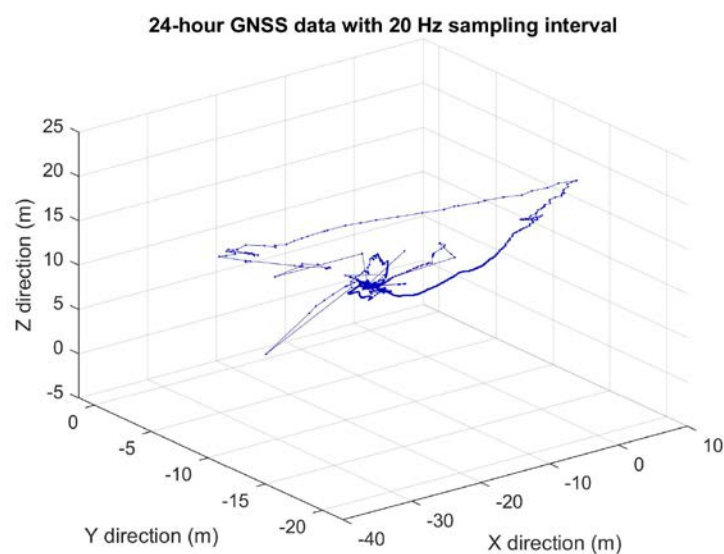


Figure 2. 3D raw GNSS data

#### 3.1. De-noising of GNSS Data with Some Filtration techniques and Fourier Transformation

Structural displacement variations can be determined for three axes (X, Y, Z). In this study, since no significant vertical movement is expected, displacement was determined only in X, Y series. The time series were examined in time and frequency dimensions, respectively, to remove noise and determine displacement changes.

**In Time Dimension:** The steps of examining the GPS data in time dimension;

In 1st step: A threshold value with 2 cm amplitude was applied to the GPS data containing noise and abnormal jumps with different amplitudes. Thus, abnormal data in the data set were removed.

In 2nd step: The empty elements in the time series were filled by interpolating with the nearest data elements. Thus, errors such as skipping and breaking during the measurement were eliminated.

In 3rd step: Considering the filter size and noise suppression rates, it has been seen that the triangle averager performs better than the others. As the filter size grows, both the moving and triangle averager outputs get closer to the signal we want to measure. The Laplace averager, on the other hand, becomes a stepped structure as the size grows and moves away from the signal we want to read. Each filter adds a phase difference to the system as well as the size of the filter. While designing the system in the real environment, it should be examined whether this phase difference affects the system and the filter should be designed accordingly. In our sample signal used in this study; Two filter sizes, 60-300 units, were applied.

In the 4th step: The sample data recorded with a sampling interval of 0.05 seconds, which was sampled for 24 hours, was resampled with a sampling interval of 1 second, taking into account the measurement time and sampling interval.

**In Frequency Dimension:** Spectrum analysis method was applied to the sample signals filtered with 60 and 300 seconds window sizes.

1st step: First, the series filtered in the time domain were separated into sub-signals by SFFT transform. It was seen that the operations performed by selecting the appropriate filtering parameters helped to reveal the dominant displacement frequencies hidden in the signal.

2nd step: All frequency values and corresponding amplitude values were calculated and their amplitudes were ordered from largest to smallest. The frequency values  $f_1$ ,  $f_2$  and  $f_3$  selected for the analyzed sample signals and the corresponding amplitude period, phase and angular frequency values are given in Tables 1,2,3 and 4, respectively.

3rd step: By choosing the first 3 frequency values with the highest amplitude, the real displacement signal was reconstructed by inverse FFT process. The standard deviation values of each reconstructed X, Y signal are presented in Table 5. It was observed that the Root Mean Square Error (RMSE) values of the reconstructed Y-direction series were lower than those of the X-direction series, which were reconstructed.

And 4th step: X and Y signals generated with significant frequency values were plotted as 2D position change time-dependent position change (Figure 3).

Table 6. Dominant frequencies selected as a result of spectrum analysis in the X-signal with a 60 second sampling interval.

Frq. No	Frequencies (Hz)	Period (sec.)	Amplitudes (m)	Phases (Deg.)	Angular Freq. (Hz)
$f_1$	0.00001157	86400.00	0.0482	-179.96455	0.00007272
$f_2$	0.00013889	7200.00	0.0020	144.75748	0.00087266
$f_3$	0.00038194	2618.18	0.0017	55.39479	0.00239983

Table 2. Dominant frequencies selected as a result of spectrum analysis in the Y-signal with a 60 second sampling interval.

No	Frequencies (Hz)	Period (sec.)	Amplitudes (m)	Phases (Deg.)	Angular Freq. (Hz)
$f_1$	0.00001157	86400.00	0.0739	-179.53211	0.00007272
$f_2$	0.00010417	9600.00	0.0010	-169.30866	0.00065450
$f_3$	0.00018519	5400.00	0.0009	-121.37421	0.00116355

Table 3. Dominant frequencies selected as a result of spectrum analysis in the X-signal with a 300 second sampling interval.

No	Frequencies (Hz)	Period (sec.)	Amplitudes (m)	Phases (Deg.)	Angular Freq. (Hz)
$f_1$	0.00001157	86400.00	0.0482	-179.96457	0.00007272
$f_2$	0.00013889	7200.00	0.0019	144.79109	0.00087266
$f_3$	0.00038194	2618.18	0.0016	-55.44913	0.00239983

Table 4. Dominant frequencies selected as a result of spectrum analysis in the Y-signal with a 300 second sampling interval.

No	Frequencies (Hz)	Period (Sec.)	Amplitudes (m)	Phases (Deg.)	Angular Freq. (Hz)
$f_1$	0.00001157	86400.00	0.0739	-179.53218	0.00007272
$f_2$	0.00010417	9600.00	0.0010	-169.35240	0.00065450
$f_3$	0.00018519	5400.00	0.0009	121.50358	0.00116355

Table 5. Re-constructed signals with selected frequencies

Reconstructed Signal	Sampling Rate (Sec.)	Selected Frequencies	RMS (m)
X-direction	60	$f_1, f_2, f_3$	0.01058
Y- direction	60	$f_1, f_2, f_3$	0.00729
X- direction	300	$f_1, f_2, f_3$	0.00559
Y- direction	300	$f_1, f_2, f_3$	0.00385

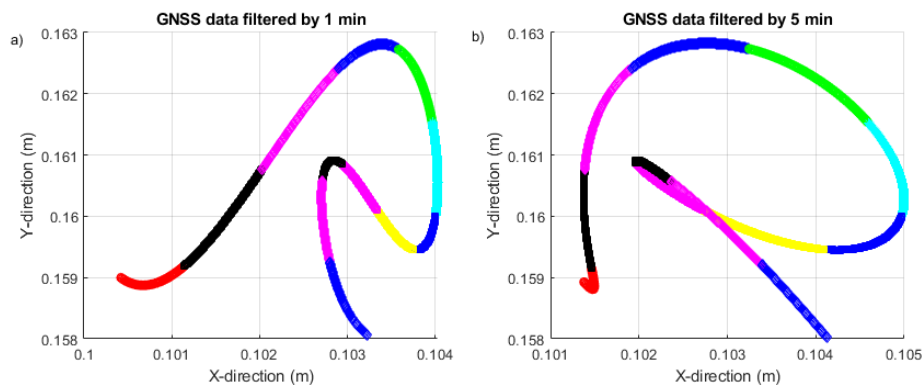


Figure 3. Filtered signals re-constructed with IFFT

In Figure 3a, 60-second sample data were reconstructed with IFFT. In Figure 3b, 300-second sample data were reconstructed with IFFT. When both new signals are plotted in 2D in the XY plane, they appear as in Figure 3. Each colour corresponds to a two-hour position change. Although it looks different in shape, the total displacement amounts are approximately equal.  $D_x=3.60$  mm,  $D_y=4.76$  mm in Figure 3a,  $D_x=3.62$  mm,  $D_y=4.81$  mm in Figure 3b.

#### 4. CONCLUSIONS

It is possible to show the structural displacements in a three-axis coordinate system (X, Y, Z). However, since GNSS series obtained with poor quality contain random noise and errors that are very difficult to model, such as multipath, etc., it is not possible to see meaningful displacements. A raw GNSS data given in Figure 2 is seen as a meaningless point cloud due to the noise and erroneous data it contains. In such cases, detailed filtering is required to debug GPS data and calculate meaningful displacement vectors.

Spectrum analysis can be applied to the filtered signal in the time dimension to reveal the meaningful components from the GNSS data recorded at high frequency. Parameters such as signal length, window size, amount of overlap and data rate are important in spectrum analysis. Structural vibrations hidden in the GNSS data can be determined or removed with the most appropriate parameters. Based on this theory, a filtration and spectral analysis algorithm are proposed for low-quality GNSS data in this study. An eight-step algorithm is presented, with these being 4 in the time domain and 4 in the frequency domain. The coarse error and noise are

relatively separated from the series that is first filtered in the time domain. Operations performed by selecting the appropriate filtering parameters reveal the dominant displacement frequencies hidden in the signal. It is then separated into sub-signals by FFT. By choosing frequencies with dominant displacement values (ie dominant modal frequencies) from here, the true displacement signal can be decomposed by inverse FFT operation.

Using these theoretical processing steps, low-quality GNSS data recorded with a sampling frequency of 20 Hz was analyzed (Fig. 2); First of all, The data were examined in the time dimension and more prominent and meaningful components were revealed in the frequency dimension. In the time dimension, it was ensured that abnormal data were extracted with an appropriate threshold value (2 centimetres), blank and omitted data were completed as a function of time with the interpolation process and resampled with an appropriate sampling interval (60 and 300 seconds). After that, three smoothing filters were tried for low-pass filtering. As a result of these trials; Considering the filter size and noise suppression rates, it was seen that the triangle averager gave a better result than the others. Thus, the XY series that we filtered in time dimension were converted into frequency dimensions with SFFT. Significant modal frequency values of time series sampled with 60 and 300 seconds are presented in tables 1, 2, 3 and 4. When the signals were reconstructed with IFFT with the first 3 frequency values found to be significant, 4 different time series were obtained in different sampling intervals, presented in Table 5. When the calculated filtered series is plotted in the XY plane; Approximately equal displacement magnitudes were calculated from the 60 and 300-second sample series (Figure 3).

However, despite such a detailed filtering process, we may not always be able to calculate the actual displacements. Namely; Due to the nature of the structural oscillations and the observation conditions, the noise content such as the structural displacement frequencies and multipath may be at the same level. In this case, the spectrum analysis approach may not be applicable in the heavily polluted signal with a noise similar in displacement size. Identifying significant displacement components from a signal containing a wide variety of noise components is a difficult task in this sense. The use of hybrid measurement systems that assist GNSS in structural displacement measurements can be helpful in solving noisy data.

## REFERENCES

- [1]. H. Pehlivan. "Frequency analysis of GPS data for structural health monitoring observations", *Structural Engineering and Mechanics*, 66(2), pp. 185-193, 2018.
- [2]. B. Rosado, J. Ramirez-Zelaya, P. Barba, A. de Gil, M. Berrocoso. "Comparative Analysis of Non-Linear GNSS Geodetic Time Series Filtering Techniques: El Hierro Volcanic Process (2010–2014)". *Eng. Proc.*, 5, 23, 2021.
- [3]. F. Moschas, S. Stiros. "Noise characteristics of high-frequency, short-duration GPS records from analysis of identical, collocated instruments". *Meas. J. Int. Meas. Confed.* 46, pp. 1488–1506, 2013.
- [4]. V. Gikas. "Ambient vibration monitoring of slender structures by microwave interferometer remote sensing". *J. Appl. Geod.* 6, 167–176, 2012.
- [5]. M. R. Kaloop, E Elbeltagi, J. W. Hu and A. Elrefai. "Recent advances of structures monitoring and evaluation using GPS-time series monitoring systems: A review", *ISPRS International Journal of Geo-Information*, 6 (12), 382, Sep. 2017.
- [6]. X. Li, C. Rizos, L. Ge and E. Ambikairajah. "Application of 3D Time-frequency Analysis in Monitoring Full-scale Structural Response", *Journal of Geospatial Eng.*, 8(1-2), 41-51, 2006.
- [7]. H. Pehlivan. The Investigation of Dynamic Behaviors in Structures with Real-Time Kinematic GPS, *PhD Thesis*. Yildiz Technical University, Istanbul, Turkiye, 2009.
- [8]. L. Ge, S. Han, C. Rizos. "Multipath mitigation using an adaptive filter", *GPS Solutions*, 4(2), 19-30, 2000.
- [9]. J. S. Walker. "Fast Fourier Transformation", 2nd ed., CRC Press, ISBN 0-8493-7163-5, 447 pp., 1996.
- [10]. L. Xu, J. Guo and J. J. Jiang. "Time Frequency Analysis of a Suspension Bridge Based on GPS". *Journal of Sound and Vibration*, 254(1), pp. 105-116, Jun. 2002.
- [11]. H. Pehlivan and H. F. Bayata. "Usability of inclinometers as a complementary measurement tool in structural monitoring". *Structural Engineering and Mechanics*, 58(6), pp. 1077-1085, 2016.
- [12]. O. Ogundipe, J. K. Lee, G. W. Roberts. "Wavelet De-noising of GNSS Based Bridge Health Monitoring Data". *J. Appl. Geod.*, 8, 273–281, Dec. 2014.
- [13]. X. Zhang, F. Zhu, X. Tao and R. Duan. "New optimal smoothing scheme for improving relative and absolute accuracy of tightly coupled GNSS/SINS integration". *Gps Solutions*, 21(3), 861- 872, 2017.
- [14]. H. Pehlivan, O. Aydin, E. Gulal, E. Bilgili. "Determining the Behavior of High-Rise Structures with Geodetic Hybrid Sensors". *Geomatic, Natural Hazards and Risk*. 2015-6(8), pp. 702-717, Published online: 05 Nov 2013.
- [15]. M. R. Kaloop, D. Kim. "De-noising of GPS structural monitoring observation error using wavelet analysis". *Geomat. Nat. Hazards Risk*, 7, 804–825, 2016.
- [16]. J. F. James. *A Student's Guide to Fourier Transforms with Applications in Physics and Engineering*, Cambridge University Press, ISBN 0-521 46298, 2,12,113. pp., 1995.

- [17]. R. Rao, C. C. Li, Y. H. Huang, X. X. Zhen, and L. Z. Wu, "Method for structural frequency extraction from GNSS displacement monitoring signals," *Journal of Testing and Evaluation*., vol. 49, no. 3, pp. 2026\_2043, 2019.
- [18]. M. R. Kaloop, E. Elbeltagi, M. T. Elnabwy. "Bridge Monitoring with Wavelet Principal Component and Spectrum Analysis Based on GPS Measurements: Case Study of the Mansoura Bridge in Egypt". *Journal of Performance of Constructed Facilities*, 29(3), pp. 04014071, 2015.
- [19]. P. Stoica, R. L. Moses. *Spectral analysis of signals*, 2005.
- [20]. A. Bruce, H. Y. Gao. "Wave shrink: shrinkage functions and thresholds", Technical report, *StatSci Division*, MathSoft, Inc., 1995.
- [21]. M. R. Kaloop, H. Li. "Sensitivity and analysis GPS signals based bridge damage using GPS observations and wavelet transform". *Measurement*, 44(5), 927-937, 2011.



# Experimental Results and Analysis of Structural Monitoring Using GNSS and Other Positioning Techniques

Huseyin Pehlivan<sup>1</sup>

---

## Abstract

*Advances in urbanization and construction technology have made buildings increasingly larger and ostentatious. These large engineering structures that push the limits of engineering and technology, it is become more affected by natural events such as wind, temperature, earthquake etc. Therefore, the construction of such structures and subsequent determination of oscillation amplitudes and spectral characteristics have become an important issue needed. In the scope of this study; GNSS receivers, electronic inclinometer, weather station and total station and reflectors for ground observations are mounted on a tower (in 165 m heights). The data collected simultaneously using this measurements instruments were analyzed and the results were evaluated. It has been observed that the displacement changes obtained from different measuring instruments are compatible with each other and are sufficient to determine this dominant oscillation mode. The movement amplitude and spectral characteristics of the structure representing the structural movements at the time of measurement were examined. The results obtained from three different measuring instruments; showed that the structure is very rigid and makes a dominant movement with a period of 24 hours. This dominant movement of the tower, which lasted for a full day, has been explained by the effect of the temperature change caused by the effect of the sun.*

**Keywords:** Structural displacement, GNSS, Tiltmeter, Total station, modal frequency.

---

## 1. INTRODUCTION

As a part of modern life, large buildings have become an indispensable part of human life in terms of their functions and services. Although these structures have a limited life span, they also contain structural health problems that may arise for a long or short period of time due to the effects of internal and external forces. The buildings, especially wind, temperature, earthquake, etc., are inevitably affected by natural events such as vibration and oscillation. For these reasons, it would be correct to consider the safety and health of buildings synonymous with human safety and health. Monitoring the oscillation amplitudes and spectral characteristics during and after the construction of large buildings is an important issue in terms of building health and public safety. With Structural Health Monitoring (SHM) studies, building behaviour can be monitored, ensuring the safety of gigantic buildings, extending their service life, and taking preventive measures to reduce the damage they may face in natural disasters ([1]-[4]).

Different measurement systems can be considered in SHM studies, taking into account the characteristics of the structure to be followed, the measurement cost and the expected accuracy. Two important parameters are decisive in this regard: The first important parameter that determines the character of the measurement system is whether it is a long or short-term measurement system, depending on the monitoring period. Short-term monitoring systems are used to determine whether a structure is healthy or damaged and to check its condition. long-term monitoring system; It is used to determine the structure's behaviour and take the necessary precautions during its standing. ([3], [4], [7]). Some studies evaluating sensors used for short- and long-term monitoring systems have been published [8]. While short-term monitoring is carried out to monitor a pedestrian bridge in the city, long-term monitoring of a dam body that threatens residential areas, a high-rise skyscraper used by thousands of people every day in the city or a very large bridge can be considered. The criterion here, when the structure is damaged, is whether it will affect human life and the economy on a large scale.

---

<sup>1</sup> Corresponding author: Gebze Technical University, Department of Geomatics Engineering, 41400, Gebze/Kocaeli, Turkey. [hpehlivan@gtu.edu.tr](mailto:hpehlivan@gtu.edu.tr)

The second important parameter in the design of the SHM system is the selection of measurement sensors that can measure the behaviour of the structure such as vibration and oscillation, in a range suitable for their frequencies. While GNSS (Global Navigation Satellite System), inclinometer and total station can be used to determine the static and semi-static behaviours of the structure, accelerometers can be used to determine its dynamic behaviours ([6], [10], [11], [13], [14], [17], [22], [23], [26]). GNSS is the most advanced geodetic monitoring system that can be used in long and short term monitoring systems ([9], [12]). In addition, with the improvement of sampling frequency in GNSS receivers, the exact behaviour of structures can be determined with high precision in time and frequency dimensions ([3], [9], [19]). Recent studies have made it possible to measure quasi-static and dynamic movements of rigid structures with a natural frequency of 3-4 Hz and a displacement of a few millimetres, with a sampling range of up to 100 Hz and new filtering techniques of GNSS ([5], [7], [16], [17], [20]). GNSS measurements; for static, quasi-static and real-time kinematics (RTK) methods, respectively; It provides positioning with 0.5–2 and 1–5 cm accuracy ([16], [17]). It has been published in experimental studies that the horizontal accuracy of dynamic measurements using the Precise Point Positioning (PPP) method approaches 2 cm, while the vertical accuracy approaches 1 cm ([3], [15], [18]).

Despite its proven advantages, GNSS measurement methods are affected by signal reflections (multipath), which is the main source of error and this is the main disadvantage of GNSS ([18], [19], [20], [24]). In order to overcome the problems such as multipath and increase the dynamic measurement accuracy of structures, different measurement techniques, auxiliary measurement tools and some signal processing methods are used with the high sampling frequency data collection capability of GNSS receivers ([3], [12], [19], [20], [22]).

This study aims to determine the displacement changes of the tower and analyze its dynamic properties by evaluating the data recorded with different measurement sensors installed on a tower structure in a GNSS-based SHM study. This designed SHM system was tested on a Tower using GNSS, tiltmeter and robotic total station (RTS) [12]. Data collected using two GPS receivers, two tiltmeters and RTS were analyzed and the results were evaluated. Thus, the behaviour of the Tower was determined by different measuring sensors. The amplitude sizes and spectral characteristics representing the movements of the structure at the time of measurement were examined and interpreted.

## 2. EXPERIMENTAL TEST AREA

The test measurement data were carried out on a TV tower (Istanbul-Turkey) with a total height of 217 meters (the height of the reinforced concrete part is 164 meters and the antenna height is 57 meters) (Figure 1.a). Between 145 and 165 meters of the reinforced concrete part of the tower, there are a revolving restaurant and viewing floors with a diameter of 30 meters (Figure 2.a). In Figure 2.b, the heights where the tower and measuring systems are mounted are shown schematically. Accordingly firstly, a GPS reference (base) station was set up at a safe point near the tower. Two GPS receivers, one in the south and one in the north direction, at a height of 164 m, are mounted on the balcony of the upper part of the reinforced concrete part of the tower. NovAtel GPS OEM4 receivers with a sampling rate of 20 Hz were used as GPS hardware. GPS observations were collected in ASCII format using the RTK- method with Novatel CDU software on the recording units floor.

Two tilt-measuring sensors are mounted at a height of 162 m and 148 m near the approximate center of the tower (Figure 2.b). Tilt measurement sensors were positioned in line with the same projection direction, with the X-axis to the north and the Y-axis to the east. Leica Nivel20 dual-axis sensor (Figure 1.c) was used with SOPOM software as a digital tilt sensor. The tilt sensor used has the capacity to measure the tilt changes in both axis directions with an accuracy of 0.001mrad (0.001 mm/m) or approximately 0.2". The operating range of the Nivel20 is  $\pm 1.5$  milliradian ( $\pm 1.5$  mm/m) and 5.2' with zero position error. Since Nivel20 sensors are very sensitive to temperature change, measurements were made by placing them in the enclosure box and the indoor temperature was also recorded during the measurement.

Total stations with robotic features are proven conventional tools for measuring structural displacements. Although it has some measurement handicaps, it is one of the first devices that comes to mind in structural monitoring studies due to its measurement precision and practical measurement capabilities. In this study, observations were made with RTS from ground control points to prisms at a certain distance. Two prisms are mounted at the bottom of the GPS antennas as seen in Figure 1.b. Observations were made using Motorized Geodimeter 600S electronic total stations (Figure 1.a). Observations were made from fixed station points to both prisms sequentially every 2 minutes and data sets (2 edge and 2 angle values) were recorded as a function of time.

Davis Vantage Pro2 Weather station (weather station), shown in Figure 1.d, was used as the meteorological data measurement sensor, and temperature, relative humidity, wind speed and direction, precipitation and pressure changes were recorded during the measurement. It is mounted on the highest accessible point (172 m elevation) of the reinforced concrete part is seen in Figure 2.b.

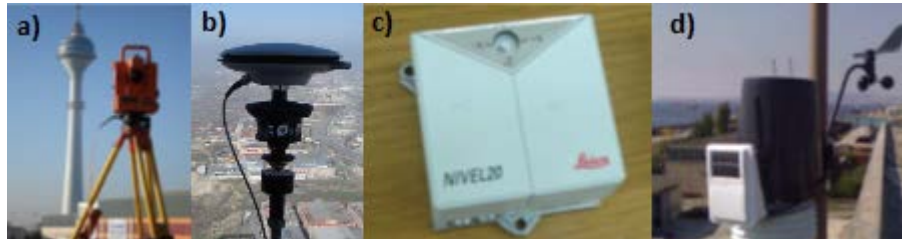


Figure 1. a) Monitoring the tower with RTS b) GNSS antenna and RTS prism just below it, c) Leica Nivel20 tilt sensor (Tiltmeter), d) Weather station

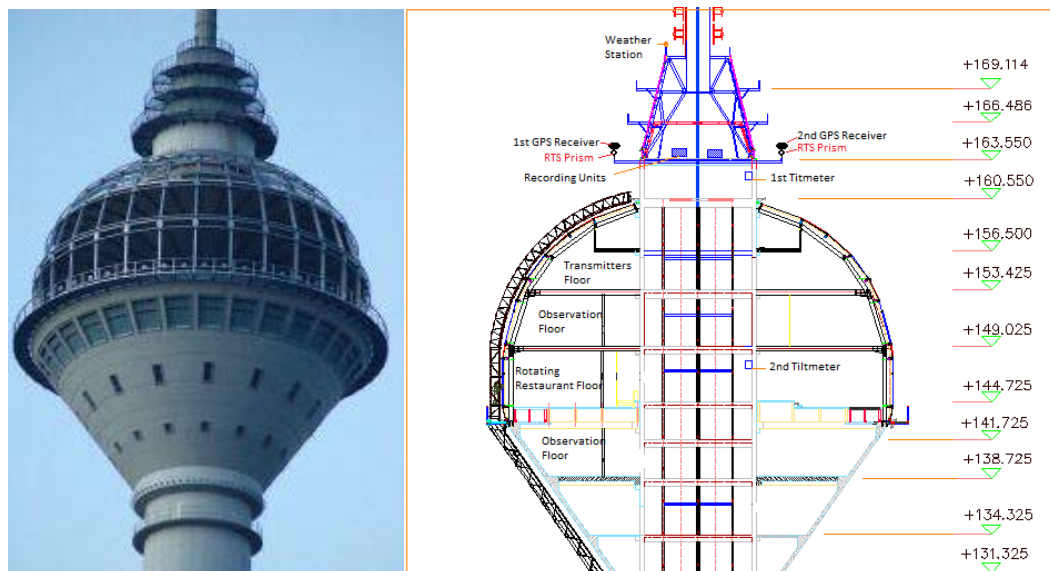


Figure 2. a) The shaft part of the Tower (between 145 and 165 meters elevations), b) The diagram showing the locations of the measuring sensors

### 3. ANALYSIS OF EXPERIMENTAL TESTS RESULTS

Obtaining the data obtained from GPS, Tiltmeter and RTS receivers and making them ready for processing is an important process step. The data characteristic and content of each sensor differs. All data operations were performed with algorithms developed in the MATLAB program. Simultaneously collected data sets were subjected to pre-evaluation filtering and some correction processes and were resampled with a sampling interval of 1 second. The amplitudes of the quasi-static-low frequency displacement changes of these three measuring methods were determined and the results were evaluated. The amplitude sizes and spectral characteristics representing the movements of the structure at the time of measurement were examined.

#### 3.1. GPS Data

Firstly, the long and short-term behaviours of the tower, namely high and low-frequency behaviours, were examined with GPS data. Firstly, coarse erroneous data were extracted from the X and Y-axis time series. For this purpose, a threshold was applied with  $\pm 5$  cm. Smoothing was performed using 10 units of window size. Ellipsoidal coordinates (X, Y, Z coordinates) obtained by the RTK GPS method were converted into local topocentric coordinates.

It was possible to determine static, semi-static and dynamic structure behaviours with GPS data. The structure motion model was drawn during the measurement from the filtered and reconstructed GPS series (Figure 3). The daily path of the tower was coloured with a different colour for each day. The tower moved in half-elliptical cycles with the long axis (3.99 cm) in the West-East direction and the short axis (2.82 cm) in the South-North direction depending on the daily temperature change. It is seen that the daily trajectories are not the same as the previous day as they change due to the daily temperature value and the sunshine duration.

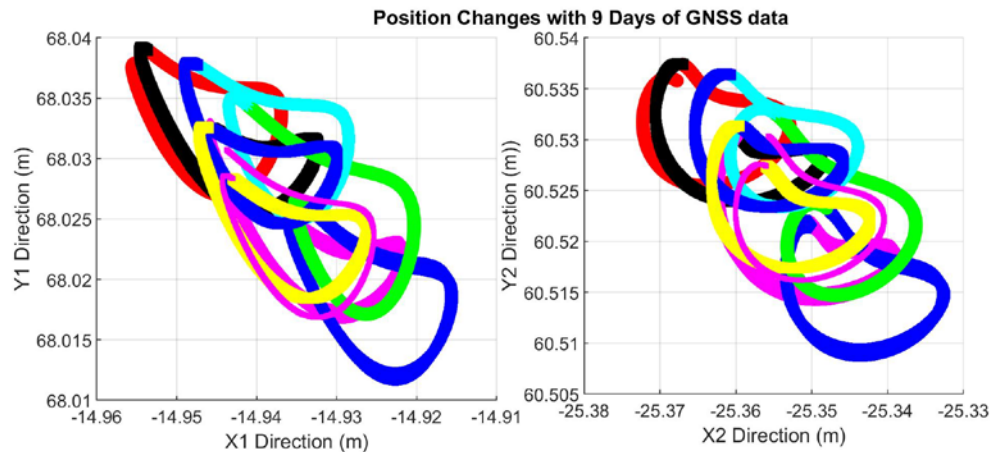


Figure 3. Amplitude values computed via different measurement methods

### 3.2. Tiltmeter Data

The Tiltmeter data set recorded at 1-second intervals was re-interpolated in order to eliminate breaks and skips. When simultaneously recorded GPS and Tiltmeter data were analyzed, the high-frequency components of the GPS time series showed random oscillations of  $\pm 2\text{mm}$ , while the high-frequency components of the Tiltmeter time series showed oscillations of  $\pm 0.1\text{mm}$ .

After filtering, GNSS and Tiltmeter data were standardized and shown on the XY axis. When we plot the model series in the X-Y plane, we can see the displacement pattern of each receiver. The 8-hour displacement models of the tower are presented in Figure 4. Figure 4, shows a comparison of the displacement changes in an area of  $15\text{ mm}^2$  with GPS and Tiltmeter receivers. These calculated series of models have provided precise information on how the tower moves for 8 hours. When we examine this movement model, we observe how the tower moves depending on the movement of the sun. After warming up at 11:00, the tower was moved to the east. The body of the tower, which started to cool down after 12:00 and 13:00, when the sun's heat was at its maximum, returned to its original position between 14:00 and 15:00.

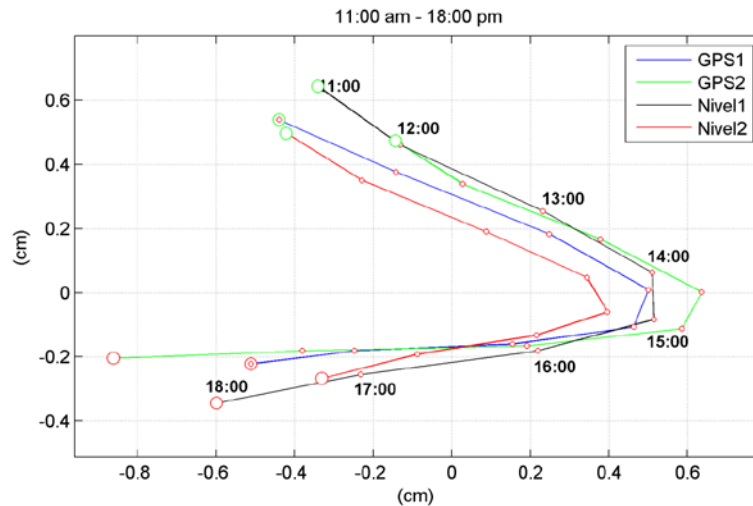


Figure 4. Amplitude values computed via different measurement methods

### 3.3. RTS Data

Observations with RTS were made using motorized Geodimeter 600S electronic total stations. Two prisms mounted on the lower part of the GPS antennas as seen in Figure 1.b were used as observation points (Figure 1.a). Observations were made from the fixed station point to the monitoring points every 1.5 minutes for 6 hours under normal meteorological conditions, and the data sets (2 edge and 2 angle values) were recorded as a function of time.

The analysis process of the data recorded with RTS is an important issue. The coordinates of the monitoring points have been determined by the recorded oblique distance, horizontal angle and vertical angle measurements. Each observation data set was analyzed in itself and it was aimed to determine the change of total displacement according to time by creating 2-minute observation sets. After data control and interpolation, the balanced coordinate values of the observation point were calculated for each half-hour between 11:00-18:00. The displacement vectors of each measurement time were calculated by calculating the coordinate values and mean errors balanced by the least-squares method. In addition, the positional errors at the observation point were calculated for each balancing time. As a result of analysis and evaluation; It was concluded that the movement of the structure was within the known and predicted limits and the measurements were made with sufficient accuracy. As seen in Figure 5, the results were found to be compatible with GPS measurements.

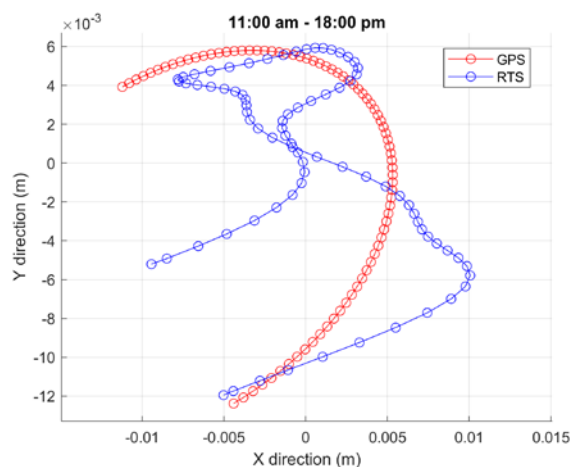


Figure 5. Amplitude values computed via different measurement methods

#### 4. CONCLUSION

In this experimental measurement system; GPS, tiltmeter and RTS were used and simultaneous measurements were evaluated. Firstly RTK GPS datasets were analyzed at low and high frequencies and it was possible to model the long and short term movements of the tower during the measurement. The calculated high-frequency values are approximately 0.16 Hz and 0.25 Hz in the X-Y directions, respectively. These values showed that the tower made oscillations with a period of about 4-6 seconds. These high-frequency values were not calculated from Tiltmeter and RTS data. However, within a period of 9 days, important components of the low frequencies could be determined and when we compared them in the X-Y direction; common period values of 24 and 12 hours were determined. The common-mode values of 24 and 12 hours at low frequencies were evaluated as the movement of the tower for 9 days (semi-static). Thus, the low-frequency behaviours of the tower were determined by three different measurement systems and it was seen that the results were compatible with each other.

When we examine the low-frequencies tower behaviour presented in Figure 3., it is understood that the Sun is correlated with radiation effect and temperature change and makes a semi-elliptical motion. Under normal meteorological conditions, it has been determined that the top (shaft part) of the Tower makes an elliptical rotation in the daily movement within daily air temperature change and the radiation effect of the sun. In a similar tower monitoring study published in 2008, Bruere explained the path of the tower's shaft as an ellipse that changes with the position of the sun on a sunny day [2].

The movement characteristic of this tower under normal air conditions can be explained as follows. The sunning surface of the tower shaft was subjected to thermal expansion due to nonsymmetrical heating. Tower horizontal displacement was induced with additional stresses due to changes in the temperature gradient inside the shaft section of the tower. While expanding the sun-exposed side, the top of the tower was bent to the side away from the sun. During the day, the sun moves from the east and continues from the south to the west, while the top of the tower followed an elliptical path in the direction of the West-North-East. The magnitude of this displacement depends on the temperature difference between the sun-exposed side and the shaded side, ie the direct solar radiation intensity. Since all sides of the tower are exposed to equal heat during the night times, the tower reaches a certain equilibrium state at night.

Some of the important points identified in this study can be listed as follows;

- Since the GPS receivers are too close to the steel shaft of the tower, they contain multipath errors. Due to the fact that the receivers are mounted on two opposite sides of the tower, they used different satellite geometries at the same time and have different multipath and instant errors. In this sense, both sensor measurements have been complementary to each other.
- It was important to compare and evaluate with the data obtained from Tiltmeter, as GPS observations are known to contain errors due to multipath and satellite geometry.
- The use of two GPS and tiltmeter receivers for control purposes has been important in terms of comparing X and Y directional data sets with each other.
- Since the Tiltmeters are mounted at different heights, their calculated amplitudes were different. Since the 2nd sensor is 14 meters lower than the 1st sensor, the slope direction is the same, but the calculated amplitudes have been smaller.
- RTS measurements gave the opportunity to measure tower movements from a distance and in a different system. Thus, the motion vectors determined by GPS and tiltmeter measurements could also be calculated with the classical measurement method.

#### REFERENCES

- [1]. V. Ashkenazi, G.W. Roberts. "Experimental monitoring of the Humber Bridge using GPS". *Proceedings of the Institution of Civil Engineers- Civil Engineers*, 120(4), pp. 177-182, 1997.
- [2]. P. Breuer, T. Chmielewski, P. Górski, E. Konopka, L. Tarczyński. "The Stuttgart TV Tower-displacement of the top caused by the effects of sun and wind". *Engineering Structures*, 30(10), pp. 2771-2781, Oct. 2008.
- [3]. M. R. Kaloop, E Elbeltagi, J. W. Hu and A. Elrefai. "Recent advances of structures monitoring and evaluation using GPS-time series monitoring systems: A review", *ISPRS International Journal of Geo-Information*, 6 (12), 382, 2017.
- [4]. H. N. Li, T. H. Yi, L. Ren, D. S. Li, L. S. Huo. "Reviews on innovations and applications in structural health monitoring for infrastructures". *Struct. Monit. Maint.* 1(1), pp. 001-045, Mar. 2014.

- [5]. F. Moschas, S. Stiros. "Measurement of the dynamic displacements and of the modal frequencies of a shortspan pedestrian bridge using GPS and an accelerometer". *Eng. Struct.*, 33, 10–17, 2011.
- [6]. P. Psimoulis, S. Stiros. "Measuring deflections of a short-span, railway bridge using a Robotic Total Station". *J. Bridge Eng.*, 18, 182–185, 2013.
- [7]. T. H. Yi, H. N. Li, M. Gu. "Recent research and applications of GPS-based monitoring technology for high-rise structures". *Struct. Control Health Monit.* 20, pp. 649–670 2013.
- [8]. V.G.M. Annamdas, S. Bhalla, C.K. Soh. "Applications of structural health monitoring technology in Asia", *Struct. Health Monit.* 16, pp. 324–346 2017.
- [9]. H. Pehlivan and H. F. Bayata. "Usability of inclinometers as a complementary measurement tool in structural monitoring". *Structural Engineering and Mechanics*, 58(6), pp. 1077-1085, 2016.
- [10]. S. B. Im, S. Hurllebaus, Y. J. Kang. "Summary Review of GPS Technology for Structural Health Monitoring". *J. Struct. Eng.* 139, pp. 1653–1664, 2013.
- [11]. X. J. Li, L. L. Ge, E. Ambikairajah, C. Rizos, Y. Tamura, A. Yoshida. "Full-Scale Structural Monitoring Using An Integrated GPS And Accelerometer System". *GPS Solutions*, 10(4), pp. 233–247, 2006.
- [12]. H. Pehlivan, O. Aydin, E. Gulal, E. Bilgili. "Determining the Behavior of High-Rise Structures with Geodetic Hybrid Sensors". *Geomatic, Natural Hazards and Risk*. 2015-6(8), pp. 702-717, Published online: 05 Nov 2013.
- [13]. J. Hwang, H. Yun, S. Park, D. Lee and S. Hong. "Optimal Methods of RTK-GPS/Accelerometer Integration to Monitor the Displacement of Structures", *Sensors*, 12, pp. 1014-1034, 2012.
- [14]. T. H. Yi, H. N. Li, G. Ming. "Recent research and applications of GPS-based monitoring technology for high-rise structures", *Structural Control and Health Monitoring*, 20(5), pp. 649-670, 2012.
- [15]. C. O. Yigit, and E. Gurlek. "Experimental testing of high-rate GNSS precise point positioning (PPP) method for detecting dynamic vertical displacement response of engineering structures". *Geomatics Natural Hazards and Risk*, 8(2), 893-904, 2017.
- [16]. C. O. Yigit. "Experimental assessment of post-processed kinematic Precise Point Positioning method for structural health monitoring". *Geomatics Natural Hazards and Risk*, 7, 360–383, 2014.
- [17]. F. Moschas, S. Stiros. "Dynamic Deflections of a Stiff Footbridge Using 100-Hz GNSS and Accelerometer Data". *Journal of Surveying Engineering* 141 (4), pp. 04015003, 2015.
- [18]. F. Moschas, A. Avallone, V. Saltogianni, S. Stiros. "Strong motion displacement waveforms using 10-Hz precise point positioning GPS: An assessment based on free oscillation experiments Fanis". *Int. Assoc. Earthq. Eng.* 44, pp. 657–675, 2015.
- [19]. H. Pehlivan. "Frequency analysis of GPS data for structural health monitoring observations", *Structural Engineering and Mechanics*, 66(2), pp. 185-193, 2018.
- [20]. T. H. Yi, H. N. Li, M. Gu. "Experimental assessment of high-rate GPS receivers for deformation monitoring of bridge". *Meas. J. Int. Meas. Confed.* 46, pp. 420–432, 2013.
- [21]. W. S. Chan, Y. L. Xu, X. L. Ding, W. J. Dai. "An integrated GPS-accelerometer data processing technique for structural deformation monitoring". *J. Geodesy*, 80, pp. 705–719, 2006.
- [22]. B. Erol. "Evaluation of High-Precision Sensors in Structural Monitoring". *Sensors*, 10, 10803-10827, 2010.
- [23]. V. Lekidis, M. Tsakiria, K. Makrab, C. Karakostasb, N. Klimisb and I. Sous. "Evaluation of Dynamic Response and Local Soil Effects of the Evripos Cablestayed Bridge Using Multi-sensor Monitoring Systems". *Engineering Geology*, 79, pp. 43–59, 2005.
- [24]. C. Ogaja, C. Satirapod, "Analysis of high-frequency multipath in 1-Hz GPS kinematic solutions," *GPS Solutions*-Springer Verlag, 11(4), pp. 269-280, 2007.
- [25]. G. W. Roberts, X. Meng, and A. Dodson. "Integrating a Global Positioning System and accelerometers to monitor deflection of bridges." *J. Surv. Eng.*, 130(2), pp. 65–72, 2004.

# Autonomous Network Management in Software Defined Networks

Recep Ibiloglu<sup>1</sup>, Arif Koyun<sup>2</sup>

---

## Abstract

*Software-defined networks (SDN), a major paradigm for autonomous network management. Due to the capability of software defined networks, autonomous network management purpose to provide the Quality of Service by use of self-organizing mechanism. This paper aims to present recent advances on autonomous network management in software defined networks. We also discuss challenges of autonomous network management and focus on self-organizing mechanisms. Additionally, this paper purpose to help for researchers from different autonomous network management fields to current artificial intelligence key issues*

**Keywords:** Autonomic Network Management, Software Defined Networks, Self-Organizing Networks

---

## 1. INTRODUCTION

The high increase of internet traffic, such as using mobile phone, wireless or wireline network, is one of the trends directing the network technology to change its traditional network management. Increasing demands of new services, network professionals and operators need to emerge solutions to efficiently regulate their network resources using more flexible and dynamic approaches. Due to the challenging network issues, software defined networks(SDN) has been appeared. At first, SDN has been implemented in campus networks. Researchers have searched and analyzed the benefits of SDN in different areas such as data center, cloud and internet of things(IOT).

Network management is usually performed manually by network professionals, who analyze data and statistical information to scan traces and behavioral patterns in order to optimize network operations [4]. This attempt is inefficient, error-prone, which prevent the quality of the services. In order to manage network operation without human impact, autonomic network management systems and models has been recommended. Thus, new autonomic management tools able to automatically analyze the network and proactively identify autonomic patterns are implemented. This new management paradigm is known as Autonomic Management [1], which support an enhancement in network reliability and quality, making administrators to quickly identify and solve difficulties.

This paper is organized as following: Section II presents basic issues and components of SDN. In Section III we present self-x network management, self-organizing networks and autonomous network management. Section IV presents the our approach for autonomic network management. Finally, in section V, we presents our conclusions.

## 2. SOFTWARE DEFINED NETWORKS

Software Defined Network is an emerging network paradigm, which separates the control plane and data plane [2]. SDN also plays crucial role in network management. SDN has three basic elements: SDN devices such as router, switches; SDN controller such as Open Flow; and applications[5]. Network traffic such as frames or packets, is transferred on the SDN devices. The SDN controller is the brain of SDN infrastructure and it manages network devices and transmit the order of SDN applications to the SDN devices. The SDN devices

---

<sup>1</sup> Corresponding author: Alanya Alaaddin Keykubat University, IT Department, Alanya/Antalya, Turkey.  
[recep.ibiloglu@alanya.edu.tr](mailto:recep.ibiloglu@alanya.edu.tr)

<sup>2</sup> Suleyman Demirel University, Department of Computer Engineering, Isparta, Turkey.  
[arifkoyun@sdu.edu.tr](mailto:arifkoyun@sdu.edu.tr)



has the task that is packet forwarding and controller performed cumbersome networking logically. The network device providers produce OpenFlow supported SDN devices.

Apart from the traditional network management, Software Defined Network (SDN) consists of three planes, namely control plane, application plane and data plane. As demonstrated in Figure 1, between the control plane and the application plane stands the Northbound Interface (NI) and they communicate each other via infrastructure API by the Northbound Interface (NI). Besides, the Southbound Interface (SI) stands between the control plane and the data plane and they communicate via API by it. Because of the logically centralized control and programmable infrastructure.

SDNs collect a large scale of network data. These data are IP parsing packets, security device logs, network traffic statistics, flow-tables in OpenFlow supported switch, system protection logs. These data contain various information for tasks. To attain valuable information from data for SDN applications and operations, it needs to be analyzed according to intended purposes.

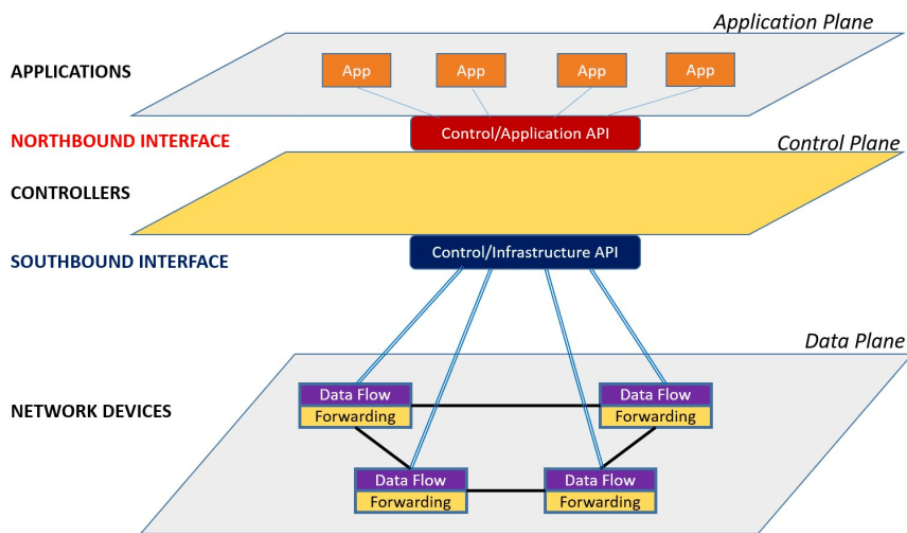


Figure 1 Software-defined networking - A high level architecture [6]

### ○ *Application Planes*

This layer consists of business and SDN applications that utilize the SDN communications and network services [3]. By the help of the controller the applications are able to impact the behavior of the infrastructure by configuring the flows so as to route packets through the best path between two nodes.

### ○ *Control Planes*

A control plane is the central of the operations [7]. It typically runs in software and builds the necessary tables for forwarding. This layer supplies the logically centralized control functionality that manages the network forwarding behavior through an API. All SDN devices that arrange the network tasks; and implements policy decisions which are routing, forwarding, load balancing.

### ○ *Data Planes*

Data planes comprise of network devices which execute packet switching and forwarding. The packet processing function determines on incoming packets where to flow entries in the flow tables.

### 3. AUTONOMOUS NETWORK MANAGEMENT

Ever-increasingly, usage of technology advances and service demands of modern networks have dramatically remained. Network management will not be almost provided by human administrators. To control this cumbersome difficulty, IBM has announced a promising paradigm helping to create self-managed systems [8]. This paradigm, called Autonomic Computing, provides to design computing equipment able to self-adapt its configuration and to self-optimize its performance. IBM has suggested autonomic computing by the help of inspiring from human body especially in biological processes. In our body some functions perform without the need for conscious direction. Autonomic computing tries to manage the operation of individual pieces of IT infrastructure through the introduction of an autonomic manager.

In autonomic management has autonomic control loop and it contains monitor, analyze, plan and execute components. The monitor network gathers data, filters and collates it as required, and then shows it to the analyze component, which seeks to understand the data and determine if the managed element is acting as desired. The plan component takes the data and determines if action should be taken to reconfigure the managed element. The execute component translates the planned actions into a set of configuration commands that can be applied to the managed element [10].

#### ○ *Self-Organizing Networks*

Self-organizing network(SON), which is able to decrease human impact in networking processes, was proposed to decrease the operational expenditures(OPEX) for network service providers in future network systems. In contrast to autonomic networking, the concept of Self Organizing Network (SON) firstly is implemented to the management and control of cellular networks. SON functionalities for Operation and Maintenance (O&M) procedures are classified into three basic categories, namely (i) self/configuration, (ii) self/optimization, and (iii) self/healing [9].

#### ▪ **Self-Configuration**

Automated configuration of components and systems follows high-level policies. Self-configuration is the capability of reconfiguring automatically and dynamically in response to changes. Removing, installing, integrating, and composing/decomposing are the element of self-configuration.

#### ▪ **Self-Optimisation**

Components and systems continually pursue opportunities to develop their own performance and efficiency. Self-optimization embraces all the set of mechanisms which optimize the network parameters during operation, based on measurements received from the network.

#### ▪ **Self-Healing**

System automatically detects, diagnoses, and repairs localized software and hardware problems. Fault management should be simplified and automated via information correlation mechanisms.

### 4. APPROACH

We planned using intelligent methods to improve autonomous networks with self-x mechanisms. We implement methods on Routing, traffic classification, Flow clustering, intrusion detection, load balancing, Fault detection, quality of experience (QoE) optimization, admission control, resource allocation in a testbed. We are planning using Machine learning methods such as supervised, unsupervised and reinforcement learning techniques for autonomic SDN.

○ **Testbed**

The testbed is established on virtual Mininet simulation platform using Linux Ubuntu operating system. POX controller platform is designated as controller. As shown in Figure 2, simulation platform is implemented edge switches.

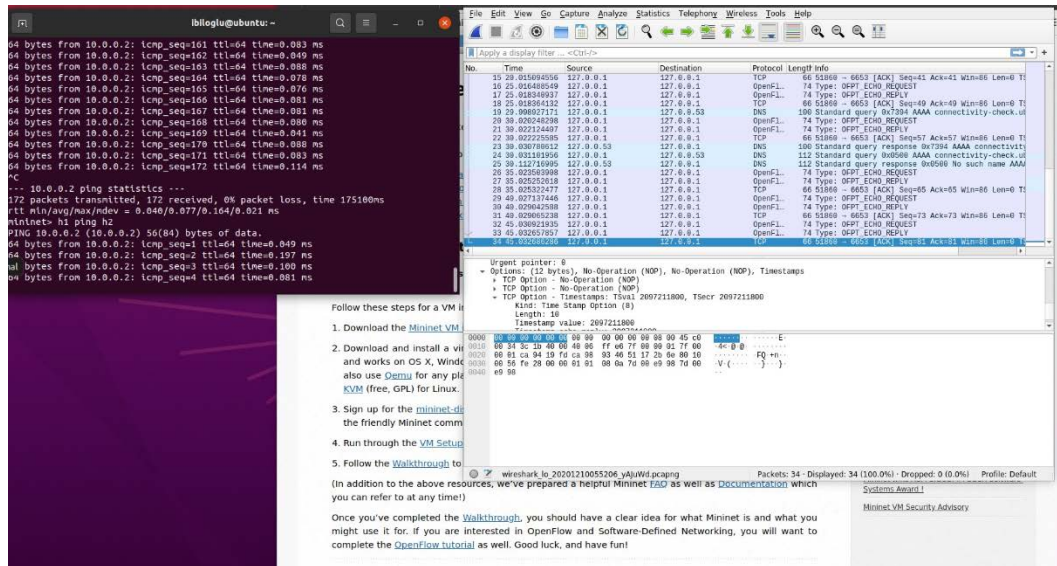


Figure 2 Screenshot of Testbed

## 5. CONCLUSION

In this paper, we indicate the importance of software defined networks and autonomous network management. With the significance of managing networks without human interventions, improving autonomous network management in SDN become indispensable. Meanwhile, we spotlighted the development on self-organizing networks that improves cellular networks. A special attention should be paid to devise computationally efficient and trustable machine learning driven network management operations. In the future, we hope that further investigations and profound analysis could be led and a simulation of a model is also vital to prove our approach.

## REFERENCES

- [1]. B.Jennings, S. van der Meer, S. Balasubramaniam, D. Botvich, M.O. Foghlu, W. Donnelly, J. Strassner, Towards autonomic management of communications networks, *Commun. Mag. IEEE* 45 (2007) 112–121.
- [2]. K. Diego et al., “Software-Defined Networking: A Comprehensive Survey,” *Proceedings of the IEEE*, vol. 103, no. 1, Jan 2015, pp. 14–76.
- [3]. P. Göransson, C. Black *Software defined networks : a comprehensive approach*, 1st edition. Waltham, Massachusetts: Elsevier, 2014.
- [4]. A.Passito, E. Mota,R.Bennesby, P. Fonseca, “AgNOS: A Framework for Autonomous Control of Software-Defined Networks” in *Proc. 28<sup>th</sup> IEEE Int. Conf. AINA, 2014*, pp. 405–412.
- [5]. B.Nunes, M. Mendonca, X.-N. Nguyen, K. Obraczka, and T. Turletti, “A survey of software-defined networking: Past, present, and future of programmable networks,” *Communications Surveys Tutorials, IEEE*, vol. 16, no. 3, 2014, pp. 1617–1634.
- [6]. (2021) The Telecommunication and Digital Economy website. [Online]. Available: <https://telsoc.org/ajtde/2015-12-v3-n4/a28>
- [7]. N. McKeown, T. Anderson, H. Balakrishnan, G. Parulkar, L. Peterson, J. Rexford, S. Shenker, and J. Turner, “OpenFlow: enabling innovation in campus networks,” *SIGCOMM Comput. Commun. Rev.*, vol. 38, no. 2, pp. 69–74, Mar. 2008.
- [8]. J. O. Kephart and D. M. Chess. The vision of autonomic computing. *Computer*, 36(1):41–50, 2003.
- [9]. M A Khan, S Peters, D. Sahinel, F D Pozo-Pardo, X T Dang, Understanding autonomic network management: A look into the past, a solution for the future, *Computer Communications*, 122, 2018, 93-117.

- [10]. B.Jennings, et al. (2007). Towards autonomic management of communications networks. Communications Magazine, IEEE. 45. 112 - 121. 10.1109/MCOM.2007.4342833.

#### **BIOGRAPHY**

Recep Ibiloglu received a diploma degree in software and information engineering from Vienna University of Technology in 2006(Austria) and he is Ph.D. candidate in computer engineering at Suleyman Demirel University, Isparta(Turkey). He is academic at Information Technology department, Alanya Alaaddin Keykubat University, Antalya (Turkey). His research interests Software Defined Networks and Machine Learning.

# The Developed FEA-Based Program for Planar Static Analysis with a Special 12x12 Rectangular Element

Ragib Sabah<sup>1</sup>, Namik Kemal Oztorun<sup>2</sup>, Baris Sayin<sup>3</sup>

---

## Abstract

There are many widely used structural programs to calculate static loads' effect on buildings, meanwhile, a set of calculations' assumptions are used as a basis of these programs. These assumptions may lead to unreal structural calculations and behaviors. One of the most important assumptions is the stiffness matrix of shear walls which is only composed of 8x8 elements ignoring the rotational stiffness values. In this study, a computational program based on the finite element method was developed using FORTRAN programming language to study the effect of static loads on planar structures. This program is called YAY2020. In the developed program, a special rectangular elements' stiffness matrix formulation with 12x12 will be used to consider rotational deformations of the share wall elements. The correctness of this formulation has been proven by comparing it with Timoshenko beam analytical analysis. The aforementioned formulation was not in the literature until recently introduced by Oztorun. All results obtained by YAY2020 will be compared with the commonly used SAP2000 software.

**Keywords:** FORTRAN, Finite element analysis (FEA), 12x12 Stiffness matrix, Planar static analysis, Structural analysis software, Timoshenko Cantilever Beam

---

## 1. INTRODUCTION

The calculation and analysis of exact loads affecting buildings is the most important part of the construction process because even if the structures are constructed correctly and there were structural analysis errors, results will be significantly reflected later causing economic and human losses. The scientific development witnessed in recent years accompanying the rapid development of programming and computer sciences have revealed a set of programs that have reduced the structural analysis calculation burdens and errors, but how are the assumptions used in these programs are correct and accurate. Therefore, the mechanism of each program must be understood and monitored before getting started using it, and always seek to develop these programs to access accurate analysis results.

Oztorun [1, 2] presented a formulation of the rectangular stress element. This formulation has three degrees of freedom at each rectangular stress element's nodes. This feature distinguished Oztorun formulation from the previous stress element formula that has only two degrees of freedom in each element node. With this formulation, 12x12 rectangular stress element stiffness matrices can be calculated. Wilson [3-6] wrote the first automated finite element structural analysis computer programs known as CAL family of programs. These programs were greatly successful and gave accurate results. In 1975 under the Computers and Structures Inc. firm's platform, he played a role in the development of structure programs such as SAP2000, SAFE and ETABS. In these programs, shear-wall stiffness matrices contain only 8x8 elements with no rotational stiffness values. Bathe [7, 8] was one of the pioneers in the field of finite element analysis and its applications. He worked with Wilson together to develop finite element analysis in structures. He wrote a book called "Finite Element Procedures" to explain the detailed procedure of finite element analysis. Turner [9] presented a set of

---

<sup>1</sup> Corresponding author: Istanbul University-Cerrahpasa, Institute of Graduate Sciences, 34320, Avclar/ Istanbul, Turkey  
[ragib.sabah@ogr.iuc.edu.tr](mailto:ragib.sabah@ogr.iuc.edu.tr)

<sup>2</sup> Istanbul University-Cerrahpasa, Department of Civil Engineering 34320, Istanbul, Turkey, [kemal@iuc.edu.tr](mailto:kemal@iuc.edu.tr)

<sup>3</sup> Istanbul University-Cerrahpasa, Department of Civil Engineering 34320, Istanbul, Turkey, [barsayin@iuc.edu.tr](mailto:barsayin@iuc.edu.tr)

arithmetic formulations for triangular and rectangular stress elements, but in these formulations, the rotational stiffness values were neglected. Griffiths [10] presented a stiffness matrix of the four-node quadrilateral element in the closed-form this quadrilateral element had just 8x8 stiffness matrix elements. Ozturun and others [11, 12] performed static and modal analyzes of a bridge using the GP-DYNA computer program developed by E. Ozturun in his doctoral thesis. As a result of the analyses, the first findings revealed that the bridge piers were strained under the effects of horizontal earthquakes, that piers and horizontal elements could be strained under vertical effects at frequencies close to the frequencies that cause the horizontal oscillations of the bridge piers; stated that this situation may be a collapse reason of a system.

In this study, a program based on the finite element method will be coded by the FORTRAN compiler [13, 14] to find the response of known geometry planar structures under static loads. The program will be called YAY2020. In principle, YAY2020 program calculates the system stiffness matrix by calculating and superposing the stiffness matrices of each system's element separately. The distinctive feature of this program, it uses of a special rectangular element formulation that add the perpendicular rotational stiffness values in the calculation of shear-wall elements' stiffness matrices with real and full-size 12x12 stiffness matrix elements. This aforementioned formulation was developed by Ozturun [1, 2]; the accuracy of this formulation had been proved by comparing it with the analytical solution presented by Timoshenko and Goodier [15]. The results of the YAY2020 program will be compared to commonly use finite element structural programs like SAP2000. In light of these features, this study aims to contribute to the literature by providing a program having more realistic structure analysis calculation methods than current programs.

## 2. MATERIALS AND METHODS

In this section, methods and formulations used in YAY2020 program will be explained.

### o *Frame Elements Stiffness Matrix*

Figure 1 shows a planar frame element with two nodes (i and j nodes) and three degrees of freedom in each node's ending. The axis across through i and j nodes is called the local x-axis and the perpendicular to the local x-axis is called the local y-axis, and these two axes formed the local coordinate system of the element. Frame element includes the properties of both beam element and truss element. Therefore, the stiffness matrix of the frame element can be written as Eq.1. [3, 8]

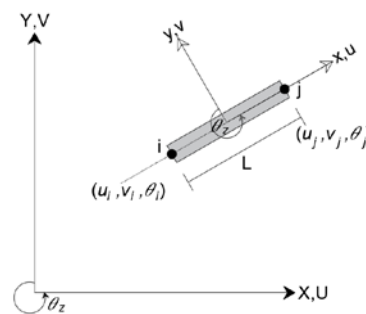


Figure 1. Planar frame element

$$K_{e.l.}^{frame} = \begin{bmatrix} AE/L & 0 & 0 & -AE/L & 0 & 0 \\ 0 & 12EI/L^3 & 6EI/L^2 & 0 & -12EI/L^3 & 6EI/L^2 \\ 0 & 6EI/L^2 & 4EI/L & 0 & -6EI/L^2 & 2EI/L \\ simetrik & & & AE/L & 0 & 0 \\ & & & 0 & 12EI/L^3 & -6EI/L^2 \\ & & & & -6EI/L^2 & 4EI/L \end{bmatrix} \quad (1)$$

The stiffness matrix written in the Eq.1 is in the local coordinates of the element. For structural analysis, a planar transformation matrix should be used to transfer from the local coordinate system of the element to the global coordinate system of the structure. The planar transformation matrix is given in Eq.2. [3, 8]

$$R = \begin{bmatrix} \cos(\theta) & \sin(\theta) & 0 & 0 & 0 & 0 \\ -\sin(\theta) & \cos(\theta) & 0 & 0 & 0 & 0 \\ 0 & 0 & 1 & 0 & 0 & 0 \\ 0 & 0 & 0 & \cos(\theta) & \sin(\theta) & 0 \\ 0 & 0 & 0 & -\sin(\theta) & \cos(\theta) & 0 \\ 0 & 0 & 0 & 0 & 0 & 1 \end{bmatrix} \quad (2)$$

Here;

$$\cos(\theta) = \frac{x_j - x_i}{L} \quad (3)$$

$$\sin(\theta) = \frac{y_j - y_i}{L} \quad (4)$$

$L$ : Element length

The frame element global stiffness matrix can be obtained by multiplying the transpose of the transformation matrix by the element local stiffness matrix and then multiplied by the transformation matrix itself again, as written in Eq.5.

$$K_{e.g.}^{frame} = [R^T] \cdot [K_{e.l.}^{frame}] \cdot [R] \quad (5)$$

Here,

$K_{e.g.}^{frame}$ : Frame element global stiffness matrix.

$R^T$ : Transpose of the transformation matrix.

$K_{e.l.}^{frame}$ : Frame element local stiffness matrix.

### ○ Shear Wall Elements Stiffness Matrix

The rectangular element is used to analyse shear walls in YAY2020. Shear walls count as one rectangular element on each floor of the building. To analyse rectangular elements, degrees of freedom must be determined for each node of the rectangular. The plane stress element which is shown in Figure 2 has three degrees of freedom at each node (1 rotation and 2 displacements). This element doesn't exist in the literature even it's presented by Oztorun [1]. Meanwhile, the previous rectangular stress element used in structural programs had just two degrees of freedom in each node (2 displacements) with no rotation. The plane stress element stiffness matrix formulation is given in Table 1.

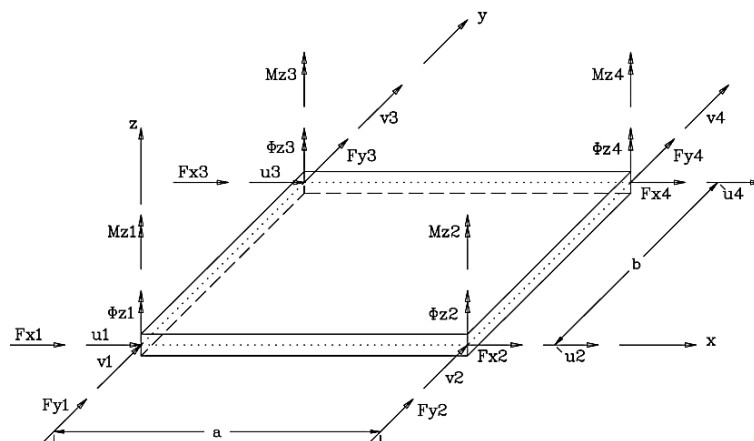


Figure 2. Generalized forces and displacements for finite plate elements for plane stress problems [1]

Table 7. Stiffness matrix of plane stress element [1]

$\Delta^T$	$\Delta_{x1}$	$\Delta_{y1}$	$\theta_{z1}$	$\Delta_{x2}$	$\Delta_{y2}$	$\theta_{z2}$	$\Delta_{x3}$	$\Delta_{y3}$	$\theta_{z3}$	$\Delta_{x4}$	$\Delta_{y4}$	$\theta_{z4}$
I/J	1	2	3	4	5	6	7	8	9	10	11	12
1	$S_{1,1}$	$S_{1,2}$	$S_{1,3}$	$S_{1,4}$	$S_{1,5}$	$S_{1,6}$	$S_{1,7}$	$-S_{1,5}$	$S_{1,9}$	$S_{1,10}$	$-S_{1,2}$	$S_{1,12}$
2		$S_{2,2}$	$S_{2,3}$	$-S_{1,5}$	$S_{2,5}$	$S_{2,6}$	$S_{1,5}$	$S_{2,8}$	$S_{2,9}$	$-S_{1,2}$	$S_{2,11}$	$S_{2,12}$
3			$S_{3,3}$	$S_{1,6}$	$-S_{2,6}$	$S_{3,6}$	$-S_{1,9}$	$S_{2,9}$	$S_{3,9}$	$-S_{1,12}$	$-S_{2,12}$	$S_{3,12}$
4				$S_{1,1}$	$-S_{1,2}$	$S_{1,3}$	$S_{1,10}$	$S_{1,2}$	$S_{1,12}$	$S_{1,7}$	$S_{1,5}$	$S_{1,9}$
5					$S_{2,2}$	$-S_{2,3}$	$S_{1,2}$	$S_{2,11}$	$-S_{2,12}$	$-S_{1,5}$	$S_{2,8}$	$-S_{2,9}$
6						$S_{3,3}$	$-S_{1,12}$	$S_{2,12}$	$S_{3,12}$	$-S_{1,9}$	$-S_{2,9}$	$S_{3,9}$
7							$S_{1,1}$	$-S_{1,2}$	$-S_{1,3}$	$S_{1,4}$	$-S_{1,5}$	$-S_{1,6}$
8								$S_{2,2}$	$S_{2,3}$	$S_{1,5}$	$S_{2,5}$	$S_{2,6}$
9									$S_{3,3}$	$-S_{1,6}$	$-S_{2,6}$	$S_{3,6}$
10										$S_{1,1}$	$S_{1,2}$	$-S_{1,3}$
11											$S_{2,2}$	$-S_{2,3}$
12												$S_{3,3}$

Parameters of the plane stress element stiffness matrix are given as follows: [1]

$$D_s = \frac{E_s \cdot t_s}{(1 - \nu_s^2)}$$

$$\beta = \frac{b}{a}$$

$$S_{1,1} = D_s \cdot \left[ \frac{13 \cdot \beta}{35} + \frac{(1 - \nu_s)}{5 \cdot \beta} \right]$$

$$S_{1,2} = D_s \cdot \frac{(1 + \nu_s)}{8}$$

$$S_{1,3} = -D_s \cdot a \cdot \left[ \frac{11 \cdot \beta^2}{210} + \frac{(9 - 19 \cdot \nu_s)}{240} \right]$$

$$S_{1,4} = D_s \cdot \left[ -\frac{13 \cdot \beta}{35} + \frac{(1 - \nu_s)}{10 \cdot \beta} \right]$$

$$S_{1,5} = D_s \cdot \frac{(3 \cdot \nu_s - 1)}{8}$$

$$S_{1,6} = D_s \cdot a \cdot \left[ \frac{11 \cdot \beta^2}{210} + \frac{(3 - 13 \cdot \nu_s)}{240} \right]$$

$$S_{1,7} = D_s \cdot \left[ \frac{9 \cdot \beta}{70} - \frac{(1 - \nu_s)}{5 \cdot \beta} \right]$$

$$S_{1,9} = D_s \cdot a \cdot \left[ \frac{13 \cdot \beta^2}{420} - \frac{(9 + \nu_s)}{240} \right]$$

$$S_{1,10} = -D_s \cdot \left[ \frac{9 \cdot \beta}{70} + \frac{(1 - \nu_s)}{10 \cdot \beta} \right]$$

$$S_{1,12} = D_s \cdot a \cdot \left[ -\frac{13 \cdot \beta^2}{420} + \frac{(3 + 7 \cdot \nu_s)}{240} \right]$$

$$S_{2,2} = D_s \cdot \left[ \frac{13}{35 \cdot \beta} + \frac{\beta \cdot (1 - \nu_s)}{5} \right]$$

$$S_{2,3} = D_s \cdot b \cdot \left[ \frac{11}{210 \cdot \beta^2} + \frac{(9 - 19 \cdot \nu_s)}{240} \right]$$

$$S_{2,5} = D_s \cdot \left[ \frac{9}{70 \cdot \beta} - \frac{\beta \cdot (1 - \nu_s)}{5} \right]$$

$$S_{2,6} = D_s \cdot b \cdot \left[ -\frac{13}{420 \cdot \beta^2} + \frac{(9 + \nu_s)}{240} \right]$$

$$S_{2,8} = D_s \cdot \left[ -\frac{13}{35 \cdot \beta} + \frac{\beta \cdot (1 - \nu_s)}{10} \right]$$

$$S_{2,9} = -D_s \cdot b \cdot \left[ \frac{11}{210 \cdot \beta^2} + \frac{(3 - 13 \cdot \nu_s)}{240} \right]$$

$$S_{2,11} = -D_s \cdot \left[ \frac{9}{70 \cdot \beta} + \frac{\beta \cdot (1 - \nu_s)}{10} \right]$$

$$S_{2,12} = D_s \cdot b \cdot \left[ \frac{13}{420 \cdot \beta^2} - \frac{(3 + 7 \cdot \nu_s)}{240} \right]$$

$$S_{3,3} = D_s \cdot a \cdot b \cdot \left[ \frac{1}{105} \cdot \left( \beta^2 + \frac{1}{\beta^2} \right) + \frac{(27 - 37 \cdot \nu_s)}{720} \right]$$

$$S_{3,6} = D_s \cdot a \cdot b \cdot \left[ -\frac{1}{420} \cdot \left( 4 \cdot \beta^2 + \frac{3}{\beta^2} \right) + \frac{(9 + \nu_s)}{720} \right]$$

$$S_{3,9} = D_s \cdot a \cdot b \cdot \left[ -\frac{1}{420} \cdot \left( 3 \cdot \beta^2 + \frac{4}{\beta^2} \right) + \frac{(9 + \nu_s)}{720} \right]$$

$$S_{3,12} = D_s \cdot a \cdot b \cdot \left[ \frac{3}{420} \cdot \left( \beta^2 + \frac{1}{\beta^2} \right) - \frac{(9 + \nu_s)}{720} \right]$$

○ **Calculation of Joints Displacements, Support Reactions, and End Forces of Frame Elements**

Static analysis performed by YAY2020 follows the regular finite element solution method YAY2020 software superposing element load vector to create a system's general load vector. Combining the loads affect the degrees of freedom of each element, the local load vector of the elements is created. Using Hooke's law which is given in Eq.6, unknown system joints displacements, support reactions, and end forces of frame elements can be calculated.

$$F_{(n*1)}^{system} = K_{(n*n)}^{system} * U_{(n*1)}^{system} \quad (6)$$



Here,  $n$  is the size of the system stiffness matrix and simultaneously the system degrees of freedom.

### 3. RESULTS AND DISCUSSION

In this section, two numerical examples of YAY2020 program will be given and compared with the SAP2000 program.

○ **Timoshenko Cantilever Beam**

Timoshenko cantilever beam as seen in Figure 3 shows a plate represented by a coarse mesh of 12 rectangular elements with a total vertical concentrated load of 1000N applied to the free edge nodes of the plate. The calculated values by YAY2020 program for  $u$  and  $v$  displacements in the  $x$  and  $y$  directions, respectively, are shown in Figure 3 adjacent to each node. In addition, the values shown in parentheses are analytical solutions for  $u$  and  $v$  displacements obtained by Timoshenko and Goodier from equations based on the classical theory of Elasticity. The plate element modulus of elasticity  $E = 30 \times 10^6 N/cm^2$ , Poisson ratio  $\nu = 1/3$  and plate thickness  $t = 0.1 cm$ . Figure 3 indicates that YAY2020 gives almost the same results as Timoshenko's analytical solution and the error ratio is on the order of 1%. Table 2 shows the results getting with YAY2020 program is closer to Timoshenko's analytical solutions than Sap2000 with the same number of meshing elements. In the SAP2000, using more meshing element displacements results is getting closer to YAY2020 and therefore getting closer to Timoshenko analytical solution. Some results in YAY2020 have a different sign from those of SAP2000 due to the sign notation used in the programs.

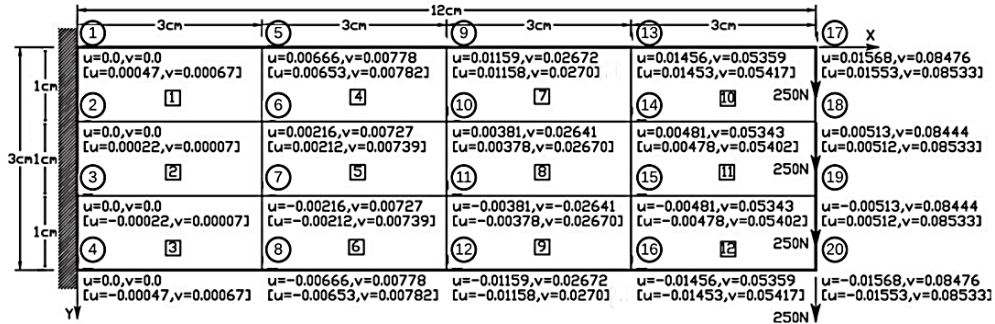


Figure 3. Comparison of displacements (cm) calculated by YAY2020 and elasticity theory [shown in parentheses][1]

Table 2. Joints displacements of Timoshenko beam calculated by YAY2020 and Sap2000

SAP2000 - Joint displacements				YAY2020 - Joint displacements			
Joint No	U1 cm	U3 cm	R2 Radius	Joint No	U1 cm	U3 cm	R2 Radius
1	0	0	0	1	0	0	0
2	0	0	0	2	0	0	0
3	0	0	0	3	0	0	0
4	0	0	0	4	0	0	0
5	8.01E-03	6.77E-03	4.87E-03	5	-7.78E-03	-6.66E-03	4.44E-03
6	7.42E-03	2.14E-03	4.55E-03	6	-7.27E-03	-2.16E-03	4.67E-03
7	7.42E-03	-2.14E-03	4.55E-03	7	-7.27E-03	2.16E-03	4.67E-03
8	8.01E-03	-6.77E-03	4.87E-03	8	-7.78E-03	6.66E-03	4.44E-03
9	2.72E-02	1.18E-02	7.96E-03	9	-2.67E-02	-1.16E-02	7.87E-03
10	2.70E-02	3.91E-03	8.01E-03	10	-2.64E-02	-3.82E-03	7.89E-03
11	2.70E-02	-3.91E-03	8.01E-03	11	-2.64E-02	3.82E-03	7.89E-03
12	2.72E-02	-1.18E-02	7.96E-03	12	-2.67E-02	1.16E-02	7.87E-03
13	5.46E-02	1.48E-02	1.02E-02	13	-5.36E-02	-1.46E-02	9.88E-03
14	5.45E-02	4.85E-03	9.91E-03	14	-5.34E-02	-4.81E-03	9.85E-03
15	5.45E-02	-4.85E-03	9.91E-03	15	-5.34E-02	4.81E-03	9.85E-03
16	5.46E-02	-1.48E-02	1.02E-02	16	-5.36E-02	1.46E-02	9.88E-03
17	8.61E-02	1.58E-02	1.07E-02	17	-8.48E-02	-1.57E-02	1.10E-02
18	8.60E-02	5.23E-03	1.07E-02	18	-8.44E-02	-5.13E-03	1.04E-02
19	8.60E-02	-5.23E-03	1.07E-02	19	-8.44E-02	5.13E-03	1.04E-02
20	8.61E-02	-1.58E-02	1.07E-02	20	-8.48E-02	1.57E-02	1.10E-02

○ **Shear Wall-Frame Structure**

To compare the shear wall-frame structure of the YAY2020 program with Sap2000, a 3-storey 4-span system is taken as shown in Figure 4. All Storey heights are  $h = 350 \text{ cm}$  and span distances  $L = 300 \text{ cm}$ . Shear walls are located between the 3rd and 4th axes in the x-direction. All Frame elements are square in shape and have the same material properties. Frame elements cross-sectional area  $A = 2500 \text{ cm}^2$ , Modulus of elasticity  $E = 13025000 \text{ N/cm}^2$ , a moment of inertia  $I = 520833.33 \text{ cm}^4$  and mass per unit volume  $\rho = 0.00025 \text{ kg/cm}^3$ . Shear wall elements have the same modulus of elasticity and mass per unit volume as frame elements. Shear wall elements thickness  $t = 50 \text{ cm}$  and Poisson ratio  $\nu = 0.2$ .  $1000 \text{ N}$  single loads applied on the top-left and top-right points of the structure.

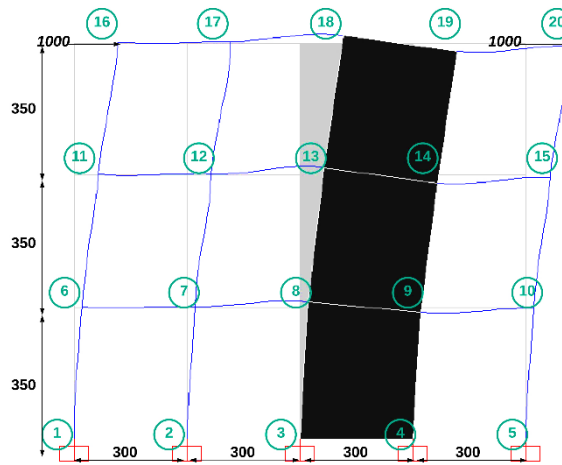


Figure 4. Shear Wall-Frame Structure

System joints deformations values obtained with YAY2020 compared with SAP2000 are given in Table 3. Some results in YAY2020 have a different signal from the SAP2000 results due to the sign notation used in the programs. System support reactions are given in Table 4. Selected five columns' and beams' end forces calculated by YAY2020 and SAP2000 are given in Tables 5 and 6.

Table 3. Joints displacements of Shear Wall-Frame Structure by YAY2020 and Sap2000

SAP2000 - Joint displacements				YAY2020 - Joint displacements			
Joint No	U1 cm	U3 cm	R2 Radius	Joint No	U1 cm	U3 cm	R2 Radius
1	0	0	0	1	0	0	0
2	0	0	0	2	0	0	0
3	0	0	0	3	0	0	0
4	0	0	0	4	0	0	0
5	0	0	0	5	0	0	0
6	1.96E-04	1.50E-05	6.40E-07	6	1.88E-04	1.48E-05	-6.15E-07
7	1.95E-04	1.90E-05	2.09E-07	7	1.87E-04	1.93E-05	-1.82E-07
8	1.91E-04	1.39E-04	9.28E-07	8	1.84E-04	1.33E-04	-9.35E-07
9	1.91E-04	-1.38E-04	9.31E-07	9	1.83E-04	-1.33E-04	-9.35E-07
10	1.93E-04	-3.40E-05	3.77E-07	10	1.85E-04	-3.53E-05	-3.46E-07
11	6.26E-04	2.50E-05	1.03E-06	11	6.00E-04	2.57E-05	-9.83E-07
12	6.24E-04	3.30E-05	3.97E-07	12	5.98E-04	3.35E-05	-3.61E-07
13	6.20E-04	2.06E-04	1.37E-06	13	5.94E-04	1.96E-04	-1.33E-06
14	6.20E-04	-2.05E-04	1.36E-06	14	5.94E-04	-1.95E-04	-1.33E-06
15	6.22E-04	-6.00E-05	7.34E-07	15	5.96E-04	-6.12E-05	-6.95E-07
16	1.20E-03	2.90E-05	8.82E-07	16	1.14E-03	2.97E-05	-8.44E-07
17	1.16E-03	4.00E-05	-6.83E-08	17	1.11E-03	4.09E-05	8.85E-08
18	1.14E-03	2.20E-04	1.41E-06	18	1.09E-03	2.07E-04	-1.34E-06
19	1.14E-03	-2.19E-04	1.43E-06	19	1.09E-03	-2.08E-04	-1.37E-06
20	1.17E-03	-7.10E-05	1.67E-07	20	1.12E-03	-7.29E-05	-1.41E-07

Table 4. Support reactions of Shear Wall-Frame Structure by YAY2020 and Sap2000

SAP2000 - Support reactions				YAY2020 - Support reactions			
Joint	F1	F2	M2	Joint	F1	F2	M2
No	cm	cm	N-cm	No	N	N	N-cm
1	-36.69	-331.28	-9446.43	1	-37.3408	-337.14	9445.47
2	-69.26	-425.07	-13110.66	2	-72.0459	-437.871	13470
3	-921.3	-3867.53	-59314.1	3	-915.959	-4627.6	-65504.4
4	-917.18	3842.16	-58652.07	4	-916.836	4600.8	-64137.4
5	-55.58	781.72	-11509.42	5	-57.8184	801.811	11753.8

Table 5. Selected five columns' end forces calculated of Shear Wall-Frame Structure by YAY2020 and Sap2000

Column	YAY2020 - Column end forces						SAP2000 - Column end forces					
	i end			j end			i end			j end		
	P	V2	M3	P	V2	M3	P	V2	M3	P	V2	M3
No	N	N	N-cm	N	N	N-cm	N	N	N-cm	N	N	N-cm
1	-337.14	37.34	9445.47	337.14	-37.34	3623.81	331.28	36.69	9446.43	331.28	36.69	-3393.52
3	801.81	57.82	11753.80	-801.81	-57.82	8482.65	-781.72	55.58	11509.42	-781.72	55.58	-7942.00
5	-321.95	146.50	26485.00	321.95	-146.50	24790.60	316.64	141.61	25669.83	316.64	141.61	-23893.73
7	-91.67	104.23	17582.50	91.67	-104.23	18899.30	90.64	103.66	17438.36	90.64	103.66	-18844.01
9	266.45	174.46	27904.40	-266.45	-174.46	33155.50	-263.86	171.06	27251.77	-263.86	171.06	-32619.40

Table 6. Selected five beams' end forces calculated of Shear Wall-Frame Structure by YAY2020 and Sap2000

Beam	YAY2020 - Beam end forces						SAP2000 - Beam end forces					
	i end			j end			i end			j end		
	P	V2	M3	P	V2	M3	P	V2	M3	P	V2	M3
No	N	N	N-cm	N	N	N-cm	N	N	N-cm	N	N	N-cm
1	23.91	-91.30	-16084.80	-23.91	91.30	-11304.10	-23.71	89.60	15815.36	-23.71	89.60	-11064.86
3	-48.39	-213.19	-35232.20	48.39	213.19	-28723.60	47.19	204.53	33741.36	47.19	204.53	-27618.59
5	111.91	-306.86	-40670.80	-111.91	306.86	-51387.00	-112.63	298.83	39456.15	-112.63	298.83	-50193.37
7	895.77	-91.67	-18899.30	-895.77	91.67	-8602.10	-896.34	90.64	18844.01	-896.34	90.64	-8346.82
9	-825.54	-266.45	-46779.80	825.54	266.45	-33155.50	828.94	263.86	46537.54	828.94	263.86	-32619.40

## 4. CONCLUSIONS

Frame elements give roughly the same results in both Sap2000 and YAY2020 because of formulas used in these programs are close to each other.

In rectangular elements (which are used in shear-wall elements), in Sap2000 if only the plane stress element is used, the rotation values will be neglected, resulting in unreal element behavior. In the rectangular element formulation which used in YAY2020 program, the lateral and vertical displacements in addition to the rotation of element joints can be calculated. This formulation is closer to the real element behavior.

To obtain the real behavior of the rectangular element in Sap2000, it is necessary to use a large number of meshing shell elements instead of using a plane stress element. However, this takes a long time to analyze the system and increases the computational burden.

YAY2020 rectangular elements analysis results are closer to Timoshenko's analytical solution than those obtained with Sap2000.

In the calculation of support reactions and end forces of elements, both YAY2020 and SAP2000 give close results. However, some results show different signs because of the sign notation acceptance of the used formulation.

The results of joints deformations in YAY2020 program are lower than those of SAP2000 because the stiffness matrix in YAY2020 program is bigger than the other used in SAP2000.

## ACKNOWLEDGMENTS

This paper is prepared using the data of the master thesis titled "Behavior of High-Rise Planar Shear-Wall-Frame Structures under Dynamic Loads" by Ragib Sabah. The thesis is supervised by Prof. Namik Kemal

Oztorun. The other author, Baris Sayin, put a lot of effort into organizing data, conceptualizing, methodology, writing-reviewing, and editing.

## REFERENCES

- [1]. Oztorun N.K., (2006) "A rectangular finite element formulation", Finite Elem. Anal.Des. 42 (12), 1031–1052.
- [2]. Oztorun N.K., (2007) Reply to "discussion on: 'Rectangular finite element formulation'", Finite Elements in Analysis and Design 43 (2007) 733 – 736.
- [3]. Ed. Wilson, (2002) "Three-Dimensional Static and Dynamic Analysis of Structures", Computers and Structures Inc. University of California, Berkeley, USA.
- [4]. Ed. Wilson, (1991) "Computer Assisted Learning of Static and Dynamic Analysis of Structural Systems user's manual", University of California, Berkeley, USA.
- [5]. Ed. Wilson, E. Ray, W. Clough, (1952) "Dynamic response by step-by-step matrix analysis", Computers in Civil Engineering Symposium.
- [6]. Computers and Structures, Inc. (2016) "SAP2000 CSI Analysis Reference Manual, Structural Analysis Program", California, Berkeley, USA.
- [7]. Bathe K.J. Wilson, E. L. (1976) "Numerical Methods in Finite Element Analysis", Prentice-Hall, New Jersey, 528s.
- [8]. Bathe K.J., (2014) "Finite Element Procedures Second edition", Prentice-Hall, Pearson Education, Inc. 978-0-9790049-5-7.
- [9]. M. Turner, R. Clough, H. Martin, L. Topp, (1954) "Stiffness and Deflection Analysis of Complex Structures", New York, January 25-29.
- [10]. D. V. Griffiths, (1994) "Stiffness matrix of the four-node quadrilateral element in the closed-form", Colorado School of Mines, Golden, Colorado 80401, USA.
- [11]. E., Oztorun, 2020, "Koprulerin Deprem Etkileri Altındaki Davranislari", Thesis (PhD), Istanbul University.
- [12]. E., Oztorun, C., Alhan, S., Erdem ve N.K., Oztorun, 2017, "Koprulerin Deprem Etkileri Altındaki Davranislari", 20. Ulusal Mekanik Kongresi, 05-09 Eylül. 2017, Uludag Universitesi, Bursa, 938-947.
- [13]. Adams J.C., Brainerd W.S., Martin J.T., Smith B.T., Wagener J.L. (1992) "Fortran 90 Handbook". Library of Congress Catalog Card Number 91-77211.
- [14]. William H. Press, Saul A. Teukolsky, William T. Vetterling, Brain P.Flannery, (1996) "Fortran 90 Numerical Recipes". V.2 Library of Congress catalog card number 96-5567.
- [15]. Timoshenko S., Goodier J.N., (1951) "Theory of Elasticity", McGraw-Hill, New York.

## BIOGRAPHY

Ragib Sabah was born in 1993. He is also known as Ragheb Alsabbagh. In 2014 Mr. Sabah started his undergraduate degree in the Civil Engineering Department at Pamukkale University in Turkey and graduated in 2018 with high honor degree. In 2021, Mr. Sabah completed his master's degree at Istanbul University-Cerrahpasa. He is interested in computational sciences, applicable technology, and management areas.

# The Developed FEA-Based Program for Planar Dynamic Analysis with a Special 12x12 Rectangular Element

Ragib Sabah<sup>1</sup>, Namik Kemal Ozturun<sup>2</sup>, Baris Sayin<sup>3</sup>

---

## Abstract

There are several widely used structural softwares to analyze buildings under dynamic loads, but many of these programs use arithmetic formulations to calculate the mass and stiffness matrices of shear walls with only 8x8 elements that ignore the rotational mass and stiffness values. Also, during the dynamic analysis, a system diagonal mass matrix containing only elements in the x and y directions is used. The previously mentioned calculation assumptions may lead to unrealistic structural calculations besides these assumptions should be replaced by more realistic calculation formulas and methods. In this paper, a two-part FEA computational program was developed to provide actual structural dynamic analysis. The first part of the program is called YAY2020-Static encoded by FORTRAN compiler and the second one is called YAY-Dynamic encoded by MATLAB interpreter. In YAY2020 program, a special rectangular element formula with 12x12 elements and three degrees of freedom at each element's nodes is used to calculate shear wall mass and stiffness matrices to obtain system full-size stiffness and mass matrices that contain both diagonal and non-diagonal elements. Results obtained using YAY2020 software will be compared with some structural analysis techniques such as shear building and wide column, to study the feasibility of using these techniques. All obtained results by YAY2020 will be compared with the commonly use FEA structure software SAP2000.

**Keywords:** Dynamic analysis software, FORTRAN, Finite element analysis (FEA), 12x12 Mass matrix, Shear building, Wide column

---

## 1. INTRODUCTION

Turkey is one of the countries which settled in a strong seismic active location due to the presence of many seismic faults. These seismic movements cause significant physical and economic damages to building elements, which leads to catastrophic damage and loss of life. Dynamic loads are the most important factors causing structural collapse. Although many dynamic loads such as wind and blast loads may cause significant damage to buildings, earthquakes effect are the most dangerous dynamic load that structures are exposed to, because earthquakes not only affect a single building such blast loads but also affect a large scale, causing damage to entire cities and to many buildings at the same time.

Ozturun [1, 2] started his works on finite element methods in the structural engineering field, in 2006 presented the first rectangular stress elements with 12x12 matrix elements adding rotational values and the mass matrix with real and full diagonal and non-diagonal values. Wilson [3-7] introduced a set of finite element structural analysis programs which called CAL programs. In 1975 his studies were considered bases for many programs such as SAP2000, SAFE, and ETABS. In these programs, shear-wall stiffness and mass matrices contain only 8x8 elements with no stiffness and mass rotation values. So there is no rotation of the element in the vertical direction. The rotation and stress of the joints are calculated depending on the joint's movement laterally or vertically. Bathe [7, 8] presented the detailed procedure of the finite element in his book "Finite Element

---

<sup>1</sup> Corresponding author: Istanbul University-Cerrahpasa, Institute of Graduate Sciences, 34320, Avcilar/ Istanbul, Turkey [ragib.sabah@ogr.iuc.edu.tr](mailto:ragib.sabah@ogr.iuc.edu.tr)

<sup>2</sup> Istanbul University-Cerrahpasa, Department of Civil Engineering 34320, Istanbul, Turkey, [kemal@iuc.edu.tr](mailto:kemal@iuc.edu.tr)

<sup>3</sup> Istanbul University-Cerrahpasa, Department of Civil Engineering 34320, Istanbul, Turkey, [barsavin@iuc.edu.tr](mailto:barsavin@iuc.edu.tr)

Procedures ". This book has been a reference for many researchers in the field. Newmark [9] developed the one-step integration method to solve structural dynamics problems under blast and seismic loads. For 60 years, Newmark's method has been applied in the dynamic analysis of many applications such as structures. Chopra [10] explained the procedures of structural dynamic analysis in his book "Dynamics of Structures: Theory and Applications to Earthquake Engineering", with different methods of calculations. Oztorun and others [11, 12] made dynamic analyses of structural systems using the GP-DYNA computer program developed by Oztorun in his doctoral thesis; stated that current analysis methods may not provide sufficient assurance if vertical earthquake records are used.

During calculating the effect of earthquakes on structures general system mass and stiffness matrices must be calculated. Many literature programs considered the mass matrix as a diagonal matrix, and the mass of each floor is the same in the x and y directions with no rotational mass values. Also in calculating mass and stiffness matrices of shear wall elements, literature programs calculate it as just a matrix with 8x8 elements ignoring the rotational values. In this study, a two-part computational program based on the finite element method will be encoded using the FORTRAN compiler and MATLAB interpreter to find the response of a planar structure with a known geometry under dynamic loads. This program is called YAY2020. In principle, FORTRAN encoded YAY2020-Static software calculates the mass and stiffness matrices for each of the system elements individually and superposing them together to get system general mass and stiffness matrices. Then these matrices will be used in dynamic calculation by YAY2020-Dynamic. The system mass and stiffness matrices computed in this study contain both diagonal and non-diagonal elements as well as 12x12 elements of shear walls mass and stiffness matrices. To achieve this special formulation is used to calculate the rotational degrees of the plate elements. This formula is developed by Oztorun [1-2], and the accuracy of this formulation had been proven and demonstrated by comparing it with Timoshenko and Goodier [2, 13] analytical solution. All results obtained by YAY2020 will be compared with widely used FEA software such as SAP2000. In light of these features, this study aims to present a program that has different and more realistic calculation methods than the existing ones.

## 2. MATERIALS AND METHODS

In this section, the YAY2020-Static and YAY2020-Dynamic mechanisms are introduced with an overview of used mathematical formulas.

### ○ *Frame Elements Mass Matrix*

The frame element is shown in Figure 1. The element has two nodes (i and j) with three degrees of freedom at each end. The axis across from I to J is called the local x-axis and the perpendicular on the local x-axis is called the local y-axis these two axes formed the local coordinate system of the planar frame element.

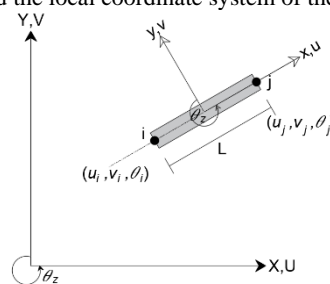


Figure 1. Planar frame element

The element length  $L$  is calculated as Eq.1.

$$L = \sqrt{(X_j - X_i)^2 + (Y_j - Y_i)^2} \quad (1)$$

Frame element local mass matrix is written as Eq.2. [3, 8]

$$M_{e.l.}^{Frame} = WA \frac{1}{420} \begin{bmatrix} 140 & 0 & 0 & 70 & 0 & 0 \\ & 156 & 22L & 0 & 54 & -13L \\ & & 4L^2 & 0 & 13L & -3L^2 \\ & & & 140 & 0 & 0 \\ & & & & 156 & -22L \\ & & & & & 4L^2 \end{bmatrix} \quad (2)$$

*symmetrical*

Where,

A = cross-sectional area and W = mass density

The mass matrix in Eq.2 is obtained for the local coordinates of the element. To transfer it to a global structure coordinate system a transformation matrix must be used. The planar transformation matrix is given in Eq.3. [3, 8]

$$R = \begin{bmatrix} \cos(\theta) & \sin(\theta) & 0 & 0 & 0 & 0 \\ -\sin(\theta) & \cos(\theta) & 0 & 0 & 0 & 0 \\ 0 & 0 & 1 & 0 & 0 & 0 \\ 0 & 0 & 0 & \cos(\theta) & \sin(\theta) & 0 \\ 0 & 0 & 0 & -\sin(\theta) & \cos(\theta) & 0 \\ 0 & 0 & 0 & 0 & 0 & 1 \end{bmatrix} \quad (3)$$

Here;

$$\cos(\theta) = \frac{X_j - X_i}{L} \quad (4)$$

$$\sin(\theta) = \frac{Y_j - Y_i}{L} \quad (5)$$

The global frame element mass matrix is obtained by multiplying the transpose of the transformation matrix by the local mass matrix and then multiplies the result by the transformation matrix itself, as given in Eq.6.

$$M_{e.g.}^{frame} = [R^T] \cdot [M_{e.l.}^{frame}] \cdot [R] \quad (6)$$

Here,

$M_{e.g.}^{frame}$ : Frame element global mass matrix.

$R^T$ : Transposition of the transformation matrix.

$M_{e.l.}^{frame}$ : Frame element local mass matrix.

### ○ Shear Wall Elements Mass Matrix

The shear wall element is analyzed as a rectangular stress element. A special formulation presented by Oztorun is used to analyze rectangular stress elements in YAY2020 program. Figure 2 shows the plane stress rectangular element with four nodes and three degrees of freedom at each node (1 rotation and 2 displacements). The plane stress element mass matrix is given in Table 1.

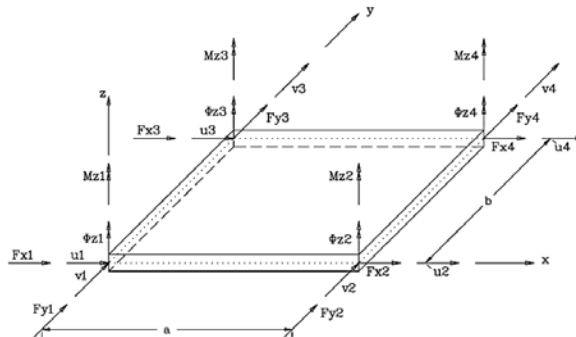


Figure 2. Generalized forces and displacements for finite plate elements for plane stress problems [1]

Table 8. Stiffness matrix of plane stress element [1]

$A^T$	$A_{X1}$	$A_{Y1}$	$\theta_{Z1}$	$A_{X2}$	$A_{Y2}$	$\theta_{Z2}$	$A_{X3}$	$A_{Y3}$	$\theta_{Z3}$	$A_{X4}$	$A_{Y4}$	$\theta_{Z4}$
I/J	1	2	3	4	5	6	7	8	9	10	11	12
1	$M_{S1,1}$	0	$M_{S1,3}$	$M_{S1,4}$	0	$M_{S1,6}$	$M_{S1,7}$	0	$M_{S1,9}$	$M_{S1,10}$	0	$M_{S1,12}$
2		$M_{S1,1}$	$M_{S2,3}$	0	$M_{S1,7}$	$M_{S2,6}$	0	$M_{S1,4}$	$M_{S2,9}$	0	$M_{S1,10}$	$M_{S2,12}$
3			$M_{S3,3}$	$M_{S1,6}$	$-M_{S2,6}$	$M_{S3,6}$	$-M_{S1,9}$	$M_{S2,9}$	$M_{S3,9}$	$-M_{S1,12}$	$-M_{S2,12}$	$M_{S3,12}$
4				$M_{S1,1}$	0	$M_{S1,3}$	$M_{S1,10}$	0	$M_{S1,12}$	$M_{S1,7}$	0	$M_{S1,9}$
5					$M_{S1,1}$	$-M_{S2,3}$	0	$M_{S1,10}$	$-M_{S2,12}$	0	$M_{S1,4}$	$-M_{S2,9}$
6						$M_{S3,3}$	$-M_{S1,12}$	$M_{S2,12}$	$M_{S3,12}$	$-M_{S1,9}$	$-M_{S2,9}$	$M_{S3,9}$
7							$M_{S1,1}$	0	$-M_{S1,3}$	$M_{S1,4}$	0	$-M_{S1,6}$
8								$M_{S1,1}$	$M_{S2,3}$	0	$P_{1,7}$	$M_{S2,6}$
9									$M_{S3,3}$	$-M_{S1,6}$	$-M_{S2,6}$	$M_{S3,6}$
10										$M_{S1,1}$	0	$-M_{S1,3}$
11											$M_{S1,12}$	$-M_{S2,3}$
12												$M_{S3,3}$

Plane stress element mass matrix parameters are given as follows: [1]

$$K_S = \frac{\rho_S \cdot a \cdot b \cdot t_S}{176400}$$

$$M_{S_{1,1}} = K_S \cdot 21840$$

$$M_{S_{1,6}} = -K_S \cdot 1540 \cdot b$$

$$M_{S_{1,10}} = K_S \cdot 3780$$

$$M_{S_{2,6}} = -K_S \cdot 1820 \cdot a$$

$$M_{S_{3,3}} = K_S \cdot 560 \cdot (a^2 + b^2)$$

$$M_{S_{3,12}} = -K_S \cdot 210 \cdot (a^2 + b^2)$$

$$M_{S_{1,3}} = -K_S \cdot 3080 \cdot b$$

$$M_{S_{1,7}} = K_S \cdot 7560$$

$$M_{S_{1,12}} = K_S \cdot 910 \cdot b$$

$$M_{S_{2,9}} = K_S \cdot 1540 \cdot a$$

$$M_{S_{3,6}} = K_S \cdot 140 \cdot (-3a^2 + 2b^2)$$

$$M_{S_{1,4}} = K_S \cdot 10920$$

$$M_{S_{1,9}} = K_S \cdot 1820 \cdot b$$

$$M_{S_{2,3}} = K_S \cdot 3080$$

$$M_{S_{2,12}} = -K_S \cdot 910 \cdot a$$

$$M_{S_{3,9}} = K_S \cdot 140 \cdot (2a^2 - 3b^2)$$

### ○ Equation of Motion of the Dynamical System

The system has mass, stiffness, and damping and has movement in just u direction is called a single degree of freedom (Figure 3). According to Newton's second law of motion, the equation of motion of this system is written as Eq.7 [10].

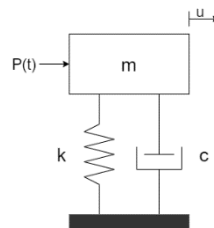


Figure 3. Single degree of freedom system

$$m\ddot{u} + c\dot{u} + ku = -m\ddot{u}_g \text{ or } p(t) \quad (7)$$

Where;

$u$  : Displacement vector

$\dot{u}$  : Velocity vector

$\ddot{u}$  : Acceleration vector

$\ddot{u}_g$  : Ground motion acceleration vector (Earthquake data)

$m$  : System mass

$k$  : System stiffness

$c$  : System damping

$p(t)$ : Dynamic load

### ○ Time History Analysis

Time history analysis was performed in YAY2020 software using the Newmark method. Newmark method depends on numerical integration methods to solve Eq.7. In systems of multi-degree freedom, there is a mode



that corresponds to each degree of freedom. To consider these modes and study structure as a single part, the equation of motion should be written as Eq.8 [3-8, 10].

$$\Phi^T m \Phi \ddot{q} + \Phi^T c \Phi \dot{q} + \Phi^T k \Phi q = -\Phi^T m \ddot{u}_g(t) \quad \text{or} \quad \Phi^T p(t) \quad (8)$$

Eq.8 can be written also as Eq.9.

$$M \ddot{q} + C \dot{q} + K q = F(t) \quad (9)$$

Here,

**M**: Modal mass matrix

**K**: Modal stiffness matrix

**C**: Modal damping matrix

**q**: Modal displacement vector

**I**: The identity matrix equal in size with the system degree of freedom

The modal matrices M, K, and C here are diagonal matrices. Meanwhile, m, k, and c system matrices have both diagonal and non-diagonal elements

In the Newmark numerical calculation method, the displacement and velocity changes by the time  $\Delta t$  according to Taylor's series are given in Eqs.10 and 11.

$$u_t = u_{t-\Delta t} + \Delta t \dot{u}_{t-\Delta t} + \frac{\Delta t^2}{2} \ddot{u}_{t-\Delta t} + \frac{\Delta t^3}{6} \dddot{u}_{t-\Delta t} + \dots \quad (10)$$

$$\dot{u}_t = \dot{u}_{t-\Delta t} + \Delta t \ddot{u}_{t-\Delta t} + \frac{\Delta t^2}{2} \dddot{u}_{t-\Delta t} + \dots \quad (11)$$

Newmark abbreviated Eq.10 and Eq.10 by using  $\beta$  and  $\gamma$  Newmark constants as Eqs.12 and 13.

$$u_t = u_{t-\Delta t} + \Delta t \dot{u}_{t-\Delta t} + \frac{\Delta t^2}{2} \ddot{u}_{t-\Delta t} + \beta \Delta t^3 \ddot{u}_{t-\Delta t} \quad (12)$$

$$\dot{u}_t = \dot{u}_{t-\Delta t} + \Delta t \ddot{u}_{t-\Delta t} + \gamma \Delta t^2 \ddot{u}_{t-\Delta t} \quad (13)$$

The acceleration equation can be written in Eq.14 assuming that the acceleration is linear in the time step.

$$\ddot{u}_t = \frac{(\dot{u}_t - \dot{u}_{t-\Delta t})}{\Delta t} \quad (14)$$

If Eq.14 is written in Eq.12 and Eq.13 the standard form of Newmark equations is obtained as Eqs.15 and 16.

$$u_t = u_{t-\Delta t} + \Delta t \dot{u}_{t-\Delta t} + \left(\frac{1}{2} - \beta\right) \Delta t^2 \ddot{u}_{t-\Delta t} + \beta \Delta t^2 \ddot{u}_t \quad (15)$$

$$\dot{u}_t = \dot{u}_{t-\Delta t} + (1 - \gamma) \Delta t \ddot{u}_{t-\Delta t} + \gamma \Delta t \ddot{u}_t \quad (16)$$

Displacements, velocities, and accelerations of each node of the system are obtained by iteration of the last two equations by the time.

### ○ Shear Building Analysis

The type of structure that is expected to move only horizontally under various static or dynamic loads without rotation of a horizontal section on the floor level is called Shear Building. It's also a type of idealization of a building to resist only shear forces without any bending as shown in Figure 4.

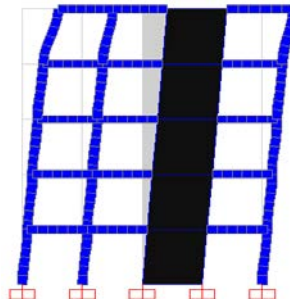


Figure 4. Shear building system example

This method is a quick method for determining the dominant period of structures. It is based on calculating the mass and stiffness of each floor separately and obtaining the general mass and stiffness matrices of the structure. The mass and stiffness matrices of a 5-storey shear structure like shown in Figure 4 are written as Eqs.17 and 18, respectively [14].

$$M_{sis} = \begin{bmatrix} m_1 & 0 & 0 & 0 & 0 \\ 0 & m_2 & 0 & 0 & 0 \\ 0 & 0 & m_3 & 0 & 0 \\ 0 & 0 & 0 & m_4 & 0 \\ 0 & 0 & 0 & 0 & m_5 \end{bmatrix} \quad (17)$$

$$K_{sis} = \begin{bmatrix} k_1 + k_2 & -k_2 & 0 & 0 & 0 \\ -k_2 & k_2 + k_3 & -k_3 & 0 & 0 \\ 0 & -k_3 & k_3 + k_4 & -k_4 & 0 \\ 0 & 0 & -k_4 & k_4 + k_5 & -k_5 \\ 0 & 0 & 0 & -k_5 & k_5 \end{bmatrix} \quad (18)$$

Here,

$M_{sis}$ : System mass matrix

$K_{sis}$ : System stiffness matrix

$m_i$ : Total mass of i floor

$k_i$ : Total stiffness of i floor

### ○ Wide Column Analysis

A wide column is an easy method to analyze structure without using shear wall formulations. It depends on replacing the shear wall with a wide column that has the same rigidity and mass as the shear wall and places rigid beams at each floor level as shown in Figure 5.

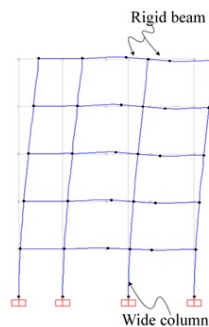


Figure 5. Wide column system example

## 3. RESULTS AND DISCUSSION

In this section, some examples will be solved dynamically using YAY2020 and compared with SAP2000.

### ○ Shear Wall-Frame Structure

A 3-storey 4-span shear wall-frame structure is analyzed by YAY2020 (Figure 6). All storey heights are  $h = 350 \text{ cm}$  and span distance  $L = 300 \text{ cm}$ . Shear walls are located between the 3rd and 4th axes. The properties of all frame elements are the same and they are square in shape. Frame elements cross sectional-area  $A = 2500 \text{ cm}^2$ , Modulus of elasticity  $E = 13025000 \text{ N/cm}^2$ , a moment of inertia  $I = 520833.33 \text{ cm}^4$  and mass per unit volume  $\rho = 0.00025 \text{ kg/cm}^3$ . Shear wall elements have the same modulus of elasticity and mass per unit volume of frame elements. Shear wall elements thickness  $t = 50 \text{ cm}$  and Poisson ratio  $\nu = 0.2$ . A  $1000 \text{ N}$  single loads applied on the top-left and top-right points of the structure. Figure 7 shows the results of the time history analysis of the shear wall-frame structure as a displacement-time graph of joint 20 in x-direction under the Chūetsu 6.6 magnitude earthquake which happened in Japan in 2007. The obtained modal analysis result

by YAY2020 and Sap2000 are given in Table 2. The table shows that YAY2020 can find 45 modes meanwhile; the SAP2000 can just find 30 modes.

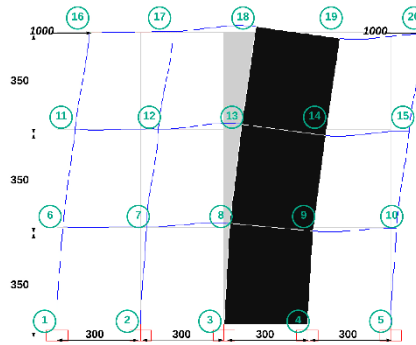


Figure 6. Shear Wall-Frame Structure

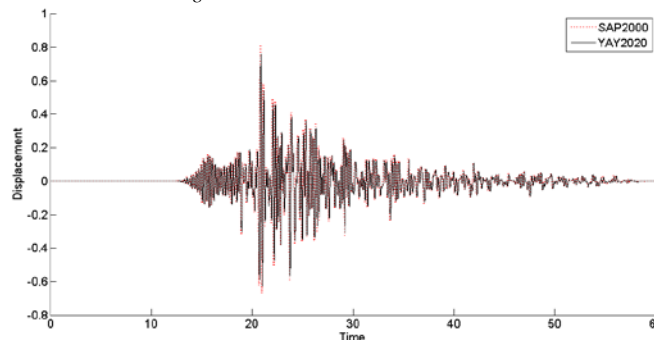


Figure 7. Shear wall-frame structure displacement-time graph

Table 2. Modal analysis of the shear wall-frame structure

SAP2000 – Modal analysis					YAY2020 - Modal analysis				
Mode	Period	Frequency	Angular frequency	Eigenvalues	Mode	Period	Frequency	Angular frequency	Eigenvalues
No	sec	cyc/sec	rad/sec	rad2/sec2	No	sec	cyc/sec	rad/sec	rad2/sec2
1	0.23965	4.17	26.22	687.40	1	0.2365	4.23	26.56	705.65
2	0.06172	16.20	101.80	10363.00	2	0.0798	12.52	78.69	6191.98
3	0.05064	19.75	124.09	15397.00	3	0.0554	18.06	113.45	12871.27
4	0.04506	22.19	139.45	19446.00	4	0.0488	20.50	128.78	16583.93
5	0.04456	22.44	141.01	19884.00	5	0.0415	24.11	151.47	22943.98
6	0.04011	24.93	156.66	24543.00	6	0.0407	24.55	154.25	23794.06
7	0.03809	26.26	164.97	27214.00	7	0.0392	25.54	160.45	25745.63
8	0.03180	31.45	197.59	39040.00	8	0.0339	29.47	185.19	34296.32
9	0.02797	35.75	224.64	50464.00	9	0.0327	30.63	192.44	37032.71
10	0.02589	38.63	242.71	58910.00	10	0.0312	32.00	201.09	40436.20
11	0.02038	49.06	308.24	95012.00	11	0.0306	32.65	205.15	42087.69
12	0.01981	50.49	317.24	100640.00	12	0.0293	34.14	214.49	46007.44
13	0.01924	51.99	326.64	106690.00	13	0.0254	39.32	247.06	61039.49
14	0.01721	58.12	365.16	133340.00	14	0.0239	41.77	262.47	68888.93
15	0.01717	58.25	365.99	133950.00	15	0.0223	44.82	281.64	79322.14
16	0.01715	58.31	366.35	134220.00	16	0.0206	48.59	305.32	93219.59
17	0.01605	62.30	391.42	153210.00	17	0.0192	52.08	327.24	107082.83
18	0.01513	66.09	415.27	172450.00	18	0.0175	57.20	359.39	129157.94
19	0.01470	68.01	427.32	182600.00	19	0.0170	58.82	369.58	136591.09
20	0.01435	69.68	437.82	191680.00	20	0.0164	61.11	383.95	147418.32
21	0.01432	69.85	438.85	192590.00	21	0.0146	68.61	431.06	185811.85
22	0.01315	76.04	477.78	228270.00	22	0.0142	70.38	442.20	195536.48
23	0.01285	77.80	488.82	238950.00	23	0.0137	72.90	458.03	209794.57
24	0.01248	80.15	503.61	253630.00	24	0.0135	74.33	467.02	218111.60
25	0.01247	80.18	503.79	253810.00	25	0.0127	78.71	494.52	244554.70

26	0.01197	83.54	524.89	275510.00	26	0.0127	79.05	496.68	246693.99
27	0.01120	89.26	560.86	314560.00	27	0.0119	83.72	526.05	276732.32
28	0.01105	90.50	568.64	323360.00	28	0.0112	89.25	560.75	314445.91
29	0.00981	101.96	640.62	410400.00	29	0.0110	91.19	572.95	328270.69
30	0.00859	116.48	731.88	535640.00	30	0.0104	96.59	606.92	368355.92
					31	0.0103	96.81	608.31	370036.87
					32	0.0097	102.68	645.13	416195.93
					33	0.0090	110.94	697.06	485895.27
					34	0.0085	117.96	741.16	549313.12
					35	0.0083	120.35	756.16	571784.18
					36	0.0075	134.11	842.62	710005.68
					37	0.0072	138.05	867.40	752382.60
					38	0.0066	152.30	956.93	915721.14
					39	0.0059	168.39	1058.01	1119385.88
					40	0.0051	196.84	1236.81	1529695.64
					41	0.0050	200.00	1256.63	1579119.41
					42	0.0048	206.24	1295.86	1679246.66
					43	0.0048	208.54	1310.32	1716941.94
					44	0.0043	230.93	1450.97	2105302.50
					45	0.0033	300.63	1888.88	3567881.43

○ **Period-Based Comparison of Shear Building and Wide Column**

A 5-story planar shear wall-frame system which is shown in Figure 4 adopted to study.

Table 3. Period analysis-based comparison of the normal FEM, shear building, and wide column methods

Mode number	Normal FEM		Wide Column		Shear building	
	YAY2020	SAP2000	YAY2020	SAP2000	YAY2020	SAP2000
1	0.48545	0.49573	0.47530	0.50270	0.50559	0.51791
2	0.13537	0.12554	0.11294	0.12730	0.17419	0.17843
3	0.10084	0.07821	0.07723	0.07825	0.11179	0.11452
4	0.07569	0.07005	0.06807	0.07022	0.08861	0.09077
5	0.06379	0.06517	0.06001	0.06517	0.07951	0.08145
6	0.06220	0.06092	0.05429	0.06076		
7	0.05564	0.05791	0.04881	0.06001		
8	0.04458	0.04064	0.03564	0.04266		
9	0.03848	0.03692	0.03460	0.03779		
10	0.03543	0.03243	0.03135	0.03150		
Max. mode No.	75	50	60	40	5	5

All floors' height is 350 cm. All elements Modulus of elasticity =  $3180098.312 N/cm^2$ , Poisson ratio  $\nu = 0.2$  and unit volume mass of concrete  $\rho = 0.00025 kg/cm^3$ . All frame elements cross sectional-area  $A = 2500 cm^2$  and moment of inertia =  $520833.33 cm^4$ . Table 3 comparing the first system 10 periods calculated with normal FEM, wide column, and shear building analyzing methods.

#### 4. CONCLUSIONS

In the modal analysis, YAY2020 can find more modes than SAP2000. Since SAP2000 isn't added the angular rotation perpendicular to the plate into the calculation of shear wall stiffness and mass matrices and the system mass matrix has just diagonal elements. These reasons decreased the degree of freedom of the system causing decreased mode's number.

The displacement values calculated by YAY2020 are lower than those calculated by SAP2000 because YAY2020 uses a full stiffness matrix, which a little bit increased the rigidity of the structure.

The modal analysis values obtained using a wide column are close to the values obtained using a regular shear wall. Because the wide column and shear building have the same mass and stiffness values. So, building mass and stiffness matrices are preserved as a whole.

Shear building analysis quickly gives the dominant period of the structure and this value is close to the real one.

#### ACKNOWLEDGMENTS

This paper is prepared using the data of the master thesis titled "Behavior of High-Rise Planar Shear-Wall-Frame Structures under Dynamic Loads" by Ragib Sabah. The thesis is supervised by Prof. Namik Kemal

Oztorun. The other author, Baris Sayin, put a lot of effort into organizing data, conceptualizing, methodology, writing-reviewing, and editing.

## REFERENCES

- [1]. Oztorun N.K., (2006) "A rectangular finite element formulation", Finite Elem. Anal. Des. 42 (12), 1031–1052.
- [2]. Oztorun N.K., (2007) Reply to "discussion on: 'Rectangular finite element formulation'", Finite Elements in Analysis and Design 43, 733 – 736.
- [3]. Ed. Wilson, (2002) "Three-Dimensional Static and Dynamic Analysis of Structures", Computers and Structures Inc. University of California, Berkeley, USA.
- [4]. Computers and Structures, Inc. (2016) "SAP2000 CSI Analysis Reference Manual, Structural Analysis Program", California, Berkeley, USA.
- [5]. Ed. Wilson, (1991) "Computer Assisted Learning of Static and Dynamic Analysis of Structural Systems user's manual", University of California, Berkeley, USA.
- [6]. Ed. Wilson, E. Ray, W. Clough, (1952) "Dynamic response by step-by-step matrix analysis", Computers in Civil Engineering Symposium.
- [7]. Ed. Wilson, Bathe K.J., L. Farhoomand, (1973) "Nonlinear dynamic analysis of complex structures", earthquake engineering and structural dynamics, 1, 241-252
- [8]. Bathe K.J., (2014) "Finite Element Procedures Second edition", Prentice-Hall, Pearson Education, Inc. 978-0-9790049-5-7.
- [9]. Newmark, (1959) "A method of computation for structural dynamics'", Engineering Mechanics Division. 2094.
- [10]. Chopra, A.K., (1995) "Dynamics of Structures: Theory and Applications to Earthquake Engineering", Prentice-Hall, Englewood Cliffs, New Jersey, ISBN: 0-13-855214-2.
- [11]. E., Oztorun, 2020, "Koprulerin Deprem Etkileri Altındaki Davranislari", Thesis (PhD), Istanbul University.
- [12]. E., Oztorun, N.K., Oztorun ve C., Alhan 2019, "Yapilarin Dusey Deprem Etkisi Altındaki Davranislari: Bir Kopru Ornegi", 21. Ulusal Mekanik Kongresi, 02-06 Eylul. 2019, Nigde Omer Halisdemir Universitesi, Nigde, 57-65.
- [13]. Timoshenko S., Goodier J.N., (1951) "Theory of Elasticity", McGraw-Hill, New York.
- [14]. Paz M., Leigh W., (1991) "Structural Dynamics", Kluwer Academic Publishers Springer Science Business Media Dordrecht.
- [15]. Adams J. C., Brainerd W.S., Martin J.T., Smith B.T., Wagener J.L., (1992) "Fortran 90 Handbook", Library of Congress Catalog Card Number 91-77211.

## BIOGRAPHY

Ragib Sabah was born in 1993. He is also known as Ragheb Alsabbagh. In 2014 Mr. Sabah started his undergraduate degree in the Civil Engineering Department at Pamukkale University in Turkey and graduated in 2018 with high honor degree. In 2021, Mr. Sabah completed his master's degree at Istanbul University-Cerrahpasa. He is interested in computational sciences, applicable technology, and management areas.

# Sparse Matrix Converter Modelling And Simulation

Waleed Abdulrazaq<sup>1</sup> Ahmet Mete Vural<sup>2</sup>

---

## Abstract

*Sparse matrix converter (SMC) is a direct AC-to-AC power electronic converter which does not contain any storage elements. SMC has an indirect topology in which there are both rectification and inversion stages with a fictitious DC link between them. This arrangement greatly reduces the size of the converter and increases reliability. Due to these advantages, SMC is used in AC drives, marine thrust systems, aerospace industry, renewable energy applications and more. In SMC, the input is directly connected to the output via a set of bidirectional power semiconductor switches. The input and output of the SMC often contains a filter to attenuate harmonic content. The output voltage magnitude and frequency can be controlled using a proper switching modulation scheme. In this work, after a short theoretical introduction to matrix converters, a three-phase SMC is modelled and simulated under different operating conditions. An LCL filter is adapted to the output. IGBT is chosen as the power semiconductor switch in rectifier and inverter stages which are controlled by sinusoidal pulse width modulation technique. It is verified by simulation cases that the designed SMC is able to operate without a storage element at the fictitious DC link under different switching frequencies and different amplitude and gain selections for rectifier and inverter stages. The switching frequency can be adjustable in the range between 20-50 kHz. It is also shown that the required SMC output voltage can be attained by varying the amplitude and gain of the rectifier and inverter.*

**Keywords:** Sparse matrix converter, indirect matrix converter, AC-to-AC power conversion, simulation.

---

## 1. INTRODUCTION

There is a converter arrangement for a direct AC-to-AC power conversion in the literature without intermediate power transformation to the DC form. This adaptation enables the control of voltage and frequency at the output of the converter from a fixed input AC voltage. The control of the phase angle of the output voltage is also possible in such an arrangement. Such a converter is called as "matrix converter" (MC). The MC can be classified as "single-stage" or "double-stage" topology. In single-stage MC topology, there is no DC link between input and output and the required AC output voltage can be obtained without any DC power conversion process. This configuration is also called as "direct power conversion". In double-stage MC topology, there are rectifier and inverter stages in the topology. This configuration is also called as "indirect power conversion" [1], [2]. There is a fictitious DC link between them. However, the DC link contains no storage element such as capacitor or inductor which is bulky and heavy. The use of a real DC-link with a storage element used in classical AC-DC-AC power conversion is eliminated in MC topology due to the utilization of the bidirectional switches. The lack of the energy storage component is a great advantage for MC topology over other converter types. Since, this property ensures a compact circuit design, thus making the system lighter and more reliable to operate. However, the control is complicated when compared to classical AC-DC-AC power converters. The control algorithms of the rectifier and inverter stages should be synchronized to each other. In indirect MC topology, the rectifier stage first converts the input AC voltage into DC form. The inverter stage is fed from the fictitious DC-link voltage to generate controllable voltage at its output. MCs can be designed as single-phase or three-phase topology. Early MC studies relied on the thyristor technology as the bidirectional power semiconductor switch [3], [4]. However, thyristors require externally forced commutation circuits which increases the size and cost of the system. But after the development of the transistor technology, transistors are continuously being used instead of thyristors as the bidirectional power semiconductor switch in many fields [5], [6]. The real work to develop the MC in its modern form began with the publication of Venturini and Alesina, who were the first to introduce the name known as MC [7], [8]. These authors introduced the MC power circuit containing the transistors as the bidirectional power switch. One of their contributions is to describe the low-frequency behavior of the MC using a mathematical analysis. They introduced the concept of low-frequency modulation matrix. Furthermore, the direct transfer function approach was recognized in which

---

<sup>1</sup> Gaziantep University, Engineering Faculty, Electrical and Electronics Engineering Department, 27310-Gaziantep/TURKEY, E-mail: wkrm33@gmail.com

<sup>2</sup> Gaziantep University, Engineering Faculty, Electrical and Electronics Engineering Department, 27310-Gaziantep/TURKEY, mvural@gantep.edu.tr

the output voltage was gained by multiplying the modulation matrix by the input voltage. Bidirectional switches are the main components of the MC. Each switch is an electronic switch made of power semiconductors. These switches are arranged in a controlled manner to generate an output voltage with controllable magnitude, phase angle, and frequency at the stage output. In MC, the input current can be controlled regardless of the load so the input power factor can be adjustable. With this property, unity power factor condition can be established at the MC input which aids reactive power control in the power system to where MC is connected. MCs can also operate at high temperatures. All these aforementioned advantages make the MC a desirable converter choice in many fields of applications, such as, aerospace industry [9], [10], marine propulsion industry, variable speed AC drives [11], [12], embedded systems, military industry, and renewable energy systems especially based on wind energy [13], [14]. MC has become important in recent years in the field of wind energy conversion applications due to increasing research on it. Despite many advantages, MC has also downsides. For instance, they lack of fully controlled bilateral switches. Also, MC must operate at high frequencies which increase the switching losses. Moreover, the voltage ratio of the MC is limited. Many researches have emerged to reduce the number of switches in the MC, thus makes it easier to control [15]. There is a relationship between indirect MC and the modulation function, produced from the concept of direct MC topology. The advantage of this arrangement minimizes the number of switches being employed in the MC topology. For example, when the switch is removed from each phase in the rectifier stage, the number of switches will be equal to 15 instead of 18 in direct MC topology [2], [16]. With the reduced number of switches, it becomes possible to improve the zero DC-link current commutation scheme [17]. Moreover, the control algorithm becomes much easier as well as the resulting losses will reasonably be acceptable. Studies on indirect MC topology has received great attention in recent years. Several topologies and control methods have been proposed. These are included in sparse MC (SMC) family which has newer technology when compared to direct MC topology [16], [18]. As shown, the indirect MC topology has four subtypes. These are SMC, very sparse matrix converter (VSMC), ultra-sparse matrix converter (USMC), and inverting link matrix converter (ILMC) topology. In this study, a three-phase SMC is modelled and simulated under different operating conditions. It is fed from a constant three-phase voltage source. It is shown by simulation cases that the power semiconductor switches can be switched in the range between 20-50 kHz and SMC output voltage can be controlled by changing the amplitude and gain of the rectifier and inverter.

## 2. MATHEMATICAL MODEL OF INDIRECT MC

The indirect MC topology also known as “double stage topology” was developed in the early 2000s as a substitution to the direct MC topology. The power circuit of a three-phase indirect MC is shown in Figure 1. There are rectifier and inverter stages in this topology. The first stage is the rectifier stage which contains six bidirectional power semiconductor switches. Each switch is the combination of two power semiconductor switches (IGBT, IGCT or MOSFET) with anti-parallel diode connection. These switches can be either in common-emitter or common collector configuration. The rectifier stage generates a DC voltage at its output from a constant AC voltage at its input. The rectifier stage is connected to the second stage which is known as inverter stage through a fictitious DC link without any storage element such as capacitor or inductor. The inverter is actually a six-pulse two-level inverter consisting of six power semiconductor switches such as IGBT, IGCT or MOSFET. The inverter generates a controllable three-phase voltage at its output. The magnitude, phase angle, and the frequency of the output voltage can be controlled with a control algorithm and a switching modulation scheme. Equation (1) shows the connection matrix of the rectifier stage  $S_{rec}$ , where  $S_x$  represents the state of each power electronic switch available at the phase-x.  $S = 1$  means that the switch is turned on, while  $S = 0$  means that the switch is turned off. The notation  $S'$  denotes the reciprocal state of the respected switch. In time of switching for both cells, one switch is always closed [19]. The necessary conditions for the switches in the rectifier stage are expressed in Equation (2). The voltage and current relations that represent the rectifier operation of the indirect MC are expressed in Equation (3) and (4), respectively.  $v_p$  and  $v_0$  represent respectively the voltage of two points represented in Figure 1,  $v_A, v_B, v_C$  are the phase voltages of the input side,  $i_A, i_B, i_C$  are the phase input currents and  $i_{dc}$  is the DC current flowing from rectifier stage to inverter stage. The connection matrix of the inverter stage is shown in Equation (5). The necessary conditions for the switches in the inverter stage are expressed in Equation (6). The voltage and current relations that represent the inverter operation of the indirect MC are expressed in Equation (7) and (8), respectively. The matrix  $[S_{DE}]$  expressed in Equation (9) is the connection matrix of the indirect MC, which is resulted from the multiplication of the connection matrices of the rectifier and inverter stages.

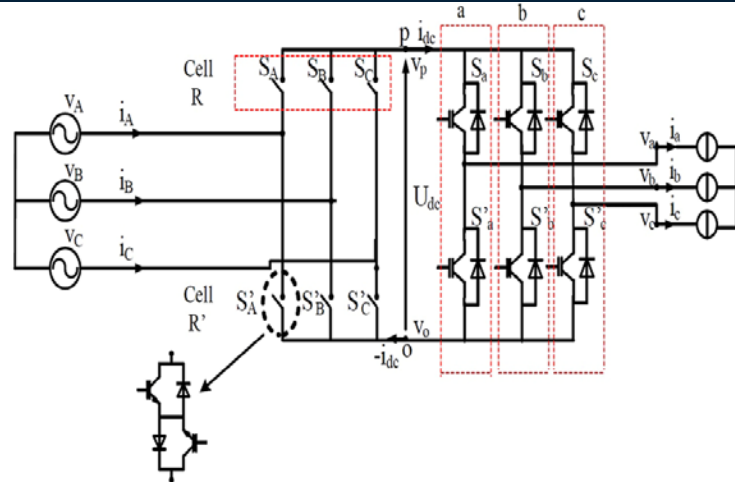


Figure 1. The power circuit of a three-phase indirect MC

$$[S_{rect}] = \begin{bmatrix} S_A & S_B & S_C \\ S'_A & S'_B & S'_C \end{bmatrix} \quad (1)$$

$$\begin{aligned} S_A + S_B + S_C &= 1 \\ S'_A + S'_B + S'_C &= 1 \end{aligned} \quad (2)$$

$$\begin{bmatrix} v_p \\ v_o \end{bmatrix} = [S_{rect}] \begin{bmatrix} v_A \\ v_B \\ v_C \end{bmatrix} \quad (3)$$

$$\begin{bmatrix} i_A \\ i_B \\ i_C \end{bmatrix} = [S_{rect}]^T \begin{bmatrix} i_{dc} \\ -i_{dc} \end{bmatrix} \quad (4)$$

$$[S_{inv}] = \begin{bmatrix} S_a & S'_a \\ S_b & S'_b \\ S_c & S'_c \end{bmatrix} \quad (5)$$

$$\begin{aligned} S_a + S'_a &= 1 \\ S_b + S'_b &= 1 \\ S_c + S'_c &= 1 \end{aligned} \quad (6)$$

$$\begin{bmatrix} v_a \\ v_b \\ v_c \end{bmatrix} = [S_{inv}] \begin{bmatrix} v_p \\ v_o \end{bmatrix} \quad (7)$$

$$\begin{bmatrix} i_{dc} \\ -i_{dc} \end{bmatrix} = [S_{inv}]^T \begin{bmatrix} i_a \\ i_b \\ i_c \end{bmatrix} \quad (8)$$

$$[S_{DE}] = [S_{inv}] \cdot [S_{rect}] = \begin{bmatrix} S_a & S'_a \\ S_b & S'_b \\ S_c & S'_c \end{bmatrix} \cdot \begin{bmatrix} S_A & S_B & S_C \\ S'_A & S'_B & S'_C \end{bmatrix} = \begin{bmatrix} S_{Aa} & S_{Ba} & S_{Ca} \\ S_{Ab} & S_{Bb} & S_{Cb} \\ S_{Ac} & S_{Bc} & S_{Cc} \end{bmatrix} \quad (9)$$

### 3. DESCRIPTION OF SMC

Figure 2 illustrates the power circuit of a three-phase SMC. The rectifier stage of the SMC is the first part that is powered by a three-phase voltage source at the input. Each phase of the rectifier contains three forced commutated power semiconductor switches such as IGBT and two diodes. One of the IGBTs does not contain anti-parallel diode. The output of the rectifier stage is connected to the input of the inverter stage. The inverter stage is a three-phase two-level voltage source inverter having a total of six forced commutated power



semiconductor switches such as IGBT with anti-parallel diode connection with each. The fictitious DC link without any storage element is between the rectifier and inverter stages. A fictitious DC voltage is produced by the rectifier stage. When a load is connected to the SMC output, a DC current flows from the rectifier to the inverter stage through fictitious DC link. To minimize the harmonic content at the input or output or both, a filter can be added at the input and output of the SMC. By this way, a low harmonic sinusoidal voltage can be generated at the SMC output and the input current harmonics are greatly minimized. Due to the absence of a DC power storage component at the fictitious DC link, a synchronization process must take place between the switching modulation schemes of the rectifier and inverter stages. This step is necessary to balance the system with the sinusoidal current.

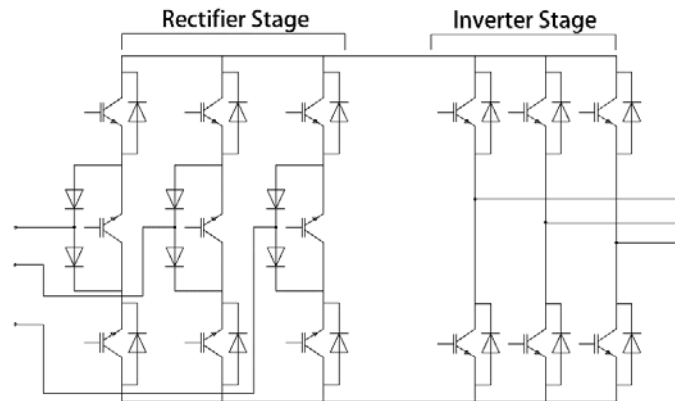


Figure 2. The power circuit of a three-phase SMC

#### 4. SMC CONTROL

Different control strategies can be used in the SMC topology. The sinusoidal pulse width modulation (SPWM) is very popular and easy to apply. Because of its easy applicability, SPWM scheme is used in this study as the switching modulation scheme for both rectifier and inverter stages of the SMC. The SPWM is the most common way to obtain a low harmonic sinusoidal waveform at the inverter stage of the SMC. In this modulation technique, a carrier and a reference signal are compared. The carrier signal is usually a sawtooth or triangular waveform while the reference signal is a pure sinusoidal signal. The frequency of the carrier signal is usually an integer multiple of the frequency of the reference signal. The frequency of the reference signal (for example 50 Hz or 400 Hz, and etc.) defines the fundamental frequency of the output voltage of the SMC. This frequency is chosen according to the load or grid requirements. By comparing the carrier and reference signals, the switching signal of each of the power electronic semiconductor switches is produced. When the triangular carrier signal is smaller than the sinusoidal reference signal, the output of the comparator becomes logic 1 which turns on the respected switch. On the other hand, when the triangular carrier signal is greater than the sinusoidal reference signal, the output of the comparator becomes logic 0 which turns off the respected switch. Depending on the number of the reference signals being used, the SPWM is called either as “unipolar” or “bipolar”. In unipolar type, only one sinusoidal signal is used as the reference. The inverter output voltage is either a positive or zero value. In bipolar type, two out-of-phase sinusoidal signals are compared with a positive and a negative triangular signal, respectively. In this case, the output voltage is either a positive or zero for the positive duration of the sine waveform, or a negative or zero for the negative duration of the sine waveform. The bipolar SPWM arrangement can be designed either for “single-phase” or “three-phase” converter. The switching modulation type used in this study is a three-phase bipolar SPWM.

#### 5. SIMULATION MODEL

Figure 3 shows the simulation model of the power circuit of three-phase SMC. The chosen power semiconductor device is IGBT with a turn on resistance of  $1\text{ m}\Omega$  and a forward voltage drop of  $1.0\text{ V}$ . The snubber resistance of the IGBT is chosen as  $0.1\text{ M}\Omega$  with a very large capacitance. The diode used in the power circuit has a turn on resistance of  $1\text{ m}\Omega$  and a forward voltage drop of  $0.8\text{ V}$ . The snubber resistance and capacitance of the diode is chosen as  $500\text{ }\Omega$  and  $250\text{ nF}$ , respectively. The rectifier stage is powered by a three-phase constant 50 Hz AC voltage source with a line-to-line voltage of  $537\text{ V rms}$ . A three-phase Y-connected pure resistive load rated at  $20\text{ kW}$  is used as the load of the SMC. When the load is connected to the SMC output, the fictitious DC current is transferred directly from the rectifier to the inverter stage. In the simulation model, SPWM scheme is adapted to control the switching of both rectifier and inverter stages. In order to improve the waveform quality of the SMC output, an LCL filter is connected between the output of the inverter stage and the load. The LCL filter is preferred over L and LC type filters due to many advantages, such as, small inductor and capacitor and superior high-frequency attenuation characteristics of  $-60\text{ dB/dec}$  [20]. The

LCL filter parameters are designed as follows: The left inductor is 0.6 mH, the right inductor is 51 mH, and the shunt capacitor is 22  $\mu$ F. No filter is used at the input of the SMC.

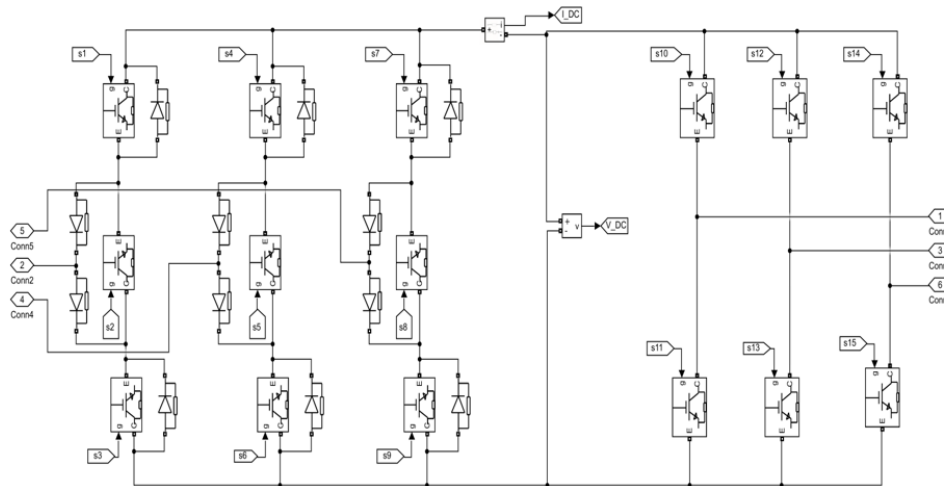


Figure 3. The simulation model of the power circuit of three-phase SMC

## 6. SIMULATION RESULTS

This section presents time domain simulation results of three-phase SMC when it is fed from a constant three-phase voltage source and feeds a three-phase purely resistive load. Regarding these simulations, the gain of the rectifier and inverter stage is set to 0.5 and 1, respectively, while the amplitude of the rectifier and inverter stage is set to 1 and 3, respectively. In these simulation studies, the switching frequency of rectifier and inverter stage is adjusted to 50 kHz and 25 kHz, respectively.

Figure 4 and 5 shows three-phase output voltage and current waveforms of the SMC after LCL filter, respectively. It is clearly observed that the LCL filter reduces the switching noise as well as harmonics in both waveforms. On the other hand, Figure 6 and 7 illustrates the source voltage and current waveforms at the input of SMC. Since no filter is used at SMC input, current waveforms contain some switching noise and harmonics due to the rectifier switching. Finally, voltage and current waveforms of the fictitious DC link are presented in Figure 8 and 9, respectively. DC-link voltage is obtained greater than 800 V which has a ripple factor of 6.75 %. To quantitatively express the harmonic content of the voltage and current waveforms, THD measurements are also carried out in the simulation studies. THD measurements before LCL filter indicates a THD of 0.83 % for the SMC output voltage, while a THD of 0.2 % for the SMC output current. Measurement after the LCL filter indicates better results. THD of SMC output voltage is reduced to 0.08 %, while the THD of the SMC output current is reduced to 0.1 % by using the LCL filter. The changes in SMC output voltage by changing the rectifier/inverter gains and amplitudes are also investigated in the simulation studies. Table 1 shows the changes in SMC output voltage for different values of rectifier and inverter gains. In this case study, the amplitude of the rectifier and inverter stage is set to 1. The rectifier switching frequency is set to 50 kHz, while inverter switching frequency is set to 25 kHz. The highest output voltage is obtained as 142 V when both rectifier and inverter gains are adjusted to 1. On the other hand, Table 2 lists the changes in SMC output voltage for different values of rectifier and inverter amplitudes when rectifier switching frequency is set to 50 kHz and the inverter switching frequency is set to 25 kHz. In this case study, the gain of the rectifier and inverter stage is set to 1. The highest output voltage is obtained as 425.5 V when the rectifier gain is adjusted to 1 and the inverter gain is adjusted to 5. Table 3 presents the changes in SMC output voltage for different values of rectifier and inverter switching frequencies. In this case study, gain and amplitude of rectifier is adjusted to 1 and 0.5, respectively, while, gain and amplitude of inverter is adjusted to 5 and 1, respectively. From Table 3, it can be concluded that if higher output voltage is needed, relatively high switching frequencies for rectifier and inverter can be used. However, this situation increases converter switching losses, so a trade-off between high output voltage and low losses should be considered by the designer. Finally, Table 4 lists the change in SMC efficiency for different values of rectifier and inverter amplitudes. It is observed that around 98 % of SMC efficiency is measured which can be considered as sufficient.

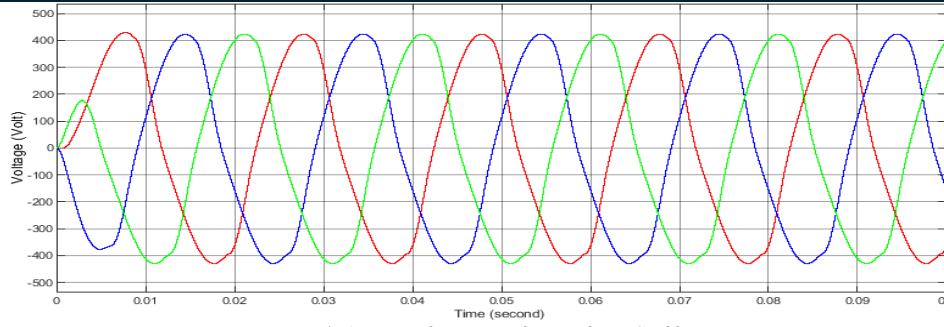


Figure 4. Output voltage waveforms after LCL filter

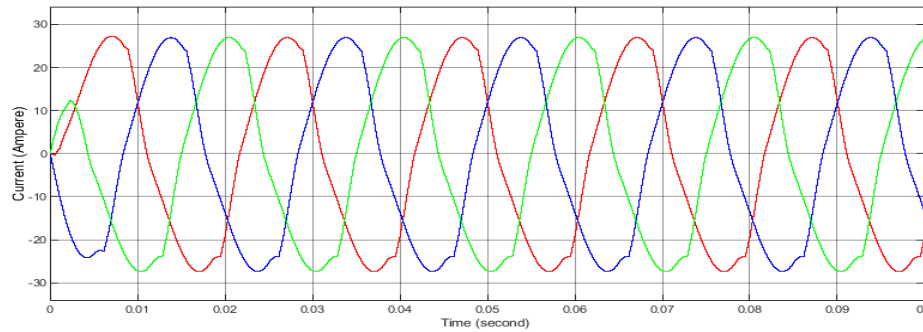


Figure 5. Output current waveforms after LCL filter

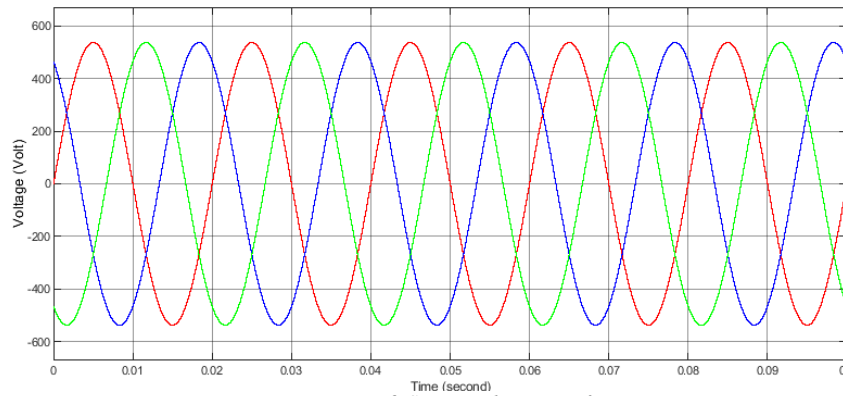


Figure 6. Source voltage waveforms

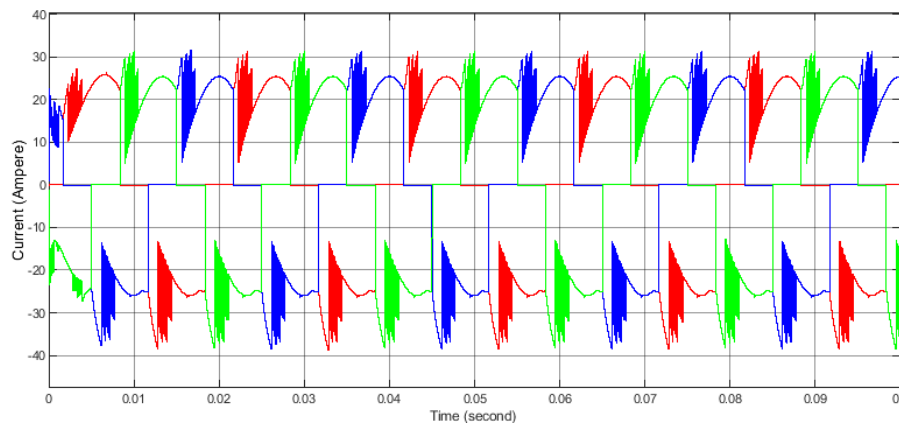


Figure 7. Source current waveforms

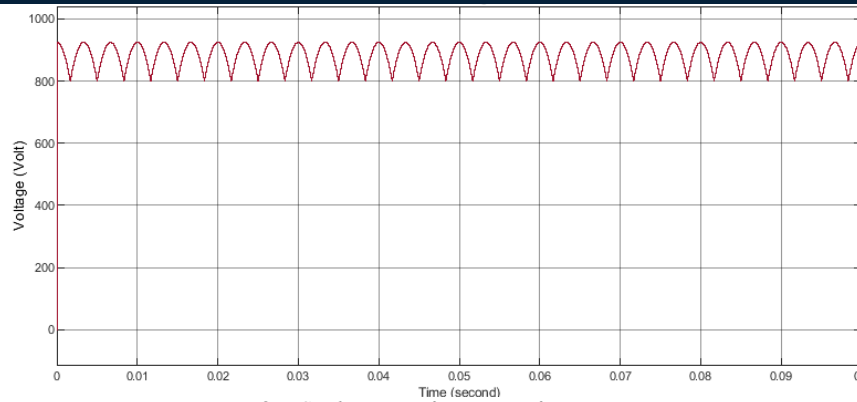


Figure 8. DC voltage waveform at rectifier stage output

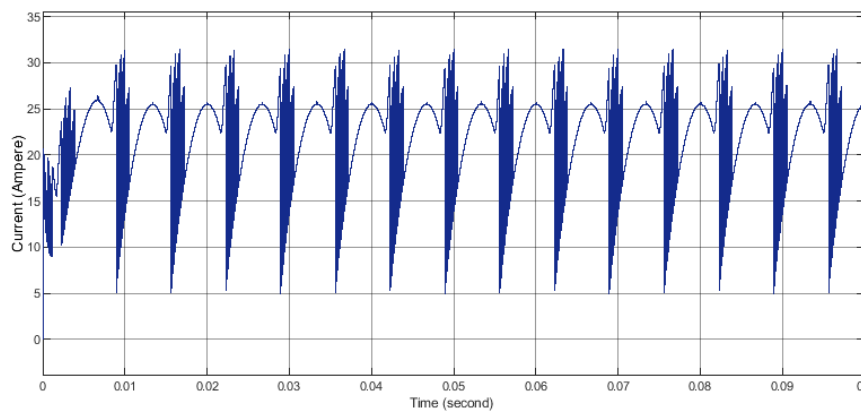


Figure 9. DC current waveform at rectifier stage output

Table 1. The change in SMC output voltage for different values of rectifier and inverter gains (rectifier switching frequency is 50 kHz, inverter switching frequency is 25 kHz)

Rectifier gain (G)	Inverter gain (G)	Output voltage
1	1	142 V
1	0.5	31.37 V
1	0.2	31.37 V
1	0.1	31.37 V
0.5	1	143.7 V
0.2	1	143.7 V
0.1	1	143.7 V
0.5	0.5	31 V
0.2	0.2	31 V

Table 2. The change in SMC output voltage for different values of rectifier and inverter amplitudes (rectifier switching frequency is 50 kHz, inverter switching frequency is 25 kHz)

Rectifier amplitude	Inverter amplitude	Output voltage
0.5	1	170 V
1	1	142 V
2	1	6.5 V
1	0.5	31.37 V
1	2	420.5 V
1	3	424.3 V
1	5	425.5 V
0.5	0.5	31.37 V
2	2	54.9 V
3	3	66.8 V

Table 3. The change in SMC output voltage for different values of rectifier and inverter switching frequencies (the gain and amplitude of the rectifier is 1 and 0.5, the gain and amplitude of the inverter is 5 and 1).

Rectifier switching frequency	Inverter switching frequency	Output voltage
50 kHz	50 kHz	425.5 V
50 kHz	40 kHz	426.4 V
50 kHz	30 kHz	426.8 V
50 kHz	20 kHz	425.8 V
50 kHz	25 kHz	426 V
40 kHz	50 kHz	238.4 V
30 kHz	50 kHz	211.1 V
20 kHz	50 kHz	238.8 V
25 kHz	50 kHz	155.8 V

Table 4. The change in SMC efficiency for different values of rectifier and inverter amplitudes (the gain of the rectifier and inverter is 1, rectifier switching frequency is 50 kHz, inverter switching frequency is 25 kHz)

Rectifier amplitude	Inverter amplitude	SMC efficiency
0.5	1	98.8 %
1	1	98.8 %
2	1	98.8 %
3	1	98.8 %
1	0.5	98.4 %
1	2	98.9 %
1	3	98.9 %
1	5	98.9 %
0.5	0.5	98.4 %
2	2	98.8 %
3	3	98.8 %

## 7. CONCLUSION

This paper aims to present some research results of the modelling and simulation studies of a three-phase SMC. In the study, the SMC is fed from a constant three-phase voltage source and a purely resistive load is connected at its output. The results of this study will be used in near future for the adaptation of three-phase SMC to a wind energy conversion system connected to the grid. So, the advantages of SMC such as reduced number of semiconductor devices will be effectively used in a renewable energy system. This advantage also reduces the energy losses and manufacturing costs of a real renewable energy system. After a short and brief introduction to MC principle, the mathematical model of the indirect MC and the description of the SMC are briefly given in this paper. In the simulation study, the SMC control is realized by simultaneously operating two SPWM schemes for rectifier and inverter stages. It becomes then possible to change the SMC output voltage to the desired value by varying the gain and amplitude parameters of the rectifier and inverter stages. To improve voltage and current waveform quality at the output, an LCL filter is designed and added between the SMC output and the load. Simulation results verify the advantages of using such a filter. The simulation results have proven that a wide range of application areas of SMC topology is potentially available.

## REFERENCES

- [1]. L. Gyugi and B. Pelly, "Static Power Frequency Changers Theory," Performance, and Applications. *New York, Wiley*, 1976.
- [2]. E. Stacey, "An unrestricted frequency changer employing force commutated thyristors," in *Proc. IEEE PESC'76*, pp. 165–173, 1976.
- [3]. V. Jones and B. Bose, "A frequency step-up cyclo converter using power transistors in inverse-series mode," *Int. J. Electron.*, vol. 41, no. 6, pp. 573–587, 1976.
- [4]. A.R. Daniels, M.Sc, C.Eng., M.I.E.E., and D.T. Slattery, B.Sc, Ph.D. "Application of power transistors to polyphase regenerative power converters," *Proc. IEEE*, vol. 125, no. 7, pp. 643–647, July 1978.
- [5]. M. Venturini, "A new sine wave in sine wave out, conversion technique which eliminates reactive elements," in *Proc. IEEE POWERCON 7*, pp. E3\_1–E3\_15, 1980.
- [6]. M. Venturini and A. Alesina, "The generalized transformer: A new bidirectional sinusoidal waveform frequency converter with continuously adjustable input power factor," in *Proc. IEEE PESC'80*, pp. 242–252, 1980.
- [7]. Alesina, A. and Venturini, "Intrinsic Amplitude Limits and Optimum Design of 9-switches direct PWM AC-AC converters," *Proceedings of Power Electronics Specialist Conference*, vol. 2, April 1988, pp. 1284 – 1291.
- [8]. Alesina, A. and Venturini, "Analysis and Design of Optimum Amplitude Nine-Switch Direct AC- AC Converters," *IEEE Transactions on Power Electronics*, vol. 4, no.1, pp. 101-112, January 1989.

- [9]. Alesina, A. and Venturini, "Generalised Transformer: A New Bidirectional, Sinusoidal Waveform Frequency Converter with Continuously Adjustable Input Power Factor," *IEEE Power Electronics Specialists Conference*, 1980, pp. 242-252.
- [10]. Klumpner, A., Nielsen, P., Boldea, I. and Blaabjerg, "A New Matrix Converter Motor (Mcm) for Industry Applications," *IEEE Transactions on Industrial Electronics*, vol. 49, pp. 325 – 335, F. April 2002.
- [11]. Changliang, X., Yan, Y., Song, P. and Tingna, "Voltage Disturbance Rejection for Matrix Converter-Based PMSM Drive System Using Internal Model Control," *IEEE Transactions on Industrial Electronics*, vol. 59, no. 1, pp. 361-372 S. January 2012
- [12]. Casadei, D., Serra, G., Tani, A., Trentin, A. and Zarri, "Theoretical and Experimental Investigation on the Stability of Matrix Converters," *IEEE Transactions on Industrial Electronics*, vol. 52, no. 5, pp. 1409-1419, L. October 2005.
- [13]. J. W. Kolar, Vorrichtung Zur Quasi-Direkten Pulsbreitengesteuerten Energieumformung Zwischen Dreiphasennetzen Jul. 27, 2001, Austrian Patent Application (in German), filed.
- [14]. C.Klumpner, M. Lee, and P. Wheeler, "A new three-level sparse indirect matrix converter," in *Proc. IECON*, , pp. 1902–1907, Nov. 7–10, 2006.
- [15]. J. Holtz, U. Boelkens, "Direct frequency converter with sinusoidal line currents for speed-variable ac motors", *IEEE Transactions on Industrial Electronics*, Vol. 36, No. 4, pp. 475 – 478, Nov. 1989.
- [16]. Rmili, L., Rahmani, S., Fnaiech, F. and Al-Haddad, "Space Vector Modulation Strategy for a Direct Matrix Converter," *In Proc.14th international conference on Sciences and Techniques of Automatic control & computer engineering - STA'2013*, pp.1-6, K. 2013.
- [17]. Lazhar Rmili, Salem Rahmani, Kamal Al-Haddad, "A review of Indirect Matrix Converter Topologies," *Journal of Renewable Energy and Sustainable Development (RES D)*, ISSN 2356-8569, June 2015.
- [18]. Bradaschia, F., Cavalcanti, M., Neves, F. A. and Helber, "A Modulation Technique to Reduce Switching Losses in Matrix Converters," *IEEE Transactions on Industrial Electronics*, vol. 56, no. 4, pp. 1186-1195, E. P. April 2009.
- [19]. [https://en.wikipedia.org/wiki/Sparse\\_matrix\\_converter](https://en.wikipedia.org/wiki/Sparse_matrix_converter)
- [20]. Johann W. Kolar, Frank Schafmeister, Simon D. Round, "Novel Three-Phase AC–AC Sparse Matrix Converters," *IEEE TRANSACTIONS ON POWER ELECTRONICS*, VOL. 22, NO. 5, SEPTEMBER 2007.
- [21]. Szczeńsiak, "Analysis and testing matrix-reactance frequency converters," PhD thesis (in Polish), University of Zielona Góra, Zielona Góra, P 2009.

# Investigation of the Potential In Vitro Usage of Asialoglycoprotein Receptor Targeted Magnetic Nanoparticles for Hepatocellular Carcinoma

Ayca Ere<sup>1</sup>, Tugba Karakayali<sup>1</sup>, Guliz Ak<sup>1,2</sup>, Latife Merve Oktay<sup>3</sup>, Nur Selvi Gunel<sup>3</sup>, Senay Sanlier<sup>1,2</sup>

---

## Abstract

**Objective:** Hepatocellular carcinoma (HCC) is the fourth most common cause of cancer-related death worldwide. The World Health Organization stated that by 2030, the number of deaths from hepatocellular carcinoma would be more than 1 million. It is known that there is a high amount of asialoglycoprotein receptors (ASGPR) on the hepatocyte surface, and they are intensely expressed in HCC. These properties make ASGPR an attractive target for receptor-directed drug delivery to hepatocarcinoma cells. New drug delivery systems are being developed to prevent the side effects and limitations of commonly used treatment methods. As an antineoplastic agent, doxorubicin is used for the treatment of many cancers.

**Research methods:** This study aimed to perform in vitro cytotoxicity and biocompatibility tests of the synthesized asialoglycoprotein receptor-targeted and doxorubicin carrying magnetic nanoparticles to treat HCC. For this purpose, after the synthesis of magnetic nanoparticles loaded with doxorubicin, serum protein binding and hemolysis were assayed. The cytotoxicity studies were carried out on hepatocellular carcinoma cell, HEPG2, and human epithelial liver cell, THLE-2.

**Results and Conclusion:** The cytotoxicity studies were carried out on hepatocellular carcinoma cell, HEPG2, and human epithelial liver cell, THLE-2. According to the results, it was found that the prepared formulation was biocompatible, had no hemolytic effect, and created cytotoxicity in cancer cells. As a result, it is thought that the doxorubicin-loaded asialoglycoprotein targeted magnetic nanoparticle system has a high potential for use in the treatment of hepatocellular carcinoma.

**Keywords:** Asialoglycoprotein receptor, biocompatibility tests, cytotoxicity studies, doxorubicin, magnetic drug delivery system.

---

## 1. INTRODUCTION

Hepatocellular carcinoma (HCC) is the most common primary liver malignancy and is a leading cause of cancer-related death worldwide. Liver cancer remains a global health challenge, with an estimated incidence of >1 million cases by 2025[1]. The causes of HCC are chronic liver disease, particularly chronic hepatitis B and C, and alcoholic liver disease. Also, other forms of chronic liver disease are risk factors for HCC.

---

\* Corresponding author: Ege University, Department of Biochemistry, 35040 Bornova/Izmir, Turkey.

[erekayca@gmail.com](mailto:erekayca@gmail.com)

<sup>1</sup> Ege University, Department of Biochemistry, 35040 Bornova/Izmir, Turkey.

<sup>2</sup> Ege University Center for Drug Research, Development, and Pharmacokinetic Applications (ARGEFAR), 35100 Bornova/Izmir

<sup>3</sup> Department of Medical Biology, Faculty of Medicine, Ege University, 35100, Izmir, Turkey

Epidemiological data suggest that unhealthy diet, alcohol use, obesity, type 2 diabetes, or modifiable lifestyle factors contribute to the pathogenesis of hepatocellular carcinoma [2]. Doxorubicin (Dox), used in liver cancer as in many other types of cancer, is an anthracycline type drug that prevents replication by interfering between base pairs in the DNA helix and, consequently, inhibiting protein synthesis and proliferation of cancer cells [3]. Doxorubicin uses different molecular mechanisms such as inhibition of topoisomerase II enzyme, intercalation with DNA, disruption of calcium homeostasis, and production of free radicals to induce toxicity and kill cancer cells [4]. Doxorubicin has some side effects like any chemotherapeutic agent. In order to prevent or minimize the side effects without reducing the effect of doxorubicin, it is possible to load the drug into various drug delivery systems and transport it to the desired area [5]. The nanoparticulate drug delivery systems are used today to enable the drug to be more effective at low doses and to minimize its side effects. Nanoparticles have many advantages, such as high loading capacity, not being recognized by the immune system, making surface modifications to reach the target effectively, and being designed to pass through physiological barriers such as the blood-brain barrier tight intercellular junctions [6]. Magnetic nanoparticles, one of the nanoparticle drug delivery systems, respond to the applied magnetic field and can be moved in a magnetic field [7]. The magnetic targeting approach, one of the types of drug targeting, involves intravenous injection of a therapeutic agent attached to or encapsulated to a magnetic drug carrier and directing it to the tumor tissue by externally localized magnetic field application [8]. In cancer treatment, active targeting is usually accomplished by conjugating the target molecule to the drug delivery system. The most important advantage of active targeting is reducing or eliminating the systemic toxicity caused by conventional drugs and transporting the drug directly to the targeted area [9]. A receptor-mediated endocytosis mechanism is a necessary approach that enables the delivery of drugs to specific cell types. In this mechanism, the drug can reach the cell in high concentration, reaching the non-target sites at a minimum level, causing low toxicity. The asialoglycoprotein receptor (ASGPR) is one of the most striking targets in drug targeting studies to the liver [10].

Within the scope of the study, *in vitro* cytotoxicity and biocompatibility tests of doxorubicin-loaded arabinogalactan-coated magnetic nanoparticles (DANP) will be performed therapeutic potential on liver cancer was investigated.

## 2. MATERIAL AND METHOD

### ○ *Materials*

Bovine Collagen Solution (Sigma), Fibronectin, and Type I collagen were purchased from Sigma for *in vitro* studies. Fetal Bovine Serum, and Bovine Serum Albumin were obtained from Capricorn. Penicillin/Streptomycin, saline phosphate buffer (PBS), and Trypsin/EDTA were purchased from Wisent. BEGM Bronchial Epithelial Bullet Kit was obtained from Lonza. The hepatocellular carcinoma cell line with luciferase activity (AZ-AHR Stable HepG2 Luciferase Reporter Cell Line, T3102) Applied Biological Materials Inc. (ABM, Canada) and Prigrow III were obtained from ABM, normal hepatocellular carcinoma cell line HepG2 (HB-8065) and healthy liver epithelial cell line THLE-2 (CRL-2706) used as healthy control cell group were obtained from ATCC. Doxorubicin (Chemos GmbH), sodium acetate (Tekkim), sodium phosphate (Isolab), Coomassie brilliant blue G-250 (Fluka), 96% ethanol (Supelco), 85% phosphoric acid (Sigma Aldrich), Albumin (Fraction V) (It was obtained from Merck).

### ○ *In Vitro Cytotoxicity Studies Of DANP Formulation*

Cytotoxicity studies were carried out to examine the toxicity of DANP and drug-free arabinogalactan-coated magnetic nanoparticles (ANP) on healthy hepatocytes and liver cancer cells at different doses.

For HepG2 cells, Prigrow III medium with 10% FBS, 2% L-glutamine, 1% penicillin-streptomycin, 1 mM sodium pyruvate were used, and THLE-2 cells, BEGM Bronchial Epithelial Bullet Kit medium was preferred. Cultures were maintained at 37°C and in a 5% CO<sub>2</sub> humidified incubator (Thermo Electron Corporation's Class 100). After reaching 80–85% confluency, both HepG2 and THLE-2 cells were harvested utilizing trypsin/EDTA, and 100 mL cell suspension at a concentration of 1×10<sup>4</sup> cells/well was seeded into a 96-well plate for each cell line. Cells were incubated overnight at 37°C and 5% CO<sub>2</sub> conditions. DANP and Dox solution were added with serial dilution and incubated for 48 hr. Cells that were incubated with related media were named as the control group. After incubation, the MTT test was applied according to Ak et al. [11]. The upper phase was discarded, and MTT solution was added to each well following incubation for 4 hr. Then, DMSO was added for dissolving the formazan crystals. Absorbance was measured at 540 nm using a microplate reader (Thermo, Multiskan Fc). IC<sub>50</sub> values for 48 hr were calculated using Calcsyn 2.0 software.



○ ***Biocompatibility Tests of DANP Formulation***

▪ ***Serum protein binding***

The amount of serum protein binding of the DANP formulation was analyzed by modifying the method described by Cole et al. [12]. Nanoparticles were added to fetal bovine serum with serum:nanoparticle volume varying ratios (v:v) of respectively. The samples were incubated at 37°C for 2 hours at 160 rpm. After incubation, the samples were centrifuged at 13 000 rpm for 1 hour. After centrifugation, protein determination was made in the supernatant according to the Bradford method [13], and % binding values were calculated.

▪ ***Hemolysis***

The damage that the DANP formulation can cause on erythrocytes was determined by in vitro hemolysis studies and the method applied by Mayer et al. [14]. Accordingly, erythrocytes separated from whole blood were suspended in PBS. Nanoparticles and erythrocyte suspension in varying concentrations were incubated at 37°C for 2 hours. At the end of the period, the samples were centrifuged for 5 minutes, and the free hemoglobin in the supernatant was determined spectrophotometrically at 540 nm. The dispersion system of nanoparticles (PBS) was used as the negative control, and 1% Triton X-100 providing 100% lysis was used as a positive control.

### 3. RESULTS AND DISCUSSION

○ ***In Vitro Cytotoxicity Studies of DANP Formulation***

The cytotoxic effects of free doxorubicin, ANP, and DANP were determined by MTT assay using HepG2 and THLE-2 cell lines. Cells and drug groups were incubated, and results were evaluated after an incubation time of 48 hr. ANP has not shown a cytotoxic effect since there is no significant change in cell viability. Therefore, the nanocarrier was indicated as biocompatible. Cell death values of HepG2 cells increased with the increased dose of DANP and Dox, as seen in Figures 1 and 2, respectively. Also, it was found that DANP had no cytotoxic activity of the THLE-2 cell line. IC<sub>50</sub> values of DANP were less than that of free Dox against HepG2 cell lines for 48 hr.

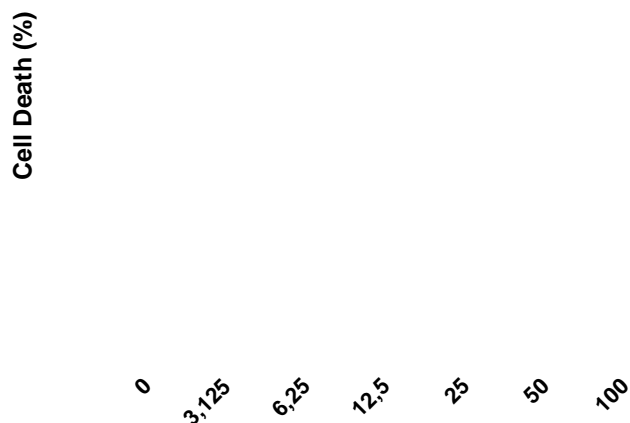


**Figure 14.** Cell death (%) after 48 hours of incubation of increasing concentrations of DANP formulation on HepG2 cells

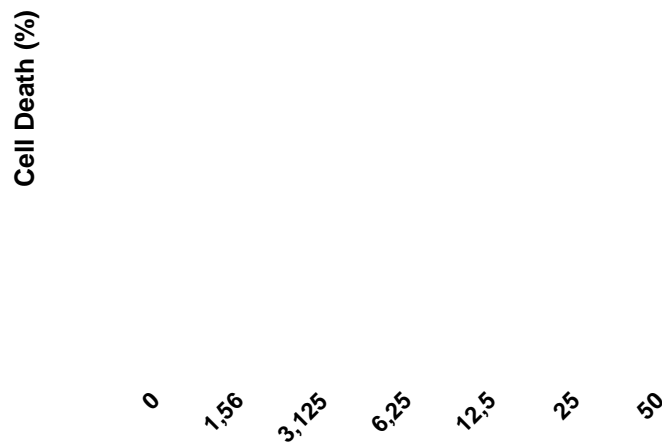


**Figure 15.** Cell death (%) after 48 hours of incubation of increasing concentrations of Dox on HepG2 cells.

In current cancer treatments, drugs must be used in high doses in order to show an effective treatment in the targeted area. The use of these high doses causes many undesirable side effects by damaging healthy cells as well as cancer cells. The primary purpose of drug delivery systems is to go directly to the cancerous area, perform long-term treatment with a controlled and slow release, and provide maximum effect with a minimum dose. [15][16]. In addition, even at the highest doses of the DANP formulation applied in the THLE-2 cell line, it was determined that there was more than 99% viability in the cells. Within the scope of the studies, liver cancer cell line and healthy cell line data were compared, and it was determined that while doxorubicin-loaded arabinogalactan-coated magnetic nanoparticles created cytotoxicity in the HepG2 cell line, it did not cause any cytotoxic effect in the THLE-2 cell line.

○ **Biocompatibility Tests of DANP Formulation**

▪ **Serum Protein binding**

In this study, protein binding amounts were determined in fetal bovine serum (FBS) of DANP formulations. Considering the serum: nanoparticle ratio, the increase in the serum ratio does not have a significant effect on the protein binding ratio. Protein binding percentages varied between 12-16%. According to all these data, it is

thought that the formulation can reach the targeted tissue at a high rate and cannot be removed from the circulation immediately due to the low protein binding efficiencies.

### ▪ Hemolysis

In order to determine the amount of hemolysis that the DANP formulation could cause, different concentrations of nanoparticles were incubated with erythrocyte solution, and hemolysis trials were carried out. The hemolysis results are shown in Figure 3.

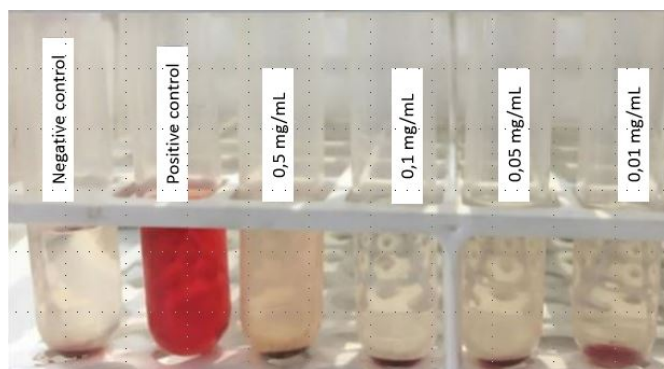


**Figure 16.** Negative control (PBS), Positive control (Triton X), Hemolysis images formed as a result of incubation of erythrocytes with doxorubicin-loaded MNP at different concentrations.

According to the results, it was determined that DANP formulations did not cause hemolysis compared to positive and negative controls.

Protein binding and hemolysis results all show the biocompatibility of the obtained formulation.

## 4. CONCLUSION

In this study, *in vitro* cytotoxicity and biocompatibility studies of DANP formulation developed for HCC treatment were performed. As a result of the studies, it was seen that the DANP formulation caused minimal damage in the normal liver cells as expected, while it showed cell growth inhibitory and anticancer activity in hepatocellular cancer cells. At the same time, it was concluded that drug release from DANPs occurred in a controlled manner, and long-term treatment could be achieved with a minimum dose. According to the data of biocompatibility tests, it was observed that the DANP formulation was biocompatible and did not cause hemolytic effects.

It can be suggested that doxorubicin-loaded asialoglycoprotein targeted magnetic nanoparticles could be a promising system for targeted hepatocellular carcinoma therapy. In future works, *in vivo* and *ex vivo* experiments should be performed for targeted HCC therapy.

## ACKNOWLEDGMENT

This work was supported by the Scientific and Technological Research Council of Turkey, TUBITAK (grant number: 119S496). The authors would like to acknowledge to Ege University Center for Drug Research, Development, and Pharmacokinetic Applications (ARGEFAR) for laboratory support.

## REFERENCES

- [1] J.D. Yang, P. Hainaut, G.J. Gores, A. Amadou, A. Plymouth and L.R. Roberts, "A global view of hepatocellular carcinoma: trends, risk, prevention and management". *Nat Rev Gastroenterol Hepatol*, vol 16, pp.589–604, 2019.
- [2] August ; Yang |, J.D. Roberts, "Hepatocellular carcinoma: a global view", *Nat Publ Gr*, vol 7, pp. 448–58, 2010.
- [3] J. Wu, J. Yuan, B. Ye, Y. W, Z. Xu, J. Chen, "Dual-Responsive Core Crosslinking Glycopolymer-Drug Conjugates Nanoparticles for Precise Hepatocarcinoma Therapy", *Front Pharmacol* 2018.
- [4] E.C. Anioغو, B.P.A. George, H. Abrahamse, "Phthalocyanine induced phototherapy coupled with Doxorubicin; a promising novel treatment for breast cancer", *Expert Rev Anticancer Ther.*, vol 17, pp. 693–702, 2017.

- [5] R. Singh, J.W. Lillard, "Nanoparticle-based targeted drug delivery", *Exp Mol Pathol.*, vol 86, pp. 215–23, 2009.
- [6] L. Zhang, T.J. Webster, Z. Zdrojewicz, M. Waracki, B. Bugaj and D. Pypno, "Nanotechnology in therapeutics : a focus on nanoparticles as a drug delivery system R eview", *Carbohydr Polym.*, vol 1, pp. 71–88, 2016.
- [7] M. Namdeo, S. Saxena, R. Tankhiwale, M. Bajpai, Y.M. Mohan and S.K. Bajpai, "Magnetic nanoparticles for drug delivery applications", *J Nanosci Nanotechnol.*, vol 8, pp. 3247–71, 2008.
- [8] G. Ak, H. Yilmaz and S.H. Sanlier, "Preparation of magnetically responsive albumin nanospheres and in vitro drug release studies", *Artif Cells, Nanomedicine Biotechnol.*, vol 42, pp. 18–26, 2014.
- [9] G. Ak, H.Yilmaz, A. Gunes, S.H. Sanlier, "In vitro and in vivo evaluation of folate receptor-targeted a novel magnetic drug delivery system for ovarian cancer therapy", *Artif Cells, Nanomedicine, Biotechnol.*, vol 46, pp. 926–37, 2018.
- [10] AA D, PV D. "Asialoglycoprotein receptor-mediated hepatocyte targeting - strategies and applications", *J Control Release*, vol 203, pp. 126–39, 2015.
- [11]G. Ak, D. Aksu, E. Capkin, O. Sari, I. Kimiz Gebologlu, S.H. Sanlier, "Delivery of pemetrexed by magnetic nanoparticles: design, characterization, in vitro and in vivo assessment", *Prep Biochem Biotechnol.*, vol 50, pp. 215–25, 2019.
- [12]A.J. Cole, A.E. David, J. Wang, C.J. Galbán, H.L. Hill and V.C. Yang, "Polyethylene glycol modified, cross-linked starch-coated iron oxide nanoparticles for enhanced magnetic tumor targeting", *Biomaterials*, vol 32, pp. 2183–2193, 2011.
- [13]. M.M. Bradford, "A rapid and sensitive method for the quantitation of microgram quantities of protein utilizing the principle of protein-dye binding", *Anal Biochem.*, vol 72, pp. 248–54, 1976.
- [14]A. Mayer, M. Vadon, B. Rinner, A. Novak, R. Wintersteiger and E. Frohlich, "The role of nanoparticle size in hemocompatibility", *Toxicology*, vol 258, pp. 139–47, 2009.
- [15]A. Zantotto-Filho, K. Coradini, E. Braganhol, R. Schroder, C.M. De Oliveira and A.Simões-Pires, "Curcumin-loaded lipid-core nanocapsules as a strategy to improve pharmacological efficacy of curcumin in glioma treatment", *Eur J Pharm Biopharm.*,vol 83 pp. 156–67 2013.
- [16]T. Garanti, A. Stasik, A.J. Burrow, M.A. Alhnan, K.W. Wan, "Anti-glioma activity and the mechanism of cellular uptake of asiatic acid-loaded solid lipid nanoparticles", *Int J Pharm.*, vol 500, pp. 305–15, 2016.

## BIOGRAPHY

Ayca EREK has Bachelor's degree at Biochemistry from Ege University. She is a master's student at Ege University, Department of Biochemistry, since 2019. She is working on the development of drug delivery nanoparticle systems for use in cancer treatment.

# Asialoglycoprotein Receptor Targeted Magnetic Nanoparticles For Hepatocellular Carcinoma Treatment

Tugba Karakayali<sup>1</sup>, Ayca Ereğ<sup>1</sup>, Guliz Ak<sup>1,2</sup>, Senay Sanlier<sup>1,2</sup>

---

## Abstract

**Objective:** Hepatocellular carcinoma is the most common type of liver cancer. Doxorubicin (Dox) is an anthracycline antibiotic and is commonly used for cancer treatment. However, Dox has severe side effects that limit efficiency, and it is used with drug delivery systems. Asialoglycoprotein receptors are membrane glycoprotein receptors and are expressed in hepatocellular carcinoma. This study, it is aimed to develop a magnetic field and asialoglycoprotein receptor-targeted, doxorubicin-loaded nanoparticle system to be used in the treatment of hepatocellular carcinoma.

**Research methods:** Magnetic nanoparticles were synthesized by the co-precipitation method. The surface was functionalized with 2-aminoethylphosphonic acid to provide the binding of arabinogalactan with magnetic nanoparticles. Then, MNP's surface was coated with arabinogalactan. After that, doxorubicin was loaded on arabinogalactan-coated magnetic nanoparticles by adsorption. The functional groups, hydrodynamic size, zeta potential, and drug encapsulation efficiency were evaluated.

**Results and Conclusion:** The SEM size of the Dox-loaded arabinogalactan-coated magnetic nanoparticle (DANP) was found to be 30-35 nm. FTIR analysis has confirmed the presence of doxorubicin on arabinogalactan-coated ANPs. Dox loading efficiency was determined as 78.54 %. Based on the results obtained, the study is thought to have potential for *in vitro*, *in vivo*, and *ex vivo* studies.

**Keywords:** Arabinogalactan, asialoglycoprotein receptor, doxorubicin, magnetic nanoparticle, targeted therapy.

---

## 1. INTRODUCTION

Hepatocellular carcinoma (HCC) is a common type of cancer that ranks first among liver cancer types and affects approximately one million people worldwide each year. While it has a high prevalence in Southeast Asia and Sub-Saharan Africa worldwide, its incidence is low in the west. A chronic infection caused by the hepatitis B virus is the most common cause of this disease. Other important causes are cirrhosis, chronic viral hepatitis (hepatitis C virus and hepatitis B plus D viruses), alcohol overuse, obesity, hemochromatosis,  $\alpha$ -1-antitrypsin deficiency, and aflatoxin-like toxins. In most cases, HCC is asymptomatic and has a low survival rate. HCC treatment applies surgical intervention, ablation, liver transplantation, chemoembolization, and systemic treatments in the treatment of HCC. These treatment options are determined according to the patient's condition and the cancer level [1]. Many anti-cancer agents are used in the systemic treatment of hepatocellular carcinoma, one of which is doxorubicin. Doxorubicin is an anthracycline-derivative antibiotic that acts by intercalating into DNA. Besides being an effective agent for cancer, doxorubicin has serious side effects that limit its effectiveness. The most common side effects are cardiotoxicity and myelosuppression [2]. Today, it is used with the drug delivery system to reduce these side effects and increase the therapeutic effect. Due to the advantages of drug delivery systems in cancer treatment, their effects are widely studied. These advantages are;

---

\* Corresponding author: Ege University, Department of Biochemistry, 35040 Bornova/Izmir, Turkey.  
[tugbakrky1@gmail.com](mailto:tugbakrky1@gmail.com)

<sup>1</sup> Ege University, Department of Biochemistry, 35040 Bornova/Izmir, Turkey.

<sup>2</sup> Ege University Center for Drug Research, Development, and Pharmacokinetic Applications (ARGEFAR), 35100 Bornova/Izmir

It is ensured that the active substances improve the aqueous solubility and chemical stability, increase the pharmacological activity and reduce the side effects in the patients by providing them to reach the desired area more easily. Nanoparticle carrier systems are also divided into many groups within themselves. These groups are polymeric nanoparticles, lipid-based nanoparticles, inorganic nanoparticles, and dendrimers. It can form nanoparticles with magnetic character obtained from iron salts in inorganic nanoparticles [3]. In addition to these magnetic nanoparticles' advantages, direct targeting of the cancerous region by applying a magnetic field with magnetic targeting is provided.

The attraction of nanoparticles for selective tumor targeting is their potential to deliver a concentrated drug dose near (or even into) target tissue and reduce drug exposure to healthy cells. This can be done through physical interactions or passive/active targeting. Active targeting can coat the surface of the nanoparticles with antibodies or ligands that specifically bind to increased receptors in cancer cells. The asialoglycoprotein receptor (ASGPR) is expressed basolaterally from hepatocytes. Targeted delivery to hepatocytes constitutes an essential strategy in hepatocellular carcinoma, and this approach can be made possible by targeted transport to overexpressed receptors in hepatocytes. As a hepatic lectin, the asialoglycoprotein receptor provides an ideal target for hepatocyte-specific delivery. Sugar-based ligands exhibit maximum affinity for ASGPR, with physicochemical properties that play a dominant role in ligand binding. Arabinogalactan (AG), a galactose-based polymer, and pullulan, a glucose-based polymer, are among the carbohydrate polymers that have been extensively studied for ASGPR-mediated targeting[4].

Within the study's scope, it aims to develop a targeted therapeutic strategy to reduce the side effects of chemotherapeutic agents used in cancer treatment and prevent high dose toxicity that restricts the use of chemotherapeutics in treatment—with the targeted drug delivery system, increasing drug delivery to the cellular levels, optimizing the concentration and release kinetics of drugs in the circulation or tissues, providing practical and safe treatment at low doses, minimizing the toxic and immunogenic properties of drugs, increasing drug stability, targeting without damaging healthy tissues. It is aimed to obtain the desired level of pharmacological response in the region. For this purpose, selective and doxorubicin-loaded nanoparticles were synthesized to the asialoglycoprotein receptor, which has magnetic properties and is known to be expressed in hepatocytes.

## 2. MATERIAL AND METHOD

### ○ *Materials*

$\text{FeCl}_2 \cdot 4\text{H}_2\text{O}$ , 2-amino ethyl phosphonic acid (APA), arabinogalactan (AG), potassium periodate, Dowex-1x4 ion exchange resin, cellulose acetate membrane (12.000-14.000 MWCO), and Ammonium hydrochloride ( $\text{NH}_4\text{OH}$ ) was purchased from Sigma. Ethanol and sodium borohydride ( $\text{NaBH}_4$ ) were purchased from Merck.  $\text{FeCl}_3 \cdot 6\text{H}_2\text{O}$  were obtained from Isolab. Boric acid from Eti Kimya, Acetic acid from Tekkim, Doxorubicin from Chemos GmBh.

### ○ *Magnetic Nanoparticle Synthesis and Functionalized with 2-aminoethylphosphonic Acid*

Magnetic nanoparticles (MNPs) were synthesized with the co-precipitation method[5].  $\text{Fe}^{+2}$  and  $\text{Fe}^{+3}$  salts dissolved at a 1:2 molar ratio at  $60^\circ\text{C}$  and mechanically stirred at 3000 rpm under a nitrogen atmosphere. After that, the  $\text{NH}_4\text{OH}$  solution was added until the pH value reached 10, and the mixture was allowed to react for two hours for nucleation of MNPs. After the nucleation reaction, the mixture was collected and washed distilled water and ethanol until the pH value reached the six with magnetic decantation. MNPs were characterized with Fourier-transform infrared spectroscopy (FTIR) (Shimadzu, IRTracer-100), Scanning electron microscopy (SEM) (Thermo Scientific Apreo S). SEM analysis was performed at Ege University Central Research Test and Analysis Laboratory (MATAL). FTIR analysis was made at Ege University Drug Development and Pharmacokinetic Research-Application Center. In addition, zeta potential and hydrodynamic size analysis were measured with the zeta-sizer (Malvern Nano ZS 90) in Izmir Katip Celebi University Central Research Laboratory.

After confirmation of MNPs synthesis, the nanoparticles functionalized with amine groups. The chemical 2-aminoethylphosphonic acid (APA) with 0.25 concentration was added to magnetic nanoparticle suspension and mixed at 2.000 rpm at  $80^\circ\text{C}$  for six-hour. Nanoparticles were precipitated by centrifugation at 12.000 rpm and washed with distilled water [5]. The obtained nanoparticles were characterized with FTIR, SEM, hydrodynamic diameter, and zeta potential analysis.

○ ***Oxidation of Arabinogalactan and Binding of APA-MNP***

For arabinogalactan (AG) to bind to nanoparticles with amine groups, hydroxyl groups were first oxidized to the aldehyde form[6]. The AG was dissolved in distilled water. To this solution, potassium periodate was added separately, and the mixture was stirred at room temperature in the dark for 2 hours. The resulting oxidized arabinogalactan (Ox-AG) were purified by Dowex-1x4 anion exchange chromatography followed by extensive dialysis against distilled water (12.000-14.000 MWCO cellulose tubing) for three days. The presence of aldehyde groups was characterized by FTIR analysis.

For oxidized arabinogalactan binding APA-MNP, Ox-AG was dissolved in borate buffer. It was stirred with APA-MNP for two days in the dark. The solution was centrifuged to remove the insoluble reactants, receiving a clear yellow solution. Sodium borohydride (NaBH<sub>4</sub>) was used to reduce the obtained to a more stable amine form. The imine conjugate and sodium borohydride were stirred at room temperature overnight. The resulting light-yellow solution was purified by dialysis against distilled water at 4°C for 48 h followed. The obtained arabinogalactan-coated nanoparticles (ANP) were dried in the oven. Characterization studies were carried out by FTIR and SEM analyzes.

○ ***Doxorubicin Loaded Arabinogalactan Coated Magnetic Nanoparticle(DANP)***

Doxorubicin was loaded onto ANP by adsorption[7][8]. For this purpose, 500 µg/mL concentration Dox was added into the dispersion of nanoparticles and mixed. Then, the nanoparticles were centrifuged. The nanoparticles were washed two times with distilled water. Dox was determined by absorbance measurements at 480 nm using a UV-VIS spectrophotometer (Agilent Technologies, Cary 60 UV-Vis) . The amount of loaded Dox (Eq.1) and the Dox loading efficiency(%) in the samples were calculated (Eq. 2). In addition, the obtained nanoparticles was characterized with FTIR and SEM analysis.

$$\text{Dox loaded Content } (\mu\text{g Dox/ mg NP}) = \frac{(\text{Initial Dox amount}(\mu\text{g}) - \text{Unbound Dox amount}(\mu\text{g}))}{\text{weight of nanoparticles}(\text{mg})} \times 100 \quad (1)$$

$$\text{Dox loading efficien}(\%) = \frac{(\text{Initial Dox amount}(\mu\text{g}) - \text{Unbound Dox amount}(\mu\text{g}))}{\text{Initial Dox amount}(\mu\text{g})} \times 100 \quad (2)$$

### 3. RESULTS AND DISCUSSION

○ ***Magnetic Nanoparticle Synthesis and Functionalized with 2-aminoethylphosphonic Acid***

Magnetic nanoparticles were synthesized by the co-precipitation method. The FTIR spectrum of MNP is given in Figure 1A. The characteristic Fe-O bond of the magnetic nanoparticle was observed at 550-600 cm<sup>-1</sup>. Figure 1B shows the SEM image of MNP, and the nanoparticle size was observed at 13 and 20 nm. The nanoparticle structure was spherical. The zeta potential value of MNP was found to be +7.03±4.52 mV. The hydrodynamic size of MNP was found to be 191.7±52.84 nm. Size measurements (hydrodynamic size) obtained with DLS are nanoparticles dispersed in a solvent. The size measurements observed by SEM correspond to nanoparticles in dried form. Nanoparticles interact with solvent molecules through various non-covalent interactions (e.g., hydrogen bonding, van der Waals interactions, π-π overlap). Therefore, particle sizes observed by SEM cannot be compared with hydrodynamic sizes because hydrodynamic size measurements can give much higher values[9].

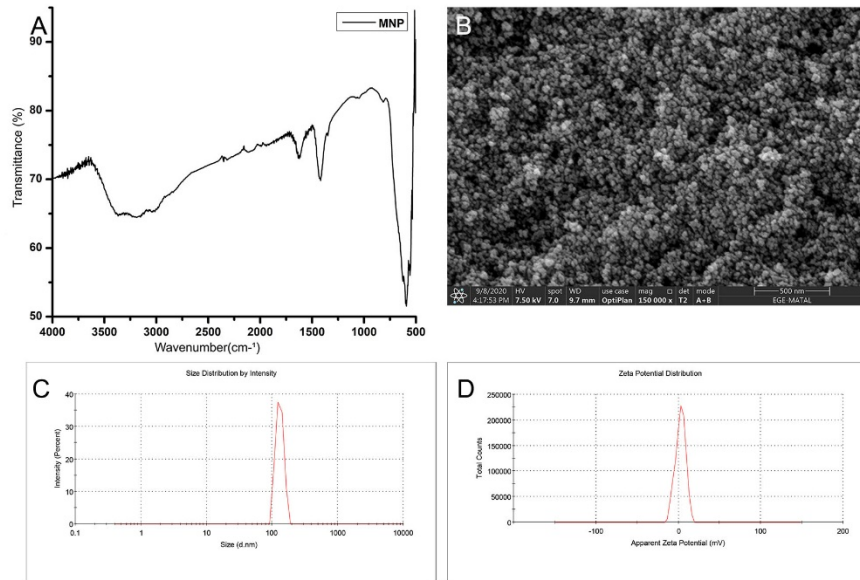


Figure 17. A) FTIR spectra of MNP. B) SEM images of MNP. C) Hydrodynamic size graphics of MNP. D) Zeta potential graphics of MNP.

The surface was functionalized with 2-aminoethylphosphonic acid to binding with arabinogalactan. The FTIR spectrum of APA-MNP is given in Figure 2.A. In the FTIR spectrum of APA-MNP, the N-C peak at  $1131\text{ cm}^{-1}$  and the N-H peak at  $1637\text{ cm}^{-1}$  were observed [5]. These peaks confirm that APA interacts with the surface of the magnetic nanoparticle. The peaks observed at  $1029\text{ cm}^{-1}$  explain the R-O-P and P=O stretch bonds found in 2-aminoethylphosphonic acid [10]. In addition, the structure of the peak belonging to the Fe-O bond is preserved between  $550\text{--}600\text{ cm}^{-1}$ , which shows the magnetic character. Thus, it is shown that the structure preserves its magnetic character. SEM images of APA-MNPs showed in Figure 2B. APA-MNP sizes range from 17-23 nm and retain their spherical morphology. The hydrodynamic size of APA-MNP was measured as  $184.7 \pm 6.36\text{ nm}$  (Fig. 2C). Zeta potential was measured as  $+7.03 \pm 4.52\text{ mV}$  in MNPs, increased to  $+22.83 \pm 1.72\text{ mV}$  in APA-MNPs due to functionalization of the structure with APA. Due to the presence of amino groups in the structure, the measured positive charge increased [10].



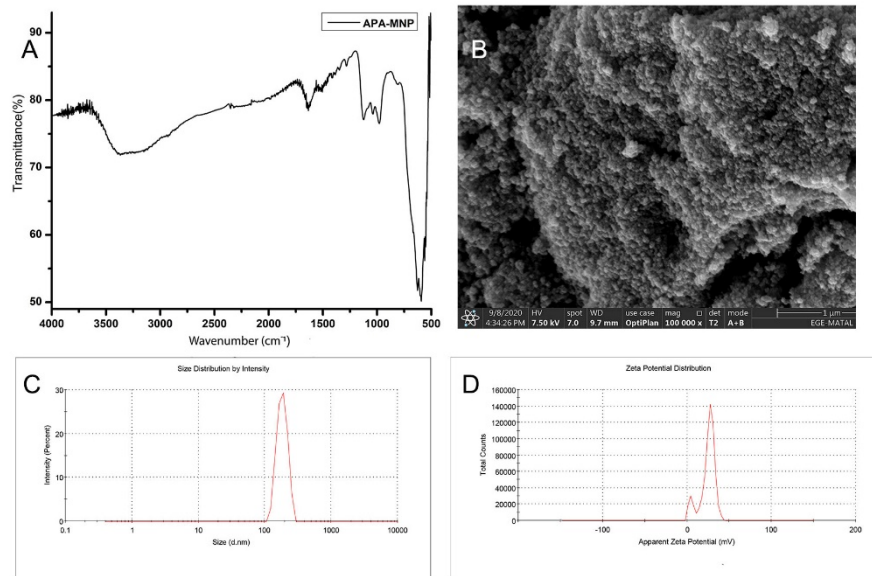


Figure 18.A) FTIR spectra of APA-MNP. B) SEM images of APA-MNP. C) Hydrodynamic size graphics of APA-MNP. D) Zeta potential graphics of APA-MNP.

### ○ Oxidation of Arabinogalactan and Binding of APA-MNP

Arabinogalactan was oxidized with potassium periodate. It has been stated in the literature that the characteristic band of Ox-AG is at  $1724\text{ cm}^{-1}$  [6]. This characteristic band at  $1724\text{ cm}^{-1}$  is also seen in our structure (data not shown). The FTIR graph of ANP the peak found at  $1724\text{ cm}^{-1}$ , indicating the oxidation of arabinogalactan, and the peak at  $1630\text{ cm}^{-1}$ , caused by the amine groups in APA-MNP, disappeared due to the binding of AGA-APA with oxidized arabinogalactan. In addition, the intensity of the peak observed at  $2878\text{ cm}^{-1}$  decreased due to binding APA-MNP. FTIR results were confirmed the successful binding of APA-MNP. SEM image of ANP is given in Figure 3. The size of ANP is between 25-35 nm, and the structures have a spherical shape. A slight increase in size was observed between APA-MNP and ANP. This increase is due to the inclusion of arabinogalactan in the structure.

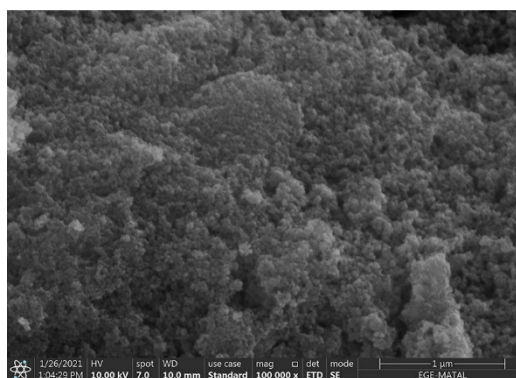


Figure 19. SEM images of ANP.

### ○ Doxorubicin Loaded Arabinogalactan Coated Magnetic Nanoparticle (DANP)

Doxorubicin was loaded onto arabinogalactan-coated magnetic nanoparticles by adsorption. The determination of drug molecules loaded on DANP was made by measuring 480 nm absorbance in a UV-Vis spectrophotometer, loaded content ( $\mu\text{g Dox/mg NP}$ ) and the loading efficiency (%) were calculated. It was observed that it contained  $79.22\text{ }\mu\text{g}$  of Dox per mg nanoparticle at  $500\text{ }\mu\text{g/mL}$  Dox concentration and the

loading efficiency of the drug was 78.17%. As a result of the drug-binding study, high binding efficiency and loaded amount were obtained. The obtained DANP was characterized using FTIR and SEM analysis. FTIR analysis was performed to confirm the DANP structure. In the spectrum of doxorubicin, peaks were observed at  $2930\text{ cm}^{-1}$  (C-H),  $1620\text{ cm}^{-1}$  (N-H),  $1400\text{ cm}^{-1}$  (C-C) and  $1055\text{ cm}^{-1}$  (C-O)  $\text{cm}^{-1}$  [11]. Based on FTIR analysis, it was confirmed the presence of doxorubicin on arabinogalactan-coated ANPs. The morphologies and size of DANPs, which were determined by SEM examinations and is given in Figure 4. DANP size is between 30-35 nm, and its morphology is spherical.

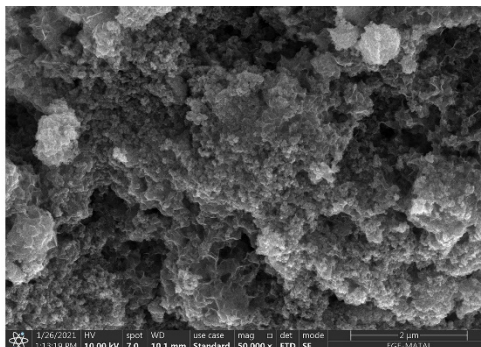


Figure 20. SEM images of DANP.

## CONCLUSION

Magnetic nanoparticles were synthesized by the co-precipitation method. The surface was functionalized with 2-aminoethylphosphonic acid to provide the binding of arabinogalactan with magnetic nanoparticles. Then, MNP's surface was coated with arabinogalactan. After that, doxorubicin was loaded on arabinogalactan-coated magnetic nanoparticles by adsorption. Characterization studies of the obtained structures were carried out. SEM images confirmed that the structure was spherical, and FTIR results also confirmed the chemical structure. In addition, the hydrodynamic size has shown to be an ideal size for cancer treatment. It is thought that Dox loaded arabinogalactan coated magnetic nanoparticles could be magnetically targeted at a desired cancerous site and asialoglycoprotein receptor-targeted could show an increased therapeutic effect for hepatocellular carcinoma. The study is thought to have potential for in vitro, in vivo, and ex vivo studies.

## ACKNOWLEDGMENT

This work was supported by the Scientific and Technological Research Council of Turkey, TUBITAK (grant number: 119S496). The authors would like to acknowledge to Ege University Center for Drug Research, Development, and Pharmacokinetic Applications (ARGEFAR) for laboratory support.

## REFERENCES

- [1]. D. Motola-Kuba, D. Zamora-Valdés, M. Uribe, and N. Méndez-Sánchez, "Hepatocellular carcinoma. An overview," *Ann Hepatol.*, vol 5, pp. 16–24, 2006.
- [2]. C.F. Thorn, C. Oshiro, S. Marsh, T. Hernandez-Boussard, H. McLeod, T.E. Klein, and R.B. Altman, "Doxorubicin pathways: Pharmacodynamics and adverse effects," *Pharmacogenet Genomics*, vol 21, pp. 440, 2011.
- [3]. M. Mishra, P. Kumar, J.S. Rajawat, R. Malik, G. Sharma, and A. Modgil, "Nanotechnology: Revolutionizing the Science of Drug Delivery," *Curr Pharm Des.*, vol 24, pp. 5086–107, 2019.
- [4]. Y. López-Franco, I. Higuera-Ciapara, F.M. Goycoolea, and W. Wang., *In: Woodhead Publishing Series in Food Science, Technology and Nutrition.*, 2nd ed. G.O. Phillips, P. A. Williams, Cambridge, England: Woodhead Publishing Ltd. ,2009.
- [5]. S. Hamarat Sanlier, G. Ak, H. Yilmaz, A.Unal, U.F. Bozkaya, G. Taniyan, Y. Yildirim, and G. Yildiz Turkyilmaz, "Development of Ultrasound-Triggered and Magnetic-Targeted Nanobubble System for Dual-Drug Delivery," *J Pharm Sci.*, vol 108 pp.1272–83. 2019.
- [6]. R.I. Pinhassi, Y.G. Assaraf, S. Farber, M. Stark, D. Ickowicz, S. Drori, A.J: Domb, and Y. D. Livney, "Arabinogalactan-folic acid-drug conjugate for targeted delivery and target-activated release of anticancer drugs to folate receptor-overexpressing cells," *Biomacromolecules*, vol 11, pp. 294–303, 2010.
- [7]. Y. Yang, J. Jiang Sen, B. Du, Z.F. Gan, M. Qian, and P. Zhang, "Preparation and properties of a novel drug delivery system with both magnetic and biomolecular targeting," *J Mater Sci Mater Med.*, vol 20 pp. 301–7, 2009.
- [8]. G. Ak, H. Yilmaz, A. Gunes, and S.Hamarat Sanlier, "In vitro and in vivo evaluation of folate receptor- targeted a

- novel magnetic drug delivery system for ovarian cancer therapy” *Artif Cells, Nanomedicine, Biotechnol.*, vol 46 pp. S926–S937, 2018.
- [9]. K. Vasić, Ž. Knez, E.A. Konstantinova, and A.I. Kokorin, “Structural and magnetic characteristics of carboxymethyl dextran coated magnetic nanoparticles : From characterization to immobilization application” *React Funct Polym.* vol 148, pp. 104481, 2020.
- [10]. M. Das, D. Mishra, T.K. Maiti, A. Basak, and P. Pramanik, “Bio-functionalization of magnetite nanoparticles using an aminophosphonic acid coupling agent: New, ultradispersed, iron-oxide folate nanoconjugates for cancer-specific targeting,” *Nanotechnology* vol 19, pp. 415101, 2008.
- [11]. S. Yalcin, P. Mutlu, G. Unsoy, R. Khodadust, and U. Gunduz, “Doxorubicin-loaded magnetic nanoparticles downregulate expression of anti-apoptotic genes in resistant breast cancer cells,” *J Mater Nanosci.*, vol 7 pp. 29–35, 2020.

## BIOGRAPHY

Tugba Karakayali has Bachelor’s degree and master degree at Biochemistry from Ege University. She is a doctoral student at Ege University, Department of Biochemistry, since 2021. In her undergraduate and master thesis, she has conducted experiments with cancer cell lines in vitro by synthesizing the targeted drug carrier nanoparticle in cancer treatment. Besides, she has been involved in various projects on drug delivery systems during her Master’s degree. Her areas of interest are the development and characterization of targeted drug delivery systems for cancer treatment.

# The Transition of Romanian Agriculture: From Traditional Agriculture to a Digital, Sustainable Agriculture

*Daniela Trifan<sup>1</sup>, George Toader<sup>2,1</sup>, Emanuela Lungu<sup>1</sup>, Alin Ionel Ghiorghe<sup>1</sup>,  
Viorica Bercea<sup>1</sup>, Cătălin-Ioan Enea<sup>3</sup>, Leonard Ilie<sup>2</sup>*

---

## Abstract

*With the accession to the European Union, Romania benefited from the legislative framework of the common agricultural policy, a policy that influenced the sale and processing of agricultural products, major decisions on the direction of agriculture in our country and on the costs of agricultural production. The image of Romania's contemporary agriculture differs a lot from the agriculture of European countries, this being structured differently from the rest of Europe. Romania is characterized by a lack of medium and small family farms because leaving the communist system has left its mark on their growth and development. Negotiations on agriculture (in Romania) began in November 2002 and were concluded in June 2004. In these negotiations, Romania benefited from an agreement similar to that of the states that joined the EU in 2004, namely better financing of agriculture, a stability of agri-food prices as well as real support measures for farmers (European non-reimbursable funds). The article aims to present in the introduction the advantages of Romania's accession to the EU, the evolution of Romanian agriculture in this context and the presentation of state-of-the-art projects that make possible a transition from traditional to digital agriculture in which artificial intelligence makes its presence felt.*

**Keywords:** sustainable agriculture, digitalization, maximizing production, transition, emerging technologies in agriculture.

---

## 1. INTRODUCTION

In the period 2002-2004, the European Union carried out a series of direct negotiations so as to carry out a series of measures to support Romanian agriculture. During these negotiations were discussed the measures of direct support (the amount of funds allocated to Romania), production quotas, new measures for the development of Romanian agriculture, as well as a series of measures and agricultural production systems necessary to adhere to EU food safety standards. (sanitary, veterinary, phytosanitary norms) (Giurcă, 2005). Romania's accession to the EU has allowed the establishment of a pattern of financing Romanian agriculture, namely the transition from an unstable agricultural policy and forms of financing (depending on electoral cycles) to the implementation of real, sustainable measures to facilitate Romania's integration into the European Union. to the support given to agriculture as well as to a financing of small farmers and young farmers through different programs (Alexandri and Luca, 2008). Romania's accession to the EU has brought a plus for Romanian agriculture by providing direct payments, the state funding being much higher after accession (Hubbard et al., 2014).

The financing of Romanian agriculture through the second pillar represented a support for the development of Romanian agriculture. The adjustment of agricultural practices and the implementation of norms and objectives for greening agricultural soils and crops as well as the trend towards non-invasive agricultural technologies, the need to implement automated systems and programs (based on artificial intelligence) have led to the development of new best practice guides. of new financing programs for Romanian farmers (Giurcă, 2005). At the same time, another advantage of Romania's accession to the EU, in the agricultural field, was represented by the increase of entrepreneurship in rural areas. This aspect had the role of developing the activity of subsistence agriculture to a transition agriculture in order to achieve a diversification of non-agricultural activities into agricultural activities, profitable for farmers. Supporting entrepreneurship in underdeveloped areas has led to the emergence of small agricultural production centers, centers that give the agri-food network the necessary food for humans and animals. Another identified aspect was the emergence of new reforms

needed in the agricultural field. These reforms have the role of managing the partner institutions in the processes of allocating and using the funds that will be allocated for Romania, implementing the common agricultural policies (CAP) and supporting the agricultural sector in case of potential shocks.

In the accession and post-accession process, numerous networks, clusters and incubators for data collection, interpretation and transformation of information obtained into knowledge have been developed in order to obtain innovative products or technologies in the agricultural field. These generators of information and knowledge have been basic pillars in the process of increasing the competitiveness of the agricultural sector, increasing and maximizing agricultural holdings, with a strong emphasis on supporting agricultural farms facing management problems, management, low level of processes. sale-purchase and supporting the renewal of generations of agricultural farmers (European Commission, 2016).

With Romania's entry into the European Union, a campaign was launched to organize and promote food chains and risk management programs in agriculture, especially on the integration of farmers in quality systems, IT and the creation of platforms that have the role of uniting farmers, providing them with information and advice on farm development, maximizing agricultural production and profit, but above all moving towards sustainable agriculture. The transition from traditional to sustainable agriculture will be gradual, with the farmer aware that in this process of transition and development farmers must conserve and strengthen agricultural ecosystems by restoring and conserving biodiversity, improving fertilization, irrigation and soil management. as well as by promoting the efficient use of agricultural resources by reducing pollution in agriculture and the use of non-invasive technologies for soil, culture, environment, man and animals.

## 2. MATERIAL AND METHOD

Before Romania's accession to the European Union, the contribution of agriculture to the formation of GDP was approx. 14% in 2004. The share of agriculture in the country's gross domestic GDP decreased to 8.8% (in 2006). The decrease of the contribution of the agricultural field to the GDP presented a decrease even after Romania's accession to the EU, in 2008 the index being of 7.5%. The relative share of GDP compared to the EU average remained a source of instability of GDP values, because this instability was attributed to climatic factors, the level of technology of farms and the socio-economic situation of Romania. The tendency to reduce this share is an important result from the perspective of decreasing the contribution of agricultural supply to GDP fluctuations, against the background of increasingly unstable climatic conditions and low farm capitalization. The reduction of the contribution of Romanian agriculture to the formation of GDP was due to some important fluctuations of agricultural production (table 1). The year 2008 represented the year in which the Romanian agriculture registered a major growth, compared to 2007. The positive dynamics of the gross value added (GVA) was due to the low productions from 2007, this year being one of the most unfavorable years from the point of view. climate change, throughout the transition to a market economy.

Table 1. Dynamics of agricultural production in Romania (pre-accession period)

Specification	2003	2004	2005	2006	2007	2008
Agricultural production * in Romania (millions of lei current)	22835,2	31030,1	24277,9	26898,2	23454,8	32566,4
Dynamics of agricultural production * (%) (year 2000 = 100%)	125,7	149,2	123,3	127,4	106,4	129,2
(year 2002 = 100%)	105,2	124,9	103,2	106,6	89,0	108,1

The pre-accession period was a bad period for Romanian agriculture, obtaining financing projects from the state was a difficult test for farmers. At the same time, the farmers in the pre-accession period went on bank credit lines, which, compared to the pedo-climatic conditions of the pre-accession years, represented an obstacle for the farmers. Romania's post-EU accession period was a "relaxation" for farmers because the new amendments, orders and laws were in their favor. The fact that farmers were able to access non-reimbursable European funds for the purchase of new agricultural equipment and machinery and the expansion of their farms was an important step in increasing Romania's domestic GDP and increasing and maximizing agricultural production and farmers' profits. Romania's accession to the European space means for farmers and access to new technologies for agriculture, non-invasive technologies for the environment, soil, crops, productivity and profitability.

Thus, farmers had access to new technologies such as online platforms for disseminating information on technologies applied to crops, access to knowledge generation, some technologies such as drones, weather

stations, satellite stations and a number of equipment needed for the application. fertilizers, plant protection products or even for soil disinfection. As materials, the research part used a weather station, ground sensors, state-of-the-art drone (equipped with artificial intelligence to make orthophotoplans - georeferenced maps and NDVI maps), detection sensors (recording of soil moisture, density, temperature, permeability, electroconductivity, etc.), data recording, processing, storage and dissemination system.

### 3. RESULTS AND DISCUSSIONS

After accession, farmers were able to access new agricultural information, based on which farmers implemented new technologies on their farms in order to reduce agricultural costs, maximize crop yields and develop sustainable agriculture. , sustainable based on these new non-invasive technologies. After accession, most farmers tried to implement non-existent technologies in Romania. Their implementation led to the emergence of Agriculture 4.0 which combined traditional agriculture with the digital environment, the Internet of Things and artificial intelligence. Thus, farmers have implemented in their own farms a series of technologies such as sensors, drones, robots, an interconnection of these equipments through the Internet. The role of these technologies was to produce adaptability, to adapt themselves to environmental conditions, without human intervention. A first example was the implementation of small drones (Figure 1) in agricultural crops in the Netherlands. The role of drones was to search for, identify and eliminate insects harmful to crops, without using invasive or chemical solutions. Based on interconnected software and sensors, the software identifies the pest, its degree of attack in the respective culture and the non-invasive ways to combat them (Figure 2).



Figure 1. Precision drones used in agriculture



Figure 2. Diagram of drone use in agriculture

Globally, the use of drones in agriculture is constantly increasing, because compared to other methods of aerial monitoring, drones generate more and more accurate data on the state of crops. Also, the economic nature of the use of drones is not to be neglected, for the monitoring of holdings with a size of less than 50 hectares, the drones being cheaper than surveillance by airplanes or satellite images. Data obtained through drones are used in various ways to improve the performance of a farm. The increasingly frequent use of drones in precision agriculture aims to obtain high and quality production, optimizing economic profits, integrated environmental protection.

By using drones in agriculture, farmers can benefit from maps containing information on vegetation signs. Through these maps, farmers would be able to spray fertilizer where the soil is poorer, could only irrigate drier areas and treat only plants that need to be protected from pests. In this way considerable potential savings can

be achieved, the plants would be healthy and higher yields of the monitored crops are obtained. Here is a model of the situation that everyone benefits from: a way to practice agriculture using technology. Figure 3 shows the schematic diagram of the use of drones in agriculture.

The year 2020 brought with it an unfortunate period for Romanian agriculture, a period marked by two major events: extreme drought and coronavirus pandemic. The extreme drought that occurred in 2020 was the worst in the last 50 years, as mentioned by farmers, which had a negative impact on crop productivity and, implicitly, on farmers' profits. The coronavirus pandemic has had a negative effect on the production and distribution chain of agricultural products. Thus, the restrictions imposed by the authorities had a negative effect on farmers' ability to sell their products. Although in some European countries these technologies have been used since 2003-2004, in Romania the use of drone technology has been placed much less than it should be.

An example of a project that combined traditional agriculture with modern agriculture (Agriculture 4.0) was the project carried out within the Research-Development Station for Agriculture Brăila, a project entitled AGRODATA. This was based on the desire of researchers from SCDA Brăila to help farmers in their production processes of agricultural crops and to guide them in good agricultural practices. Based on these guidelines farmers were able to access a number of innovative technologies, necessary to increase, develop and maximize the productivity of agricultural crops but especially, their conversion from a traditional agriculture to a digital agriculture.

The role of this project implemented in Romanian agriculture was to arouse the interest of farmers for digitalization, for the use of new non-invasive technologies, friendly to the environment, technologies that have the role of substituting classical fertilization technologies, application of chemical fertilizers and plant protection products. With the help of the drone used in this project, a series of flights were carried out with the aim of making orthophotoplanes that identified certain aspects such as the content of phosphorus (figure 3), mobile potassium (figure 4), the total content of salts (figure 5).

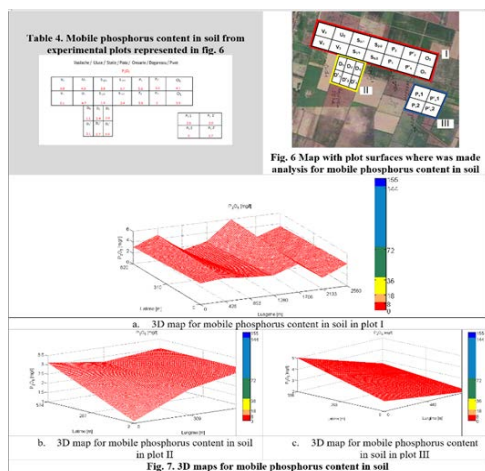


Figure 3. Phosphorus content in the soil

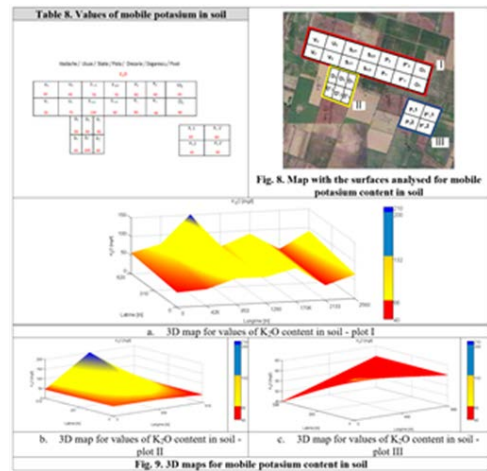


Figure 5. Potassium content of the soil

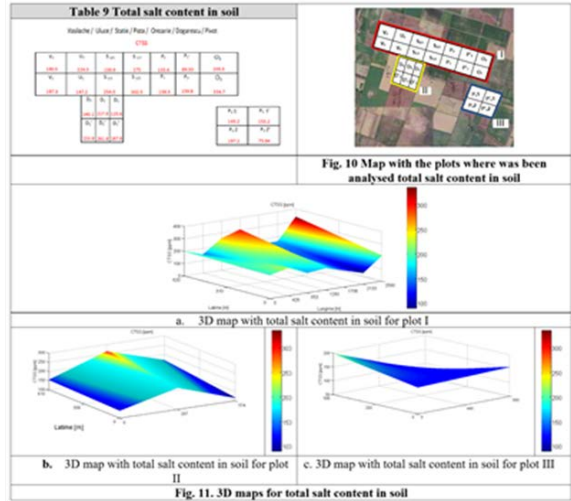


Figure 6. Total soil salt content

In order to make a series of determinations on agricultural crops, a series of UAV drone flights were carried out on the maize crop in the experimental fields of SCDA Brăila, a drone that has the role of making orthophotoplans. Based on the results obtained by the drone, depending on the specificity of each crop, specialists made a series of observations on crops, observations such as plant emergence, density, observation of crop abnormalities (disease attack, pests), estimating and monitoring the content of minerals in soil, estimating the degree of pest attack, monitoring and their diseases in agricultural crops and estimating crop productivity, based on the above (Figure 6).

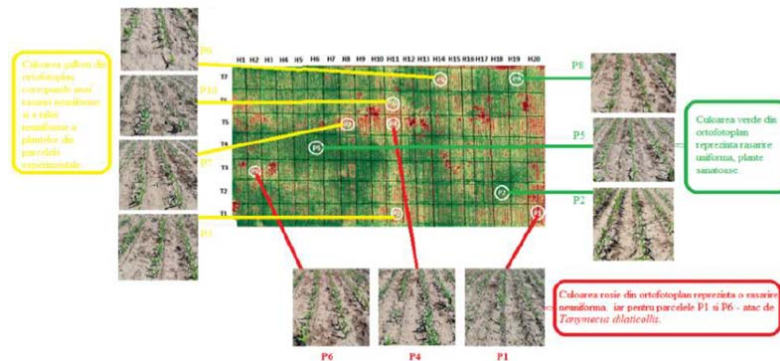


Figure 7. Realization of flights with drone UAV corn culture CE Chiscani

Following the drone flights, a series of data were identified and, following their analyzes and interpretations, the researchers from SCDA Brăila made determinations for each scanned culture. Following the interpretation of the data, at the level of certain lots (P1, P2 and P6 - the red plots identified with the red color in the orthophotoplan) different problems were identified such as: small amount of nitrogen (in the soil structure), a "ragged" appearance of corn, as well as the appearance of the burning phenomenon on the leaves of corn plants (*Setosphaeria turcica*) and the appearance of embers (*Shacelotheca reiliana*) (Figure 7).



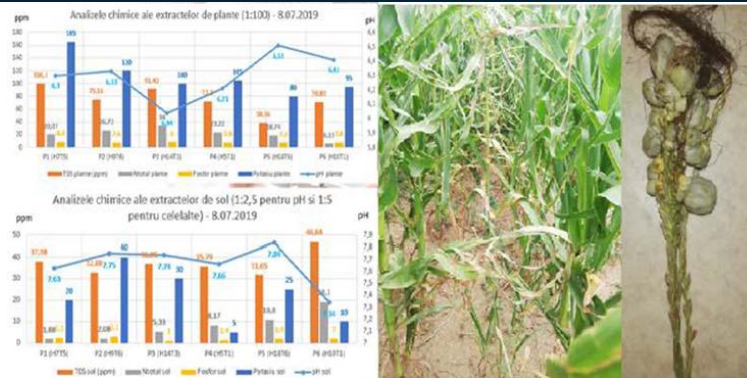


Figure 8. Agrochemical results and field observations (corn crop orthophotoplan SCDA Brăila)

After collecting and interpreting the data, an online database was created - the Blue Monitor system, a system with the role of storing pedo-climatic data received from: the weather station, ground sensors, UAV drone flight data. The purpose of this system is to disseminate knowledge on the (early) detection of diseases and pests, the preparation of reports on the typology of pests and diseases, the recommendations of specialists for crop treatment, prevention and diagnosis of agricultural crops. The AGRODATA online platform can provide (by interconnecting these technologies) a series of reports on the evolution of pedo-climatic indices, the degree of attack of diseases and pests, weather forecasts as well as optimal methods and technologies for applying fertilization and protection products. of plants, non-invasive products for the environment, humans and animals.

## CONCLUSIONS

After Romania's accession to the European Union, agriculture went through a transition from a classic, traditional agriculture to a sustainable, sustainable agriculture friendly to the environment, human and animal health. Promoting resource efficiency and supporting the transition to a low-carbon economy, resistant to socio-political changes and transitions, by increasing the efficiency of water consumption in agriculture (irrigation), the use of solar energy in agriculture, facilitating the supply and use of renewable sources (wind) and the reduction of nitrogen and methane oxides in agriculture were among the first points of discussion and negotiation at European level.

These new technologies have the role of facilitating the work of farmers, of protecting the environment and of increasing the productivity of agricultural crops by implementing these technologies at farm level. Post-accession technologies have had the effect of protecting the environment by conserving and regenerating the resources of agricultural agroecosystems. The implementation of the AGRODATA project in agriculture in the north of Bărăgan is an important step in the post-accession period, a period in which some farmers have developed both production technologies, processing technologies and cost reduction per hectare.

The development of these online platforms and the adherence of farmers to them represented a much faster circulation of information as well as a dissemination of results obtained in agricultural crops, recommendations on treatments, recommended doses per crop, based on this information forming a basis that provides farmers information on the optimal pedo-climatic conditions (for each crop), plant health, degree of attack of diseases and pests, as well as recommendations of specialists from SCDA Brăila, recommendations on maximizing production, profit and reducing costs in agriculture.

**ACKNOWLEDGMENT**

This work was supported by a grant of the Romanian National Authority for Scientific Research and Innovation, CNCS/CCCDI – UEFISCDI, project number PN-III-P2-2.1-PTE-2019-0085, within PNCDI III”

**REFERENCES**

- [1]. Alexandri, C., Luca, L. (2008). Romania and CAP Reform, Agricultural Economics and Rural Development, New Series, V(3-4): 161-180,
- [2]. Comisia Europeană (2017f). Proposal for a Regulation Of The European Parliament And Of The Council on establishing a single digital gateway to provide information, procedures, assistance and problem solving services and amending Regulation (EU) No 1024/2012, [file:///C:/Users/Oana/Downloads/PART-2017-156445V1%20\(1\).pdf](file:///C:/Users/Oana/Downloads/PART-2017-156445V1%20(1).pdf)
- [3]. Giurcă, D. (2005). Elemente de impact pre- si post-aderare – evaluari pentru sectorul agroalimentar si rural din România, Oeconomica, 1, 561-594,
- [4]. Hubbard, C., Hubbard, L. (2008). Bulgaria and Romania: Paths to EU Accession and the Agricultural Sector, Centre for Rural Economy Discussion Paper Series no. 17,

# Taxidermy effluent characterisation: A case study in the City of Tshwane

Anoesjka Masilela<sup>1</sup>, Martie A.A Coetzee<sup>2</sup>, Lizzy Mpenyana-Monyatsi<sup>3</sup>

---

## Abstract

South Africa is a well-known destination for local and international trophy hunters. The hunted animal carcasses are processed to produce game trophies at taxidermies, which are mostly situated in the vicinity of hunting farms. Processing of skins and skulls produce effluents containing chemicals which could pose environmental risks. Furthermore, data about the quantity and quality of taxidermy effluents are scarce. This investigation monitored a taxidermy on the outskirts of City of Tshwane, South Africa, which discharged their effluent into an evaporation pond, known to emit bad smells. Effluents from the different processes were sampled for COD, chrome, chloride, fats and oils, sulphates, sodium, pH and conductivity, over a period of two years. In the same period an estimation was made of the volumes of water used in each of the treatment processes. A mass balance approach was used to determine the concentrations of the pollutants in the final effluent. The concentration of major pollutants in the effluent were as follows: 11 166 mg O<sub>2</sub>/L (COD), 2 269 mg Cr/L, 2 486 mg fats and oils /L. The pH and conductivity ranged between pH 3.2 - 7.9 and 120 - 9 741 mS/m, respectively. The volume of the effluent produced was ca 34 m<sup>3</sup>/a, which resulted in mass loads of 377 kg COD/a, 16 kg Cr/a, and 64 kg fats and oils/a. These pollutants would dilute out if discharged into a large water body but the high concentrations of COD, fats and oils, and Cr pose serious environmental risks. The high COD, fat and oils concentrations just below effluent outfall would create anaerobic conditions which could negatively impact the aquatic environment. Chromium (III) could accumulate in the environment to toxic levels. Therefore, it is recommended that the effluent should be treated to remove fats and oils and to reduce the COD and chromium.

**Keywords:** taxidermy effluent, production of animal trophies, water pollution

---

## 1. INTRODUCTION

South Africa has a large number of different wild animal's species which can be hunted. It is also a favoured destination for international trophy hunters [6]. The financial contribution of the taxidermy industry towards the South African wildlife economy is estimated at approximately R1,5 billion [4]. The hunted animals are processed to produce game trophies at the taxidermy. The game trophies are usually fully tanned skins and/or mounts i.e. full, half and shoulder in a life like manner for display. This includes the treatment of skulls (bones), horns/antlers, hooves, claws, teeth [3].

Effluents from taxidermies could be high in organic matter, dissolved salts, chromium, acids and fats and oils.

Majority of taxidermies are located in areas where there is no sewer reticulation resulting in the discharge of effluent into ponds or other on-site treatment facilities. The taxidermy that was investigated is situated in the periphery of the City of Tshwane, in an area where there is no sewer reticulation system. The effluent produced from the processing of skins and skulls is currently discharged into an evaporation pond. There was a rotten egg smell emitted from the evaporation pond.

The aim of this study was to determine the quality and quantity of the effluent discharged by the taxidermy

---

<sup>1</sup>Corresponding Author: Department of Environmental, Water and Earth Sciences, Faculty of Sciences, Tshwane University of Technology, P/B X 680, Pretoria, 0001, South Africa. [anoesjkam@gmail.com](mailto:anoesjkam@gmail.com)

## 2. MATERIALS AND METHODS

### ○ Operation of the taxidermy

The taxidermy produced flat skins, mounted skins and bleached skulls. The skins were processed in a series of batch operations. Most of the operations were done in 200 L – 2 000 L containers, filled with a mixture of water and the chemicals required in each process. When skins were taken to the next process some of the liquid was absorbed onto the skin, which resulted in topping up the level in the previous process container. When the liquid became too contaminated the contents were drained to an on-site evaporation pond.

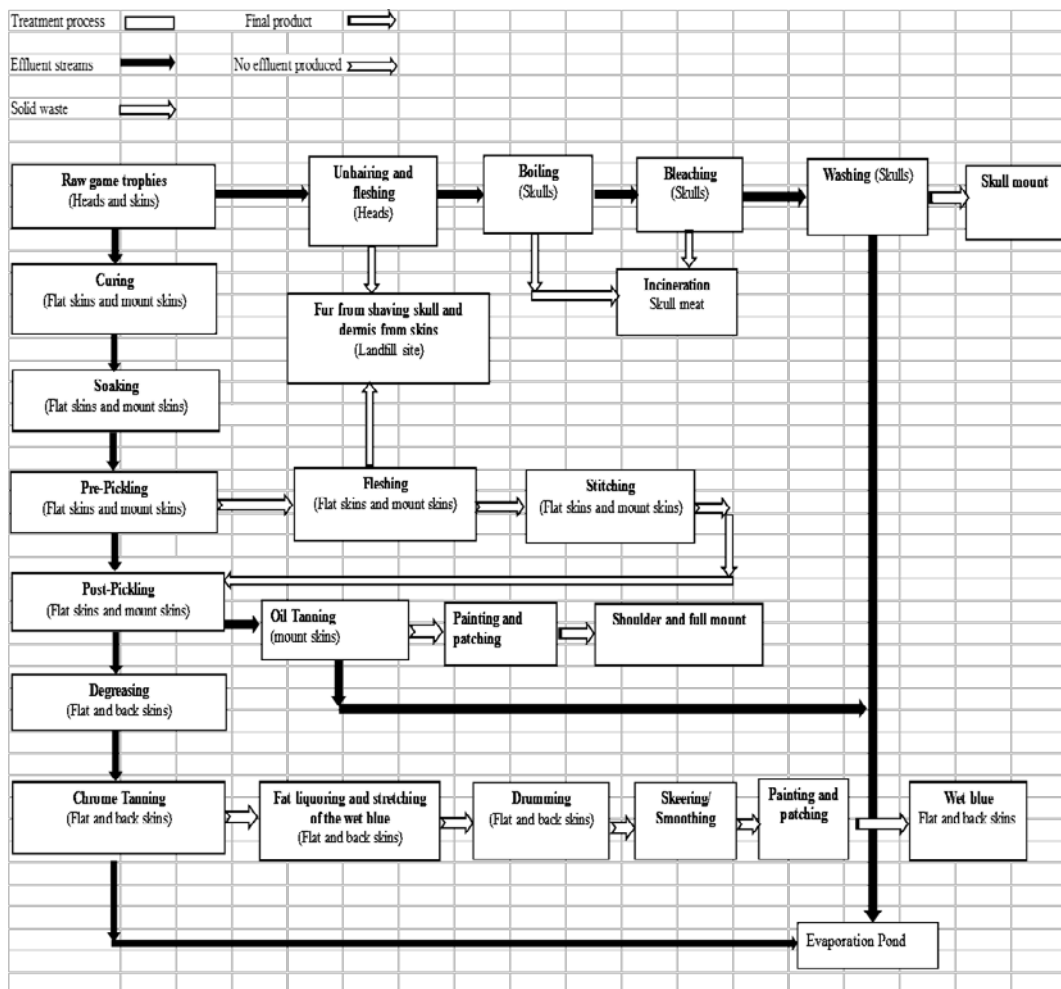


Figure 1: Flow diagram of effluent generation during treatment of game trophies (heads and skins) at a taxidermy

Table 1: Chemicals used in the Taxidermy treatment processes

Process	Chemicals
<b>Skins</b>	
<b>Curing</b>	Sodium Chloride
<b>Soaking</b>	Sodium Chloride washed out of cured hides and skins Detergent which was discontinued
<b>Pre-pickling</b>	Sodium Chloride Formic Acid
<b>Post-pickling</b>	Sodium Chloride Formic Acid
<b>Oil Tanning</b>	Sodium Chloride Eskatan GLH Liquid
<b>Degreasing</b>	Bicarbonate of soda Gelcon PK Degreaser Conc Sodium chloride
<b>Chrome Tanning</b>	Aluminum Sulphate Chromosol B (chrome (III) sulphate) Eskatan GLH Liquid Lutan FN (aluminum complex salt) Sodium Chloride
<b>Skulls</b>	
<b>Boiling</b>	Sodium Chloride
<b>Bleaching</b>	Hydrogen peroxide (Bleach)
<b>Washing</b>	Detergent

The volume for each process discharged was estimated by determining the dimensions of the containers using the following calculation  $\pi \times r^2 \times h$  and  $(L \times W) \times h$ . The h being the height of the liquid in the container when discharged and the frequency of discharge.

Effluent samples from soaking, pre-pickling, post-pickling oil tanning, degreasing, chrome tanning, boiling, bleaching and washing processes were collected weekly, bi-weekly and monthly for a period of two years.

The concentration of the pollutants in the final effluent was calculated from the annual mass load and the total volume annual discharged.

## 4.2. Sample analysis

### Methods used to analyse the parameters of concern

#### Determination of Ammonia, Chlorides Orthophosphates and Sulphates

Thermo Scientific Aquakem 250 Instrument, Standard Methods for the Examination of Water and Wastewater [2]

#### Determination of Chromium and Sodium

Optical Emission Spectrometer 5300 DV Instrument, Standard Methods for the Examination of Water and Wastewater [2]

#### Determination of Chemical oxygen demand

Open Reflux Method [2]

#### Determination of Electrical Conductivity and Ph

Measured onsite with a multi meter Hatch HQ40d

#### Determination of Fats and Oils

Partition-Gravimetric Method [2]

### 3. RESULTS

#### Number of skins/skulls processes

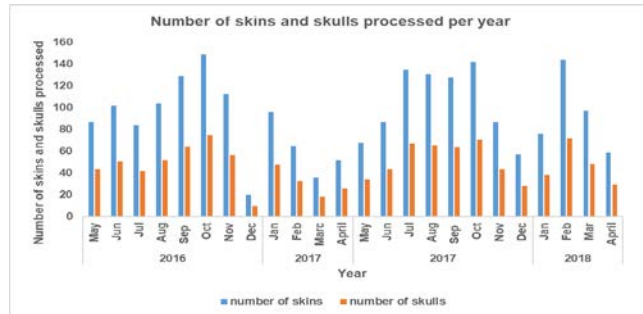


Figure 2: Number of skins and skulls processed between May 2016 and April 2018

Table 2: Volume of effluent produced per annum during the taxidermy effluent treatment processes

Process	Number of skins produced per annum	Effluent produced per year (m <sup>3</sup> )
<b>Skins</b>		
Soaking	1 124 ± 123	1.75 ± 0.27
Pre-pickling	1 124 ± 123	1.16 ± 0.001
Post-pickling	1 124 ± 123	1.02 ± 0.001
Oil Tanning	337 ± 37	1.12 ± 0.001
Degreasing	787 ± 86	1.10 ± 0.12
Chrome Tanning	787 ± 86	3.37 ± 0.37
<b>Total for skins</b>	1124 ± 123	6.15 ± 0.29
<b>Skulls</b>	-	-
Boiling	562 ± 62	16.86 ± 1.85
Bleaching	562 ± 62	3.15 ± 1.06
Washing	562 ± 62	2.86 ± 0.31
<b>Total for skulls</b>	562 ± 62	22.87 ± 3.22

#### Chemical Oxygen Demand

The average chemical oxygen demand concentration for the taxidermy treatment processes which were above 5000 mg O<sub>2</sub>/L were as follows; pre-pickling 15 028 ± 3 742.12 mg O<sub>2</sub>/L, post pickling 16 720.91 ± 4 072.83 mg O<sub>2</sub>/L, oil tanning 23 863.21 ± 10 610.51 mg O<sub>2</sub>/L, degreasing 23 272.38 ± 7 937.81 mg O<sub>2</sub>/L, chrome tanning 21 799.40 ± 10 071.66 mg O<sub>2</sub>/L, boiling 8 479.16 ± 3 432.09 mg O<sub>2</sub>/L, bleaching 6 307.42 ± 5 707.74 mg O<sub>2</sub>/L and washing 5 974 ± 3 124.07 mg O<sub>2</sub>/L. The calculated COD concentration in the effluent would be 11 166.03 mg O<sub>2</sub>/L with a mass load of 376.70 kg O<sub>2</sub>/a. The highest COD mass loads from Figure 3 were from Chrome Tanning 102.91 ± 47.55 kg O<sub>2</sub>/a, and Boiling 142.96 ± 57.87 kg O<sub>2</sub>/a processes.

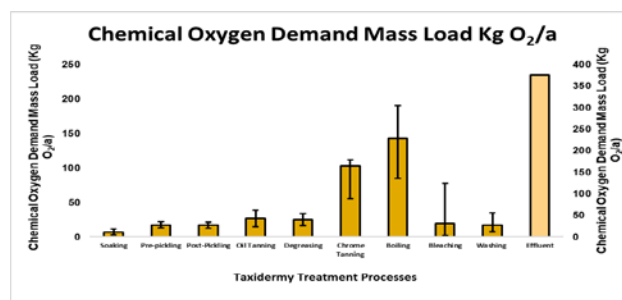


Figure 3 : Chemical Oxygen Demand Mass Load, kg O<sub>2</sub>/a, for the different taxidermy treatment processes

**Nitrogen compounds (Ammonia, Nitrate and Nitrite)**

**Ammonia**

Soaking process was the only process with a high ammonia concentration and mass load, namely  $74.73 \pm 28.29$  mg N/L and  $0.13 \pm 0.05$  kg N/a. Other treatment processes less than 1 mg N/L.

**Nitrate/ Nitrite**

Nitrate/Nitrite concentration for taxidermy treatment processes was less than 1 mg N/L.

**Ortho- phosphate**

The ortho-phosphate concentration for the treatment processes above 8 mg P/L were as follows; soaking  $18.64 \pm 5.63$  mg P/L, pre-pickling  $17.61 \pm 1.28$  mg P/L, post-pickling  $29.23 \pm 25.87$  mg P/L, for skins. For the game skulls; boiling  $15.18 \pm 5.82$  mg P/L, bleaching  $0.83 \pm 1.16$  mg P/L and washing  $0.37 \pm 0.14$  mg P/L. The calculated orthophosphate concentration in the effluent would be 10 mg P/L with a mass load of 0.35 kg P/a. The orthophosphate mass loads as shown in Figure 4 were all less than 1 kg P/a.

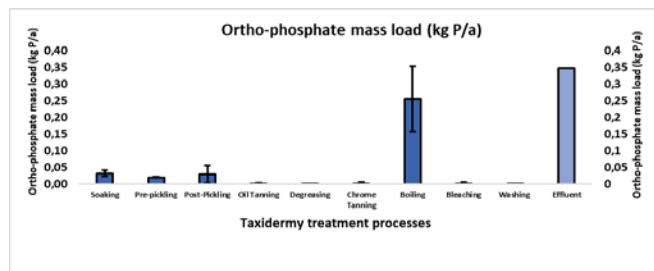


Figure 4: Ortho-phosphate Mass Load in, kg P/a, for the taxidermy treatment processes

**Chlorides**

The results for the chlorides in the taxidermy process liquors which were above 69 mg Cl/L as indicated in were as follows: soaking  $16\ 799.33 \pm 1\ 971.62$  mg Cl/L, pre-pickling  $20\ 694.31 \pm 2\ 282.51$  mg Cl/L, post pickling  $20\ 733.91 \pm 2\ 409.61$  mg Cl/L, degreasing  $16\ 171.03 \pm 1\ 595.79$  mg Cl/L, oil tanning  $18\ 938.72 \pm 2\ 181.49$  mg Cl/L, chrome tanning  $15\ 491.60 \pm 5\ 342.62$  mg Cl/L, for skull treatment boiling  $1\ 313.87 \pm 566.43$  mg Cl/L, bleaching  $295.39 \pm 488.90$  mg Cl/L and washing  $76 \pm 27.61$  mg Cl/L. The calculated chloride concentration in the effluent was  $6\ 222.46$  mg Cl/L with a mass load of 209.92 kg Cl/a. The highest chlorides mass load from Figure 5 was 73.14 kg Cl/a from Chrome tanning.

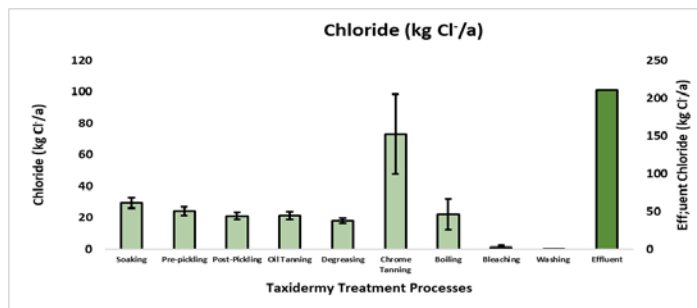


Figure 5: Chlorides mass load in, kg Cl/a, for the taxidermy treatment processes

**Sodium**

Analysis results obtained for sodium which was above 300 from the following processes soaking process  $15\ 125.97 \pm 3\ 442$  mg Na<sup>+</sup>/L, pre-pickling  $27\ 279.79 \pm 4\ 774.97$  mg Na<sup>+</sup>/L, post-prickling  $28\ 737.55 \pm 4\ 462.02$  mg Na<sup>+</sup>/L, oil tanning  $21\ 916 \pm 2\ 737.75$  mg Na<sup>+</sup>/L, degreasing  $24\ 492.65 \pm 4\ 186.35$  mg Na<sup>+</sup>/L, chrome tanning  $22\ 711.49 \pm 4\ 466.81$  mg Na<sup>+</sup>/L, boiling  $1\ 043.25 \pm 592.57$  mg Na<sup>+</sup>/L of skulls. The calculated sodium concentration in the effluent would be  $7\ 835.95$  mg Na<sup>+</sup>/L with a mass load of 264.35 kg Na<sup>+</sup> /a. The highest sodium mass load from Figure 6 was 107.22 kg Na<sup>+</sup> /a from Chrome tanning.

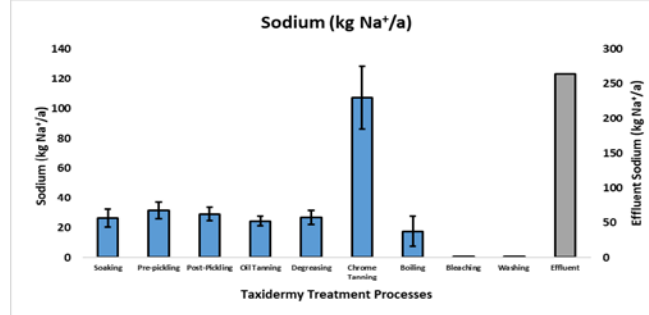


Figure 6: Sodium mass loads in kg Na<sup>+</sup> /a for the taxidermy treatment processes

### Sulphates

Analysis results obtained for sulphates above the limit of 1800 were as follows; soaking process 1 173 ± 281.69 mg SO<sub>4</sub><sup>2-</sup>/L, pre-pickling 2 370.23 ± 780.76 mg SO<sub>4</sub><sup>2-</sup>/L, post pickling 2 179.45 ± 1 529.06 mg SO<sub>4</sub><sup>2-</sup>/L, oil tanning 3 812.67 ± 292.58 mg SO<sub>4</sub><sup>2-</sup>/L, degreasing 1 978.37 ± 1 587.01 mg SO<sub>4</sub><sup>2-</sup>/L chrome tanning 7 592.52 ± 2 060.39 mg SO<sub>4</sub><sup>2-</sup>/L. The calculated sulphates concentration in the effluent was 1 580 mg SO<sub>4</sub><sup>2-</sup>/L. The highest sulphates mass load from Figure 6 was 35.84 ± 9.72 kg SO<sub>4</sub><sup>2-</sup>/yr from chrome tanning . The calculated sulphates mass load would be 53.44 kg SO<sub>4</sub><sup>2-</sup>/a.

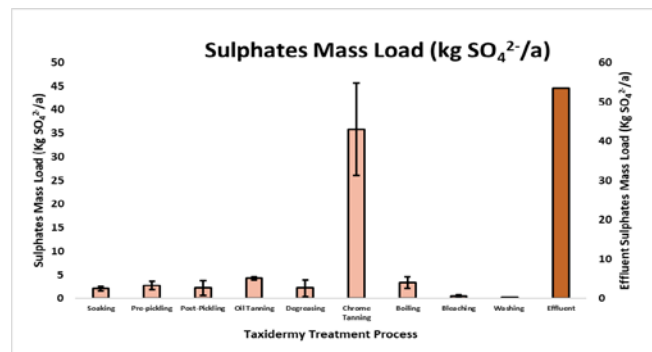


Figure 6: Sulphates mass loads, kg SO<sub>4</sub><sup>2-</sup>/a for the taxidermy treatment processes

### Total Chromium

Chromium was only found in the following treatment processes: pre-pickling (18.5 ± 2.08 mg Cr/L), degreasing (3.69 ± 1.26 mg Cr/L) and chrome tanning (3 352.55 ± 750.22 mg Cr/L). The final concentration was found to be 2 269 mg Cr/L with mass load of 16 kg Cr/a.

### Total Fats and Oils

Fats and oils were detected in the following processes, tanning oil 10 528 ± 4 434.51 mg/L, chrome 3 962 ± 1 576.89 mg/L, boiling 1 788.13 ± 570.11 mg/L and bleaching 1 157.53 ± 1 170 mg/L. Mass load and effluent concentration were 64.28 kg/a and 2 486.74 mg/L respectively. The highest mass load in Figure 7 was from the boiling 30.15 ± 9.61 kg/a



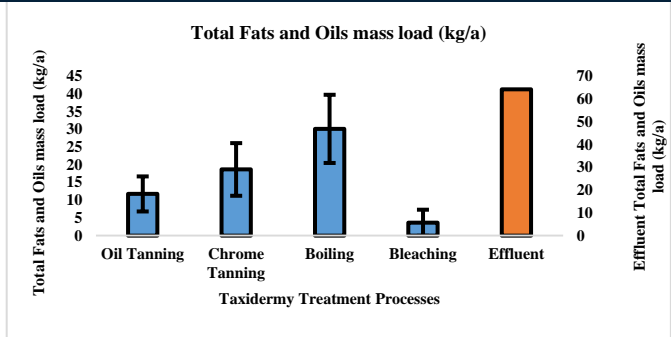


Figure 7: Total Fats and Oils in kg/a, for the taxidermy treatment processes

**pH**

The pH values for each process were as follows: soaking  $7.12 \pm 0.36$  pH, degreasing  $7.17 \pm 0.43$  pH, pre pickling  $3.18 \pm 0.12$  pH, post pickling  $3.14 \pm 0.31$  pH, oil tanning  $3.4 \pm 0.18$  pH, chrome tanning  $3.19 \pm 0.28$  pH, boiling  $7.00 \pm 0.51$  pH, bleaching  $7.59 \pm 0.5$  pH and washing  $7.92 \pm 0.43$  pH.

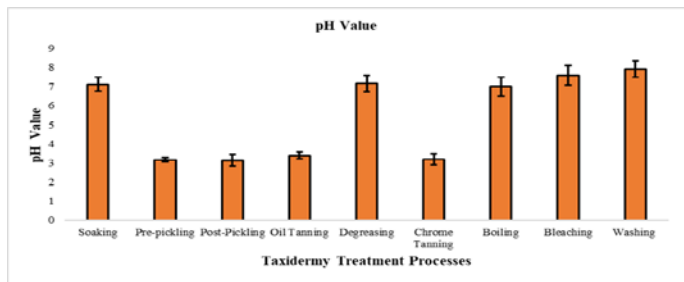


Figure 8: pH Value for the taxidermy treatment processes

**Electrical Conductivity**

The electrical conductivity measured for the soaking process  $5631.16 \pm 1243.93$  mS/m, pre-pickling  $9678 \pm 1602.48$  mS/m, post pickling  $9741.55 \pm 1478.01$  mS/m, oil tanning  $7320 \pm 1035.06$  mS/m, degreasing  $667.59 \pm 1177.73$  mS/m, chrome tanning  $7240.50 \pm 891.72$  mS/m, boiling  $835.72 \pm 343.12$  mS/m, bleaching  $154.17 \pm 45.98$  mS/m and washing  $120 \pm 27.11$  mS/m

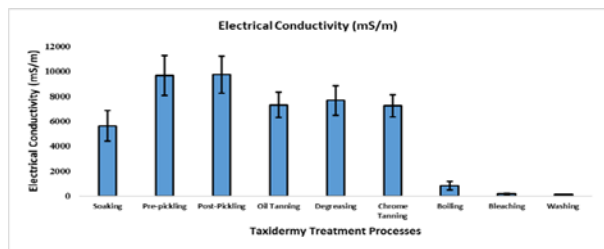


Figure 9: Electrical conductivity in mS/m for the taxidermy treatment processes

Table 4: Calculated final effluent concentrations and mass loads discharged from the taxidermy

Parameter	Calculated concentrations in the final effluent discharged to the pond.	Limits set by City of Tshwane (mg/L)
Ammonia (mg N/L)	4	31
Chemical Oxygen Demand (mg O <sub>2</sub> /L)	11 166	700 - 5000
Chloride (mg Cl <sup>-</sup> /L)	6 222	69*
Chrome (Total), Cr <sup>3+</sup> (mg Cr/L)	2 269	20
Ortho-phosphate (mg P/L)	10	8
Fats and oils (mg/L)	2 486	500 - 2000
Sulphates (mg SO <sub>4</sub> <sup>2-</sup> /L)	1 580	1800
Sodium (mg Na <sup>+</sup> /L)	7 835	300

\* Chloride limit determined by designated wastewater treatment works inflow chloride concentration

## DISCUSSIONS

The high concentrations were due to the chemicals added as well as the physical properties of the skins and skulls.

The **high COD** was mainly due to the skulls as they were boiled with some fat attached to them. High chemical oxygen demand would result in depletion of dissolved oxygen within surface water which can displace aquatic ecosystem

The **fats and oils** originated from processing of skulls and skins. From the skulls during boiling and bleaching. From the skins during fatliquoring and addition of fatliquor to the treatment processes such as chrome tanning and oil tanning.

- **Major pollutants of concern:**

### Chromium

- Mainly in the form of Cr<sup>3+</sup> is less toxic than Cr<sup>6+</sup>.
- While Cr<sup>3+</sup> is a nutrient for human in trace amounts.
- The oxidation of Cr (III) to Cr(IV) is mostly very slow and of little concern [1].
- However disinfectants which are commonly used in the treatment of drinking water can oxidize Cr(III) to Cr(IV), especially when chlorine and ozone were used as oxidants [5].

The presence of **fats and oils** in high concentrations can lead to the following; blockage of municipal sewer line leading to sewer manhole overflows and reduced oxygen transfer from the atmosphere into surface water due to formation of oil and fat layer.

The **low pH** of the effluent can result in loss of non-permeable nature of lining due to corrosive nature of the acidic taxidermy effluent which could result with ground water pollution.

The **high TDS** is due to the increased use of sodium chloride and other inorganic salts. Although the concentrations of some pollutants were high, due to the small volumes used the mass loads were relatively low, which could reduce the impact on receiving waters. High concentrations could severely impact the environment just below the outfall.

Recommended that Fats and oils, COD and Cr<sup>3+</sup> are removed before discharge.

## 5. CONCLUSION

The effluent contains high concentrations of the following parameters which could pose an environmental risk: Chemical Oxygen Demand (COD) with a concentration of 11 166 mg O<sub>2</sub>/L, Chrome (Total), Cr<sup>3+</sup> 2 269 mg Cr/L, Fats and Oils 2 486 mg/L It is recommended that these pollutants are removed before discharge into the environment or an alternative would be discharge into a municipal sewer in line with municipal regulations. Further studies should be done to determine the most efficient and cost effective method for discharge.

## 6. ACKNOWLEDGMENT

The authors would like to thank;

- City of Tshwane for their collaboration and access to laboratory for sample analysis
- The Taxidermy providing access to sampling and trade methods
- Tshwane University of Technology for support in conducting this research

## REFERENCES

- [1]. A.D, Amita, V. Tare, P. Bose.,2006. Extent of oxidation of Cr (III) to Cr (VI) under various conditions pertaining to natural environment. *Journal of Hazardous Materials*, B128, Nov; 164–174
- [2]. APHA, AWWA and WEF (2012) *Standard Methods for the Examination of Water and Wastewater*, 22nd ed. Washington, DC.
- [3]. Department of Agriculture, Forestry and Fisheries. Standards for the registration of a veterinary approved taxidermy or dip and pack facility. Pretoria: National Directorate Animal Health, South Africa.2009.
- [4]. M. Rantlha. South African Taxidermy Industry Development Plan. Industrial Development Division Department OF Trade AND Industry East London International Convention Centre, Eastern Cape.2018.
- [5]. N.D. Rogers. "Chromium Oxidation by Disinfectants and Oxidants Used in Drinking Water Treatment, " *MSC.thesis*, Utah State University, USA, 2016.
- [6]. Van Coller. Trophy hunting's contribution towards South Africa's GDP. AgriSA /WRSA Action Shop 27 October 2017.

# The Importance Of Successive Or Double Agricultural Crops In South-Eastern Of Romania, In The Climatic Change Perspective

*Daniela Trifan<sup>1</sup>, Emanuela Lungu<sup>1</sup>, Alin Ionel Ghiorghe<sup>1</sup>, Nicolae Popescu<sup>1</sup>, George Toader<sup>2</sup>, Valentin Bărdăhan<sup>3</sup>*

---

## Abstract

*Climate change in southeastern Romania has been observed especially in the last decade, by increasing average seasonal and annual temperatures, decreasing average annual rainfall, but especially by extreme phenomena of heat, strong wind, hail and desertification. Due to this, in the dry years, such as the last two agricultural years, the productions decreased very drastically even in the irrigated areas, feeling the need to practice double or successive crops, in order to increase the productions per hectare. This paper presents a multifactorial experience, with 5 species of agricultural crops, sown with different densities and fertilized differently, going through all stages, from motivating the graduation of experimental factors, to soil analysis methods and production results obtained, including efficiently economic and recommendations made for farmers.*

**Keywords:** successive/double crops, agriculture, climatic change conditions

---

## 1. INTRODUCTION

Climate change is one of the most complex issues we face today. This involves many dimensions - science, economics, society, politics but also moral and ethical questions - and is a global problem, felt on a local scale, which will exist in the coming decades and centuries. Climate change mitigation involves reducing the flow of greenhouse gases that capture heat into the atmosphere, either by reducing the sources of these gases or by improving filters that can accumulate these gases, such as oceans, forests and soil. (<https://climate.nasa.gov/solutions/adaptation-mitigation>).

According to climate scenarios for global warming, an increase in average temperature by 2090 is forecast, compared to the period 1980 - 1990 (historical data) with values between 1.8°C and 4.0°C, as seen in attached figure. In Europe, for the projected water deficit, there is an increase in the southern and south-eastern regions. There is currently a significant deficit in the south-western part of Europe, but if no measures are taken to reduce greenhouse gas emissions in the coming years, there will be an increase in global warming, which will lead to a deficit of 35 to 100 mm of rainfall annually in the plain areas and an increase of 60 to 100 and even more than 100 mm of rainfall / year in mountainous areas. Recently, in South-Eastern Romania, there has been a significant increase in average annual temperatures and a decrease in average rainfall, so that the phenomenon of desertification is much more obvious and agricultural crops become inefficient.

At present, Romanian agriculture is facing serious problems related to climate change, in the sense of expanding aridization in large agricultural areas. These changes are manifested by the decrease of the annual precipitation level, by an uneven distribution of them both in time and space and especially by a delay of the water intake compared to the critical moments of the plants, by an increase of the diurnal temperatures and an intensification of the winds, through a reduction of the characteristics of some seasons (there were years in which it can be stated that we had only two seasons).

---

<sup>1</sup> Corresponding author: Agricultural Research and Development Station of Brăila, Romania, Sos. Vizirului km. 9, Brăila, Romania [dana.trifan@yahoo.com](mailto:dana.trifan@yahoo.com)

<sup>2</sup> Corresponding author: Romvac SA Romania, Șos. Centurii, Nr.7, Voluntari, Ilfov, Romania. [toadergeorge92@gmail.com](mailto:toadergeorge92@gmail.com)

<sup>3</sup> Lower Danube University of Galati, Romania, Str. Domneasca nr. 29, Galati, Romania, [vali.bard@yahoo.com](mailto:vali.bard@yahoo.com)

Over the last decade, there has been an increase in demand for agricultural products - both for food and fuel. One way to increase agricultural production is by expanding cultivated land, but multiannual studies by the United States Department of Agriculture (USDA) indicate that about one-third of the expansion of maize-growing areas has changed from hay production in the Program Conservation Reserve (CRP) registration or use of grazing land (Wallander et al., 2011).

Thus, the expansion of agricultural land is not without negative consequences on the environment and land that remains pasture greatly helps the nature and habitat of wildlife (Claassen et al., 2011), including carbon reduction benefits (Horowitz and Gottlieb, 2010).

Another way to increase the production and economic profitability of agriculture is by intensifying the use of existing agricultural land, respectively by successive or double crops, on the same land, in an agricultural year. However, there are authors who do not recommend the practice of successive crops because the phenomenon of soil fatigue occurs by degrading the soil structure, excessive consumption of mineral elements and decreased microbiological activity. That is why there is a need for in-depth research, both in terms of developing crop technologies and economic efficiency of double crops, and in terms of the influence of successive crops on soil fertility.

In Romania, the most practiced successive agricultural crops are those with a vegetation period of less than 100 days for grain harvesting, or species used as green fodder. The fact that in the South-East of Romania the autumn season has become warmer and longer, and the soils are fertile and with the possibility of being irrigated, denotes the possibility for farmers to obtain on the same land two crops in the same year, if they use appropriate technologies, based on agrochemical laboratory analyzes and correct fertilization plans and irrigation norms.

**2.MATERIAL AND METHOD**

A multi-annual analysis of the main climatic parameters (air temperature and precipitation) over a period of 120 years (1900-2020) attests to the changing trends for the North Baragan area, with profound implications in the behavior of cultivated plants and the requirements of technological retreats. By analyzing the multiannual dynamics of air temperatures, it attests in 2018 that, compared to the period 1945 - 2000, with thermal values mostly below 11°C (average over 118 years), from 2000 until now the thermal values have increased progressively, with a rate of 0, 05°C / year. Starting from this rate, there is a prospect of increasing the average temperature by 0.4°C by 2025 (respectively reaching values of 12.1°C), and by 1.6oC in 2050 (respectively reaching the value of 13.3°C) (Fig. 1).

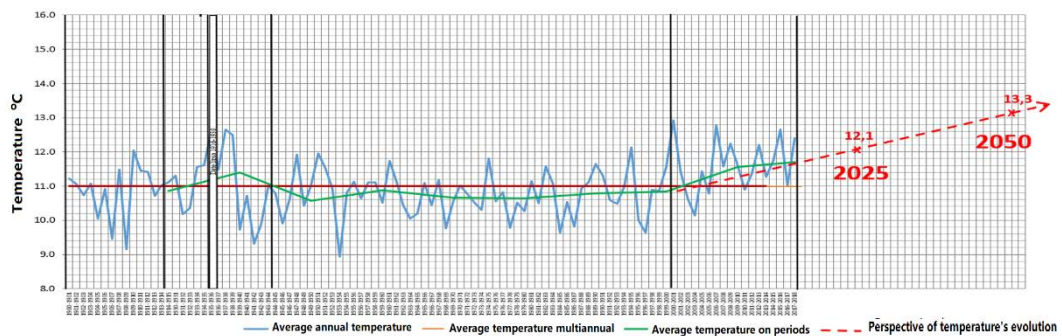


Figure 1. Graph of temperatures evolution in period 1900 – 2020 and perspective for the next 50 years

At SCDA Brăila, the experience from the project with successive crops was located in 2020 after the wheat crop, in the area represented in the map in figure 2, the center of the experimental plot having the GPS coordinates 45 ° 12'14.7 "N 27 ° 55'00.5" E.



Figure 2. Satellite map of the location of the experience with successive crops, within CE Chiscani - SCDA Brăila, 2020

As experimental factors, the proposed successive crop species were used (V1 - maize - hybrid P9241 FAO 330, V2 - sunflower - hybrid P64LE99, V3 - soybean - Triumph variety, V4 - hemp - Successive variety), different densities of sown to the first three different species and basic fertilization rules, as well as the introduction of a new drought - resistant species (sorghum - hybrid ES Alize - V5), according to the scheme in figure 3.

	V1			V2			V3			V4	V5
F2	V1D1	V1D2	V1D3	V2D1	V2D2	V2D3	V3D1	V3D2	V3D3	V4D1	V5D1
F1	V1D1	V1D2	V1D3	V2D1	V2D2	V2D3	V3D1	V3D2	V3D3	V4D1	V5D1
	V1			V2			V3			V4	V5

LEGEND

F1	Starter fertilization with NPK 18:46:0 - 200kg/ha	Different densities		
F2	Starter fertilization with NPK 18:46:0 - 400 kg/ha	D1	D2	D3
V1	Corn - Hybrid P9241	60000 bg/ha	70000 bg/ha	80000 bg/ha
V2	Sunflower Hybrid P64LE99	50000 bg/ha	60000 bg/ha	70000 bg/ha
V3	Soybean - Triumf variety	450000 bg/ha	550000 bg/ha	650000 bg/ha
V4	Hemp - Succesiv variety	350.000 bg/ha	-	-
V5	Sorghum - ES Elize variety	236.000 bg/ha	-	-
	Green culture for study about increasing soil fertility			
	Successive feed culture - Control for study about influence of green double crops on increasing soil fertility			

Figure 3. The scheme of experience about successive cultures, with different doses of fertilizer and different densities

The experience of successive crops was located after the wheat harvest, on 10.07.2020, using two norms of basic fertilizer, respectively the norm of 200 kg / ha NPK 18-46-0, commonly used, and the double norm, of

400 kg / ha NPK 18-46-0, corroborated with different sowing norms, in order to determine at harvest, which are the most efficient sowing and fertilizing norms, for the increase of the productions to the successive crops, in the conditions of the climatic changes felt in Bărăganul de Nord.

Immediately after harvesting the wheat crop, the sowing of successive experimental crops began, both for the study of fodder production, but also for use as green manure, to increase soil fertility. The disadvantage is the high costs of preparing the field (preparing the soil for sowing) and the risk of growing and developing plants in case of drought.

Therefore, soil preparation began immediately after harvest, and the depth of tillage was reduced to a minimum to keep moisture in the soil. Due to the insufficiency of water in the soil, it is risky to use successive crops before sowing autumn crops. On lands with a high level of weed infestation, especially perennials, such as: palamida, susaiul, volbura, etc. deep plowing and / or loosening or loosening with the arrow coulters is used to cut the entire surface to the depth established for the aburians difficult to remove. If there are no problems with perennial weeds, the costs of tillage and the risk of moisture loss can be reduced by surface tillage or by using direct sowing in the stubble (No-Till). For the successful cultivation of successive crops as green manures it is necessary that the period between harvesting the previous crop and sowing the next crop is at least 45–60 days, and soil moisture is sufficient for germination and plant growth. On dry lands and in dry years there is a danger of decreasing the production per hectare of subsequent crops due to the drying up of water reserves in the soil profile. This is especially true in dry areas, on easily dry soils and poorly fertile soils in dry localities.

Depending on the cultivation technologies and the estimation of the harvests for each experimental variant, the economic efficiency was calculated and recommendations were formulated regarding the practice of successive crops in the pedoclimatic conditions from the Brăila Plain.

### 3.RESULTS AND DISCUSSION

Taking into account that the location of the experiment with successive crops was in irrigated system, after harvesting the wheat, the weeding work was carried out at 20cm, followed by basic fertilization with two norms in the two blocks F1 and F2, then discussed, for incorporation in soil and preparation of the germination bed, after which the sowing was done with different norms.

The graduations of the experimental factors were established with the help of Solorrow application, which provides prescription maps of fertilization doses and sowing densities by satellite soil scanning and averaging over the last 5 years the distribution of biomass development, determined by the fertility of the surface. With the help of this application, the minimum application rate of the basic fertilizer was determined, respectively 200kg / ha, and for comparison, two experimental blocks were created, one with fertilization of 200kg / ha and one with double norm, of 400kg / ha (Fig. 4 a). For the treatment with foliar fertilizers, establishing a norm of 1l Gekka / 200 l water / ha (Fig. 4 b) and for the sowing densities 3 different densities were chosen for corn, sunflower and soybean, and only a sowing density for hemp and sorghum in the two differently fertilized blocks (Fig. 4 c).

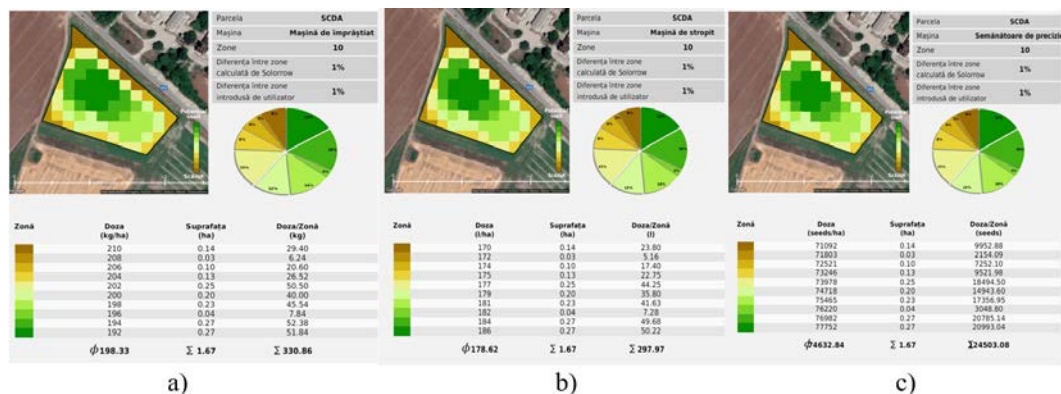


Figure 4. Determination of fertilization doses and sowing densities using the Solorrow application, within the experience with successive cultures at SCDA Brăila 2020

At SCDA Brăila, in the climatic conditions of extreme drought registered in 2020, after the application of 5 irrigation norms with 500mc / ha each, the productions of corn, sunflower, soybean, hemp and sorghum successively cultivated were differentiated only by technology applied.

Figure 5 shows images from the experience with successive crops at SCDA Brăila, in different phases of vegetation, respectively at sunrise, in the block fertilized with 200kg / ha NPK 18: 46: 0 (F1) and in the fertilized block with double dose (F2 - 400kg / ha 18: 46: 0).

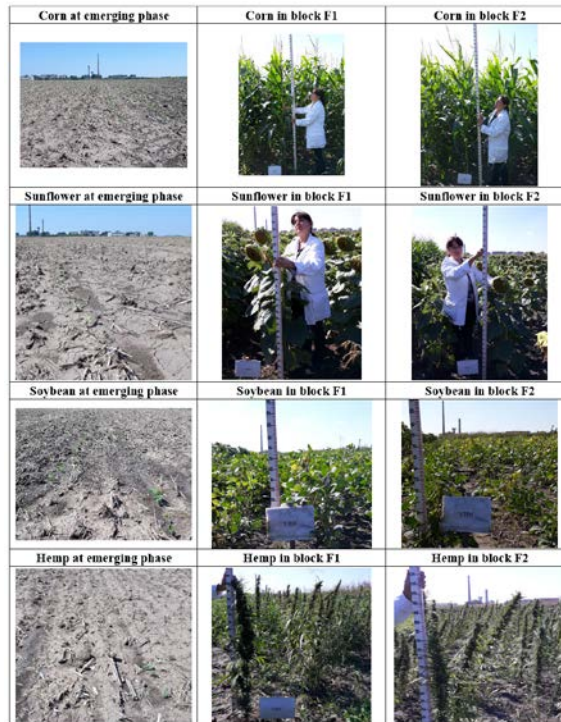
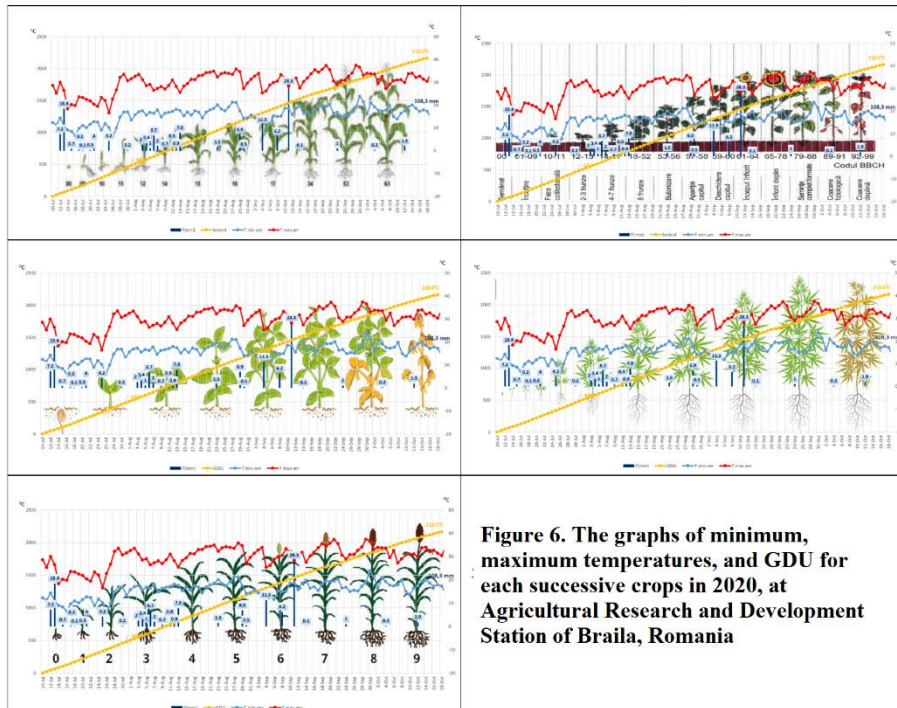


Figure 5. Images from different phases of successive crop in 2020 year

Based on the climatic data recorded daily at CE Chiscani, SCDA Brăila, it was possible to make a graph of minimum and maximum temperatures, the amount of useful degrees accumulated from sowing to harvesting, as well as the accumulated precipitation during this period (fig. 6).

It is observed that the need for useful degrees above 60C accumulated between July 10, 2020 - October 18, 2020 was sufficient for corn, sunflower, soybeans and hemp, but insufficient for sorghum cultivation, which is a thermophilic species, with a required GDU between 2500 - 3500, which was also observed in the lower productions obtained by sorghum in successive cultivation.





The maximum estimated maize production per hectare was obtained by the double fertilized variant (400kg NPK 18: 46: 0) and with the minimum sowing density of 70000 bg / ha, followed by the single fertilized variant (200kg NPK 18: 46: 0) with the sowing norm of 80,000 bg / ha (fig.7 a).

The sunflower production cultivated successively at SCDA Brăila, with different fertilization doses and sowing densities was higher at the dose of 400kg NPK 18: 46: 0 and the sowing density of 65000 bg / ha, followed in descending order by the variant fertilized with a dose of 400kg NPK 18: 46: 0 and the sowing density of 55000 bg / ha, and the variant fertilized with 200kg NPK 18: 46: 0 and the sowing density of 75000 bg / ha (fig. 7b). In soybean cultivation, the highest yields were obtained by the fertilized version with a dose of 400 kg / ha NPK 18: 46: 0 and the sowing density of 550000 bg / ha, followed by the variant fertilized with 200 kg / ha NPK 18: 46: 0 and the sowing density of 450000 bg / ha and the variant fertilized with 200kg / ha NPK 18: 46: 0 and the sowing density of 550000 bg / ha (fig. 7c). In the successive crops of hemp and sorghum, fertilized with different doses, the highest yields were obtained by the variants fertilized with 400kg / ha of N: P: K 18: 46: 0 (fig. 7d), with a production difference of 20kg / ha for hemp and 253 kg / ha for sorghum.

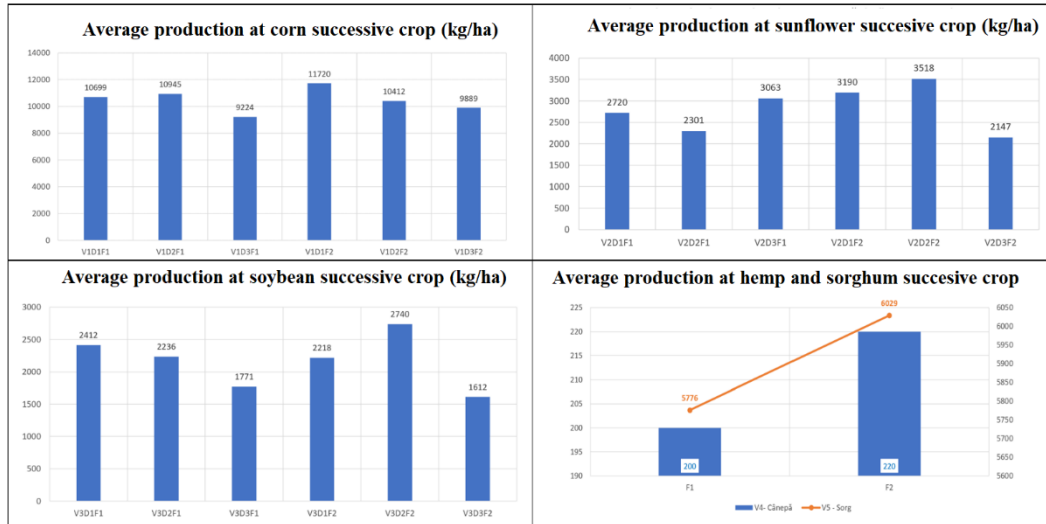


Figure 7. Average production at corn, sunflower, soybean, hemp and sorghum in successive crop, in 2020

The economic efficiency was estimated according to the technological links within each successive crop and experimental variant, initially calculating a cost price per kg, and according to the estimated productions per hectare and the selling price from 2020 (0.6 lei / kg corn, 1.3 lei / kg sunflower and soybeans, 30 lei / kg hemp C1, 0.5 lei / kg sorghum), the profit was calculated by difference for each experimental variant of species x fertilization dose x sowing density (fig. 8 ).

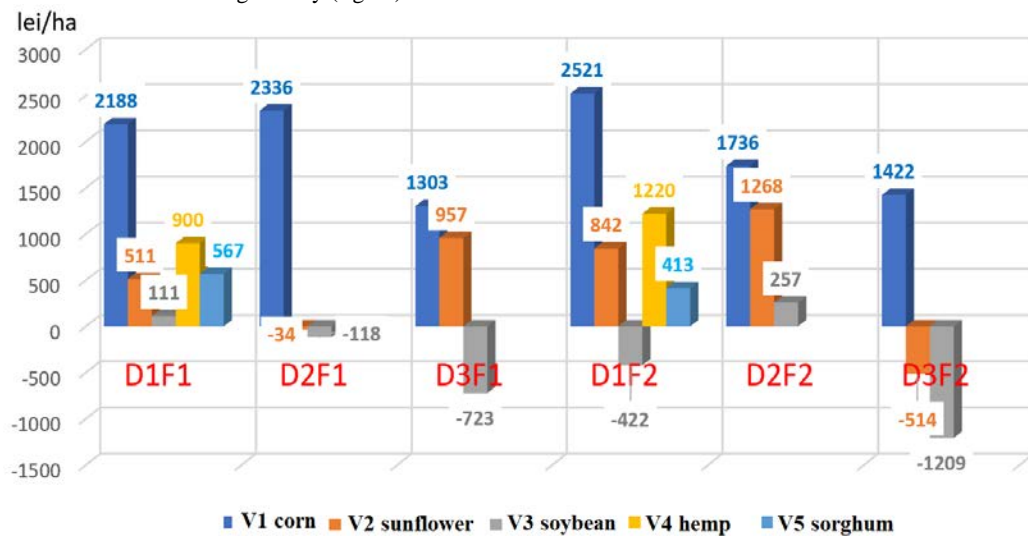


Figure 8. Efficiency of successive crops in climatic condition of year 2020, South Eastern of Romania

Calculating the average profit for each experimental variant, a comparative analysis of the profit obtained (in relative values -%) of each successive crop fertilized and sown with variable rates was prepared, in order to then formulate technology recommendations for successive crops in the Brăila Plain.

For maize in successive cultivation, the most significant results regarding the economic efficiency obtained within SCDA Brăila in 2020 compared to the average of 1917 lei / ha were achieved by the sown variant with a density of 60,000 bg / ha, double fertilized (400kg complex 18: 46: 0), followed by the variant sown with 70,000 bg / ha fertilized with a single dose of 200kg complex 18: 46: 0 and the variant sown with a density of 60,000 bg / ha simply fertilized, the percentage differences from the average profit being + 31% , respectively

22% and 14%. For sunflower, a very significant percentage difference was obtained compared to the average profit of 505 lei / ha for the D2F2 variant - with sowing density of 60,000 bg / ha fertilized with double dose (151%) and distinctly significant for the D3F1 variant - with density of 70,000 bg / ha simply fertilized (90%), followed by the D1F2 variant - sown with 50,000 bg / ha, fertilized with double dose (67%).

In soybeans in successive crops, all experimental variants obtained negative results on the profit per hectare, compared to the average profit per successive crop (-351 lei / ha), and in hemp and sorghum it was possible to highlight the increase of profit by doubling the fertilization norm only at hemp, while in sorghum the profit was higher for the fertilized version with normal dose, this result being explained by the different selling price of the two products (much lower in sorghum, compared to hemp).

For a more succinct highlighting of the suitability of successive crops in the Brăila Plain, based on the results obtained in the experience with successive crops in 2020 at SCDA Brăila, a comparative analysis of profit was made for each variant with the average experience (724.4 lei / ha) (Fig. 9).

It can be concluded that the best species for successive crops are corn, followed by sunflower and hemp. Sorghum and soybeans, although they can add value per unit area, the crops are far too small to cover the cost per hectare.

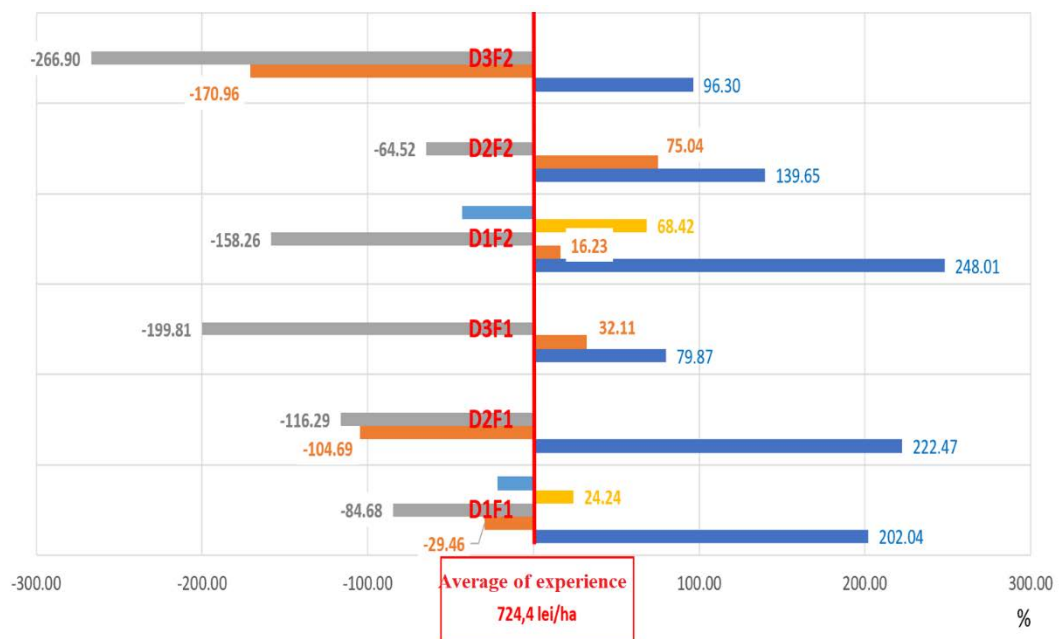


Figure 9. Graph of the percentage differences between the profit of each experimental variant with the average profit on each successive crop, obtained at SCDA Brăila, in 2020

## CONCLUSIONS

- The year 2020 was an extremely difficult year from the climatic point of view in the Brăila Plain area, due to the extreme pedological drought, lack of precipitation, atmospheric heat recorded during flowering and fruiting, which is why the experimental results cannot be generalized, it is necessary to continue the studies started.
- However, it can be noted that the profit per hectare can be significantly increased in areas with the possibility of irrigation, by corroborating technological links with climatic factors and cultivated species and by developing efficient technologies for successive crops.
- From the experience of the five successive crops practiced at SCDA Brăila in 2020, in irrigated system, we can conclude that the most efficient species for increasing economic efficiency per hectare could be corn, followed by sunflower and hemp, with technological requirements specific to each crop, respectively a low or medium sowing density and a double dose at basic fertilization.
- It should be specified that the experience was in the first year of study, and the year 2020 was extremely dry and atypical in terms of climate compared to previous years, which is why it will be

necessary to continue studies on the practice of successive crops in pedoclimatic conditions from the Brăila Plain.

#### ACKNOWLEDGMENT

We thank to the Ministry of Agriculture and Rural Development, ADER Sector Program, for financing the ADER project 3.3.2. - "Research on the improvement of sowing technologies for successive or double crops of corn, sunflower, soybeans and fiber hemp and seeds" - Contract no. 332 / 04.10.2019.

#### REFERENCES

- [1]. Claassen, R., F. Carriazo, J. Cooper, D. Hellerstein, and K. Ueda. 2011. Grassland to Cropland Conversion in the Northern Plains: The Role of Crop Insurance, Commodity, and Disaster Programs, ERR-120, U.S. Department of Agriculture, Economic Research Service. Available at: <http://www.ers.usda.gov/publications/err-economic-research-report/err120.aspx>, USA
- [2]. Forcos, G. (September 2020). Cel mai dificil an agricol. Cercetătorii de la SCDA Brăila: "Producțiile au fost afectate într-o măsură fără precedent de lipsa precipitațiilor și arșiței" <https://www.b1.ro/stiri/eveniment/exclusiv-cel-mai-dificil-an-agricol-cercetatorii-de-la-scdabraila-productiile-au-fost-afectate-intr-o-masura-fara-precedent-de-lipsa-precipitatiilor-siarsitei-344639.html>
- [3]. Horowitz, J., and J. Gottlieb. 2010. The Role of Agriculture in Reducing Greenhouse Gas Emissions, EB-15, U.S. Department of Agriculture, Economic Research Service, USA
- [4]. Katharina Waha, Jan Philipp Dietrich, Felix T. Portmann, Stefan Siebert, Philip K. Thornton, Alberte Bondeau, Mario Herrero, 2020. Multiple cropping systems of the world and the potential for increasing cropping intensity, Global Environmental Change 64 (2020) 102131, [www.elsevier.com/locate/gloenvcha](http://www.elsevier.com/locate/gloenvcha)
- [5]. Trifan Daniela, Alin Ionel Ghiorghe, Emanuela Lungu, Nicolae Popescu, 2020. Research about Adaptation of Agricultural Technologies for Successive Crops, in the Conditions of Current Climate Changes and Desertification Phenomena in South-Eastern Territory of Romania, <https://www.dpublication.com/wp-content/uploads/2020/11/1-3001.pdf>
- [6]. Wallander, S., R. Claassen, and C.J. Nickerson. 2011. The Ethanol Decade: An Expansion of U.S. Corn Production, 2000-2009. U.S. Department of Agriculture, Economic Research Service, Rep. EIB-79, USA

# Fever Detection from Human Thermal Images with Deep Learning Methods

Aysen Ozun Turkcetin<sup>1</sup>, Mustafa Onurcan Sahan<sup>2</sup>, Humbat Nasibov<sup>3</sup>

---

## Abstract

Fever is one of the most widely appeared symptom in influenza and similar diseases. Therefore the detection of the fever is important for revealing of these diseases. In this regard, remote and non-contact measurement of human body temperature has an importance role, and became a mandatory action during pandemic, especially in the Covid-19. During both epidemic, SARS and Covid-19, remote fever screening has importance in preventing the spread of the disease in public places, such as airports, shopping malls, schools, and hospitals, etc. Thermal cameras have become important tool in fever mass scans because of their remote and fast measurement capabilities. In the pandemic period, it has become mandatory to wear a face mask, which has deteriorated the ordinary use of thermal cameras for fever detection. Most traditional face detection algorithms used for fever detection with thermal cameras failed, since the mask affects head thermograms of a person. Last years, various artificial intelligence-based systems to process thermal camera thermograms have demonstrate tremendous results. In this study, we employed a deep learning method, particularly different variations of YOLO algorithms, to assess the human body temperature and detect the fever by real time processing of face mask wore human face thermograms. We compared the success rates of these algorithms in detecting the human face, mask, glasses, and temperature value from the thermograms.

**Keywords:** Artificial Intelligence, Deep Learning, Face Detection, Fever Detection, Mask Detection, Thermal Camera Images

---

## 1.INTRODUCTION

Pandemic diseases caused by similar to Covid-19 viruses have appeared many times in the human history and often altered ordinary lifestyle. One of example of such alteration is the wearing of the face mask during the last pandemic. Most diseases caused with influenza and Covid-19 viruses are resulted in the increase of human body temperature, i.e. a fever. While the normal human temperature is about 36.5-37 °C, the body temperature of patients carrying viruses reaches up to 37.5-39 °C [1]. The human body temperature (i.e. fever) is used to detect a person with the possible disease for the further prevention of other people to contact with him.

There are several types of thermometers to measure the human body temperature. Last years along with the classical thermometers (contact thermometers), infrared thermometers and thermal cameras have been used widely to measure human body temperature [2]. With the introducing the social distance during the last pandemic the significance of the remote and non-contact human temperature measurements became obvious[3]. Therefore, thermal cameras with a long-distance temperature measurement capability and fast detection ability are most demanded tools for human fever detection at places where a human flow rate is high. Briefly, thermal cameras converts the thermal radiation from the human body (i.e. from face) to an electrical signal, where the value of this signal is proportional to the temperature (and emissivity) of the corresponding point of the scene under the test. The thermography (temperature measurements with a thermal imager) method is passive and non-contact. The digitized out of thermal cameras is a thermal image, often named as a thermogram. The

---

<sup>1</sup> Suleyman Demirel University, Department of Mechanical Engineering, 100/2000 Scholarship Doctoral Student, BIDEB-TUBITAK-UME COVID-19 Star Scholarship 41400, Gebze/Kocaeli, Turkey. [aysenozun@gmail.com](mailto:aysenozun@gmail.com)

<sup>2</sup> BIDEB-TUBITAK-UME COVID-19 Star Scholarship 41400, Gebze/Kocaeli, Turkey. [sahanonurcan@gmail.com](mailto:sahanonurcan@gmail.com)

<sup>3\*</sup> Corresponding author: TUBITAK-UME-National Metrology Institute, Thermodynamic Metrology Laboratory, 41400, Gebze/Kocaeli, Turkey. [humbet.nasibli@tubitak.gov.tr](mailto:humbet.nasibli@tubitak.gov.tr)

thermogram bears the information about the temperature distribution of the scene within the field of view the cameras. An example of a human face thermogram is shown in Fig.1.



Figure 1. The area where the best temperature measurement will be made in the human body is the inner canthus in the eye.

The best position on the human face to measure a human body temperature is the dimples of both eyes away from the nose [4]. In Fig. 1, the eye inner canthus is shown as the region where body temperature is best measured for human beings. Therefore, a system for automatized detection of fever at public places should be able to acquire a human face thermogram, locate the eye inner canthus and asses the temperature. It becomes more difficult when people wears a face mask, eye glasses, etc. These artifacts significantly deteriorate the results of conventional object detection methods, especially in thermograms. Nowadays, artificial-intelligence-based models are most widely used approaches for object detection. Recently, in visible image processing domain deep learning methods are demonstrated significant results in detection of people with and without the face mask [5].

In this work we present the results of application of deep learning methods to the object detection in thermograms. Particularly, the work is focused on the detection of the human face, a face mask, eye glasses and region of the eye inner canthus in thermal images. For this purpose we created a new dataset with thermograms of people with and without the face mask, at different distances and with various spatial resolutions. Then we used this dataset to train two versions of YOLO, namely YOLO-Tiny and YOLO V4 to detect the human face, mask, eyeglasses and finally to locate the forehead area. As a result of the training of both algorithms and their comparison were made and for both approaches the success rates higher than 99% were obtained. The algorithms were implemented in a real time fever detection system comprising a FLIR T1020 model thermal camera conjugated with a computer system, which was established at the entrance of TUBITAK UME and employed during last year.

## 2.MATERIALS AND METHODS

### ○ *Thermal Dataset*

The thermograms for the dataset were collected from more than 35 volunteers during a month. The thermograms contain thermal images obtained ate different face poses from different angles of view (Fig.2.). Besides, images were recorded at different groups of people with and without eyeglasses and a face mask. The dataset contains 606 thermal images with various spatial resolutions and background. Another step is the labeling process of the collected data. We labeled images as the face, mask, glasses, and eye area.



Figure 2. Thermal data set containing the person poses used in the study.

o **YOLO based Deep Learning Models**

Briefly, in the YOLO approach the algorithm initially accepts the input image as an  $S \times S$  dimensional grid [6]. Then, the input image is processed for: i) the determination of the border boxes for prediction of objects, and ii) for producing predictive class maps. YOLO uses convolution layer architecture on its basis. There are convolution layers within the DarkNet framework. YOLO usually uses the ImageNet dataset and DarkNet framework for the training [7]. Fig. 3 shows a simplified model architecture of the YOLO.

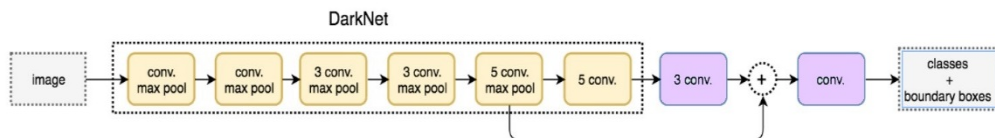


Figure 3. YOLO model architecture [8].

For each box, 5 prediction parameters have  $C$  conditional probability:

- Midpoint of  $x, y$  grid cells ( $x \in [0..1]$ )
- $w, h$  : width, height
- $obj_{conf}$  : Confidence Score (Objectness)
- $C_1, C_2, \dots, C_n$  : Conditional Class Probability

For each box the trust score calculation is given in Equation 1:

$$Obj_{conf} = Pr(Object) * IOU^{truth,prediction} \tag{1}$$

Conditional class probability is given by Equation 2:

$$C_i = Pr(Class_i | Object) \tag{2}$$

Equation 3 depicts the box confidence estimation and multiple conditional class probability for each class:

$$Pr(Class_i) = Pr(Object) * Pr(Class_i | Object) \tag{3}$$

Five parameters are assigned for each box. Two of them are assigned to the center of the box, and three as the score that includes length, width, and target.

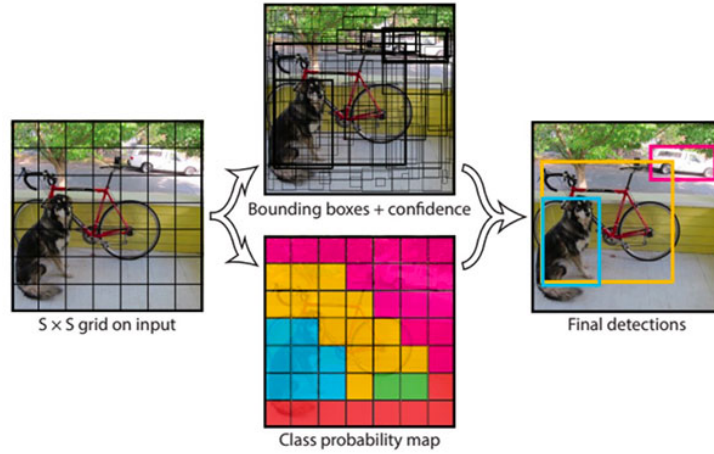


Figure 4. Used YOLO model for face, mask, glass, and temp area detection results [9].

○ **Performance Metric**

In the study, the confusion matrix was used as a performance metric for the transfer learning model. The reference table of the confusion matrix is given in Table 2.

Table 1. Confusion matrix references table [10]

		Actual Values	
		Positive (1)	Negative (0)
Predicted Values	Positive (1)	TP	FP
	Negative (0)	FN	TN

Precision is the positive of the measurements to each other. The precision calculation is given in Equation 4. Recall is to find all relevant instances in a data set. The recall calculation is given in Equation 5. F1 score is the harmonic mean of precision and recall. The f1 score calculation is given in Equation 6.

$$Precision = TP / (TP + FP) \tag{4}$$

$$Recall = TP / (TP + FN) \tag{5}$$

$$F1\ Score = 2 * Precision * Recall / (Precision + Recall) \tag{6}$$

This includes the correct classification of True-positive (TP) positive samples, correct classification of True-negative (TN) negative samples. False-positive (FP) and false-negative (FN) give the rate of incorrect classification [10].



### 3.RESULTS AND DISCUSSION

A special system comprising the thermal camera, thermogram recording and analysis systems was developed in this work.

The models were implemented in a real time fever detection system comprising a FLIR T1020 model thermal camera conjugated with a computer system, which was established at the entrance of the main building of TUBITAK UME and employed during the last year.

The camera was absolutely calibrated at Radiation Temperature Laboratory of UME. A flat surface radiating source with emissivity of about 0.98 was used as a reference source. The tractability of calibration to the International Temperature Scale was performed by means of transfer radiation thermometer.

According to the information in literature, the region the eye socket areas around the inner canthi is the best area for temperature determination.

In our study, fever detection from human body temperature is performed by detecting the highest temperature in the area between the eyes (Fig. 5).

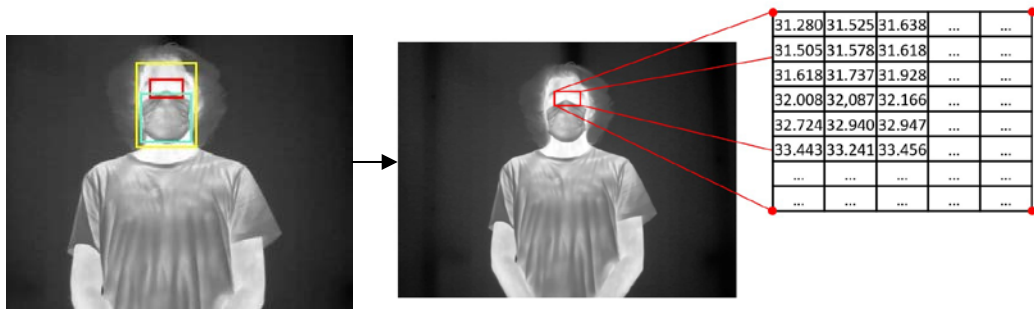


Figure 5. Detected existing labels and assessments the highest temperature matrix from eye sockets coordinates

We planned to identify a general area, as it is our area of highest interest when retrieving the two points in the orbit (Fig. 6.) By detecting the highest temperature in this area, we aimed to prevent an incorrect temperature value in another part of the body or in the camera frame for any reason.

$$\max \left( \begin{array}{|c|c|c|c|c|} \hline 31.280 & 31.525 & 31.638 & \dots & \dots \\ \hline 31.505 & 31.578 & 31.618 & \dots & \dots \\ \hline 31.618 & 31.737 & 31.928 & \dots & \dots \\ \hline 32.008 & 32.087 & 32.166 & \dots & \dots \\ \hline 32.724 & 32.940 & 32.947 & \dots & \dots \\ \hline 33.443 & 33.241 & 33.456 & \dots & \dots \\ \hline \dots & \dots & \dots & \dots & \dots \\ \hline \dots & \dots & \dots & \dots & \dots \\ \hline \end{array} \right) = 36,729^{\circ}\text{C}$$

Figure 6. Get maximum temperature value from matrix

It is the development phase of a real-time human fever detection system via interface over trained data. We have made the interface design over the visual studio for real-time fever detection. The visual studio interface is shown in figure 7.



Figure 7. Displayed temperature over system program

With a thermal camera placed at the entrance of the TUBITAK Metrology Institute building, it has been observed that the real-time fever detection system detects the face mask with an accuracy of 99% over a period of approximately 8-9 months, and when the data of the last 6 months are considered, it has been observed to perform at 100% in temperature measurement. The training data results of the YOLO-V4 and YOLO Tiny deep learning algorithms are given in Table 2 and Figure 8.

Table 2. YOLO and YOLO-Tiny deep learning algorithm training results for thermal dataset

	Precision	Recall	F1-Skor
YOLO -V4	0,94	0,99	0,97
YOLO Tiny	0,99	0,99	0,99

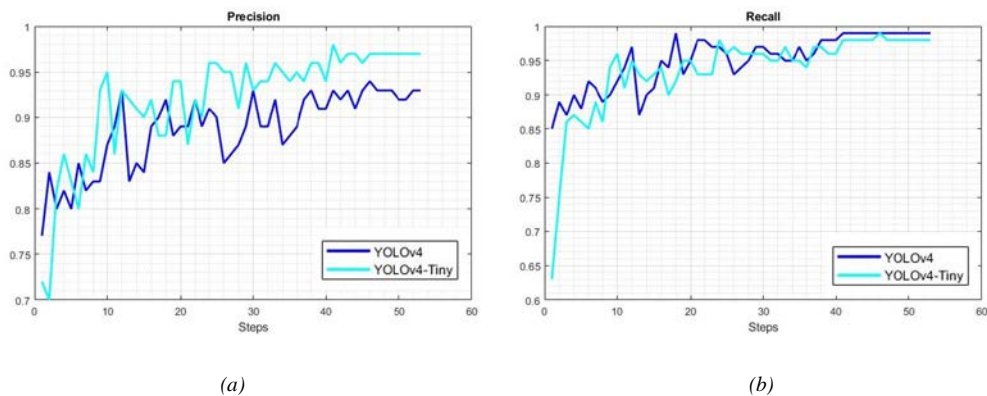


Figure 8. Chart of model precision and recall results for FLIR T1020 thermal imager data set

#### 4.CONCLUSIONS

As stated by the World Health Organization, social distance and face masks are of great importance in the COVID-19 process. On the other hand, the properly detection of the human fever in public places plays significant role in the preventing the spread of the disease. In this study, we developed a remote human temperature assessment system based on a thermal camera, computer system and YOLO based deep learning data processing method. The main aim of the system was to recognize visitors with and without a face mask, locate the area between the eyes and to assess the human body temperature. The system was used at the main entrance in our institute and was used for a more than one year period. The results of this work demonstrated that the YOLO Tiny based object detection method is powerful approach for object detection in human face thermograms. It was demonstrated that the method can be utilized in real time thermal image processing routines running in computers with moderate configuration.

#### ACKNOWLEDGMENT

We would like to express our sincere thanks to TUBITAK – BIDEB COVID-19 STAR researcher scholarship.

#### REFERENCES

- [1]. Ng, Eddie Y-K. "Is thermal scanner losing its bite in mass screening of fever due to SARS?." *Medical physics* 32.1 (2005): 93-97.
- [2]. Wu, Y. M. "Stop outbreak of SARS with infrared cameras." *Thermosense XXVI*. Vol. 5405. International Society for Optics and Photonics, 2004.
- [3]. Yurushkin, M., (2020), How Computer Vision Can Help Fight the Pandemic, Access site: <https://broutonlab.com/blog/computer-vision-to-fight-pandemic>
- [4]. R. Vardasca, et al. "Bilateral assessment of body core temperature through axillar, tympanic and inner canthi thermometers in a young population." *Physiological measurement* 40.9 (2019): 094001.
- [5]. S. Budzan, and R. Wyżgolik. "Face and eyes localization algorithm in thermal images for temperature measurement of the inner canthus of the eyes." *Infrared Physics & Technology* 60 (2013): 225-234.
- [6]. G. Silva, et al. "Face Detection in Thermal Images with YOLOv3." *International Symposium on Visual Computing*. Springer, Cham, 2019.
- [7]. P. Adarsh, R. Pratibha, and M. Kumar. "YOLO v3-Tiny: Object Detection and Recognition using one stage improved model." *2020 6th International Conference on Advanced Computing and Communication Systems (ICACCS)*. IEEE, 2020.
- [8]. Hui, J., 2018, What do we learn from single shot object detectors (SSD, YOLOv3), FPN & Focal loss (RetinaNet)? Access site: <https://jonathan-hui.medium.com/>
- [9]. J. Redmon, et al. "You only look once: Unified, real-time object detection." *Proceedings of the IEEE conference on computer vision and pattern recognition*. 2016.
- [10]. T. Fawcett, "An introduction to ROC analysis." *Pattern recognition letters* 27.8 (2006): 861-874.

# Prediction of long-term modulus, and correlation of local to global strain for polyester geogrids under services loading

Abdelwahab Tahsin<sup>1</sup>, Rami El-Sherbiny<sup>2</sup>

---

## Abstract

Geosynthetics have started to play a major role to effectively eradicate a numerous strew of geotechnical engineering problems, and are being widely used as a cost-effective sustainable soil- reinforcement solution. Consequently, a comprehensive look into the short and long-term properties of the geosynthetics will enable us to get a greater perception of its vital role. Comparable all polymeric products, geosynthetics are susceptible to creep. However, creep data is not published by manufactures for community to disclose stiffness modulus degradation with elapsed time, which is necessary for finite element numerical modelling. This paper assesses creep effect on long-term properties of polyester (PET) geogrid and derive calibration factor between global to local strains using in-isolation tensile response derived from the constant strain rate CSR loading tests. Hence, polyester (PET) geogrid specimens Fortrac 35T, 55T, 80T, 110T, and 150T were examined at the Machine Direction MD under CSR loading tests, ASTM D6637 using “multi-rib tensile” method. Series of CRS tests were conducted with strain rates of 20, 10, 6, 3, 1, and 0.05%/min. The long-term stiffness value decreases in non-linear manner with increasing logarithm of time but after 1000 hours, is considerably constant of 75% of the secant modulus at 2% strain (working loads). Outcome is in good agreement with consensus that, for polyester (PET) geogrid, time-dependent stiffness reductions will be minimal (25-15%). Calibration Factor CF between global to local strains ranged from 2.08 to 1.99 was introduced appropriately for the tested polyester geogrid specimens at stain domain of 2%. This derived CF is in worthy agreement with comparable PET geogrid CF of 2.2, which was introduced by Allen et al. (2002). Calibration Factor values slightly increased as strain rate decreased. Nevertheless, CF derived based on the slow rate of strain loading 0.05%/min. seems fitting to simulate the actual loading conditions at site.

**Keywords:** Secant modulus, creep effect, calibration factor, Constant Strain Rate test, geosynthetics, stiffness degradation, global/local strain.

---

## 1. INTRODUCTION

Geosynthetics have started to play a major role to effectively eradicate a numerous strew of geotechnical engineering problems, and are being widely used as a cost-effective sustainable soil- reinforcement solution. Consequently, a comprehensive look into the short and long-term properties of the geosynthetics will enable us to get a greater perception of its vital role. Comparable all polymeric products, geosynthetics are susceptible to creep. However, creep data is not published by manufactures for community to disclose stiffness modulus degradation with elapsed time, which is necessary for finite element numerical modelling. Advanced numerical analysis in conjunction with proper geosynthetics characterization through experimental tests are pragmatically deemed to perform accurate representative studies on associated response mechanisms of geosynthetics reinforced soil.

Creep phenomenon is a classically time-dependent elongation aspect for geosynthetics that affect the long-term performance and sustainable durability of the geosynthetic-reinforced structures. Creep impact is also function of the ambient temperature and service life after installation period. Globally, the creep behavior of geosynthetics is somewhat complicated phenomenon, index to the interaction and complexity of the subsequent

---

<sup>1</sup> Corresponding author: ACE Consulting Engineers, Cairo, Egypt, [abdelwahab.tahsin@gmail.com](mailto:abdelwahab.tahsin@gmail.com)

<sup>2</sup> Civil Engineering department, Cairo University, Egypt, [rsherbiny@gmail.com](mailto:rsherbiny@gmail.com)

components: (1) polymer nature and structure, (2) geosynthetics structure (nonwoven, woven, and integral structure), (3) rate of loading/ unloading, (4) temperature, and (5) soil environmental conditions at filed.

Filed monitoring strain readings of high-elongation strain gauges glued to geosynthetics materials must be calibrated against the “true” global strain as reported by Allen et al., (2002). Strain gauges bonded to woven geosynthetics typically generate a local “hard spot” causing under-registration of global actual tensile strains.

Based on series of Constant Strain Rate CSR tests, this manuscript aims to: (a) announce an overview about the geosynthetics behavior, non-linear tensile force– strain relationship (b) assess influence of creep on long-term performance and stiffness degradation, and (c) derive calibration factor between global to local strains, that can be used to predict geosynthetics behavior under service loadings rather than incipient collapse.

## 2. MATERIALS AND METHODS

### 2.1. OVERVIEW

The current research includes laboratory testing for 5 sets of designated specimens of geosynthetics geogrids Fortrac 35T, 55T, 80T, 110T, and 150T with varying strength and stiffness. Table 1 listed the disclosed physical properties as per the technical data sheet introduced by the manufacturer HUSKER. The standard raw material is the high-modulus polyester (PET), which of high stiffness, low creep, and uniform product strength.

*Table 1. Physical properties for the tested geogrid types as per HUSKER data sheets*

PROPERTY	TEST	35T	55T	80T	110T	150T
Ultimate wide width (MD) Tensile Strength (kN/m)	ASTM D-6637	35	55	80	110	150
Elongation at ultimate tensile strength –MD	ASTM D-6637	≤10%	≤10%	≤10%	≤10%	≤10%
Long term design strength- MD (kN/m)	GRI GG4	18.8	29.5	42.9	59	81

### 2.2. TEST APPARATUS AND SPECIMEN PREPARATION

TESTOMETRIC M500- 50CT Universal Testing machine was used to perform the geogrid load-extension under Constant Strain Rate CSR. The apparatus comprises main tensile machine, pressure jack and computer control unit. The tensile machine consists mainly of clamps, sensors for recording the tensile force, and other sensors to monitor the extent of grips separation. The clamps must be attached with suitable pressure to avoid slippage. Clamping pressure must be equal for all specimens under the same test to manage consistent judgment between the anticipated results. According to the Multi-Rib tensile method of ASTM D6637 “Standard Test Method for Determining Tensile Properties of Geogrids by the Single or Multi-Rib Tensile Method”; the specimen is schematically illustrated at Figure 1 to be a minimum of 200 mm wide and contains five ribs in the cross-test direction by at least three junctions or 300 mm long in the direction of the testing. The outermost ribs are cut prior to testing to prevent slippage from occurring within the clamps as instructed by ASTM D6637, clause 8.2.4. Thus, the width of intact ribs is 120 mm. The room ambient temperature was 20°C during test procedures to avoid adverse impact of the temperature in the test results. Figure 2 shows the particular test setup adopted for derivation of Calibration Factor CF between global to local strains. During the in-isolation tensile testing, strain gauge was mounted on one side of the geosynthetic specimen using soft glue adhesive. A KYOWA gauge type is used with model name KFG-5-120-C1-11L1M2R. Quarter bridge connection was used for 1-gauge 120Ω.

Five single tests were performed on the Machine Direction (MD) for each specimen of Fortrac 35T, 55T, 80T, 110T, and 150T, in accordance with ASTM D6637 using the multi- rib tensile method. Constant Strain Rate CSR of 20%, 10%, 6%, 3%, 1% to slow rate loading 0.05% strain/min. were performed. The sample total width is 200 mm, while the intact width is limited to 120 mm. According to ASTM D6637, clause 8.2.4 “within test methods A, B, and C the outermost ribs are cut prior to testing to prevent slippage from occurring within the clamps. For those cases where the outermost ribs are severed, the test results shall be based on the unit of width associated with the number of intact ribs”. Hence, calculation of the secant modulus ( $J = EA_1$ ) at certain strain domain shall be the maximum tensile force divided by the total intact width per meter.

For CSR of 0.05%/min, an interval of local strain readings (by automotive data logger) equals to 2 min is utilized to reveal 30 readings through strain domain of 3%. While, for CSR 10%/min, and due to the sensitivity of relatively rapid test loading; two sets were examined for local strain readings of intervals 2 sec and 1 sec, to result in approximately 30 and 60 readings, respectively to reach the failure.

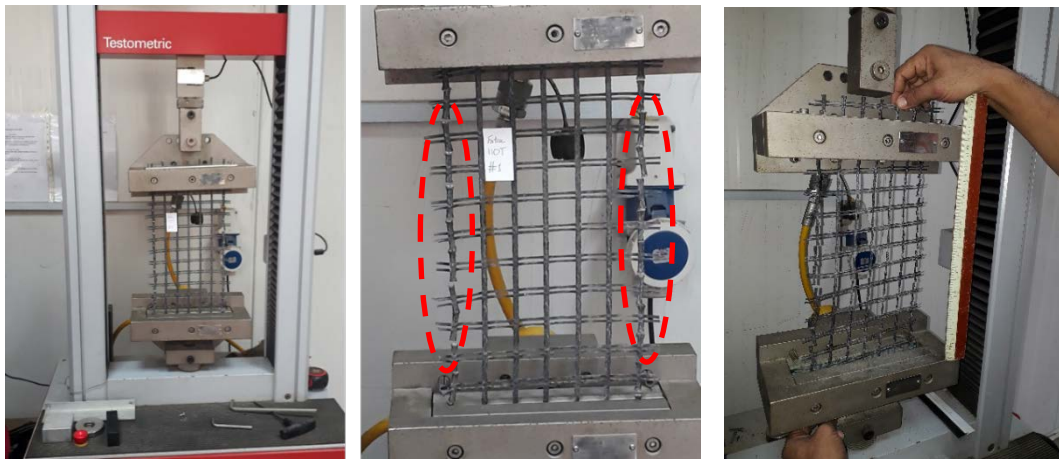


Figure 1. Specimen configuration; Multi-Rib tensile method -ASTM D6637



Figure 2. Test setup for Calibration Factor between local to global strain using CSR tensile test

### 3. RESULTS AND DISCUSSION

#### 3.1. ASSESSMENT FOR VARIATION OF STIFFNESS WITH TIME (CREEP)

Creep phenomenon is a classically time-dependent elongation aspect for geosynthetics that affect the long-term performance and sustainable durability of the geosynthetic-reinforced structures. Creep impact is also function of the ambient temperature and service life after installation period. In general, creep phenomena can be divided into three main phases: (1) Primary creep phase, starts at a rapid rate and reduces with time, (2) Secondary creep phase, has a relatively uniform rate, and (3) Tertiary creep phase, has an accelerating sudden creep rate and ends up by failure of material at rupture time as reported by Han-Yong Jeon (2017).

As geosynthetics are generally manufactured from polymer materials, they exhibit a viscoelastic behavior, time, load, and temperature-dependent, under a sustained constant load. At time  $t$ , the total strain  $\varepsilon(t)$  can be expressed from the following equation:  $\varepsilon(t) = \varepsilon_0 + \varepsilon_I + \varepsilon_{II} + \varepsilon_{III}$ . Where:  $\varepsilon_0$  is the instantaneous strain and  $\varepsilon_I$ ,  $\varepsilon_{II}$ , and  $\varepsilon_{III}$  are the primary, secondary, and tertiary creep strains, respectively. Nevertheless, the final sudden progressive creep strain increase before rupture does not necessarily occur; it is normally revealed for Polyethylene (PE) and polypropylene (PP) not for Polyester (PET) at standard load levels and temperature. Since the material is a polyester (PET) geogrid, time-dependent stiffness reductions are minimal (approximately 25-15% or less) as concluded by (Allen and Bathurst 2001). Also, temperature sensitivity of PET is not as great as that for HDPE or PP geosynthetics. For typical geosynthetics applications, the ratio of the modulus value at typical working conditions (i.e., strains on the order of 2% and loading times of approximately 1,000 hours) relative to the modulus obtained from typical CRS wide-width test (at strain 10%/min. ASTM D 4595) can be estimated for various Geosynthetics polymer types. Allen and Bathurst (2001) introduced a ratio stiffness modulus at 1000 hours  $J_{1000hrs}/J_{D4549}$  for polyester (PET) = 0.75 to 0.85. To convert the measured reinforcement strain to the most accurate estimate of the actual reinforcement load, each measured strain to be multiplied by the secant stiffness value that corresponds to the elapsed time. The stiffness value used was taken at a strain equal to the measured strain, but not more than the stiffness value at 1% strain. The time used to calculate the stiffness values was taken with respect to when the layer was installed in the field (Allen and Bathurst, 2014). Consequently, series of CRS tests were conducted and stress strain curves were obtained for different strain rates of 20%/min, 10%/min, 6%/min, 3%/min, 1%/min, and 0.05%/min. From the test results and measurement, the loads and time to reach 1% and 2% strains are calculated, and then secant stiffness as well. Long-term stiffness for strain equaled 2% at 1000 hour (creep data from Walters et al.,(2002)) was estimated as 0.75 multiplied by secant modulus at strain 2% measured from CSR of 10%/min (ASTM D 4595). Ratios between stiffness ( $J_{2\%}$ ) to stiffness ( $J_{1\%}$ ) at the same time are evaluated as presented in Table 2. Using average of these ratio, stiffness at strain 1% after 1000 hour can be estimated. Stiffness value decreases with increasing logarithm of time but is reasonably constant after 1000 hours, as reported by (Miyata and Bathurst, 2007).

For practical use, Figure 3 presents correlation design charts for the assessment of stiffness variation at J1% and J2% strains for the examined specimens versus logarithm of the elapsed time. These charts can be simply used to predict the secant modulus (after creep effect) corresponds to the elapsed time of each geosynthetics geogrid layer during staged construction at filed. Figure 4 proves comparative trend for variation of stiffness with time between 1% and 2% strain. The vertical dashed line was plotted for reference to identify modulus JD4549 estimated at CSR 10%/min. Figure notifies behavioral features: (a) non-linear degradation of secant modulus with elapsed time, (b) the derived modulus at strain1% is larger than corresponding at 2% regardless strain rate of loading, and (c) the higher the strength, the higher the stiffness irrespective to strain rate of loadings.

	CSR %/min.	time to 1% strain (hr)	time to 2% strain (hr)	Force at 1% strain (kN)	Secant modulus $J_{1\%}$ (kN)	Force at 2% strain (kN)	Secant modulus $J_{2\%}$ (kN)	Ratio $J_{2\%}/J_{1\%}$
<b>110T</b>	20	0.0008	0.00167	17.92	1792	25.34	1267	1.41
	10	0.0017	0.00333	15.83	1583	22.55	1128	1.40
	6	0.0028	0.00556	15.00	1500	21.84	1092	1.37
	3	0.0056	0.01111	13.96	1396	20.86	1043	1.34
	1	0.0167	0.03333	13.54	1354	20.66	1033	1.31
	0.05	0.3333	0.66667	12.08	1208	19.51	976	1.24
	Creep 0.75	1000	1000		1127		846	1.33
<b>80T</b>	21	0.0008	0.0016	11.87	1187	17.97	899	1.32
	10	0.0017	0.0033	11.04	1104	17.37	868	1.27
	6	0.0028	0.0056	10.63	1063	16.11	806	1.32
	3	0.0056	0.0111	10.13	1013	15.48	774	1.31
	1	0.0167	0.0333	9.88	988	15.10	755	1.31
	0.05	0.3333	0.6667	9.17	917	14.97	749	1.22
	Creep 0.75	1000	1000		838		651	1.29
<b>55T</b>	25	0.0007	0.0013	9.24	924	13.47	674	1.37
	10	0.0017	0.0033	7.29	729	10.72	536	1.36
	6	0.0028	0.0056	6.56	656	10.26	513	1.28
	3	0.0056	0.0111	6.25	625	9.90	495	1.26
	1	0.0167	0.0333	5.83	583	9.42	471	1.24
	0.05	0.3333	0.6667	5.21	521	9.12	456	1.14

	Creep 0.75	1000	1000		505		402	1.26
<b>35T</b>	20	0.0008	0.0017	5.80	580	8.84	442	1.31
	10	0.0017	0.0033	5.21	521	7.80	390	1.34
	6	0.0028	0.0056	4.79	479	7.18	359	1.33
	3	0.0056	0.0111	4.58	458	6.96	348	1.32
	1	0.0167	0.0333	3.96	396	6.30	315	1.26
	0.05	0.3333	0.6667	3.96	396	6.20	310	1.28
	Creep 0.75	1000	1000		381		292	1.30
<b>150T</b>	20	0.0008	0.0017	23.75	2375	32.56	1628	1.46
	10	0.0017	0.0033	19.58	1958	27.92	1396	1.40
	6	0.0028	0.0056	18.75	1875	27.56	1378	1.36
	3	0.0056	0.0111	16.67	1667	27.24	1362	1.22
	1	0.0167	0.0333	15.21	1521	25.02	1251	1.22
	Creep 0.75	1000	1000		1362		1047	1.30

Table 2. Summary of the derived Secant modulus at 1% & 2% strain for Fortrac 110T, 80T, 55T, 35T, and 150T.



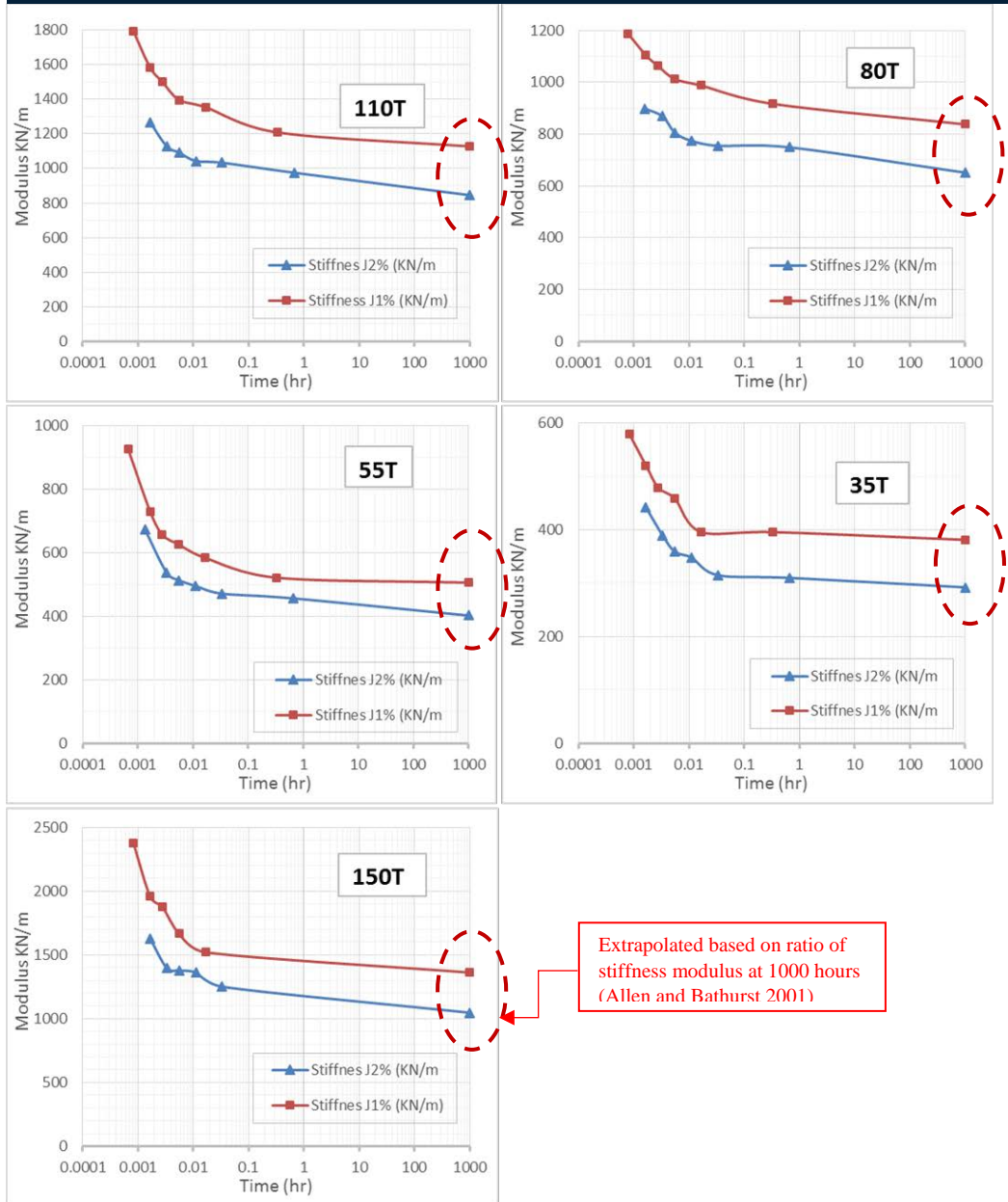


Figure 3. Correlation design charts for variation of secant modulus at 1% and 2% strain with elapsed time

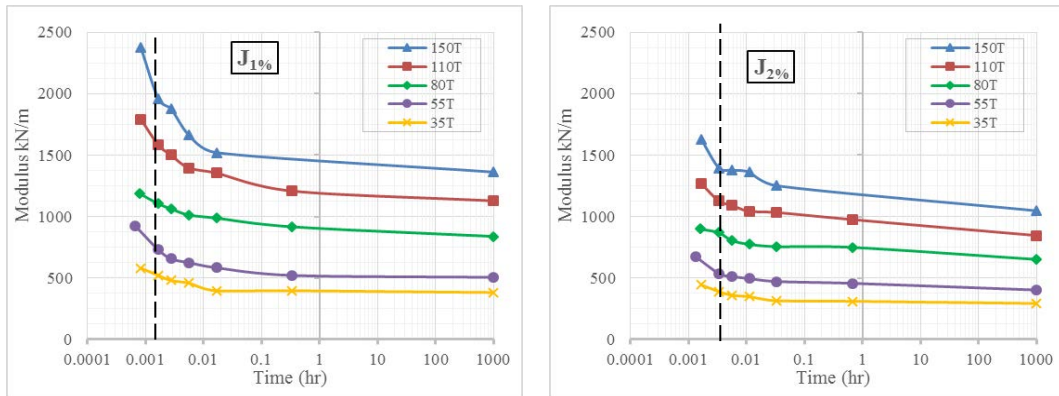
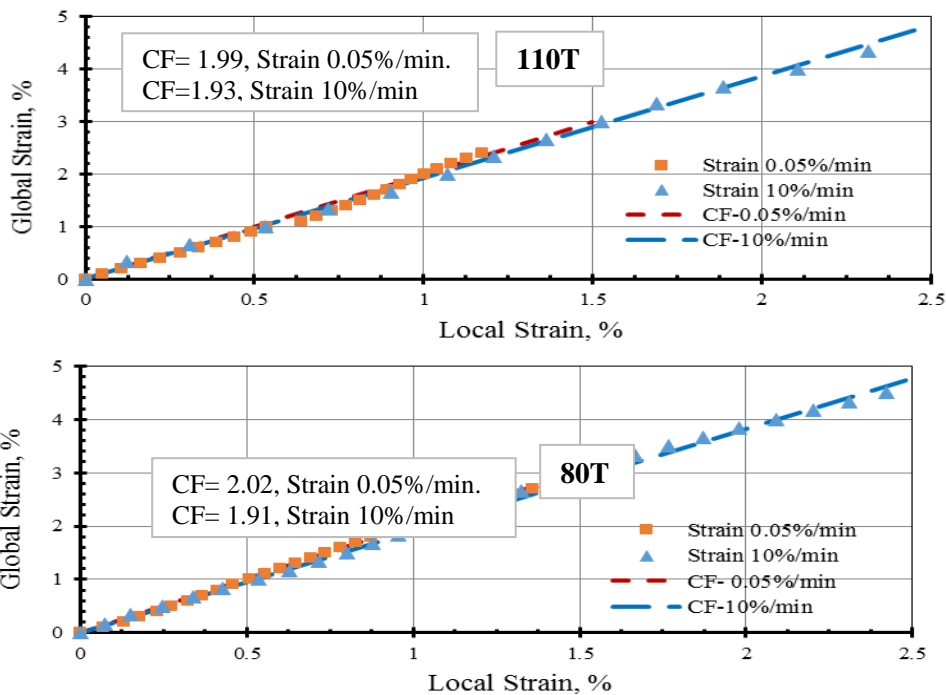


Figure 4. Comparative trend for variation of secant modulus with elapsed time between 1% and 2% strain

### 3.2. CALIBRATION FACTOR BETWEEN LOCAL TO GLOBAL STRAIN

Strain readings from high-elongation strain gauges glued to geosynthetics reinforced materials must be calibrated against the “true” global strain in the reinforcement as reported by Allen et al., (2002). In the current research, “local strain” or “gauge strain” values denotes strains recorded by a strain gauge at the point of attachment. “Global strain” refers to strain averaged over a length that is much larger than the strain gauge. Strain gauges bonded to woven geosynthetics typically generate a local “hard spot” causing under-registration of global actual tensile strains.

The Calibration Factor CF for a particular combination of gauge, bonding technique, geosynthetics polymer type, and location of gauge is typically established from constant strain rate in-isolation wide-width strip tensile testing in accordance with ASTM D4595 as reported by Allen et al., (2002). Hence, strain gauge readings in the field must be corrected to true global strains by factor derived from in- isolation tensile tests.



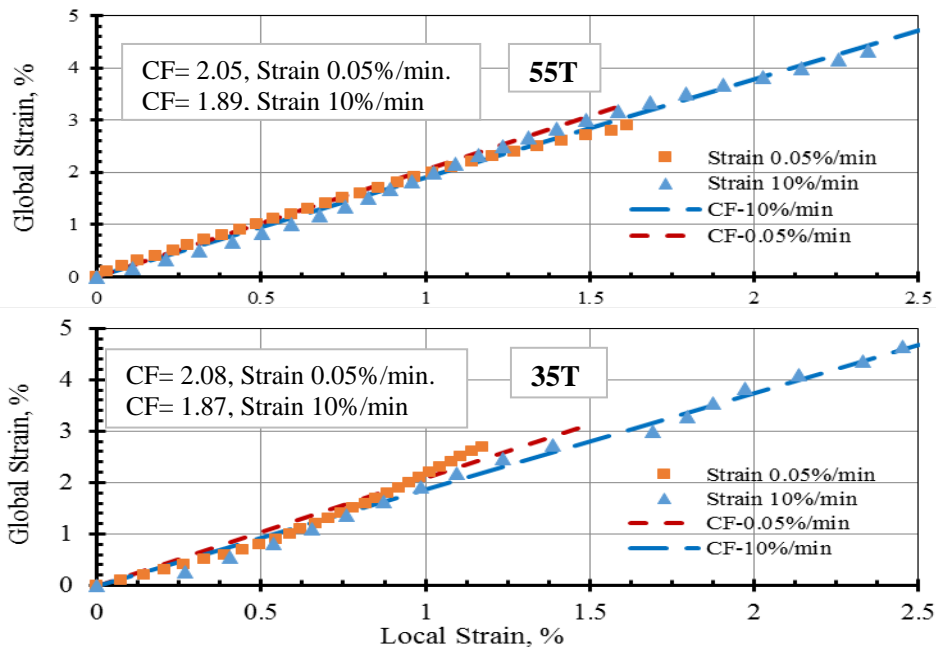


Figure 5. In-isolation local strain gauge response versus global strain for Fortrac 110T, 80T, 55T, and 35T

In order to better match the realistic (slower) loading conditions of a geosynthetic geogrid layer placed during staged construction, the data from the 0.05 %/min CRS test was used for consistent calibration. The geosynthetic PET geogrid types Fortrac 110T, 80T, 55T, and 35T were tested under CSR of 10%/min as nominal value introduced by ASTM 4595 and at a relatively low strain range of loading 0.05%/min in the domain of 0 to 3% strain, to match the maximum anticipated working conditions under service loadings (no need to reach the strain at break). Strain gauges were mounted on one side of the geosynthetic specimen during the in-isolation tensile testing using quarter-bridge. For CSR testing of 0.05%/min, an interval of local strain readings equals to 2.0 min is utilized to reveal approximately 30 readings (by automotive data logger) through the strain domain of 3%. While, for CSR 10%/min, and due to the sensitivity of relatively rapid test loading and possible associated missing/ errors for recording the initial significant readings of local strain by data logger; two sets were examined for local strain readings of intervals 2 sec and 1sec, to result in approximately 30 and 60 readings, respectively to reach the failure. However, only limited number of readings (approximate to 10 or 20) at domain of strain 3% is not liable relative to CSR of 0.05%/min.

Figure 5 plots response curves of the in-isolation local strain versus global strain for various tested specimens 35T, 55T, 80T, and 110T that used to derive the calibration factor. The response curves for constant-rate-of-strain tensile loading fall within a relatively narrow band. The significant under-registration of global strains is considered to be the result of the impregnation of the longitudinal polyester fiber bundles by the gauge epoxy glue, which creates a locally stiff region (hard spot). It should be pointed out that, bonded strain gauges during testing often gave a nonlinear response (or failed in the field) at strains  $\geq 3\%$ , hence, extensometers acknowledged the sole practical guaranteed devices of measuring geosynthetic strains at large strain domains.

Calibration Factor (CF) values slightly increased as strain rate decreased. A nominal average best fit values for CF of 2.08, 2.05, 2.02 and 1.99 were derived appropriate for such foil strain gauges glued to Husker PET geogrid type 35T, 55T, 80T, and 110T, respectively. A single-value calibration factor from this data over a range of 0 to 2% strain is approximately 2. In other words, the strain gauge values must be doubled to represent “true” global strains. This CF estimation for strain levels  $\leq 2\%$  is in worthy agreement with comparable PET geogrid CF of 2.2, which was introduced by Allen et al., (2002). It can be argued that the actual loading history of a geosynthetic reinforcement layer during construction falls between the two idealized loading conditions performed in the laboratory. It was identified that, to adapt the measured reinforcement strain to the most accurate estimate of the actual reinforcement load, each calibrated measured (global) strain to be multiplied by

the secant stiffness value that corresponds to the elapsed time (after considering creep effect). The time used to calculate the stiffness values to be taken with respect to when the layer was installed in the field (Allen and Bathurst 2014).

#### 4. CONCLUSIONS AND RECOMMENDATIONS

The current paper focuses largely on, how to better identify the short and long-term response and material characterization of geosynthetics polyester (PET) geogrid under service loadings rather than incipient collapse. Like all polymeric products, geosynthetics are susceptible to creep. However, creep data is not published by manufacturers for community to disclose stiffness modulus degradation with elapsed time, which is necessary for finite element numerical modelling. This manuscript aims to assess creep effect and derive calibration factor between global to local strains. Field monitoring strain “local” readings of high-elongation gauges glued to geosynthetics must be calibrated against “true” global strain. Hence, sets of geosynthetics polyester (PET) geogrid specimens Fortrac 35T, 55T, 80T, 110T, and 150T were examined at the Machine Direction MD under Constant Strain Rate CSR loading tests, in accordance with ASTM D6637 using the “multi-rib tensile” method. A series of CRS tests were conducted wide strain rates of 20%/min. (relatively high rate), 10%/min, 6%/min, 3%/min, 1%/min, and 0.05%/min (relatively slow rate). Correlation design charts were plotted to predict stiffness modulus reduction versus logarithm of elapsed time. The main outcomes are as follows:

- The measured tensile force –strain relationship exposed a non-linear response of the examined geosynthetics PET geogrid specimens.
- The long-term stiffness value decreases in non-linear manner with increasing logarithm of time but after 1000 hours, is considerably constant of 75% of the secant modulus at 2% strain (working loads). Outcome is in good agreement with consensus that, for polyester (PET) geogrid, time-dependent stiffness reductions will be minimal (approximately 25-15% or less).
- The linear approximation of secant modulus after creep consideration is considerable accepted in the strain domain up to 2% which covers a wide scatter of geosynthetics reinforced structures conditions under service loadings.
- The derived stiffness at 1% is larger than corresponding for 2% strain, which reflects phenomenon of non-linearity and stiffness relaxation with progressive elongation.
- Strain gauge readings of geosynthetics measured in the field must be corrected to true global strains using in-isolation tensile response derived from the constant strain rate CSR loading tests of the instrumented specimens. Strain gauges bonded to woven geosynthetics typically generate a local “hard spot” causing under-registration of global actual tensile strains.
- Calibration Factor CF between global to local strains ranged from 2.08 to 1.99 was introduced appropriately for the tested polyester geogrid specimens at strain domain of 2%. In other words, the strain gauge measured values must be doubled to represent “true” global strains. This derived CF estimation for strain levels of 2% or less is in worthy agreement with comparable PET geogrid CF of 2.2, which was introduced by Allen et al. (2002).
- Calibration Factor values slightly increased as strain rate decreased. For example; specimen 35T; derived CFs are 2.08 and 1.87 for strain 0.05%/min. and strain 10%/min, respectively. Nevertheless, the CF derived based on the slow rate of strain loading 0.05%/min. seems appreciate to simulate the actual loading conditions and staged construction at site.

#### ACKNOWLEDGMENT

The authors would like to express their gratitude to the technical support of Dr. Mohy El-Mashad, and members of Geotechnical Institute Laboratory, National Irrigation Research Center in Qanater, Egypt

#### REFERENCES

- [1]. AASHTO (2002). Standard Specifications for Highway Bridges. American Association of State Highway and Transportation Officials, 17th Ed., Washington, DC, USA.
- [2]. Allen, T. M., and Bathurst, R. J. (2002a). “Observed long-term performance of geosynthetic walls, and implications for design.” *Geosynthetic Int.*, 9(5–6), 567–606.
- [3]. ASTM D 6637. "Standard test method for determining tensile properties of geogrids by the single or multi-rib tensile method." American Society for Testing and Materials, Pennsylvania, USA.
- [4]. ASTM D4595 "Standard test method for tensile properties of geotextiles by the wide-width strip method." American Society for Testing and Materials, West Conshohocken, Pennsylvania, USA

- [5]. Bathurst, R.J., Allen, T.M., and Walters, D.L., (2002), "Short-term strain and deformation behavior of geosynthetic walls at working stress conditions", *geosynthetics international*, vol. 9, nos. 5-6, pp. 451-482.
- [6]. Boyle, S.R, Gallagherand, M. Holtz, R.D. (1996). "Influence of strain rate, specimen length and confinement on measured geotextile properties." *Geosynthetics International Journal*, 3 (2), pp. 205-225.
- [7]. Hatami, K. and Bathurst, R. J. (2005). "Development and verification of a numerical model for the analysis of geosynthetic-reinforced soil segmental walls under working stress conditions." *Journal of Geotechnical and Geoenvironmental Engineering*, ASCE, 132(6), 673-684.
- [8]. Han-Yong Jeon (2017). "Review of Long-Term Durable Creep Performance of Geosynthetics by Constitutive Equations of Reduction Factors". DOI: 10.5772/intechopen.72330.
- [9]. Miyata, Y. and Bathurst, R. J. (2007a). "Evaluation of K-Stiffness method for vertical geosynthetic reinforced granular soil walls in Japan." *Soils and Foundations*, 47 (2), pp. 319-335.
- [10]. Richard J. Bathurst (2019). "Developments in MSE Wall Research and Design". *Proceedings of the 3rd GeoMEast International Congress and Exhibition, Egypt 2019 on Sustainable Civil Infrastructures*. Pages 22-50
- [11]. Sawicki, A., and Kazimierowicz-Frankowska, K. (2002). "Influence of strain rate on the load-strain characteristics of geosynthetics." *Journal of Geosynthetics International*, 9 (1), pp. 1-19.
- [12]. Saunders, D., 2001, "The Performance of Two Full-Scale Reinforced Segmental Soil Retaining Walls", M.Sc. Thesis, Civil Engineering Department, Royal Military College of Canada, Kingston, Ontario, Canada, 304 p.
- [13]. Walters, D. L., Allen, T. M., & Bathurst, R. J. (2002). "Conversion of geosynthetic strain to load using reinforcement stiffness." *Geosynthetics International*, 9 (5-6), pp. 483-523.
- [14]. Yan Yu, Bathurst, R. J., and Allen, T. M. (2016). "Numerical modelling of the SR-18 geogrid reinforced modular block retaining walls." *Journal of Geotechnical and Geoenvironmental Engineering*, ASCE, 142 (5): 04016003.

## BIOGRAPHY

*Abdelwahab Tahsin* has completed his MSc. and PhD in Civil engineering from Faculty of Engineering, Cairo University, Egypt. Research work is focused on civil, geotechnical, and foundation engineering. Special care was considered in the topics of soil-structure interaction, deep excavation supporting system, slope stability, mechanically stabilized earth walls, Geosynthetics, field monitoring, and numerical modeling (3D finite element). He is a professional Consultant engineer, certified PMP and design director at ACE consulting office, Cairo, Egypt. Participating and managing large complicated civil engineering projects across multiple asset classes in Egypt, Gulf, Middle East, and Africa. Strong experience of international standards through interactive collaboration with International Managed Joint Ventures. He is an Assistant professor (Instructor part-time basis) supervising graduation projects at the Egyptian Russian and 6<sup>th</sup> of October Universities, Egypt. He has been serving as a reviewer of research journal "Innovative Infrastructure Solutions" (IISS). He is sharing at numerous conferences, workshops, and invited talks. He is an associate organizing member of GEOAFRICA 2023 international conference, hosted by the International Geosynthetics Society IGS, Egypt chapter.

# Performance Analysis of Long Baseline GPS RTK

Omer Faruk Atiz<sup>1</sup>, Sermet Ogutcu<sup>2</sup>, Salih Alcay<sup>3</sup>

---

## Abstract

The Global Positioning System (GPS) has been used for many years to determine the precise position of a receiver in real-time. In the classical real-time kinematic (RTK) positioning method the distance between reference and rover is limited (<25 km) due to the radio communication, atmospheric conditions, and orbital errors. If the communication between the rover and the base station is supplied over the Internet, the limitations of radio modems are removed. However, the ionospheric-tropospheric errors are still a problem that cannot be easily eliminated by double-difference in long baseline RTK. This study examines the latest GPS RTK performance on four different lengths of baselines (200-, 300-, 400-, 500-km) by estimating slant total electron content (STEC) of the ionosphere and zenith total delay (ZTD) of the troposphere. RTKLIB (RTK Library) software package is used to process GPS data. 24-hour data of four baselines at 1-sec epoch interval is used to get long baseline RTK solutions. The results show that as the baseline length increases, the ambiguity fixing rate decreases. The root mean square (RMS) error of 500-km baseline is 1.9, 2.9, and 5.4 cm for the north, east, and up components, respectively, considering only ambiguity fixed coordinates. In addition, the error of broadcast ephemeris should be taken into consideration when the baseline distance over 200 km.

**Keywords:** GPS, RTK, STEC, ZTD

---

## 1. INTRODUCTION

The Real Time Kinematic (RTK) method is one of relative positioning methods has been widely used in surveying that it eliminates many errors such as receiver-satellite clock offsets, and troposphere-ionosphere delays with double differencing (DD) technique [1]. The RTK method provides centimeter level accuracy in real time when the baseline distance between rover and base is less than 25 km. In classical RTK, the radio modems are used to communicate between reference and rover. In the present, the GSM services are used to form the communication link for RTK with the development of Internet protocol (NTRIP) [2]. Therefore, the restrictions of radio modems are eliminated. Moreover, the Continuously Operating Reference Station (CORS) networks are established for using Network-RTK. In this way, the RTK corrections are taken from a network of permanently installed reference stations using a system such as Virtual Reference System (VRS) [3]. Although the baseline distance is expanded, it stills not enough for some extrapolation areas. However, as the baseline distance increases, the atmospheric and orbital errors become larger. The DD technique cannot easily eliminate ionospheric errors on the long baselines. Therefore, the long baseline RTK algorithms are developed with some improvements on the classical RTK approach. Reference [4] developed an algorithm based on Kalman filter with the estimation of troposphere and ionosphere. They propose the use of near real time orbit products (ultra-rapid) to eliminate the broadcast ephemeris error up to 1000 km baselines. However, using a combination of different GNSSs' (GPS, GLONASS, Galileo, Beidou) observations and partial ambiguity fixing approaches are used for a more reliable long baseline RTK [5], [6]. Reference [7] proposes a triple-frequency long baseline RTK approach and investigates the contribution of QZSS to multi-GNSS long baseline RTK. The

---

<sup>1</sup> Corresponding author: Necmettin Erbakan University, Department of Geomatics Engineering, 42080, Meram, Konya, Turkey. [ootiz@erbakan.edu.tr](mailto:ootiz@erbakan.edu.tr)

<sup>2</sup> Necmettin Erbakan University, Department of Geomatics Engineering, 42080, Meram, Konya, Turkey. [sermetogutcu@erbakan.edu.tr](mailto:sermetogutcu@erbakan.edu.tr)

<sup>3</sup> Necmettin Erbakan University, Department of Geomatics Engineering, 42080, Meram, Konya, Turkey. [salcay@erbakan.edu.tr](mailto:salcay@erbakan.edu.tr)

main difference of long baseline RTK from short baseline is that ionospheric residuals cannot be removed effectively with iono-free (IF) combination [4].

The studies above are generally focus on a maximum of 100-200 km baseline distances. In this study, the GPS RTK performance with the estimation of ionosphere Slant Total Electron Content (STEC) is assessed on different baselines varying from ~200 to ~500 km. The RTKLIB software package was used for long baseline RTK processing.

## 2.METHOD

According to Reference [4], the double difference equations can be written as:

$$\phi = \rho - I + T + \lambda N + \varepsilon_{\phi} \quad (1)$$

$$P = \rho + I + T + \varepsilon_P \quad (2)$$

where  $\phi$  and  $P$  are the single-difference phase and pseudorange measurements between two satellites, respectively;  $I$  is the ionospheric delay in meter,  $T$  is the tropospheric delay in meter,  $\lambda$  is the wavelength in meter,  $N$  is the ambiguity term in cycle,  $\varepsilon_{\phi}$  and  $\varepsilon_P$  are the measurement noises in meter for phase and pseudorange measurements, respectively. The difference of this model from short baseline DD equations is the estimation of ionospheric delay instead of removing it by IF combination. The receiver-satellite clock errors are eliminated by DD equations. A Kalman filter can be adopted to estimate ambiguity-float solutions. Then float ambiguities are solved to integer values using a method such Least Square Ambiguity Decorrelation (LAMBDA) [8]. After solving float ambiguities to integer values, the unknown parameters are re-estimated. The studies in Reference [4] and Reference [7] demonstrates the use of broadcast ephemeris over 100-200 km largen the orbit error and decrease the probability of ambiguity fixing. However, a good float solution is always a necessity to obtain a reliable ambiguity fixing. In this study, the broadcast ephemeris was used to assess the performance of long baseline GPS RTK by using both ambiguity-float and ambiguity-fixed solutions.

Four different baselines (~200 to ~500 km) were established to evaluate the long baseline GPS RTK performance. The FinnRef GNSS stations were used [9] which are included in EUREF Permanent GNSS Network. The location of selected GNSS stations is shown in the Figure 1. All stations had the same GNSS receiver and firmware version during the measurements.

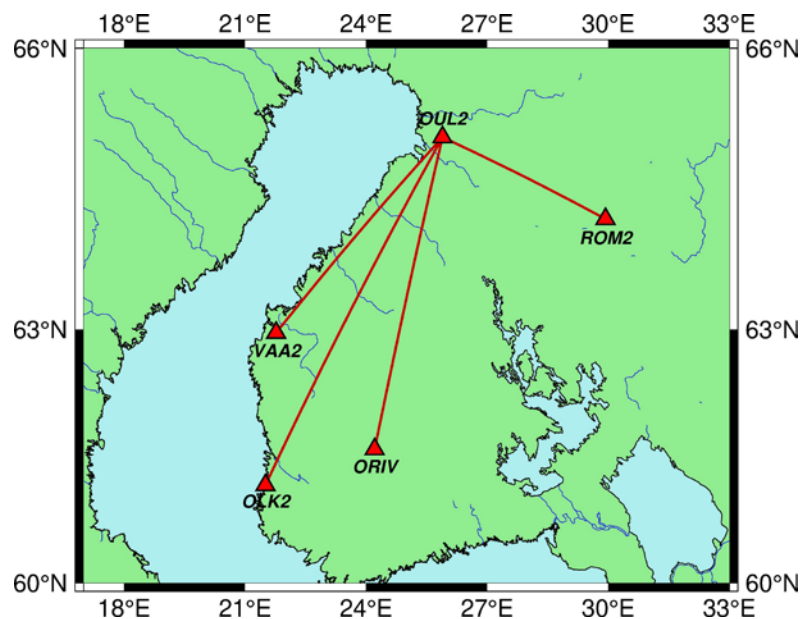


Figure 1. The location of selected GNSS stations

The further details about the baselines are given in Table 1.

*Table 9. The information about baselines*

<b>Baseline</b>	<b>Length (km)</b>	<b><math>\Delta H</math> (m)</b>
OUL2-ROM2	215.9	43.2
OUL2-VAA2	310.9	73.3
OUL2-ORIV	395.8	24.2
OUL2-OLK2	486.9	160.4

As shown in Table 1, the baseline distances vary from 216 km to 487 km, and the ellipsoidal height differences vary from 43 m to 160 m. The height difference from the reference station can negatively affect the troposphere estimation [10]. In this study, the effect of height difference may not be obvious when considered the baseline distances are long.

The 24 hourly data of four baselines on April 11, 2021, was processed using RTKLIB 2.4.3 b34 software package. The RTK solutions were computed offline to prevent data loss caused by the Internet connection. The detailed processing strategy is given in Table 2.

*Table 2. RTKLIB 2.4.3 b34 processing strategy*

<b>Parameter</b>	<b>Strategy</b>
GNSS	GPS
Frequencies	L1+L2
Adjustment model	Extended Kalman Filter
Epoch interval	1 s
Cut-off angle	10 °
Measurement noises	Phase: 0.01 m; Code: 1.00 m
Satellite orbit	Broadcast ephemeris
Ambiguity resolution	Fix and Hold (Minimum 10 epochs)
Ambiguity Validation	The ratio test with 2.0 threshold value
Ionosphere	STEC is estimated as random walk model.
Troposphere	ZTD and gradients are estimated as random walk model.
A priori troposphere	Saastamoinen
Mapping Function	Global Mapping Function (GMF)
Estimated parameters	Rover coordinates, ZTD, and STEC
Antenna phase center	Corrected using igs14.atx file.
Solid Earth Tides	Corrected.

The rover coordinates, ZTD, and STEC values of four baselines were computed for 86400 epochs.

### 3.RESULTS

The reference coordinates of base and rovers were taken from latest release of the EUREF station positions [11]. The RTK coordinates were converted to topocentric coordinate system (north, east, up). The statistical analysis below completed using north, east, and up components. First, the valid satellite numbers on four baselines were analyzed in Figure 3.



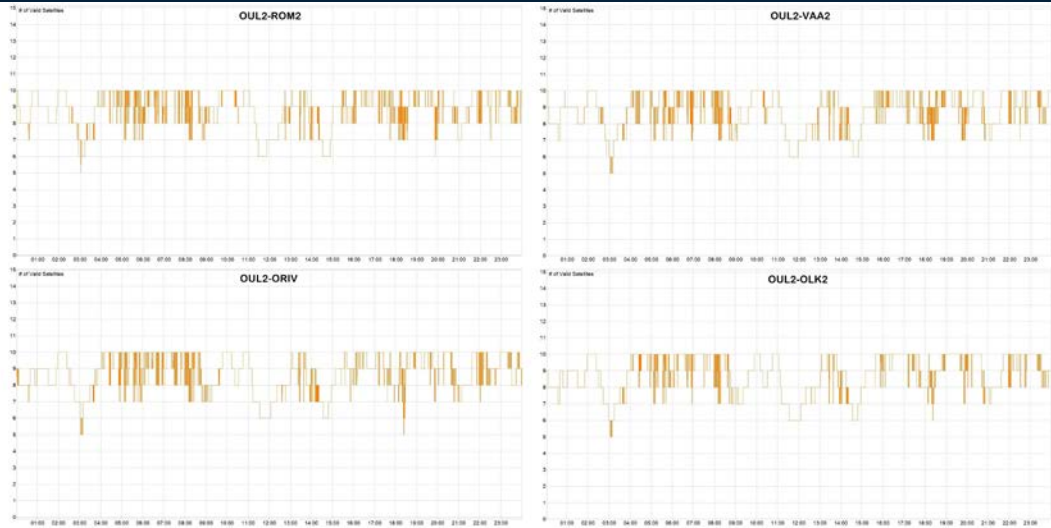


Figure 3. The valid satellites number of each RTK solution

As seen in the Figure 3, the average valid satellite numbers are about 9 for all baselines. This shows there was not any data gap. Then the ambiguity fix rates were calculated (Table 3).

Table 3. The information about baselines

Baseline	Ambiguity Fix Rate
OUL2-ROM2	70.6%
OUL2-VAA2	58.5%
OUL2-ORIV	42.4%
OUL2-OLK2	24.5%

According to Table 3, the OUL2-ROM2 baseline has the maximum ambiguity fixing rate (70.6%), and the OUL2-OLK2 baseline has the minimum ambiguity fixing rate (24.5%). This confirms that as the baseline distance longer the success of ambiguity fixing lower. Moreover, considering the baseline distance of OUL2-ORIV (396 km), the 42.4% of ambiguities are fixed. The root mean square errors (RMSE) were computed to clarify the accuracy of ambiguity fixed solutions of four long baselines (Table 4).

Table 4. RMSE of ambiguity-fixed solutions

Baseline	North (cm)	East (cm)	Up (cm)
OUL2-ROM2	0.8	0.9	3.4
OUL2-VAA2	3.6	2.5	5.0
OUL2-ORIV	2.3	3.1	5.0
OUL2-OLK2	1.9	2.9	5.4

As depicted in Table 4, the RMSE of 200 km baseline is lower than 1.0 cm at the horizontal components. For the longest baseline, the RMSEs of horizontal components are better than 3.0 cm. However, the up components are between 3.4 cm and 5.0 cm on four long baselines. In addition, the RMSE of all solutions (Fixed+Float) were computed (Table 5).

Table 5. RMSE of Fixed+Float solutions

Baseline	North (cm)	East (cm)	Up (cm)
OUL2-ROM2	1.2	1.3	4.6
OUL2-VAA2	5.9	3.6	6.0
OUL2-ORIV	2.8	3.8	8.0
OUL2-OLK2	4.2	4.4	6.3

The RMSE of the OUL2-ORIV baseline in horizontal components better than 3.9 cm. Moreover, the OUL2-OLK2 baseline demonstrated an RMSE of 4.2 cm and 4.4 cm for the north, and east components, respectively. Considering 75.5% of the solutions are float at the OUL2-OLK2 baseline, the results are still comparable. That can be explained by the quality of float solutions are quite well. All the results above include the initializing time to first fix. The coordinate time series of four baselines are illustrated in Figures 4-7.



Figure 4. The coordinate time series of ROM2 station

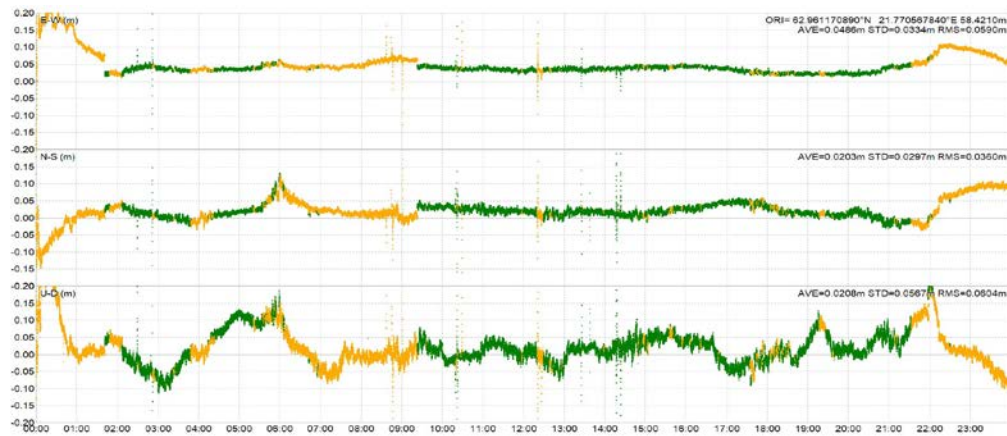


Figure 5. The coordinate time series of VAA2 station



Figure 6. The coordinate time series of ORIV station

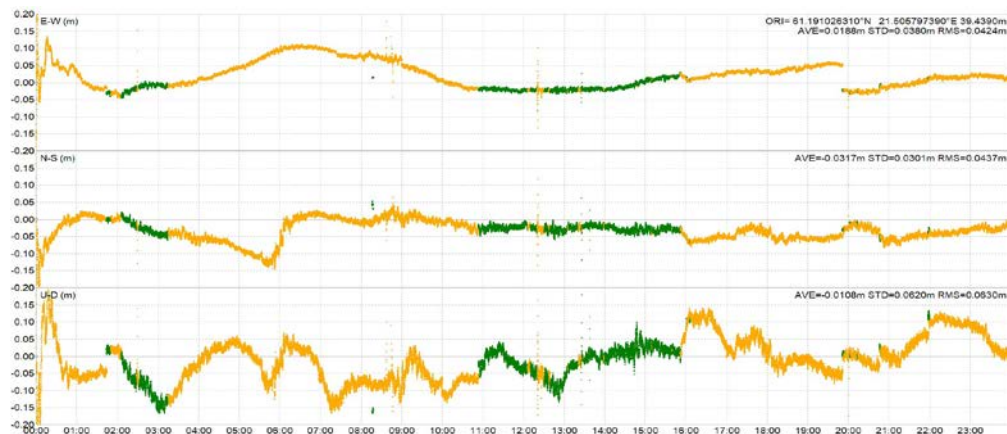


Figure 7. The coordinate time series of OLK2 station

The first 1-hours of all four baseline solutions were removed from the RMSE analysis to reduce the effect of initialization times. After this, the RMSEs were computed again (Table 6).

Table 5. RMSE of Fixed+Float solutions after removal of first 1-hours

Baseline	North (cm)	East (cm)	Up (cm)
OUL2-ROM2	1.0	1.1	4.1
OUL2-VAA2	4.7	3.4	5.2
OUL2-ORIV	2.2	3.4	6.3
OUL2-OLK2	4.1	4.2	6.1

The RMSEs of four baselines were slightly reduced after the removal of initialization times. In particular, the RMS error of the up component of OUL2-ORIV baseline was reduced by about two cm. In addition, the RMSE of the north component of the OUL2-VAA2 baseline was reduced by 1.2 cm.

#### 4. CONCLUSIONS

In this study, the latest GPS RTK performance on four different long baselines (~200- to ~500-km) was analyzed. Since the ionospheric delay cannot be neglected if the baselines are longer than 200 km, it was estimated as a random walk process. The experimental results showed the ambiguity fixing ratios are 70.6%, 58.5%, 42.4%, and 24.5% for the 200-, 300-, 400-, and 500 km baselines. The use of broadcast ephemeris over 200 km largen the orbit error and decrease the probability of ambiguity fixing. The RMSEs of the 200 km baseline were computed as 1.2 cm, 1.3 cm, and 4.6 cm for the north, east, and up components, respectively. However, the ambiguity float solutions were found comparable. As a consequence of this study, the long baseline GPS RTK by estimating ionosphere can be used at the areas distant to the reference stations after waiting for the first initialization.

#### ACKNOWLEDGMENT

The authors thank to Tomoji Takasu for providing RTKLIB software, and EUREF for providing the GNSS data.

#### REFERENCES

- [1]. Leick, L. Rapoport, and D. Tatarnikov, "GPS satellite surveying," *John Wiley & Sons*, 2015.
- [2]. G. Weber, D. Dettmering, and H. Gebhard, "Networked transport of RTCM via internet protocol (NTRIP)". *In A Window on the Future of Geodesy*, Springer, Berlin, Heidelberg, pp. 60–64, 2005.
- [3]. Rizos, and S. Han, "Reference station network based RTK systems-concepts and progress," *Wuhan University Journal of Natural Sciences*, vol. 8 (2), pp. 566–574, 2003.
- [4]. T. Takasu, and A. Yasuda, "Kalman-filter-based integer ambiguity resolution strategy for long-baseline RTK with ionosphere and troposphere estimation," *In Proceedings of the 23rd international technical meeting of the satellite division of the institute of navigation (ION GNSS 2010)*, pp. 161–171, 2010.
- [5]. A.Brack, "Rapid initialization for long baseline RTK positioning: combined GPS+Galileo+BDS+QZSS+GLONASS with partial ambiguity resolution," *In 2020 European Navigation Conference (ENC)*, pp. 1–9, 2020.
- [6]. C.Konukseven, O. F. Atiz, S. Alcay and S. Ogutcu, "Analysis of the contribution of the multi-GNSS to long-distance RTK," *First Intercontinental Geoinformation Days (IGD)*, Mersin, Turkey, pp. 190–193, 2020.
- [7]. Y Zhang, N. Kubo, J. Chen, F. Y. Chu, H. Wang, and J. Wang, "Contribution of QZSS with four satellites to multi-GNSS long baseline RTK," *Journal of Spatial Science*, vol. 65 (1), pp. 41–60, 2020.
- [8]. P. Teunissen, P. Joosten, C. Tiberius, "A comparison of TCAR, CIR and LAMBDA GNSS ambiguity resolution," *In Proceedings of the 15th International Technical Meeting of the Satellite Division of the Institute of Navigation (ION GPS 2002)*, pp. 2799–2808, 2002.
- [9]. (2021) FinnRef GNSS Stations Website. [Online]. Available: <https://www.maanmittauslaitos.fi/en/research/research/other-research-and-measuring-stations/finnref-gnss-stations>
- [10]. S. J. Edwards, P. J. Clarke, N. T. Penna and S. Goebell, "An examination of network RTK GPS services in Great Britain," *Survey Review*, vol. 42 (316), pp. 107-121, 2010.
- [11]. EUREF Permanent GNSS Network [Online]. Available: [http://www.epncb.oma.be/\\_productsservices/coordinates/index.php](http://www.epncb.oma.be/_productsservices/coordinates/index.php)

#### BIOGRAPHY

Omer Faruk Atiz received his B.Sc. degree in Geomatics Engineering from Selcuk University (Turkey). He is currently an M.Sc. candidate at the Geomatics Engineering Department of Necmettin Erbakan University (Turkey). His studies focus on GNSS precise positioning.

Salih Alcay is an Associate Professor at Necmettin Erbakan University, Geomatics Engineering Department. He has received his PhD from Selcuk University. His research interest includes GNSS-based positioning, deformation analysis, and ionosphere modelling.

Sermet Ogutcu is an Associate Professor at Necmettin Erbakan University, Geomatics Engineering Department. His research interest includes PPP, Network-Based RTK techniques.

# Prevalance of *Wolbachia* in *Culex pipiens* populations in Turkey

Naciye Sena Cagatay<sup>1</sup>, Nurper Guz<sup>1\*</sup>

---

## Abstract

Mosquitoes are a common group of insects comprising of 112 genera and approximately 3500 species [1]. The majority of the described mosquito species are considered nuisance species while only few are implicated as major vectors in the transmission of infectious diseases to humans and other vertebrate hosts. Notably, countries within the tropic and temperate climatic zones face an increased Mosquito Borne Diseases (MBD) burden and transmission risk as they display a rich mosquito biodiversity including important vector species. In recent years, Turkey, has witnessed the emergence and resurgence of a number of MBDs. In the absence of protective human vaccines against most MBDs vector control, aiming to reduce the vector population size predominantly using insecticides is key to preventing and managing disease outbreaks. Both pyrethroids and DFB are amongst the most widely used insecticides in Turkey for mosquito control [2, 3] due to their high efficacy and low mammalian toxicity [4]. However, a serious public health problem associated with the extensive use of insecticides in vector and agricultural pest control is the development of insecticide resistance in many mosquito species [5, 6, 7]. Therefore, endosymbiotic bacteria has received considerable attention as a mechanism to control insect vectors. Among symbiotic bacteria, *Wolbachia* is widely distributed with about 70% of all insect species [8, 9] which regulates host reproduction through cytoplasmic incompatibility (CI), feminization, male killing, and parthenogenesis [10, 11]. *Culex pipiens* group are infected with *Wolbachia* wPip strains belonging to five genetically distinct groups (wPip-I to V) within the *Wolbachia* B supergroup. In this study, we analyzed the prevalence of *Wolbachia* infection Turkish *Cx. pipiens* populations. We also evaluated the phylogenetic relationship between *Wolbachia* strains isolated from various insects and constructed a phylogenetic tree of other arthropod sequences under the NJ method. Knowledge on the prevalence of *Wolbachia* in Turkey might be useful for *Cx. pipiens* control in the region.

**Keywords:** *Wolbachia*, *Culex pipiens*, Endosymbiont, wsp, phylogenetic tree

---

## 1.INTRODUCTION

The endosymbiotic bacteria in insects are found commonly. They have diverse effect on the host biology [12, 13] including providing nutrient and vitamin [14], protection from natural enemies [15], host plant preference [16], manipulation of host sexuality [17], and adaptation to environmental conditions and depending on the type of symbiotic association changes. [18, 19]. The insect interaction with microbial fauna is important in terms of the host's fitness, evolutionary biology, and ecology [20].

*Wolbachia* is widely distributed with about 70% of all insect species [8, 9]. It is maternally inherited symbiotic bacteria that modifies host biology and may cytoplasmic incompatibility (CI), induce feminization, male killing, and parthenogenesis [21, 22]. It has been shown to have deleterious effects on their host's life history traits [23, 24]. Recently, *Wolbachia* is shown as a biological control agent for mosquito borne diseases [27].

Among mosquito species *Culex pipiens*, is major a pest of with all of the world which is distributed in most parts of Turkey [28, 29, 30, 31]. It is vector of arbovirus such as West Nile, which has also been detected to exist in Turkey [32, 33].

---

<sup>1</sup> Ankara University, Faculty of Agriculture, Department of Plant Protection, 06010, Diskapi/Ankara.

\*Corresponding author: Ankara University, Department of Plant Protection, 06010, Diskapi/Ankara, Turkey.  
nurperguz@agri.ankara.edu.tr

Studies showed that mosquito species were infected with different strains of *Wolbachia* at an almost 100% rate throughout most of their geographical distribution [34, 35, 27]. However, *Wolbachia* prevalence in *C. pipiens* differed in the rates of 60% - 62% in Central Anatolian, Aegean of Turkey, respectively [36, 37].

In this study, mosquito samples were collected from different geographic locations of Mugla from Turkey. The prevalence of *Wolbachia* infection in *C. pipiens* populations were detected. Furthermore, the phylogenetic relationships between and within the super groups of *Wolbachia* analyzed in *C. pipiens* mosquitoes.

## 2.MATERIALS AND METHODS

### ○ *Mosquito Collection*

*C. pipiens* larvae were collected from Mugla Province in Turkey (Table 1). A total of 110 mosquitoes were sampled from irrigation channels, swimming pool, cesspits, and swamps. The collected mosquitoes were identified morphologically to species level [38, 39]. The specimens were preserved in 100% ethanol and stored at -20°C until molecular analysis.

Table 1. Mosquito collection sites and map coordinates

Location	Coordinates(N-E)
Fethiye	36,338871 N-29,244941 E
Koycegiz	36,965970 N-28,697766 E
Dalaman	36,806107N-28,791138 E
Milas	37,278691N-27,668347 E
Bodrum	36,971742N-27,275690 E
Marmaris	36,756289N-28,137134 E
Mentese	37,218910N-28,366016 E
Ula	37,039613N-28,386455 E
Datca	36,767225N-27,796084 E
Seydikemer	36,420193N-29,261748 E
Ortaca	36,845870N-28,633774 E

### ○ *DNA Extraction, Detection of Wolbachia by using PCR, Sequencing*

Genomic DNA was extracted from individual *C. pipiens* larvae using High pure PCR template preparation Kit as described in the manufacturer's protocol (Roche Diagnostic, Mannheim, Germany). The quality and quantity of DNA extracts were estimated using electroporation in a 1% agarose gel and with a NanoDrop2000 spectrophotometer (Thermo Scientific, USA).

In order to detect *Wolbachia*, wsp primers were used in PCR amplifications (wsp 81 F: 5'TGGTCCAATAAG TGA TGAAGAAAC 3' and wsp 691 R: 5'AAAAATTAACGCTA CTCCA 3') [40]. PCR reactions were set up in total volume of 50 µl by using 1 µl of DNA template Taq DNA Polymerase Master Mix RED (Ampliqon, Denmark) according to manufacturer's instructions: Taq 2x Master Mix, 10 mM of each primer and 100ng of mosquito DNA .The PCR conditions were as follows: an initial denaturation step at 95 °C for 5 min, followed by 35 cycles of 95 °C for 30 s, 55 °C for 40 s and 72 °C for 30 s, followed by a final extension step at 72 °C for 5 min. HCO\_LCO primers were considered universal for insect mtDNA amplifying an approximately 700 bp DNA fragment [41].

The PCR products were electrophorised on a 2 % agarose gel and purified with Wizard SV Gel and PCR Clean up System (Promega, Madison, USA). PCR purified product were amplified with DTCS Quick Start Kit (Beckman Coulter, CA, USA). The nucleotide sequence determined in this study have been deposited in the DNA Genbank of NCBI.

### ○ *Molecular Sequence Data Analysis*

Sequence analysis was performed using blast at NCBI ([www.ncbi.nih.gov/BLAST](http://www.ncbi.nih.gov/BLAST)). Mutiple alignments were generated using the program Clustal W [42]. The phylogenetic tree was inferred using the Neighbor-Joining method [43]. The optimal tree is shown. The percentage of replicate trees in which the associated taxa clustered together in the bootstrap test (1000 replicates) are shown next to the branches [44]. The evolutionary distances were computed using the Kimura 2-parameter method [45] and are in the units of the number of base

substitutions per site. There was a total of 482 positions in the final dataset. Evolutionary analyses were conducted in MEGA11 [46].

### 3.RESULT AND DISCUSSION

In this study a total 110 individuals belonging to *C. pipiens* species were screened in terms of *Wolbachia* by PCR assay using species specific *wsp* gene primers. About 600 bp fragment of the *wsp* gene was amplified and sequenced from the endosymbiont of *Culex pipiens* with species specific primers. The infection status of each samples tested, and the number of specimens screened are listed in Table 2. In total, 71 of 110 tested samples were PCR positive which means that 65 % were infected with *Wolbachia*. The populations from Dalaman (33%) and Mentese (33%) were found to harbor low *Wolbachia*. On the other hand, rest of the populations the infection rates of *Wolbachia* varied among ranging from 40 % to 87 %.

Prevalence of *Wolbachia* bacteria in *Culex* has been reported in previous studies [34, 47, 35, 48, and 36]. Our *Wolbachia* infection findings were similar to previous studies Kayseri province and Aegean of Turkey [36, 37]. However, the infection rate of *Wolbachia* endosymbiont in *C. pipiens* was found different in different regions of Mugla. The sampling method and period of the insects may cause differences in *Wolbachia* infection prevalence [49].

Table 2. Prevalence of the *Wolbachia* infection rates

Populations	N	+ WSP	% +WSP
Fethiye	17	10	59
Koycegiz	2	1	50
Dalaman	3	1	33
Milas	23	20	87
Bodrum	21	17	81
Marmaris	17	9	53
Mentese	10	3	33
Ula	4	2	50
Datca	5	2	40
Seydikemer	3	2	67
Ortaca	5	4	80

The obtained *Wolbachia* sequence from *C. pipiens* has been submitted to GenBank. BLAST analysis revealed that this sequence displayed the highest homology with 99.81% identity to *Wolbachia* endosymbiont of *C. pipiens* (KT964225.1), *Culex quinquefasciatus*(LC276757.1), *Operophtera brumata* (KY587652.1), *Operophtera brumata* (KY587653.1) and *Hypolimnas bolina* (MG934359.1).

The *wsp* gene sequence could be used to resolve phylogenetic relationships from different *Wolbachia* strains [50]. The phylogenetic reconstruction 17 *Wolbachia* supergroup (A-Q) have been reported [51]. Our results have been found in previous studies two *Wolbachia* supergroup, and clustered in supergroup B [52, 36, 50, 27]. A phylogenetic tree of all the *Wolbachia* strains found in infected *C. pipiens* species was constructed. The phylogenetic relationship between *Wolbachia* strains isolated from various insects, we constructed a phylogenetic tree (Figure 3) of 21 arthropod sequences under the NJ method, and the tree topology of all subjected sequences revealed two supergroups (A and B). The first cluster (supergroup B) consisted of the orders including Diptera, Lepidoptera, Hemiptera, Coleoptera, Hymenoptera, and Lepidoptera, whereas the second cluster (supergroup A) showed a relationship between Formicidae, Diptera, Lepidoptera, Hymenoptera, and Coleoptera. The phylogenetic tree showed that the *Wolbachia* sequence from *C. pipiens* and different Diptera and Lepidopteran species were clustered.

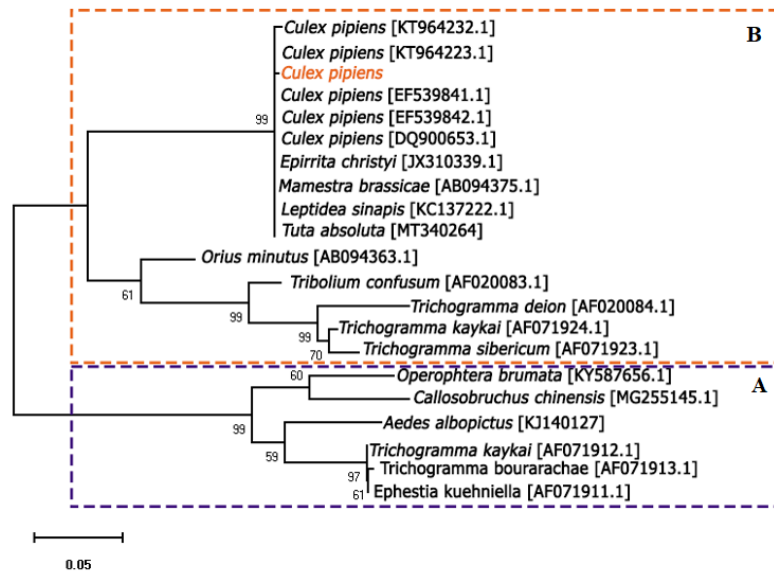


Figure 3. Phylogenetic analysis of *Wolbachia* in *C. pipiens* species

#### 4.CONCLUSION

*Wolbachia* infections were detected in the field populations of Mugla, from Turkey. Determining the infection frequency of *Wolbachia* is an important step in understanding the impact of these bacteria on insect evolution and dispersal ability in different habitats. The symbiont host interactions are important for the development and use of *Wolbachia*-based biological control methods.

#### ACKNOWLEDGMENT

N.S.C, was supported by 100/2000 YOK PhD Scholarship in Ankara University and TUBITAK [The Scientific and Technological Research Council of Turkey] 2211-A PhD Scholarship Programs.

#### REFERENCES

- [1] R. E. Harbach, C. L. Culverwell, and I. J. Kitching, "Phylogeny of the nominotypical subgenus of *Culex* (Diptera: Culicidae): insights from analyses of anatomical data into interspecific relationships and species groups in an unresolved tree," *System. Biodivers.*, vol. 15, pp 296-306, 2017.
- [2] M. Laurito, and R. Hoyos-López, "First record of *Culex* (*Culex*) *bidens* (Diptera: Culicidae) in Colombia: Taxonomic and epidemiological implications," *Acta Trop.*, vol. 188, pp 251-257, 2018.
- [3] M.M. Akiner. "Insecticide resistance of *Culex pipiens* (Diptera: Culicidae) in Turkey," *J. Pestic. Sci.*, pp 0908080092-0908080092, 2009.
- [4] R. Feyereisen, W. Dermauw, and Van Leeuwen, T. *Genotype to phenotype, the molecular and physiological dimensions of resistance in arthropods.* *Pestic Biochem Physiol.*, vol. 121, pp 61-77, 2015.
- [5] J. G. Scott, M. H. Yoshimizu, and S. Kasai, "Pyrethroid resistance in *Culex pipiens* mosquitoes," *Pestic. Biochem. Physiol.*, vol. 120, pp 68-76, 2015.
- [6] N. Guz, N.S. Cagatay, E. A. Fotakis, E. Durmusoglu, and J. Vontas, "Detection of diflubenzuron and pyrethroid resistance mutations in *Culex pipiens* from Mugla," *Turkey. Acta Trop.*, vol. 203, pp 105294, 2020.
- [7] B. G. Taskin, T. Dogaroglu, S. Kilic, E. Dogac, and V. Taskin, "Seasonal dynamics of insecticide resistance, multiple resistance, and morphometric variation in field populations of *Culex pipiens*," *Pestic. Biochem. Physiol.*, vol. 129, pp 14-27, 2016.
- [8] H. E. Amuzu, K. Tsyganov, C. Koh, R. I. Herbert, D. R. Powell, and E.A. McGraw, "*Wolbachia* enhances insect-specific flavivirus infection in *Aedes aegypti* mosquitoes," *Ecol. Evol.*, vol. 8, pp 5441-5454, 2018.
- [9] J. Bi, and Y. F. Wang, "The effect of the endosymbiont *Wolbachia* on the behavior of insect hosts," *Insect Sci.*, vol. 27, pp 846-858, 2020.
- [10] J. H. Werren, "Biology of *Wolbachia*," *Annu. Rev. Entomol.*, vol. 42, pp 587-609, 1997.



- [11] R. Stouthamer, J. A. Breeuwer, and G. D. Hurst, "*Wolbachia pipientis*: microbial manipulator of arthropod reproduction," *Annu. Rev. Microbiol.*, vol. 36, pp71-102, 1999.
- [12] H. Feldhaar, "Bacterial symbionts as mediators of ecologically important traits of insect hosts," *Ecol. Entomol.*, vol. 6, pp 533-543, 2011.
- [13] J. H. Werren, L. Baldo, and M. E. Clark, "*Wolbachia*: master manipulators of invertebrate biology," *Nat. Rev. Microbiol.*, vol. 43, pp741-751. 2008.
- [14] A. E. Douglas, "Nutritional interactions in insect-microbial symbioses: aphids and their symbiotic bacteria *Buchnera*," *Annu. Rev. Entomol.*, vol. 43, pp 17-37,1998.
- [15] J. C. Brownlie, and K. N. Johnson, "Symbiont-mediated protection in insect hosts," *Trends Microbiol.*, vol. 18, pp 348-354, 2009.
- [16] S. H. Chung, E. D. Scully, M. Peiffer, S.M. Geib, C. Rosa, K. Hoover, and G. W. Felton, "Host plant species determines symbiotic bacterial community mediating suppression of plant defense," *Sci. Rep.*, vol.7, pp 1-13, 2017.
- [17] J. Ferrari, and F. Vavre, 2011. "Bacterial symbionts in insects or the story of communities affecting communities," *Philos. Trans. R. Soc. Lond., B, Biol. Sci.*, vol. 366, pp 1389-1400, 2011.
- [18] N. Guz., A. Dageri, A., and S. Aksoy, "*The impacts of endosymbiotic bacteria on insects*," *Turk Entomol Bull.*, vol. 5, pp 101-113, 2015.
- [19] P. A. Jose, M. Ben-Yosef, E. Jurkevitch, and B. Yuval, "Symbiotic bacteria affect oviposition behavior in the olive fruit fly *Bactrocera oleae*," *J. Insect Physiol.*, vol. 117, pp 03917, 2019.
- [20] K. Guring, B. Wertheim, and J. Falcao Salles, "*The microbiome of pest insects: it is not just bacteria*," *Entomol. Exp.*, vol. 167, pp 156-170, 2019.
- [21] G. D. Hurst, F. M. Jiggins, J. Hinrich Graf Von der Schulenburg, D. Bertrand, S. A. West, I. I. Goriacheva, I. A. Zakharov, J. H. Werren, R. Stouthamer and M.E. N. Majerusand, "Male-killing *Wolbachia* in two species of insect," *Roc. Royal Soc. B P Roy Soc. B-Biol. Sci.*, vol. 266, pp 735-740. 1999.
- [22] R. Stouthamer, J. A. Breeuwer, and G. D. Hurst, "*Wolbachia pipientis*: microbial manipulator of arthropod reproduction," *Annu. Rev. Microbiol.*, vol. 53, pp 71-102,1999.
- [23] K. T. Min, and S. Benzer, "*Wolbachia*, normally a symbiont of *Drosophila*, can be virulent, causing degeneration and early death," *PNAS*, vol. 94, pp 10792-10796, 1997.
- [24] A. R. Weeks, M., Turelli, W. R. Harcombe, K. T. Reynolds, and A. A. Hoffmann, "From parasite to mutualist: rapid evolution of *Wolbachia* in natural populations of *Drosophila*," *PLoS Biol.*, vol. 5, pp e114. 2007.
- [25] L. Klasson, T. Walker, M. Sebaihia, M. J. Sanders, M. A. Quail, A. Lord, S. Sanders, J. Earl, S. L. O'Neill, N. Thomson, S. P. Sinkins, J. Parkhill, "Genome evolution of *Wolbachia* strain *wPip* from the *Culex pipiens* group," *Mol Biol Evol.*, vol. 25, pp 1877-1887, 2008.
- [26] S. P. Sinkins, T. Walker, A. R. Lynd, A. R. Steven, B. L. Makepeace, H. C. J. Godfray and J. Parkhill, "*Wolbachia* variability and host effects on crossing type in *Culex* mosquitoes," *Nature*, vol. 436, pp 257-260, 2005.
- [27] M. Karami, S. H. Moosa-Kazemi, M. A. Oshaghi, H. Vatandoost, M. M. Sedaghat, R. Rajabnia, M. Hosseini, N. Maleki-Ravasan, Y. Yahyapour, and E. Ferdosi-Shahandashti, "*Wolbachia endobacteria* in natural populations of *Culex pipiens* of Iran and its phylogenetic congruence," *J. Arthropod-Borne Dis.*, vol. 10, pp 347-363, 2016.
- [28] E. B. Vinogradova, "*Culex pipiens pipiens* mosquitoes: taxonomy, distribution, ecology, physiology, genetics, applied importance and control," 2nd ed., S. I. Golovatch, Ed. Sofia: Bulgari, Pensoft Publisher, 2000.
- [29] V. A. Brugman, L. M. Hernández-Triana, J. M. Medlock, A. R. Fooks, S. Carpenter, and N. Johnson, "The role of *Culex pipiens* L. (Diptera: Culicidae) in virus transmission in Europe," *Int. J. Environ. Res. Public Health.*, vol. 15, pp 389, 2018.
- [30] Gunay, F., B. Alten, F. Simsek, A. Aldemir, and Y.M. Linton, "Barcoding Turkish *Culex* mosquitoes to facilitate arbovirus vector incrimination studies reveals hidden diversity and new potential vectors," *Acta Trop.*, vol. 143, pp 112-120, 2015.
- [31] H. Cetin, A. Yanikoglu, and J. E. Cilek, "Larvicidal activity of selected plant hydrodistillate extracts against the house mosquito, *Culex pipiens*, a West Nile virus vector," *Parasitol. Res.*, vol. 108, pp 943-948, 2011.
- [32] K. Ergunay, F. Gunay, K. Oter, O.E. Kasap, S. Orsten, A.Z. Akkutay, H. Erdem, A. Ozkul, and B. Alten, "Arboviral surveillance of field-collected mosquitoes reveals circulation of West Nile virus lineage 1 strains in Eastern Thrace, Turkey," *Vector-Borne Zoonot.*, vol. 13, pp 744-52. 2013.
- [33] Ergunay K, F. Gunay, O. Erisoz Kasap, K. Oter, S. Gargari, T. Karaoglu, S. Tezcan, M. Cabalar, Y. Yildirim, G. Emekdas, B. Alten, A. Ozkul, *Serological, molecular and entomological surveillance demonstrates widespread circulation of west nile virus in Turkey*, *PLoS Neglect Trop D.*, vol. 8, pp 1-10, 2014.
- [34] J. L. Rasgon, and T.W. Scott, "*Wolbachia* and cytoplasmic incompatibility in the *California Culex pipiens* mosquito species complex: parameter estimates and infection dynamics in natural populations," *Genet. Res.*, vol. 165, pp 2029-2038, 2003.
- [35] I.P. Sunish, R. Rajendran, R. Paramasivan, K.J. Dhananjeyan, B.K. Tyagi, "*Wolbachia endobacteria* in a natural population of *Culex quinquefasciatus* from filariasis endemic villages of South India and its phylogenetic implication," *Trop Biomed.*, vol. 28, pp 569-576, 2011.
- [36] A. Yildirim, I. Abdullah, O. Duzlu, Z. Onder, and A. Ciloglu, "Detection and molecular characterization of the *Wolbachia endobacteria* in the *Culex pipiens* (Diptera: Culicidae) specimens collected from Kayseri province of Turkey. *Ankara University Faculty of Vet. J.*, vol. 60, pp 189-194, 2013.
- [37] B. Morcicek, B. G.Taskin, E. Dogac, T. Dogaroglu, and V. Taskin, "Evidence of natural *Wolbachia* infections and molecular identification of field populations of *Culex pipiens complex* (Diptera: Culicidae) mosquitoes in western Turkey," *J. Vector Ecol.*, vol. 53, pp 44-51, 2018.

- [38] N. Becker, A. Jost, and T. Weitzel, "The *Culex pipiens* complex in Europe." J. Am. Mosq. Control Assoc., vol. 28, pp 53-67, 2012.
- [39] E. Schaffner, G. Angel, B. Geoffroy, J.P. Hervy, A. Rhaiem, J. Brunhes, "The Mosquitoes of Europe (CD-Rom)," Institut de Recherche Pour le Développement, Montpellier, France ,2001.
- [40] H. R. Braig, W. Zhou, S.L. Dobson, and S. L. O'Neill, "Cloning and characterization of a gene encoding the major surface protein of the bacterial endosymbiont *Wolbachia pipientis*," J. Bacteriol., vol. 180, pp 2373-2378. 1998.
- [41] O. Folmer, Hoeh, W. R., M. B. Black, and R.C. Vrijenhoek, "Conserved primers for PCR amplification of mitochondrial DNA from different invertebrate phyla," Mol Membr Biol., vol. 3, pp 294-299,1994.
- [42] J. D. Thompson, D. G. Higgins, and T. J. Gibson, "CLUSTAL W: improving the sensitivity of progressive multiple sequence alignment through sequence weighting, position-specific gap penalties and weight matrix choice," Nucleic Acids Res., vol. 22, pp 4673-4680,1994.
- [43] N. Saitou and M. Nei, "The neighbor-joining method: A new method for reconstructing phylogenetic trees," Mol. Biol. Evol., vol. 4, pp 406-425. 1987.
- [44] J. Felsenstein, "Confidence limits on phylogenies: An approach using the bootstrap," Evol., vol. 39, pp 783-791, 1985.
- [45] M. Kimura, "A simple method for estimating evolutionary rate of base substitutions through comparative studies of nucleotide sequences," J. Mol. Evol., vol. 116, pp 111-120,1980.
- [46] K. Tamura, G. Stecher, and S. Kumar, "MEGA 11: Molecular Evolutionary Genetics Analysis Version 11," Mol. Biol. Evol., vol. 1870-1874, 2021. <https://doi.org/10.1093/molbev/msab120>
- [47] O. Duron, M. Raymond, and M. Weill, "Many compatible *Wolbachia* strains coexist within natural populations of *Culex pipiens* mosquito," Heredity, vol. 106, pp 986-993,2011.
- [48] A. Behbahani, "*Wolbachia* infection and mitochondrial DNA comparisons among *Culex* mosquitoes in South West Iran," Pak J Biol Sci., vol. 15, pp 54-57,2012.
- [49] M. Hoffmann, M. R. Coy, H. N. Kingdom Gibbard, and K. S. Pelz-Stelinski. "*Wolbachia* infection density in populations of the Asian citrus psyllid (Hemiptera: Liviidae)," Environ. Entomol., vol. 43, pp 1215-1222, 2014.
- [50] W. Zhou, F. Rousset, and S. O'Neill, "Phylogeny and PCR-based classification of *Wolbachia* strains using wsp gene sequences," Proc. Royal Soc. B. P. Roy. Soc. B-Biol. Sci., vol. 265, pp 509-515.1998.
- [51] E. Glowaska, A. Dragun-Damian, M. Dabert, and M. Gerth, "New *Wolbachia* supergroups detected in quill mites (Acari: Syringophilidae)," Infect. Genet. Evol., vol. 30, pp 140-146, 2015.
- [52] V.J. Pidiyar, K. Jangid, M.S. Patole, and Y.S. Shouche, Detection and phylogenetic affiliation of *Wolbachia* sp. from Indian mosquitoes *Culex quinquefasciatus* and *Aedes albopictus*," Curr Sci, vol. 84, pp 1136-1139,2003.

## BIOGRAPHY

Naciye Sena Catagay has received her B.S degree in Faculty of Agriculture from Suleyman Demirel University (2013), her M.S degree in Insect Toxicology (2016, Suleyman Demirel University. In the first years of her M.S, she joined Erasmus Program (Warsaw life Science University Poland) and she studied molecular analysis of M.S degree thesis Erasmus + programme (Vontas Lab., Greece). She has studied her Ph.D degree in Ankara University since 2017. Her research interests include Entomology, Insecticide resistance, Molecular biology.

# Validation of QuEChERS Method for the Analyses of Chlorpyrifos-methyl, Lambda-cyhalothrin and Tebuconazole Residues in Grapes\*

Aysegul Duman<sup>1</sup>, Osman Tiryaki<sup>2</sup>

---

## Abstract

Method validation (MV) is an important quality parameter in pesticide residue analyses and has a direct impact on the quality of data. MV is the process of verifying that a method is fit for purpose. All methods used in pesticide analyses must be validated prior to original samples. Working with validated methods is also a basic requirement in ISO 17025 and OECD - GLP quality systems. This study was carried out to validate QuEChERS Official Method 2007.01 method using grapes spiked at 0.1 x MRL, 1 x MRL and 10 x MRL levels of the three (chlorpyrifos-methyl, lambda-cyhalothrin and tebuconazole) pesticides. For the extraction and cleanup, QuEChERS 2007.1 version was followed, then the samples were subjected to LC-MS/MS for chromatography. For the quantification representative (apple) matrix-matched calibration (MC) was used to compensate matrix effect. Detection limit of three pesticides below the EU-MRLs. The recovery ranges were 91.3%-131.4% (mean 114.80%), 85.8%-133.2% (mean 108.05%), 90.3%-111.6% (mean 102.96) for chlorpyrifos-methyl, lambda-cyhalothrin and tebuconazole, respectively. The overall recovery of the QuEChERS method was 108.6% with a relative standard deviation (RSD) of 11.8% (n= 108). These figures are within the recovery limits (60-140%) and the values specified for the repeatability (RSD ≤ 20%). The calibration curves of three pesticides were linear ( $R \geq 0.999$ ). Precision, accuracy and linearity were also within the required limits. All the required method validation criteria were met in this study. QuEChERS method was found suitable for the analyses of chlorpyrifos-methyl, lambda-cyhalothrin and tebuconazole residues in grape under our laboratory conditions.

**Keywords:** Grape, method validation, pesticide residue, QuEChERS Official Method 2007.01

---

## 1. INTRODUCTION

Pesticides are the most critical component of agriculture and will constitute an important input of agriculture in the future. Agricultural foods should not include any pesticide or should have residues less than specified MRL [1].

QuEChERS method is developed by Anastassiades et al [2] and has been used for the analysis of a large number of pesticides in a wide variety of agricultural product. Modification of QuEChERS method was used in this study [3].

According to SANCO/SANTE Guidelines method validation (MV) is an important quality parameter in pesticide residue analyses and has a direct impact on the quality of data. MV is the process of verifying that a method is fit for purpose. MV shows most common potential problems in the method. All methods used in

---

<sup>1</sup> Canakkale Onsekiz Mart University, School of Graduate Studies, Department of Plant Protection, Canakkale, Turkey  
[aysegulduman1997@gmail.com](mailto:aysegulduman1997@gmail.com)

<sup>2</sup> Corresponding author: Canakkale Onsekiz Mart University, Faculty of Agriculture, Plant Protection Department, Canakkale, Turkey, [osmantiryaki@yahoo.com](mailto:osmantiryaki@yahoo.com)

\*This study is a part of the master degree thesis of the first Aysegul Duman (School of Graduate Studies, Department of Plant Protection, Canakkale Onsekiz Mart University). This work was also supported by Canakkale Onsekiz Mart University The Scientific Research Coordination Unit, Project number: FYL-2020-3359.

pesticide residue analysis must be validated prior to original laboratory samples. Working with validated methods is also a basic requirement in ISO 17025 and OECD - GLP quality systems. Despite the widespread use of the QuEChERS method in well-equipped laboratories, there is still a need for validation for local conditions of any laboratories. Recovery limit was specified in SANTE Guidelines as 60-140% with the RSD  $\leq 20\%$  [4], [5], [6], [7],[8].

The world grape production is about 79.1 Mt in 2018. With an annual production of 4.100.000 tons, Turkey has the 6<sup>th</sup> place in world grape production. About 83% of grape exported from Turkey is sent to EU (European Union) countries. Grape and its processed products are extensively consumed all over the world [9].

This study focused to validate analytical procedure for chlorpyrifos-methyl, lambda-cyhalothrin and tebuconazole residues in grape. Spiked grape samples were analysed with QuEChERS method, followed by determination using LC-MS/MS. The the validity of the method were also performed by method-validation parameters ([6]-[7], [8]).

## 2.MATERIALS AND METHOD

### ○ *Material*

#### 2.1.1. Reagents and Chemicals

Chlorpyrifos-methyl, lambda-cyhalothrin and tebuconazole pesticide standards were supplied from Dr. Ehrenstorfer Laboratories GmbH, Germany, with the purity of 98.73%, 98.6% and 99.69%, respectively. Some physicochemical and toxicological properties of pesticides are given in Table 1. MgSO<sub>4</sub>\*7H<sub>2</sub>O, sodium acetate (NaAC), acetonitrile (MeCN), methanol (MeOH) were supplied from Merck, with the purity of 99.5%, 99.0%, 99.9%, 99.0% and 99.9%, respectively. PSA (Primary-secondary amine 40  $\mu$ m, 100 g) was sourced from Agilent (Santa Clara, CA, USA).

#### 2.1.2. Instrumentation

Chromatographic analyses were carried out with LC-MS/MS (Waters I Class Plus UPLC + Xevo TQ-S micro MS Detector) equipped with Acquity UPLC BEH C<sub>18</sub> column (1.7  $\mu$ m, 2.1 mm x 100 mm). Injection volume, flow rate and total run time were 1  $\mu$ L, 0.35 mL/min and 15 min, respectively. Centrifuge (Hettich EBA 280, 4500 rpm), 50 mL Falcon tubes, price balance (Shimadzu), vortex (VELP scientifica), Waring blender, glass GC vials (1.5 mL) and other glassware used in the study.

Table 1. Physicochemical and toxicological properties of the fungicide of some pesticides

Parameters	Chlorpyrifos-methyl	Lambda-cyhalothrin	Tecuconazole
Chemical formula	C <sub>7</sub> H <sub>7</sub> Cl <sub>3</sub> NO <sub>3</sub> PS	C <sub>23</sub> H <sub>19</sub> ClF <sub>3</sub> NO <sub>3</sub>	C <sub>16</sub> H <sub>22</sub> ClN <sub>3</sub> O
Group	Organophosphates	Pyrethroids	Triazole
Mode of action	Non-systemic acetylcholinesterase (AChE) inhibitors nerve action	Non-systemic sodium channel modulatorsnerve action	Systemic with protective, curative and eradicant action.
<b>Physicochemical property</b>			
LogP: Octanol-water partition coefficient at pH 7, 20 °C	4.7	5.5	3.7
Solubility - In water at 20 °C (mg/L)	2.74	0.005	36
Melting point (°C)	46	49.2	105

Boiling point (°C)	Decomposes before boiling	Decomposes before boiling	Decomposes before boiling
Degradation point (°C)	175	275	350
Molecular mass (g/mol)	322.53	449.85	307.82
GUS index	0.08	-2.09	1.86
<b>Toxicological property</b>			
ADI: Acceptable Daily Intake (mg/kg/bw/day)	0.01000	0.0025	0.0300
EU MRL (mg/kg)	1.0	0.08	0.5
ARfD: Acute Reference Dose (mg/kg/bw/day)	0.100	0.005	0.030
MPI: The maximum amount permitted to be taken daily (mg / person / day)	0.60	0.15	1.80
Mammals - Acute oral LD <sub>50</sub> (mg/kg)	5000	56	1700
Mammals - Dermal LD <sub>50</sub> (mg/kg)	2000	632	2000
Mammals - Inhalation LC <sub>50</sub> (mg/L)	>0.670	0.066	> 5.090
Koc	4645	283707	-
WHO Classification *	III	II	II
Health issues	Reproductive / Growth effects Neurotoxic Cholinesterase inhibitor	Endocrine disruptor Eye irritant Skin irritant	Reproductive / growth effects, eye irritant

\* II, moderately hazardous; III, Less hazardous

### 2.1.3. Preparation of standard solution and fortification solution

Chlorpyrifos-M, lambda-cyhalothrin and tebuconazole stock solutions of 400 µg/mL were prepared with toluene. Working standard solutions (1.0 µg/mL) of 3 pesticides was obtained from stock solution by serial dilutions. Calibration solutions were prepared in MeCN with the range of 20-4000 pg / µL, 10-2000 pg / µL and 1-200 pg / µL, for chlorpyrifos-M, lambda-cyhalothrin and tebuconazole, respectively. For matrix-matched calibration (6 level), a representative commodity (apple) was used ([8],[10]). Fortification standard solutions were also prepared, corresponding to 0.1 x MRL, 1.0 x MRL and 10.0 x MRL levels. Spiking level of 10 times MRL were diluted to fit calibration.

### 2.1.4. Fortification trials and analyses

According to EU Guide [11] 1 kg of blank (pesticides free sample) grape sample homogenized with blender. 15 g homogenized sample spiked with 100 µL MeCN mixed above mentioned pesticide fortification solutions (Table 2). Tubes vortexed for 30 s and will left for 15 min for matrix penetration. Four analytical portions of

15 g was taken from each spiking level. Analysis of samples was performed with AOAC Method 2007.01 and LC-MS/MS. Schematic diagram of the method are illustrated in Figure 1.

Table 2. Spiking levels for chlorpyrifos-methyl, lambda-cyhalothrin, tebuconazole.

Fortification level	Code	Spiking levels $\mu\text{g}/\text{kg}$		
		Chlorpyrifos-methyl	Lambda-cyhalothrin	Tebuconazole,
0.1 X MRL	F1/1-4	100	8	50
1 X MRL(*)	F2/1-4	1000	80	500
10 X MRL	F3/1-4	10000	800	5000
Control	F0/1-3			

(\*)EU MRL,  $\mu\text{g}/\text{kg}$

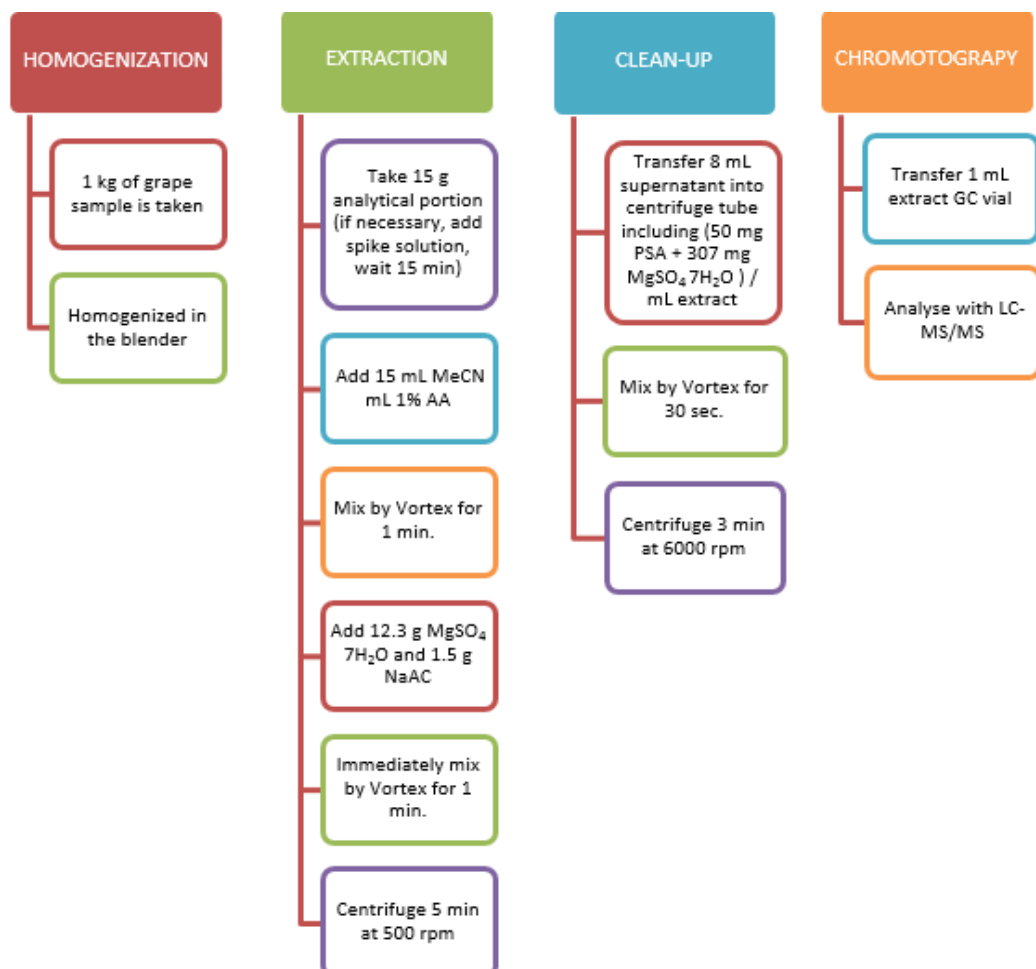


Figure 1. Schematic presentation of QuEChERS-AOAC Official Method 2007.01.

## 2.2 Method

### 2.2.1. Method validation

Validation of the method for chlorpyrifos-M, lambda-cyhalothrin and tebuconazole residues in grape was performed by spiking at 3 concentration (0.1 x MRL, 1.0 x MRL and 10.0 x MRL levels) with 4 replicate analysis. Then the evaluation was carried out with the single method validation approach [12]. The method performance was evaluated by considering some validation criteria ([8], [13]).

## 3.RESULTS AND DISCUSSION

### 3.2. Method performance and method validation

#### 3.2.1. Linearity

Chromatogram and calibration curve of pesticide were represented in Figure 2. Calibration curves of chlorpyrifos-M, lambda-cyhalothrin and tebuconazole, standard in representative sample matrix were linear over the range of 20-4000 pg/μL, 10-2000 pg/μL and 1-200 pg/μL, respectively, with R<sup>2</sup>, (R<sup>2</sup> ≥ 0.999). In matrix-matched calibrations, regression equation is known as analytical function [14]. The analytical functions of pesticides were used for quantification of the analytes.

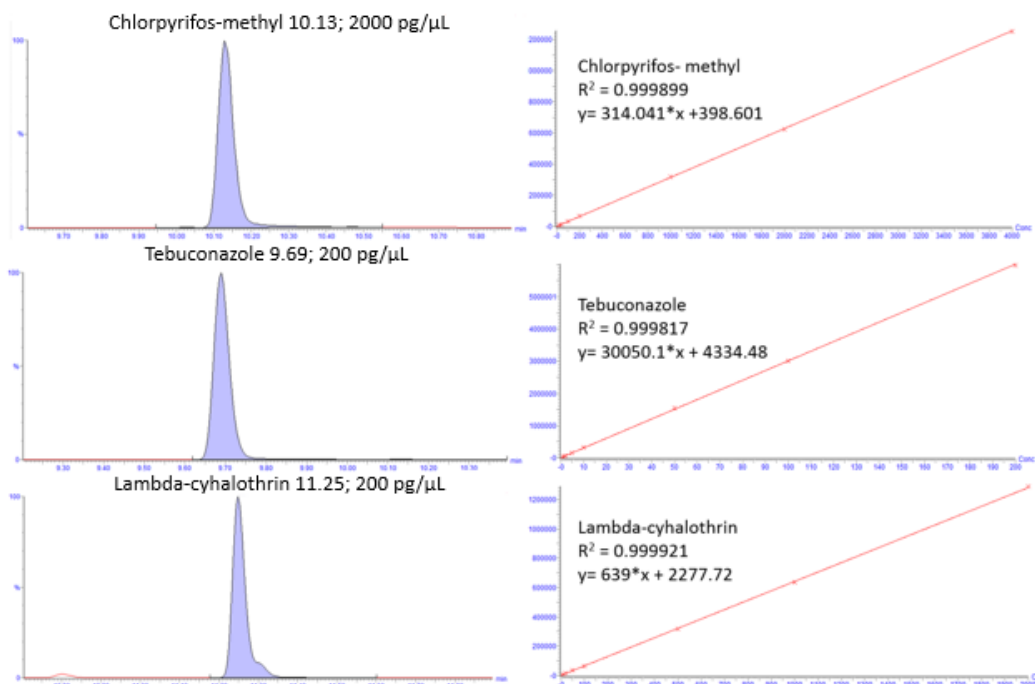


Figure 2. Chromatogram and Calibration Curve of 3 Compounds in Matrix-matched Calibration

#### 3.2.2. Chromatographic repeatability

Chromatographic repeatability was also assessed in the study. The retention time of the compounds in the extract should correspond to that of the calibration standard with a tolerance of ±0.1 min ([8],[15]). Retention times in all calibration range of chlorpyrifos-M (20-4000 pg/μL range), lambda-cyhalothrin (10-2000 pg/μL range) and tebuconazole (1-200 pg/μL range) were 10.13, 11.25 and 9.69, respectively.

#### 3.2.3. Detection limit (LOD)

Detection limit of chlorpyrifos-M, lambda-cyhalothrin and tebuconazole running method was 20, 10 and 1 μg/kg respectively. These figures, which is obtained from LC-MS/MS software programme, were less than MRL. MRL value of chlorpyrifos-M, lambda-cyhalothrin and tebuconazole for grapes were 1000, 80 and 500 μg/kg, respectively (Table 1).

### 3.2.4. Recovery, precision and accuracy

The recovery, precision and accuracy were identified in 3 parallels of analytical portions at 3 fortification levels of chlorpyrifos-methyl, lambda-cyhalothrin and tebuconazole. The recovery is the ratio of determined quantity to spiking level of the pesticide. Pesticides recoveries varied between 86-133%. The recovery ranges and mean recoveries were 91.3-131.4% (mean 114.50%), 85.8-133.2% (mean 108.05%), 90.3-111.6% (mean 102.96%) for chlorpyrifos-methyl, lambda-cyhalothrin and tebuconazole, respectively. The overall recovery of the method was 108.6% with a RSD of 11.8% (n= 108). Considering the precision of the method (closeness of repeated analyses), RSD value were identified as 11.02%, 14.15%, and 6.15% for chlorpyrifos-methyl, lambda-cyhalothrin and tebuconazole, respectively. Overall recovery of the method, standard deviation and RSD values (n=108) were 108.6%, 12.87 and 11.85%, respectively. All individual recoveries and accuracies of 3 compound as overall recovery and repeatability as RSD were within the required limit ( $60\% \leq Q \leq 40\%$  and  $RSD \leq 20\%$ ) for 3 pesticide in grape [8]. Accuracy is the closeness of the measured value to actual values. Accuracy values are given in Table 3.

Table 3. Method validation criteria obtained from recovery trials with 3 fortification levels of pesticides

Analyte	Spiking ug/kg	Found ug/kg	Recovery % (As a tool for trueness)	SD	RSD % (As a tool for trueness)	Accuracy %
Lambda-cyhalothrin	8	9.72	121.57	16.78	13.80	
	80	77.74	97.17	7.25	7.46	
	800	843.25	105.40	8.47	8.04	
	Mean recovery, n=36		108.05	15.27	14.13	108.05
	Recovery range, 85.8-133.2%					
Chlorpyrifos-methyl	100	128.69	128.69	2.02	1.57	
	1000	1123.23	112.32	8.53	7.59	
	10000	10340.55	103.40	8.60	8.32	
	Mean recovery, n=36		114.80	12.65	11.02	114.80
	Recovery range, 91.3-131.4%					
Tebuconazole	50	54.48	108.96	2.47	2.26	
	500	501.33	100.26	5.77	5.76	
	5000	4983.07	99.66	5.36	5.40	
	Mean recovery, n=36		102.96	6.33	6.15	102.96
	Recovery range, 90.3-111.6%					



Overall recovery of the method (accuracy of the method): 108.60% (n=108, SD=12.87, RSD=11.85);

Recovery range: 86-133%

#### 4.CONCLUSIONS

In this study the required method validation criteria were met. QuEChERS method was found suitable to perform 3 pesticide residue analysis in grapes under our laboratory conditions the method validation revealed high performance in terms of precision (RSD), recovery and accuracy.

#### ACKNOWLEDGMENT

This study is a part of the master degree thesis of the first Aysegul Duman (School of Graduate Studies, Department of Plant Protection, Canakkale Onsekiz Mart University). This work was also supported by Canakkale Onsekiz Mart University The Scientific Research Coordination Unit, Project number:FYL-2020-3359.

#### REFERENCES

- [1]. EC. EU Pesticide Database, <http://ec.europa.eu/food/plant/pesticides/eu-pesticides-database/public/?event=pesticide.residue.selection&language=EN> Accessed 1 Jan 2019, 2019.
- [2]. Anastasiades, M. Lehotay, S.J. Stajnbaher, D. Schenck, F.J., "Fast and easy multiresidue method employing acetonitrile extraction/partitioning and dispersive solid-phase extraction for the determination of pesticide residues in produce" J.AOAC Int., vol. 86, pp. 412–431, 2003.
- [3]. S.J. Lehotay, "Determination of pesticide residues in foods by acetonitrile extraction and partitioning with magnesium sulfate: collaborative study" J. AOAC Int., vol 90, pp. 485–520, 2007
- [4]. P.Y. Omeroglu, D. Boyacioglu, A. Ambrus, A. Karaali, S. Saner, "An Overview on steps of pesticide residue analysis and contribution of the individual steps to the measurement uncertainty" Food Analytical Methods., vol.5, pp.1469-1480, 2012.
- [5]. O. Tiryaki, "Method validation for the analysis of pesticide residues in grain by thin-layer chromatography" Accreditation and Quality Assurance., vol 11(10), pp.506-514, 2006.
- [6]. O. Tiryaki, "Validation of QuEChERS Method for the determination of some pesticide residues in two apple varieties" Journal of Environmental Science and Health Part B-Pesticides Food Contaminants and Agricultural Wastes, vol.51(10), pp. 722-729, 2016.
- [7]. O. Tiryaki, "Pestisit Kalinti Analizlerinde Kalite Kontrol (QC) ve Kalite Guvencesi (QA)", Nobel Yayinevi, p. 2, ISBN 978-605-320-604-0, 2017.
- [8]. SANTE, Guidance document on analytical quality control and method validation procedures for pesticides residues analysis in food and feed. SANTE/11813/2017.
- [9]. (2020) The TUIK website. [online]. Available: <https://biruni.tuik.gov.tr/medas/?locale=tr>
- [10]. CAC, Representative commodities/samples for validation of analytical procedures for pesticide residues. In Codex Alimentarius Commission Guidelines on good laboratory practice in pesticide residue analysis. CAC/GL 40-1993. [http://www.fao.org/input/download/standards/378/cxg\\_040e.pdf](http://www.fao.org/input/download/standards/378/cxg_040e.pdf). Accessed 1 Jan 2019.
- [11]. EC, Commission Directive 2002/63/EC of 11 July 2002 Establishing community methods of sampling for the official control of pesticide residues in and on products of plant and animal origin and repealing. <https://eur-lex.europa.eu/legal-content/EN/TXT/PDF/?uri=CELEX:32002L0063&from=EN> Accessed 1 Jan 2019, 2002.
- [12]. M. Thompson, S.L.R. "EllisonWood, R. Harmonized guidelines for single laboratory validation of methods of analysis" Pure Appl. Chem, vol. 74(5), pp. 835–855, 2002.
- [13]. B.Kanrar, S. Mandal, A. Bhattacharyya, "Validation and uncertainty analysis of a multiresidue method for 42 pesticides in made tea, tea infusion and spent leaves using ethyl acetate extraction and liquid chromatography–tandem mass spectrometry" J. Chromatogr. A. 1217, 1926–1933, 2010
- [14]. O. Tiryaki, D. Baysoyu, E. Secer, G. Aydin, "Testing the stability of pesticides during sample processing for the chlorpyrifos and malathion residue analysis in cucumber including matrix effects" Bull of Environ Contam Toxicol, vol. 80(1) pp. 38–43, 2008
- [15]. M. Branković, D. Andelković, H. Kocić, G. Kocić, "Assessment of GC–MS response of selected pesticides in apple matrices related to matrix concentration" Journal of Environmental Science and Health, Part B, 2019.

#### BIOGRAPHY

Aysegul Duman, Canakkale 18 Mart University, Faculty of Agriculture, Department of Plant Protection, Graduate Student Graduate School of Education.

# ICENS

7TH INTERNATIONAL CONFERENCE ON  
ENGINEERING AND NATURAL  
SCIENCES

